Probing inorganic and organic paths through spin-driven transport

Kostantine Katcko

Probing Inorganic and Organic Nanospintronic Paths

THÈSE DE DOCTORAT

pour obtenir le grade de

Docteur de l'Université de Strasbourg
Discipline/Spécialité : Physique

Université de Strasbourg
École Doctorale de Physique et Chimie-Physique
Institut de Physique et Chimie des Matériaux de Strasbourg

présentée par

KATCKO Kostantine

soutenue le : 25 Octobre 2019

Membres du jury:

Directeur de thèse	
Dr. BOWEN Martin	IPCMS - Université de Strasbourg
Rapporteurs	
Dr. EBELS Ursula	Spintec - Grenoble
Dr. SANCHEZ Rafael	Universidad Autonoma de Madrid
Examinateur	
Dr. MATTANA Richard	Thales - Universite Paris-Sud
Pr. MOODERA Jagadeesh Subbaiah	MIT
Pr. VAN SLAGEREN Joris	IPC - University of Stuttgart

Acknowledgment

My very first greetings are dedicated to you the dear reader of this Ph.D. manuscript. As this work takes its origins from scientific curiosity, I hope that you will be able to thirsts your curiosity and maybe even find inspiration for your research aspirations. I would like this work to be considered as a snapshot of an always ongoing exploration of solid-state physics. Most of the results presented in this document were acquired between 2016 and 2019. The theoretical basis of this work was developed in tight collaboration and mostly by my Ph.D. supervisor Dr. Martin Bowen. In this respect, I would like to continue this acknowledgment section by kindly thanking Martin Bowen first of all for taking me on board in his research team. Moreover, I am very grateful to Martin Bowen for his skillful and proficient supervision of my work. Under his guidance, I learned a lot of technical know-hows but also interpersonal skills. Most importantly, Martin Bowen thought all of us how to pursue your aspirations regardless of the external constraints. I am strongly convinced that our collaborative teamwork was very enriching and shaping and exceeds any of the initial objectives. During these three years, we were able to bring to maturity the pertinence of oxide vacancies in tunneling solid-state devices, we explored their optical addressing using different light sources, we demonstrated novel energy-harvesting concepts and we highlighted the rich potential of hybrid organic devices for next-generation information storage and processing solutions. Thereafter, I would like to thank Dr. Filip Schleicher who worked as a Postdoc in our group during my Ph.D. Filip is a skillful scientist with very strong engineering skills who thought me a myriad of technical details. Additionally, I want to thank Filip for introducing me to cleanroom microelectronic processing, plasma etching, and multifunctional characterization of individual memory stacks. Dr. Etienne Urbain is another central person who contributed to the organic spintronics exploration. Etienne's stoicism and commitment gave fruitful results under the form of a new cutting-edge process for single organic memory stacks patterning. This achievement is considered a major milestone promoting the exploration of organic spintronic devices. I show great gratitude towards Dr. Ufuk Halisdemir who successfully developed the multi-functional bench (BMF) that was used for most of the herein presented transport characterization results. Moreover, Dr. Ufuk Halisdemir was at the origin of the optical addressing of vacancies in solid-state devices. I would like furthermore to thank Pr. Mebarek Alouani and Dr. Beata Taudul and Franck NGASSAM NYAKAM for their theoretical ab-initio input which enabled us to shine a light on our most experimental observations of physical phenomena's. A tremendous theoretical input was brought by Pr. Jonas Fransson from Uppsala University in Sweden. This input consists of the development of an out-of-equilibrium spin-dependent transport model. This analytical model enabled us to shine a light on energy-harvesting processes taking birth along nanotransport paths under peculiar conditions. I would like to kindly thank Lalit Kandpal and Bhavishya Chowrira

two Ph.D. students with whom I had the pleasure to cooperate on multiple projects. You were very reliable and enthusiastic colleagues. I wish you a smooth Ph.D. defense and of course successful professional insertion. I would like to thank Pr. Sami Boukari for fruitful scientific discussions and his pertinent and guiding observations. Fruitful and inspiring discussion Sambit Mohapatra a Ph.D. student with whom we shared the office. T hank you for your involvement in the 2018 synchrotron run and the long night shifts we did together at the beam-line. Garen Avedissian a Ph.D. fellow who supported magnetometry metrology inspections on our memory stacks. I confidently believe that you dispose of a unique combination of scrupulous and dedication characters, these are very valuable for a researcher. A colossal acknowledgment is attributed to all of the Jury members, namely, Ursula Ebels, Rafael Sanchez, Richard Mattana, Jagadeesh Subbaiah Moodera, and Joris Van Slageren, who kindly accepted to assist at my Ph.D. defense and who evaluated my work with their colossal expertise on the matter. State of the art research requires cutting edge technologies; hence, I would like to acknowledge the technical staff members numerous facilities employed in this Ph.D. project. Namely, Pr. Michel Hehn and his group from IJL institute in Nancy – France for their effort in memory layers growth, Hicham Majjad and the technical staff of the STnano clean-room facility, and all of my home institute IPCMS – France engineers involved in the IBE etching of individual memory devices. I would like to express my most profound gratitude to the ones who supported me for all these long years – my family. Namely, my grand-parents, brother Yacov, mother Olga, and father Eduard. You were and are always there to back me up when needed, under the most challenging circumstances. I clearly understand that without such faithful friends the yellow brick road I followed would have been Dedalus's labyrinth. I was lucky enough to meet oodles of sincere, trustful, and enriching people, you are too many to properly name in this short preface. So just thank you very much for being there when it was really needed. Compiling this long tirade in one final sentence. I am endlessly delightful for all the ups and downs, uncertainties, oblique challenges, and for every stage of this epic odyssey.

This Ph.D. manuscript is dedicated to you my beloved father Eduard as well as you my dear reader.

Contents

Chapter 1

General introduction

The field of integrated circuits follows the trend of the constant miniaturization of its elements. Modern electronic devices are usually assembled from complex thin-film heterostructures. The use of new organic/inorganic materials, in the interest of expressing their novel properties, combined with reduced dimensionality, underscores the need to understand how a device electrically responds at the single-atom level. In this thesis manuscript, we present the results of our investigation of these nanotrasnport paths in next-generation and common-place spintronic devices. In Part I, we emphasize the role of oxygen vacancies in commonly used magnesium-oxide-based spintronics. Additionally, we discuss how to optically address these localized-states to alter and tune the spintronic properties of devices containing them. In Part II we present a novel manner to generate useful electrical power with spintronic devices by employing its magnetic energy and harvesting thermal fluctuations on paramagnetic centers. In the last Part III of this manuscript, we discuss an alternative (or parallel) branch of spintronics, namely organic spintronics. We present our novel work on bias-tunable magnetoresistance effects arising in molecular devices as a direct consequence of the formation of molecular magnetism and its electronic properties.

Traduction en Français:

Introduction Générale

Le domaine des circuits intégrés suit la tendance de la miniaturisation constante de ses éléments. Les appareils électroniques modernes sont généralement assemblés à partir d'hétérostructures complexes à couches minces. L'utilisation de nouveaux matériaux organiques / inorganiques, dans l'intérêt d'exprimer leurs nouvelles propriétés, combinée à une dimensionnalité réduite, souligne la nécessité de comprendre comment un appareil répond électriquement au niveau d'un seul atome. Dans ce manuscrit de thèse, nous présentons les résultats de notre enquête sur ces chemins de nanotrasnport dans des dispositifs spintroniques de nouvelle génération et communs. Dans la partie Part I, nous soulignons le rôle des lacunes d'oxygène dans la spintronique à base d'oxyde de magnésium couramment utilisée. De plus, nous discutons de la manière d'aborder optiquement ces états localisés pour modifier et régler les propriétés spintroniques des dispositifs les contenant. Dans la partie Part II, nous présentons une nouvelle manière de générer de l'énergie électrique utile avec des dispositifs spintroniques en utilisant son énergie magné-

tique et en récoltant les fluctuations thermiques sur les centres paramagnétiques. Dans la dernière partie Part III de ce manuscrit, nous discutons d'une branche alternative (ou parallèle) de la spintronique, à savoir la spintronique organique. Nous présentons nos nouveaux travaux sur les effets de magnétorésistance accordables en polarisation apparaissant dans les dispositifs moléculaires comme conséquence directe de la formation du magnétisme moléculaire et de ses propriétés électroniques.

Part I

Spintronics of Oxygen Vacancies

Chapter 2

Introduction to tunneling spintronics

At the beginning of the 20^{th} century science experienced its own renaissance period carried by the development of the quantum mechanical theory. This fundamentally novel approach postulates that nature at a very small scale is described by discrete quantities, hence, it is quantized. One of the most stunning effects of quantum mechanics is the probabilistic treatment of elementary particles, known under the uncertainty principle of Heisenberg. It dictates that the position and the momentum of an elementary particle can't be exactly known simultaneously therefore it should be treated in a probabilistic manner. A direct consequence of this effect is quantum tunneling. When a particle with given energy encounters a higher energy barrier it has a non-zero probability to cross the barrier. Quantum tunneling takes place in numerous natural phenomena and is utilized in many different technical solutions. Examples include the solar energy produced by the sun-generated by fusion [1] or the memory elements in our computers based on Flash technology [2]. This is why we believe that refining the current understanding of quantum tunneling in consumer electronic devices has a high impact factor on the technological advancement of our society. We perform our studies on a common-place system named magnetic tunnel junctions (MTJs). They consist of two ferromagnetic electrodes separated by a nanometers thick insulating layer. In MTJs, charge carriers tunnel from one electrode to another through the thin insulating layer. The tunneling rates of the incident charge carriers can depend on their quantum angular momentum3, namely their spins or (and) on their Bloch wavefunction in periodic systems. Ferromagnetic materials (FM) are defined by an asymmetric spin population close to the Fermi level, hence the tunneling process between the two such FM electrodes will be spin asymmetric i.e. spin-polarized [3]. In consequence, altering the magnetic configuration of the MTJ's FM electrodes by an external magnetic field results in its resistance change and gives rise to the tunneling magnetoresistance (TMR) effect. The field investigating spin-polarized transport in solid-state devices is also known as Spintronics. The first documented demonstration of the TMR effect in a ferromagnet-insulator-ferromagnet trilayer goes back to 1975 when Julliere demonstrated a pioneering 14% TMR signal at a low 4.2K temperature and in an Iron-Germanium-Cobalt junction [4] and associated it to spin-polarized tunneling. The interpretation of spin-polarized tunneling by means of the spin channels model was provided a decade later independently by Baibich et al. [5] and by Binash et al. [6]. The next big leap was the demonstration of the room-temperature TMR effect back in 1995 [7]. The current most well-known application of MTJs and the TMR effect is found in magnetic random-access memory (MRAM)

data storage technology [8], where the magnetic and thus resistance state of an MTJ is utilized to store information in a binary numeral system. The tunneling transport taking place through the MTJs spacer can alter the magnetic configuration of the device through the so-called spin-transfer torque (STT) effect [9] in which the incident spin-polarized tunneling electrons exert a torque on the magnetization of the collecting electrode, such that at high enough current densities, it is possible to switch the magnetic configuration of the MTJ device. High TMR ratios ($> 150\%$) are required for commercial storage applications since they define their information write/erase margins. However, real-life devices are continuously showing smaller than the theoretically predicted TMR signals. The most common candidate of the MTJs insulating spacer community is magnesium-oxide (MgO), due to a synergistic combination of electronic structure with that of ferromagnetic electrodes as we will see hereafter. Unavoidably, defects, and impurities appear in the MgO structure during the MTJ growth/processing steps. These point-defects generate discrete energy levels within the barrier gap of the MgO, which lower the barrier height felt by the incident charge carriers. One of the main aspirations for this research project was to pursue and refine the previous group's works [10–14] on the effect of oxygen vacancies within the MgO barrier on the magnetoresistance response of spintronic devices. In this respect, we've investigated the energy profile of the dielectric's potential step with a spectroscopical technique labeled $\hat{\mathrm{I}}$ or $\mathrm{I_{rel}}$ [10, 15]. It probes the magnetotransport response of an MTJ under bias and temperature so as to reveal the transport feature. In combination with the ab-initio theory, this technique provides helpful insight into the potential landscape of the MgO dielectric material embedded within an MTJ device. Applying this approach to commonplace MgO-based sputtered MTJs, we have demonstrated that oxygen vacancies form localized states within the band-gap of the MgO spacer and are involved in tunneling transport. These states are confined in energy and generate low-energy barrier heights that are experimentally discernable in the magnetotransport response. The first section of this part briefly introduces the magnetoresistance effect from a general standpoint in epitaxial and further in sputtered commonplace MTJs. The second section briefly depicts the technical aspects of this study such as the lithography process and basic samples characterization metrics. The third section is devoted at first to the experimental and theoretical efforts performed to investigate and attribute thermally activated magnetotransport features to low barrier heights within the band-gap of MgO and consequently to single and double oxygen vacancies. This work emphasizes that defect states inevitably affect the potential landscape of the dielectric spacer of MTJ devices especially affects their low bias-voltage room-temperature operation. Secondly, the portrayed electronic footprint of defect states can be judiciously utilized in their optical addressing to alter the spintronic properties of MTJs featuring such entities. This demonstration relies on the successful separation of the trial thermal effects of probing MTJs with photons from the optically activated electronic effects that are generated by the addressing of specific oxygen-vacancies species.

Traduction en Français:

Introduction à la spintronique à effet tunnel

Au début du 20e siècle, la science a connu sa propre période de renaissance portée par le développement de la théorie de la mécanique quantique. Cette approche fondamentalement nouvelle postule que la nature à très petite échelle est décrite par des quantités discrètes, par conséquent, elle est quantifiée. L'un des effets les plus étonnants de la mécanique quantique est le traitement probabiliste des particules élémentaires, connu sous le principe d'incertitude de Heisenberg. Il dicte que la position et la quantité de mouvement d'une particule élémentaire ne peuvent pas être exactement connues simultanément et doivent donc être traitées de manière probabiliste. Une conséquence directe de cet effet est le tunnel quantique. Lorsqu'une particule avec une énergie donnée rencontre une barrière d'énergie plus élevée, elle a une probabilité non nulle de traverser la barrière. Le tunneling quantique se produit dans de nombreux phénomènes naturels et est utilisé dans de nombreuses solutions techniques différentes. Les exemples incluent l'énergie solaire produite par le soleil générée par fusion [1] ou les éléments de mémoire dans nos ordinateurs basés sur la technologie Flash [2]. C'est pourquoi nous pensons que le raffinement de la compréhension actuelle du tunnel quantique dans les appareils électroniques grand public a un impact important sur l'avancement technologique de notre société. Nous réalisons nos études sur un système commun nommé jonctions tunnel magnétiques (MTJ). Ils sont constitués de deux électrodes ferromagnétiques séparées par une couche isolante d'une épaisseur de nanomètres. Dans les MTJ, les porteurs de charge passent d'une électrode à une autre à travers la mince couche isolante. Les taux de tunnel des porteurs de charge incidents peuvent dépendre de leur moment angulaire quantique3, à savoir leurs spins ou (et) de leur fonction d'onde de Bloch dans les systèmes périodiques. Les matériaux ferromagnétiques (FM) sont définis par une population de spin asymétrique proche du niveau de Fermi, d'où le processus de tunneling entre ces deux électrodes FM sera asymétrique en spin, c'est-à-dire polarisé en spin [3]. En conséquence, la modification de la configuration magnétique des électrodes FM du MTJ par un champ magnétique externe entraîne un changement de résistance et donne lieu à l'effet de magnétorésistance tunnel (TMR). Le domaine qui étudie le transport polarisé en spin dans les dispositifs à semiconducteurs est également connu sous le nom de spintronique. La première démonstration documentée de l'effet TMR dans un trilayer ferromagnet-isolant-ferromagnet remonte à 1975, lorsque Julliere a démontré un signal TMR pionnier à 14% à une température basse de 4,2K et dans une jonction fer-germanium-cobalt [4] et associé à effet tunnel polarisé en spin. L'interprétation de l'effet tunnel polarisé en spin au moyen du modèle des canaux de spin a été fournie une décennie plus tard de manière indépendante par Baibich et al. [5] et par Binash et al. [6]. Le prochain grand saut a été la démonstration de l'effet TMR à température ambiante en 1995 [7]. L'application actuelle la plus connue des MTJ et de l'effet TMR se trouve dans la technologie de stockage de données à mémoire vive magnétique (MRAM) [8], où l'état magnétique et donc de résistance d'un MTJ est utilisé pour stocker des informations dans un système numérique binaire. Le transport tunnel qui a lieu à travers l'entretoise MTJs peut modifier la configuration magnétique du dispositif

par l'effet dit de couple de transfert de spin (STT) [9] dans lequel les électrons tunnels incident polarisés en spin exercent un couple sur la magnétisation de l'électrode collectrice, de sorte qu'à des densités de courant suffisamment élevées, il est possible de commuter la configuration magnétique du dispositif MTJ. Des taux de TMR élevés (> 150%) sont nécessaires pour les applications de stockage commerciales car ils définissent leurs marges d'écriture / d'effacement des informations. Cependant, les appareils réels affichent en permanence des signaux plus petits que les signaux TMR théoriquement prévus. Le candidat le plus courant de la communauté des espaceurs isolants MTJ est l'oxyde de magnésium (MgO), en raison d'une combinaison synergique de la structure électronique avec celle de l'électro-ferromagnétique. trodes comme nous le verrons plus loin. Inévitablement, des défauts et des impuretés apparaissent dans la structure MgO au cours des étapes de croissance / traitement MTJ. Ces défauts ponctuels génèrent des niveaux d'énergie discrets dans l'espace de barrière du MgO, qui abaissent la hauteur de barrière ressentie par les porteurs de charge incidents. L'une des principales aspirations de ce projet de recherche était de poursuivre et d'affiner les travaux du groupe précédent [10–14] sur l'effet des lacunes d'oxygène au sein de la barrière MgO sur la réponse magnétorésistante des dispositifs spintroniques. À cet égard, nous avons étudié le profil énergétique du pas de potentiel du diélectrique avec une technique spectroscopique appelée I^ ou Irel [10, 15]. Il sonde la réponse de magnétotransport d'un MTJ sous polarisation et température afin de révéler la caractéristique de transport. En combinaison avec la théorie ab-initio, cette technique fournit un aperçu utile du paysage potentiel du matériau diélectrique MgO intégré dans un dispositif MTJ. En appliquant cette approche aux MTJ pulvérisés à base de MgO, nous avons démontré que les lacunes d'oxygène forment des états localisés dans la bande interdite de l'espaceur MgO et sont impliquées dans le transport par tunnel. Ces états sont confinés dans l'énergie et génèrent des hauteurs de barrière à basse énergie qui sont expérimentalement discernables dans la réponse du magnétotransport. La première section de cette partie présente brièvement l'effet de magnétorésistance d'un point de vue général dans les MTJ épitaxiales et plus loin dans les MTJ banales pulvérisées. La deuxième section décrit brièvement les aspects techniques de cette étude tels que le processus de lithographie et les métriques de base de caractérisation des échantillons. La troisième section est consacrée dans un premier temps aux efforts expérimentaux et théoriques réalisés pour étudier et attribuer des caractéristiques de magnétotransport thermiquement activées à de faibles hauteurs de barrière dans la bande interdite du MgO et par conséquent à des lacunes d'oxygène simples et doubles. Ce travail souligne que les états de défaut affectent inévitablement le paysage potentiel de l'entretoise diélectrique des dispositifs MTJ affecte en particulier leur fonctionnement à basse tension de polarisation à température ambiante. Deuxièmement, l'empreinte électronique représentée des états de défaut peut être utilisée judicieusement dans leur adressage optique pour modifier les propriétés spintroniques des MTJ comportant de telles entités. Cette démonstration s'appuie sur la séparation réussie des effets thermiques d'essai du sondage des MTJ avec des photons des effets électroniques activés optiquement qui sont générés par l'adressage d'espèces de lacunes d'oxygène spécifiques.

Chapter 3

Theoretical and Experimental Background

The field of spintronics describes the flow of the charge carriers with respect to their intrinsic magnetic moment generated by their angular momentum, namely their spin. Commonly studied spintronic devices are composed of an insulating material surrounded by both sides by ferromagnetic material. This heterostructure is also called magnetic tunnel junctions (MTJs). The spin imbalance at the ferromagnetic electrodes in combination with quantum tunneling gives rise to spin-dependent tunneling processes. The main objective of this section is at first to briefly introduce the reader to the so-called magnetoresistance (TMR) effect in a rather classical approach, and afterward to describe the origins of the TMR effect in most commonplace MgO-based MTJs in terms of quantum mechanical symmetries filtering.

3.1 Tunneling principles

The wavefunction of an isolated quantum system is a mathematical function describing all of its quantum degrees of freedom. In the quantum mechanical framework, when a wave-function of a given energy E encounters a higher energy barrier Φ $(\mathrm{E} < \Phi)$, a fraction is reflected whereas the other fraction is transmitted to the other side of the barrier. These reflection and transmission coefficients can be evaluated by solving the Schrodinger equation with the continuity conditions at the interface. The transmission probability is proportional to $\mathrm{P} \approx \mathrm{e}^{-\mathrm{kd}}$, where k is the decay rate in the barrier and d its thickness. When the energy barrier is thin, the wavefunction after tunneling may remain of non-zero amplitude (see Figure 3.1): the particle described by the wavefunction has effectively tunneled through the barrier.

This elementary description of quantum tunneling depicts in a first approach how charge carriers' tunnel through the insulating barrier is embedded in magnetic tunnel junctions. Yet, since the electrodes on both sides of the insulating spacer are ferromagnetic the spin population of charge carriers is imbalanced on both sides of the potential step generated by the barrier, this results in spin-dependent tunneling in MTJs.

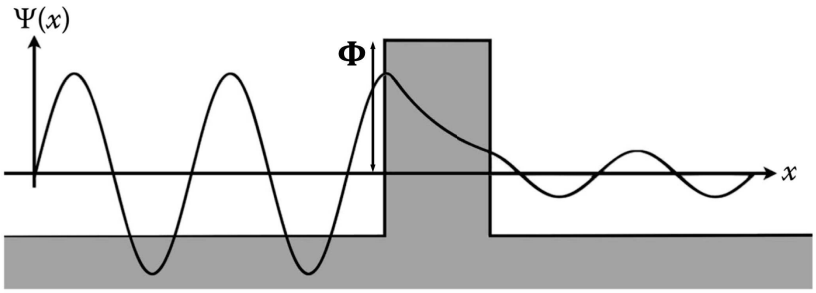

Figure 3.1: **Quantum tunneling effect:** A wavefunction encounters a higher energy barrier Φ of thickness d and tunnels to the other side. The amplitude of the tunneling wavefunction undergoes an exponential reduction during the tunneling process. Figure taken from ref [16].

3.1.1 Spin-dependent tunneling

Historically in the early '60s, Simmons et al. [17] derived the theory of tunneling current through asymmetrical metal-insulator-metal (MIM) system. Further, Brinkman refined this formalism by expanding it to the case of an asymmetrical barrier, when both metal-insulator interfaces are different in energy [18]. Both of these approaches don't take into consideration the DOS of the metallic electrodes, hence don't treat the case of spin-dependent tunneling in magnetic tunnel junctions. Further, Meservey and Tedrow worked on the experimental demonstration of spin-polarized tunneling [19, 20]. They were able to measure a spin-dependent tunneling current across a ferromagnet-insulator-superconductor trilayer. The superconductor acts as a spin-detector for the incident tunneling current whereas the FM electrode acts as a spin-injector since it is characterized by a spin-polarization (SP) at the Fermi level defined as:

$$\mathrm{SP} = \frac{\rho_{\uparrow} - \rho_{\downarrow}}{\rho_{\uparrow} + \rho_{\downarrow}} \tag{3.1}$$

Where $\rho_{\uparrow}$ and $\rho_{\downarrow}$ are the tunneling DOS of FM electrodes for the majority and minority electrons. Below the curie temperature ($\mathrm{T_C}$) of the superconductor, its DOS is characterized by a 2Δ energy gap around the Fermi level and aberrations at $\pm\Delta$, as represented in Figure 3.2.a by solid and dotted lines, respectively. These sharp features in the DOS of the detector will give generate prominent features in the conductance measurement of the device, corresponding to a stronger tunneling current at these energy values. To detect a spin-polarized tunneling current, a Zeeman splitting of $\mu_{\mathrm{B}}\mathrm{H}$ is induced within the superconductor layer by a magnetic field H applied in-plane. In consequence, the spin-up (dotted lines) and down (solid lines) DOS are split by $2\mu_{\mathrm{B}}\mathrm{H}$. The spin-split sharp features in the detector's DOS enable the detection of spin-dependent contributions to the tunneling current. Figure 3.2.b represents the case of a metal injecting electrode that gives rise to symmetric peaks in the conductance, since it's spin-unpolarized. The total conductance is the simple sum of spin up and down channels since the spin is conserved during tunneling, excluding spin-flip events. Consequently, when the metal is replaced by a ferromagnetic

electrode, the peaks are asymmetric and proportional to the spin-polarized transport channels. The spin-polarization of the ferromagnetic electrode at the Fermi level is equivalent to the values of the four conductance peaks σ_1, σ_2, σ_3 and σ_4 in the following way:

$$\mathrm{P}(\mathrm{E_F}) \approx \frac{(\sigma_4 - \sigma_2) - (\sigma_1 - \sigma_3)}{(\sigma_4 - \sigma_2) + (\sigma_1 - \sigma_3)} \tag{3.2}$$

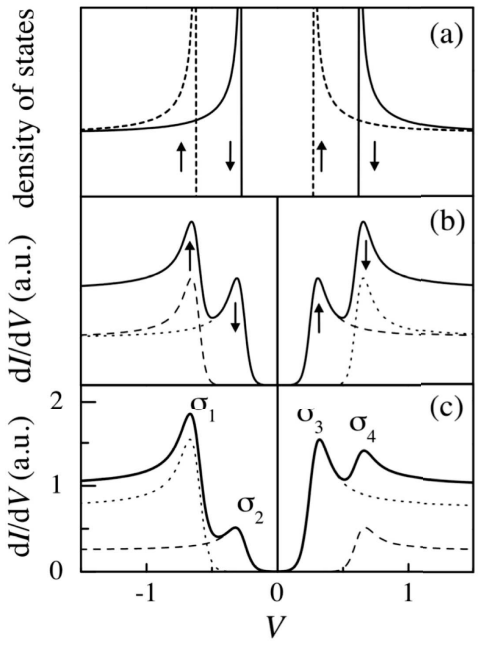

Figure 3.2: **Spin-dependent tunneling:** (a) DOS of a superconducting layer and a field-induced Zeeman splitting. The solid line for spin-down and dotted one for spin-up. (b) Conductance plot of a metal-insulator-superconductor junction. Symmetric peaks denote a spin-unpolarized tunneling current. (c) The footprint of spin-polarized tunneling current, since the metal is replaced by a ferromagnet, resulting in asymmetric conductance peaks. Figure taken from ref [21].

3.2 Tunneling magnetoresistance Effect

In 1975, a few years after the pioneering work of Meservey and Tedrow the concept of spin-polarized tunneling was further developed by Julliere [4]. Julliere proposed a formalism treating spin-polarized tunneling within a magnetic tunnel junction based on the SP-DOS (Eq: 3.1) of the two FM electrodes. His concept is based on two hypotheses: i) The electron's probability to tunnel through the insulator layer is proportional to the product of the available (in FM_1) and accessible (in FM_2) states, i.e. to other FM densities of states; ii) The tunneling charge carrier conserves its spin-state, thus doesn't undergo a spin-flip event in the barrier. In such a way, an electron of a given spin in the left electrode FM_1 can tunnel to the right electrode FM_2 only if the same state is available. Therefore, according to the two current model the total conductance is simply the sum of the majority and minority channels and can be expressed in the following way:

$$\mathrm{G_P} \approx \rho_1^{\uparrow} * \rho_2^{\uparrow} + \rho_1^{\downarrow} * \rho_2^{\downarrow} \tag{3.3}$$

$$\mathrm{G_{AP}} \approx \rho_1^{\uparrow} * \rho_2^{\downarrow} + \rho_1^{\downarrow} * \rho_2^{\uparrow} \tag{3.4}$$

Where $\mathrm{G_P}$ and $\mathrm{G_{AP}}$ are the total conductances in the parallel (P) and antiparallel (AP) configurations of the two FM electrodes and ρ_1 and ρ_2 are the respective SP-DOS available for tunneling. It is clear that the magnetic configuration of the FM electrodes alters the available densities of states, and thus affects the conductance, leading to the tunneling magnetoresistance (TMR) effect (Eq: 3.5). Figure 3.3 schematically visualizes Julliere's formalism of TMR effect and the two-current model.

In the parallel configuration, the majority electrons in the injection (FM_1) electrode find more available states in the detection (FM_2) electrode than the minority electrons in their respective channel. This results in $\rho_1^{\uparrow} * \rho_2^{\uparrow} > \rho_1^{\downarrow} * \rho_2^{\downarrow}$. On the other hand, in the antiparallel configuration the DOS of FM_2 is altered which results in majority-minority ($\rho_1^{\uparrow} * \rho_2^{\downarrow}$) and minority-majority ($\rho_1^{\downarrow} * \rho_2^{\uparrow}$) transport channels. The resulting conductances G in the two magnetic configurations are different, $\mathrm{G_P} \neq \mathrm{G_{AP}}$, and therefore we can define the tunneling magnetoresistance ratio equivalent to this difference:

$$\mathrm{TMR} = \frac{\mathrm{G_P} - \mathrm{G_{AP}}}{\mathrm{G_{AP}}} = \frac{\mathrm{R_{AP}} - \mathrm{R_P}}{\mathrm{R_P}} \tag{3.5}$$

As Meservey and Tedrow previously showed, the polarization of an FM electrode can be expressed in Eq: 3.1, hence, Julliere expressed the TMR ratio as a function of the respective electrodes spin-polarization P_1 (FM_1) and P_2 (FM_2):

$$\mathrm{TMR} = \frac{2\mathrm{P}_1\mathrm{P}_2}{1 - \mathrm{P}_1\mathrm{P}_2} \tag{3.6}$$

In his novel work, Julliere experimentally observed a 14% TMR signal at a low 4.2K temperature within a Fe-Ge-Co junction, which is slightly smaller than his own prediction of 26% using Meservey's and Tedrow's spin polarization of Fe and Co. Yet, Julliere's model of TMR remains a qualitative interpretation of spin-polarized tunneling in magnetic

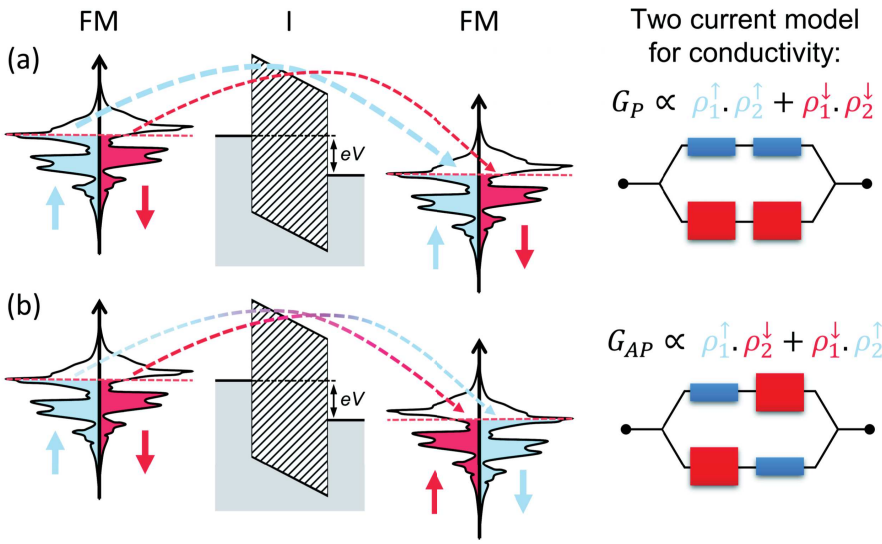

Figure 3.3: **Tunneling magnetoresistance according to Julliere's formalism:** The electron tunnels from FM_1 to FM_2 between the respective majority (↑) and minority (↓) states in (a) the parallel (P) case, while in (b) the antiparallel (AP) case the spin referential of the magnetic electrode flipped electrode is reversed. On the right, the respective conductance within the two-current model is shown. Figure taken from ref [22].

tunnel junctions. In some cases, Julliere's model is able to predict well both the sign and the amplitude of TMR in some cases [23, 24]. However, it turns out that the amplitude, and even the sign, of P depend on how orbital overlap occurs at a given MTJ interface since it impacts wavefunction hybridization toward solid-state tunneling [25, 26]. A more complete model taking into account the structural and therefore the quantum structure of the entire device in question is required. The next section 3.2.1 presents a more refined view of spin-polarized tunneling in FM-I-FM systems.

3.2.1 First principles approach in the ideal case

In the previous section, we briefly discussed the early qualitative descriptions of spin-polarized tunneling and the resulting Julliere's model of TMR. This interpretation didn't take into consideration the nature of the tunneling particles, neither the electrode-barrier interface nor the electronic structure of the insulating barrier. Therefore, it remains a pedagogical simplified model. Once the quantum mechanical properties of the entire system are considered a more complete interpretation can be given. This more detailed description will be done using the canonical example of an epitaxial Fe/MgO/Fe system since it is a relatively simple trilayer that can be theoretically investigated through first-principle calculations. It also widely contributed to the development of spintronics since highly spin-polarized currents was historically predicted in these systems [27]. We will start by introducing the crystalline structure of the epitaxial Fe/MgO/Fe trilayer parallelly evoking

the importance of the interfacial Fe/MgO structure in the tunneling process. Further, we will see why the tunneling of charge carriers along the lateral direction (*xy* plane) is essential for spin-polarized currents, thus the magnetoresistance effect. And finally, the decay rates of tunneling charge carriers in the MgO barrier gap will be addressed.

3.2.2 Crystalline structure: epitaxial Fe/MgO/Fe system

In the field of condensed-matter, the crystalline and especially interfacial structure of thin layers heterostructures is known to play a major role in their magnetic, electronic, and spintronic properties. The crystalline structure of magnesium oxide (MgO) is defined by the transfer of charges between Mg^{2+} and O^{2-} ions. MgO forms a rock-salt face-centered cubic (fcc) structure along the (001) direction characterized by the lattice parameter $\mathrm{a_{MgO}}$ = 0.421nm. On the other hand, the crystalline structure of iron (Fe) is body-centered cubic (bcc) characterized by the lattice parameter $\mathrm{a_{Fe}}$ = 0.287nm. The difference in the lattice parameters dictates that when thin layers of MgO are grown on a Fe bcc (001) structure, they rotate by 45° to compensate for the lattice mismatch ($\mathrm{a_{MgO}} = \sqrt{2}\mathrm{a_{Fe}}$). This forms a Fe(001)[110]//MgO(001) structure with a 3.7% lattice mismatch at the interface. This relatively small lattice mismatch is responsible for the proper matching of wave-functions at the Fe/MgO interface. The interfacial structure of Fe/MgO(001) is schematically represented in Figure 3.4. This structural description is relevant solely for epitaxial systems [28] and differs in sputtered textured MgO-based junctions [29].

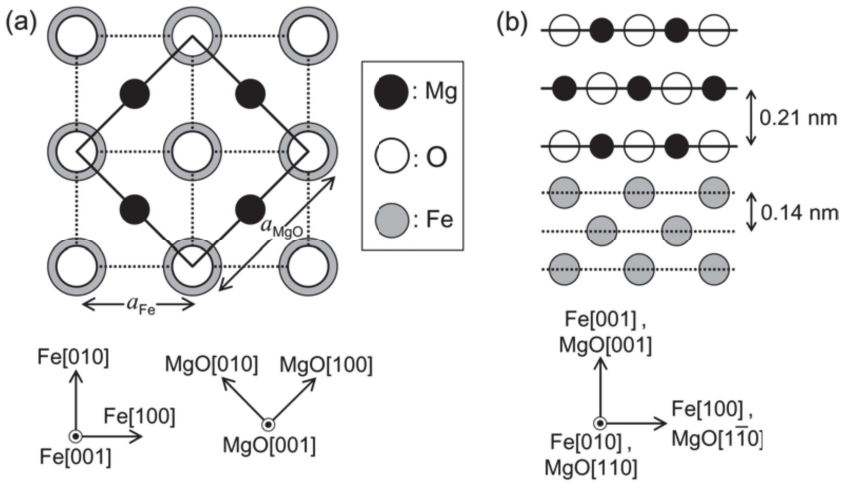

Figure 3.4: **Schematic of the interfacial Fe/MgO(001) crystallin structure:** (a) and (b) crystalline structures of rock-salt fcc MgO and bcc Fe characterized by their respective lattice parameters, $\mathrm{a_{MgO}}$ = 0.421nm and $\mathrm{a_{Fe}}$ = 0.287nm. (c) The lattice discrepancy dictates the 45° rotation of MgO in the (110) direction of Fe. Figure taken from ref [30].

3.3 Electrical transport: epitaxial Fe/MgO/Fe system

The epitaxial Fe/MgO/Fe structure was investigated by Butler et al. [31] through first-principles calculations. Since the system is periodic in the two-dimensional lateral *xy* plane the set of Bloch wave-functions is used in the calculations. Using the layer-Korringa-Kohn-Rostoker (LKKR) method Butler et al. calculated the reflection and transmission probabilities between two Fe layers separated by the thin MgO spacer. Further, inserting these coefficients into Laundauer's conductance formula, Butler et al. were able to determine the total tunneling conductance overall transversal Bloch modes:

$$\mathrm{G} = \frac{\mathrm{e}^2}{\mathrm{h}} \sum_{\mathrm{k}_{\parallel},\mathrm{j}} \mathrm{T}(\mathrm{k}_{\parallel},\mathrm{j}) \tag{3.7}$$

Where e is the charge of the electron, h is the Planck's constant and $\mathrm{T}(\mathrm{k}_{\parallel},\mathrm{j})$ the transmission probability coefficient of each respective Bloch state j along with the transversal mode $\mathrm{k}_{\parallel}$. Where $\mathrm{k}_{\parallel} = (\mathrm{k_x}, \mathrm{k_y})$ is the projection of **k** on the *xy* plane of the structure and z is the direction of the tunneling current perpendicular to the structure. In such a way, the spin-resolved tunneling conductance can be determined for each magnetic configuration of the Fe electrodes. Referring to Figure 3.5.a-b, the parallel tunneling conductance G of majority electrons over an 8 ML MgO spacer is characterized by a single peak at $\mathrm{k}_{\parallel} = (0,0)$. On the other hand, the minority conductance is three orders of magnitude weaker and has a more complicated *xy* distribution, with high peaks along with the $\mathrm{k_x} = 0$ and $\mathrm{k_y} = 0$ lines that originate from interfacial states in Fe layers and are suppressed when MgO is thicker. The antiparallel tunneling conductance represented in Figure 3.5.c possesses the transport footprints of both the majority and minority channels in the P case. One can already that the large predicted TMR amplitudes in such epitaxial systems mostly originates from the transmission along with the $\mathrm{k}_{\parallel} = (0,0)$ direction.

Since $\mathrm{k}_{\parallel} = (0,0)$ is the dominating transport vector, tunneling can be considered to take place through a simple square energy barrier $\mathrm{V_b}$ and thickness d with the resulting transmission probability proportional to $\mathrm{e}^{-2\mathrm{dk}}$ and with the decay constant $\mathrm{k} = \sqrt{(2\mathrm{m}/\hbar^2)(\mathrm{V_b}\text{˘}\mathrm{E_F}) + \mathrm{k}_{\parallel}^2}$. Furthermore, Butler et al. demonstrated that the lateral oscillations to the wavefunction define its decay rate perpendicular to these oscillations. The lateral oscillations are proportional to the number of nodes in the planar element of the wavefunction and are grouped according to their symmetry. Referring to Figure3.6, the symmetry groups $\Delta_1, \Delta_5, \Delta_2$ and $\Delta_{2'}$ are represented with the orbitals they regroup and their respective decay rates k. Since an electron of a given group tunnel with respect to states within a band that possesses this group's symmetry, evanescent tunneling will depend on the symmetry of their wave-function, giving rise to multiple decay rates within the same barrier. For instance, according to Figure 3.6 we see that Δ_1 symmetry have the lowest decay rate k_{Δ_1}, whereas Δ_5, Δ_2 and $\Delta_{2'}$ decay faster.

Furthermore, the importance of the insulating barrier's electronic structure was demonstrated through the investigation of its complex band structure in fully epitaxial systems. Several papers in the early 00s showed that the decay rates of the different Bloch symmetry groups are related to the complex k vector of the MgO crystal since the wavefunctions can

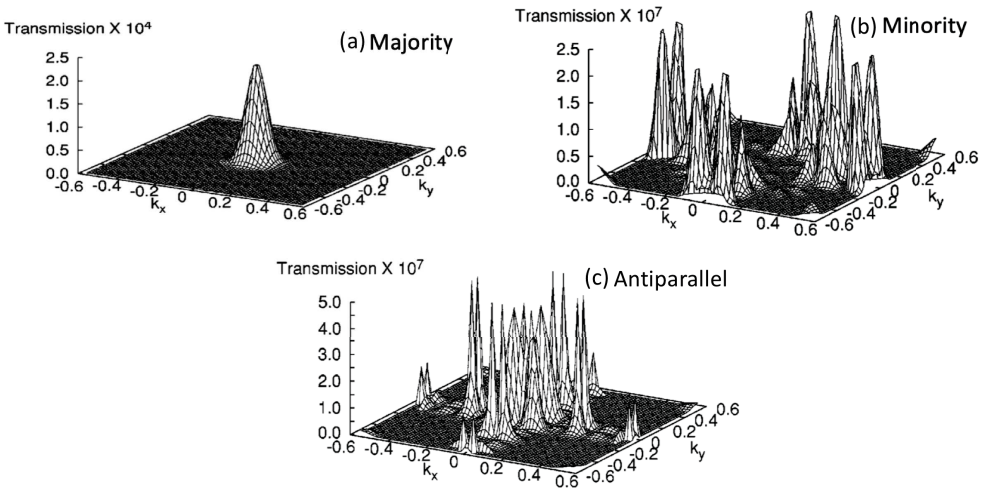

Figure 3.5: **Tunneling conductance along the $k_{||}$ in Fe/MgO/Fe system** Amplitude map of the $k_{||}$ conductance within an 8ML of MgO epitaxial structure. (a) and (b) – respectively, the majority and minority transport channel in the parallel configuration of Fe electrodes. (c) the total conductance in the antiparallel configuration. Figure taken from ref [31].

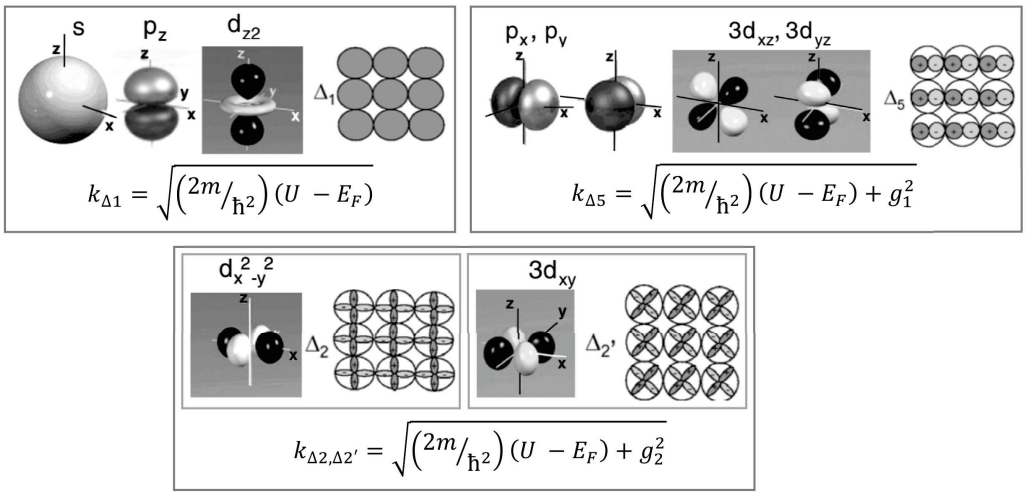

Figure 3.6: **Symmetry-related decay rates in an epitaxial system** Bloch states at $k_{||} = (0,0)$ and their characteristic symmetries equivalent to the planar oscillations of the wavefunction. The decay rate depends on the number of wavefunction's nodes in the plane XY of the structure. Figure adapted from refs [31, 32].

properly match at its interface [33, 34]. When the metallic Bloch states injected into the crystalline MgO structure match at the interface to the evanescent wavefunctions within the barrier, their decay rates are characterized by the complex k vector of MgO corresponding to that Bloch state's symmetry. In an epitaxial Fe/MgO(001)/Fe junction the wave-vector k can be expressed as the combination of $k_{||}$ and k_Z. The planar component $k_{||}$

is conserved during tunneling and should match at the interface. The decay of the wavefunction is defined by k_z. Referring to Figure 3.7.a, the symmetry resolved band structure of MgO defines the k_z value for each respective symmetry. Since dominantly the tunneling electrons are at the Fermi level E_F, the decay parameter is defined according to E_F in the complex section of k_z. As one can see Δ_1 symmetries are characterized by a much smaller decay rate k_{Δ_1} than k_{Δ_5} of Δ_5 symmetries. The symmetries Δ_2 and $\Delta_{2'}$ aren't represented here since they are characterized by a much higher decay rate.

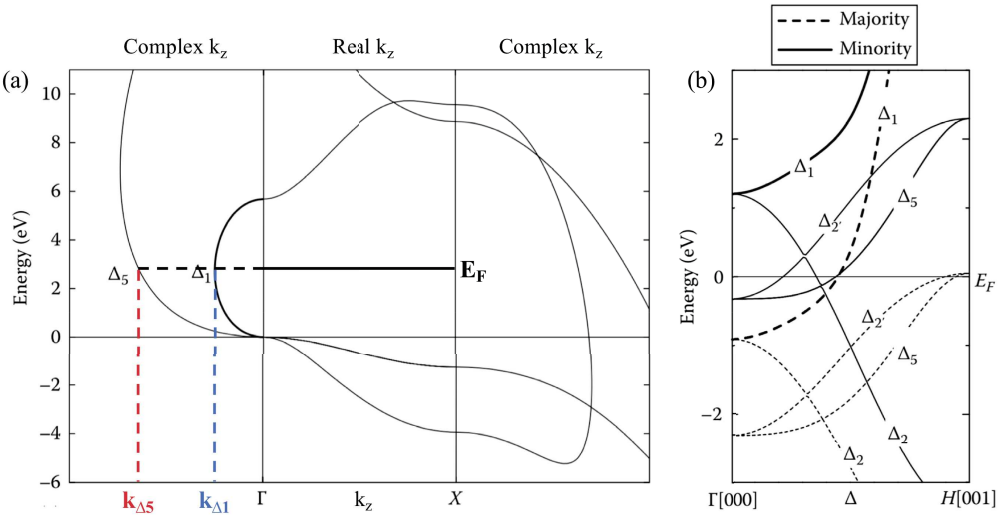

Figure 3.7: **Symmetry resolved MgO and Fe band structures.** (a) Complex and real band structures of MgO along the transport path in the reciprocal space $\Gamma - X$ direction for Δ_1 and Δ_5 symmetries. The intersection of EF and the MgO's complex band structure correspond to the decay rates of symmetries within the barrier, k_{Δ_1} and k_{Δ_5}. (b) The spin- and symmetry-resolved band structures of bcc Fe (001) along the transport path Γ˘H. The band-structure of Fe possesses electron states at E_F with Δ_1 symmetry that are fully spin-polarized. Figure taken from ref [16].

This coherent transport preserves the symmetries and spin state during tunneling of incident Bloch states: the MgO barrier acts as an electron symmetry filter [35]. Consequently, when the symmetry filtering properties of the crystalline MgO structure favor solid-state tunneling of electrons with a Δ_1 symmetry that is fully spin-polarized at E_F in the Fe electrodes, (Figure 3.7.b) this leads to a highly spin-polarized current. The peculiar description of these effects can be found in the layer resolved tunneling DOS within a Fe/MgO(8ML)/Fe epitaxial system in its parallel and antiparallel magnetic configurations [35]. Referring to Figures 3.8.a and 3.8.b, in the parallel configuration of electrodes tunneling takes place simultaneously between majority-majority and minority-minority channels. In the majority case, all three symmetry groups Δ_1 $(s, p_z, d_{3z^2-r^2})$, Δ_5 $(p_x, p_y, d_{xz,dyz})$ and $\Delta_{2'}$ (xy) are present in the majority channel of both electrodes. But since the decay rate of $\Delta_{2'}$ is the highest one it doesn't reach the collecting electrode through 8ML of MgO. In the minority case, the $\Delta_5, \Delta_2(d_{x^2-y^2})$ and $\Delta_{2'}$ are present in

the left lead, yet only Δ_5 and Δ_2 reach the right one. Therefore, the parallel conductance $G_{\uparrow\uparrow}$ is the sum over all of the contributing symmetry resolved conductances:

$$G_P = G^{\uparrow\uparrow}_{\Delta_1} + G^{\uparrow\uparrow}_{\Delta_5} + G^{\downarrow\downarrow}_{\Delta_5} + G^{\downarrow\downarrow}_{\Delta_2} \tag{3.8}$$

In the antiparallel configuration, in both the majority-minority and minority-majority channels respectively Δ_1 and Δ_2 symmetries are absent in Fe's band structure, hence, they continue to decay in the collecting electrode. This results in the G_{AP} exclusively mediated by Δ_5 symmetries:

$$G_{AP} = G^{\uparrow\downarrow}_{\Delta_5} + G^{\downarrow\uparrow}_{\Delta_5} \tag{3.9}$$

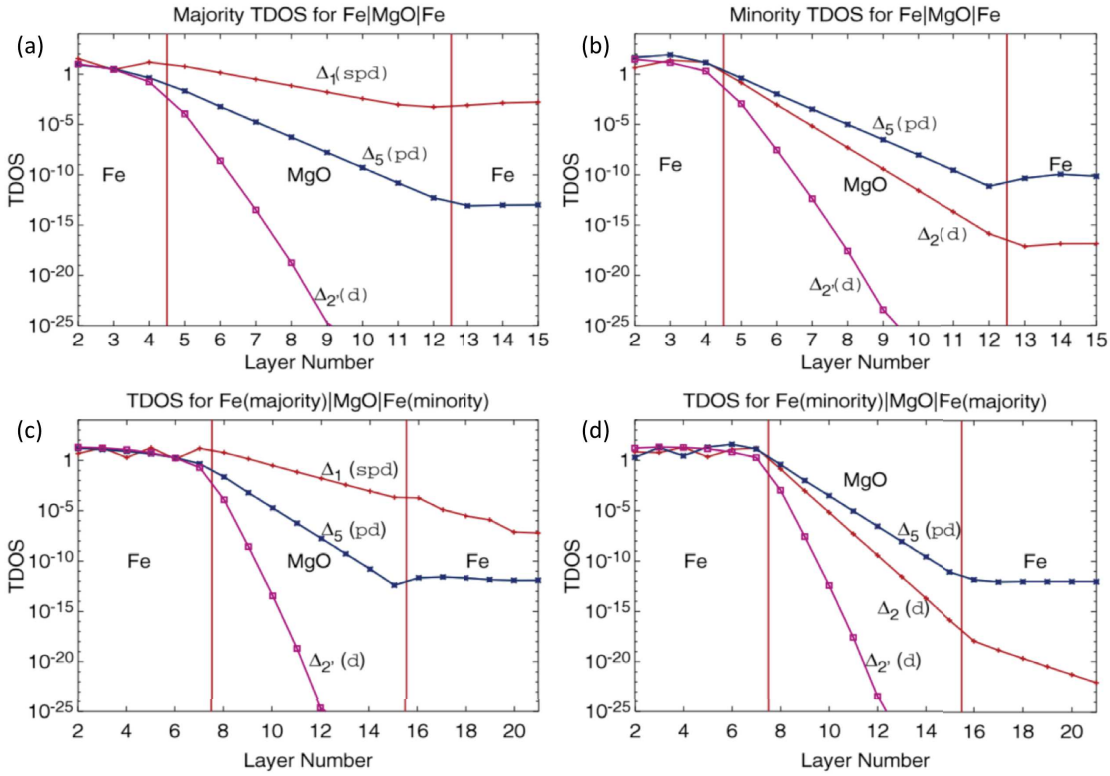

Figure 3.8: **Tunneling DOS of Fe/MgO(8ML)/Fe along** $k_{\parallel} = (0,0)$ Symmetry, spin, and layer resolved tunneling density of states (TDOS). (a) and (b) correspond to TDOS in the parallel majority-majority and minority-minority channels. (c) and (d) corresponds for TDOS in the antiparallel majority-minority and minority-majority channels. See description in the text for more details. Figure taken from ref [36].

The resulting $TMR = (G_P - G_{AP})/G_{AP}$ is high due to the dominance of Δ_1 symmetries parallel majority channel. This results in a giant imbalance between GP and GAP conductances that can generate up to 34000% of TMR according to theoretical predictions [27]. Herein, we've discussed about a more refined origin of the TMR effect arising

in epitaxial Fe/MgO/Fe epitaxial systems along the $k_{||} = (0, 0)$ direction. This interpretation takes into account the electronic structures of the metallic electrodes, the insulating barrier, and their interfacial couplings. The high predicted TMR signals in epitaxial Fe-MgO-Fe junctions take their roots in the various decay rates for the different Bloch-states within a single energy barrier. The next section 3.4 briefly describes the development path from prototypical epitaxial Fe/MgO/Fe junctions assembled by molecular beam epitaxy to industrially-grade textured CoFeB/MgO/CoFeB junctions crafted by sputtering.

3.4 Evolution of tunneling spintronics

The structural simplicity of epitaxial junctions led to a high theoretical interest in such systems. Few years after the high TMR signals predicted by ab-initio calculation they were partially confirmed experimentally. Several groups were able to assemble epitaxial Fe/MgO/Fe junctions through molecular beam epitaxy growth technique and detected sizable TMR signals. Yet, these results remained orders of magnitude lower than their theoretical counterparts and reached 180% at room-temperature [37]. This discrepancy between theory and experiments can originate from several factors, a) roughness and lattice mismatch at the interface, b) oxidation of iron atoms, the formation of a Fe-O interfacial layer, c) point defects that contribute to symmetry mixing, hence, noncoherent transport channels. Historically, epitaxial MTJs were subclassed by textured MTJs by their production and spintronic efficiency aspects. Since real-life MTJs are multilayer structures, the lattice match at each consecutive interface is very hard to control under the MBE technique. In this respect, sputtering growth is more adequate to use for mass production. In sputtered MTJs the bcc epitaxial Fe electrodes are replaced by amorphous CoFeB electrodes on top of which a textured MgO(001) is grown. It is covered by the second amorphous CoFeB film. Afterward, the semi-amorphous and textured multilayer structure is annealed at relatively high temperatures, $250°\mathrm{C} < \mathrm{T_a} < 500°\mathrm{C}$. The textured MgO layer acts as a crystallization template for the amorphous electrodes during the annealing procedure. During annealing, the B of CoFeB diffuses away and the remaining CoFe electrode crystallizes to a bcc(001) structure with a proper lattice match at the interface with MgO(001). For this reason, high TMR signals are achievable in sputtered MTJs. The first such fully sputtered device was successfully assembled by Parkin et al in 2004 [29]. On an $\mathrm{Si}(100)/\mathrm{SiO_2}$ substrate a TaN/IrMn/CoFe/MgO/CoFe/TaN structure was grown. Here, TaN is used as a wetting layer, IrMn as a pinning layer to the bottom polycrystalline CoFe electrode through exchange bias for a sharp P-AP state and the top TaN layer also serves as a capping layer. These junctions exhibited 70% of TMR at RT when as-deposited and up to 220% (RT) after the $400°\mathrm{C}$ annealing procedure. Cross-section TEM analysis of the structure shows that the MgO(011) axis is aligned along the CoFe(001) as expected in epitaxial Fe/MgO systems. It was shown that doping the Fe electrode with Co increases its TMR response. The recrystallization of amorphous CoFeB electrodes upon annealing was reported a year later by Djayapzawira et al. [38]. By the addition of boron (B) to the CoFe alloy make it amorphous, usually, its concentration doesn't exceed 20%, $\mathrm{Co_xF_{1-x}B_y}$, where x, 1-x, and y are the concentrations of the respective alloy. A high 230% TMR signal

was observed at room temperature after a 2h annealing at $360°\mathrm{C}$. Increasing the annealing temperature to even higher values is challenging, since this may activate the diffusion Ra, Mn, Ta, and B into the devices structure decreasing by that the TMR signal [39]. The current record of $604\%(1144\%)$ TMR at RT (5K) in Ta/Ru/Ta/CoFeB/MgO/CoFeB/Ta/Ru MTJs was set by Ikeda et al in 2008 [40]. This tremendous achievement is ensured in part by the high $525°\mathrm{C}$ annealing temperature, absence of the IrMn pinning layer, and the proper choice of the CoFeB alloys concentration and thickness. This later property limits the diffusion of Ta atoms into the CoFeB/MgO interface and contributes to a higher quality interface. The historical evolution of MTJs in respect to their TMR signals is represented in figure 9. It highlights the importance of annealing and utilization of amorphous CoFeB electrodes in the development of spintronics.

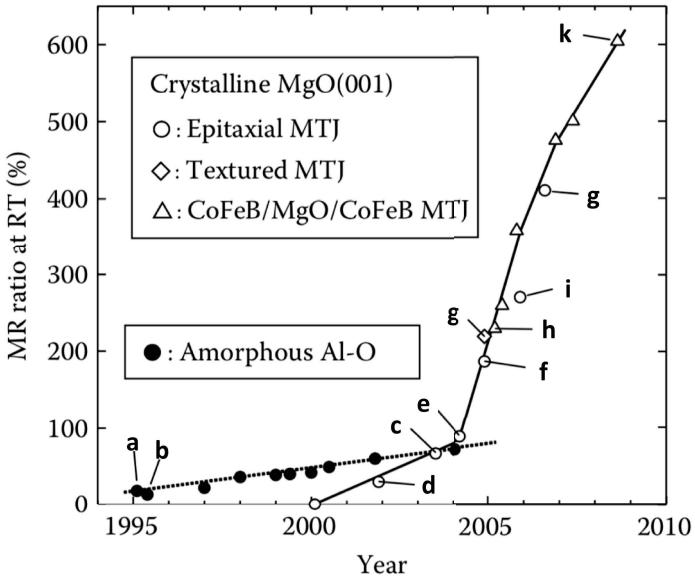

Figure 3.9: **History of room-temperature TMR in amorphous, epitaxial and textured MTJs.** The adoption of annealed textured CoFeB/MgO/CoFeB devices paved the way for high TMR signals and opened the doors to a wider implementation of such systems. Several datapoints references: a [41], b [7], c [42], d [43], e [44], f [37], g [29], h [38], I [45], g [46] and k [40]. Figure taken form ref [16].

Despite this success, several intriguing questions remain unanswered: i) The role of unavoidably present point defects and the additionally generated low barrier heights on the resistance and TMR signals of the devices. In our recent group's works, we emphasized the discrepancy between the experimentally deduced barrier heights of top-performing MTJs $(\Phi_{\mathrm{exp}} \approx 0.4\mathrm{eV})$ and the expected values for MgO-based MTJs $(\Phi_{\mathrm{MgO}} \approx 3.9\mathrm{eV})$ [10, 47]. ii) The tremendous discrepancy in the TMR amplitude between theoretically predicted and experimentally observed values [13, 31, 40]. In this respect, the next section 4 at first summarizes the current state of the art on spin-polarized transport in textured sputtered MgO-based MTJs. The section then describes the phenomenology of point defects and lo-

calized states in spintronics. Finally, it introduces the reader to the experimental technique used to investigate the potential landscape of tunneling devices.

Chapter 4

Localized States in Spintronics

As the main goal of this project was to integrate the concept of point defects in the current picture of spin-polarized tunneling this section briefly introduced a deeper understanding of transport in spintronic devices. At first, the key role of interfaces will be discussed through the interfacial lattice match and the presence of impurities. It is followed by the description of the bias voltage and temperature dependence of magnetotransport. The discussion ends with the introduction of point defects forming localized states in the MgO's potential landscape as well as the theoretical models describing their impact on the spintronic properties of devices. As we will see, the presence of oxygen vacancies plays a key role in the effective spintronic performance of MgO-based MTJs and their spin-transfer torque functionality.

4.1 Spintronic's Metrology

The quality of interfaces in spintronic devices is as essential for their proper operation as it is complicated to control. In section 3.2.2 we discussed the importance of the interfacial matching of evanescent wavefunctions in epitaxial Fe/MgO/Fe systems. One way to change the lattice parameter of a material is to dope it with a different lattice element. Bonell et al investigated the effect of interfacial dislocation on the TMR response of epitaxial devices. The authors demonstrated that by increasing the doping concentration of vanadium (V) $(\mathrm{a_V} = 303\mathrm{pmvsa_Fe} = 287\mathrm{pm})$ on the bottom Fe/MgO interface the TMR response of devices was diminished in comparison with pure Fe/MgO/Fe structure [48]. To reduce structural defects, sputtered CoFeB alloys are used: i) Boron serves to create an amorphous alloy structure, ii) The bcc $(\mathrm{a_{Co}} = 250\mathrm{pm})$ Co's band structure is much more spin-polarized at the Fermi level than bcc Fe, hence, is predicted to generate higher TMR, iii) Co undergoes a bcc to fcc transition at a few ML [46], which kills the high P of Δ_1 states at $\mathrm{E_F}$. Therefore, increasing the concentration of Co in CoFeB is both constructive and destructive at the same time. Referring to Figure 4.1, Ikeda et al. [40] altered the amount of Co from x = 0 to x = 60% in $\mathrm{Co_xFe_{80-x}B_{20}}$ for different annealing temperatures and concluded that $\mathrm{x} = 20\%$ is optimal for the device's TMR response.

Moreover, contamination at the electrode-MgO interface can affect the performance of the device in question by altering its electronic structure yet this mechanism remains complicated to determine since the interface is buried within the device. One such contaminant is oxygen atoms present at the Fe's interfacial layers forming an oxidized FeO layer [49].

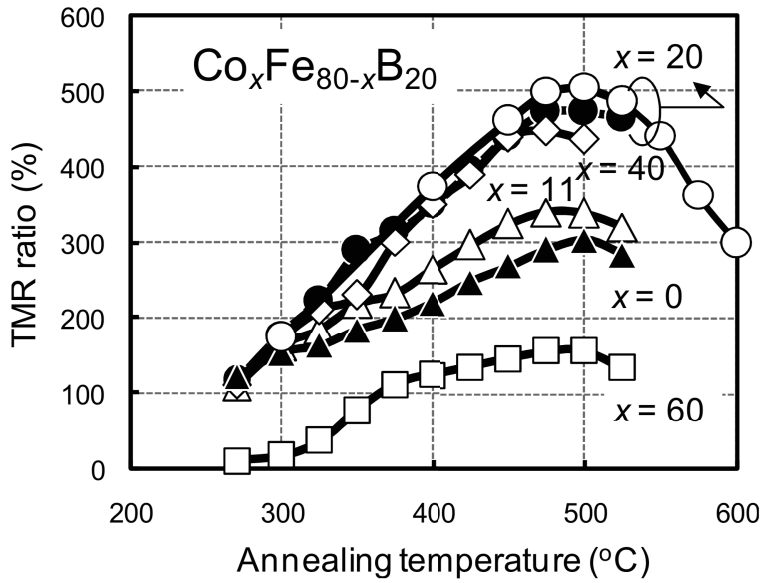

Figure 4.1: **Variation of TMR as a function of the Co concentration x in $\mathrm{Co_xFe_{80-x}B_{20}}$ and annealing temperature.** The concentration of Co alters both the lattice mismatch at the interface and the spin-polarized band structure of the alloy's electrode resulting in a linear effect on TMR. All concentrations of Co share the same annealing temperature ($\mathrm{T_a}$) behavior and the maximum TMR signal is reached at x = 20% and $\mathrm{T_a} \approx 500°\mathrm{C}$. Figure taken from ref [40].

First-principles calculations to understand the effect of interfacial FeO on spin-polarized transport in epitaxial MTJ systems were performed by Zhang et al [50]. The authors concluded that the interfacial oxidation reduced the interfacial overlap of Δ_1 states dominantly responsible for the TMR response. Experimentally this effect was confirmed by Bonell et al [51] who observed the TMR of their sample reduced by 40% between O free and a 2 monolayers of O interfacial contamination. Another contamination such as carbon atoms was reported to appear at the interface and deteriorate the TMR signal. Tiusan et al. [52] ported that the presence of Fe-C at the bottom interface of epitaxial Fe-C/MgO/Fe samples reduces their TMR signal by prohibiting the transmission of Δ_1 states. Separately, material science studies have shown that C monolayers deposited on an FM surface such as Co can generate a strongly polarized interface a.k.a a spinterface [53], hence could have a positive effect on TMR within a spintronic device [54], see Section 9.6.1 for the spinterface's formalism introduction. The Part Part II of this manuscript will present the magnetotransport results confirming the presence of carbon-generated spinterfaces in Co/MgO/Co samples. Other contamination species such as boron (B) atoms initially present in the amorphous CoFeB are prone to diffuse into the capping layers of MTJs [55, 56] and less likely to diffuse into the MgO spacer [56, 57], hence the buffer layers affects both the crystallization of the CoFeB electrodes [58] and the resulting TMR signal [59, 60] of MTJs. The choice of the buffer (capping) layers in the MTJs stack tends to be significant for the device's spintronic properties [40, 55]. Contaminations, defects, and vacancies states aren't always

detrimental to the spintronic operation of MTJs. In our recent groups works, the authors investigated the role of oxygen vacancies (OVs) in spintronics [10–12,47], they've demonstrated [47] that OVs are at the origin the spin-transfer torque (STT) low current densities experimentally reported in MgO-based devices [61, 62]. In the next sections 4.1.1 of this manuscript, the role of OVs will be discussed in detail moreover we will portray the potential landscape of MgO-based tunneling devices in presence of oxygen vacancies.

4.1.1 Magnetotransport measurements

As magnetic tunnel junctions mainly serve as electronic components in integrated circuits (IC) their electrical properties are of main interest. A set of magnetic and electric a.k.a magnetotransport measurements are performed to probe the spintronic response of devices. A most commonly used measurement protocol of IVs consists of sourcing bias voltage (V) while measuring the resulting current (I) changes upon switching between the different magnetic states of the device. Interpreting magnetotransport measurements isn't trivial since the current response at a given bias voltage is the convolution of all intrinsic and extrinsic device's properties. The last three decades of magnetotransport expertise show that the proper interpretation of the transport mechanisms requires a careful examination of multiple interlinked experimental degrees of freedom in combination with refined theoretical models.

4.1.2 Probing MTJ's electronic structure

Investigating the electric properties of MTJs results in probing the electronic structure of the whole device. Within a simplified transport model, when a bias voltage is applied to the MTJ's structure the Fermi level $\mathrm{E_F}$ of the electrodes split by eV. The positively sourced side $(\mathrm{S_+})$ shifts by +eV/2 whereas the negatively sourced one $(\mathrm{S_-})$ is shifted by -eV/2. The tunneling electrons of the $\mathrm{S_+}(\mathrm{S_-})$ electrode perceive a lower (higher) barrier height compared to the equilibrium one. As a note of mention, this description assumes that only electrons are tunneling, yet by the end of this chapter we will see that holes can also participate in the transport of MTJs. In this case, the additional allowed to tunnel electrons tunnel from $\mathrm{S_+}$ (left) into the additional empty states of $\mathrm{S_-}$(right), thus, both electrodes are been probed. Moreover, under applied bias-voltage, the rectangular potential step is transformed into a trapezoidal one as represented in the schematics of Figure 4.2. In the coherent transport scheme, sweeping bias-voltage allows probing the DOS of the electrodes by means of the tunneling current. Pronounced features within the DOS of electrodes will lead to features in the device's measured current.

Overall magnetotransport measurements performed on MgO-based devices have shown that the TMR signal steadily decreases under an increasing bias-voltage. There are several major reasons for this effect to take place: i) The increase of the conductance in the AP state, which is dominated by Δ_5 Bloch symmetries, ii) The increase of both conductances through the opening of additional inelastic channels, including zero-bias anomalies resulting from phonon and magnon processes that reduce spin-polarized transport. When

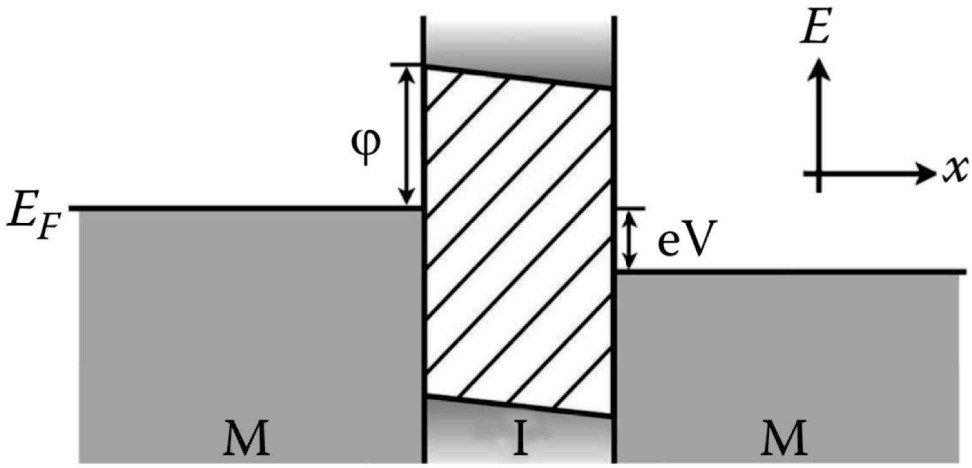

Figure 4.2: **Trapezoidal potential step under applied bias-voltage.** Figure taken from ref [16].

the energy of the tunneling electrons is high enough additional inelastic transport channels are opened. They are characterized by the exchange of the electron's energy, spin, and symmetry with the surrounding environment of the insulating spacer. Hence inelastic transport is usually assigned to incoherent transport that deteriorates the TMR signal of the device. Inelastic electron tunneling spectroscopy (IETS) allows identifying the energy required for these processes to take place. Usually, a further assignment of the inelastic transport features to a given quantum mechanical origin requires additional cross-checking measurements. IETS performed on sputtered CoFeB-MgO-CoFeB devices have shown the presence of trap states transport. These trap states are generated by impurities present within the MgO dielectric spacer. Authors even assumed that some of these states are spin-polarized and contribute to a spin-polarized tunneling [63]. In more detail, impurity-based transport will be depicted in Section 4.2.

4.1.3 Temperature addressing

The transport mechanisms under which the magnetic tunnel junction operates can be interpreted according to its temperature dependence. Several key effects arise when additional thermal energy is brought to the system: i) The increased temperature provokes the smearing of the Fermi energy, resulting in a lower effective barrier height felt by the electrons and a higher overall tunneling current, ii) The spin-imbalance that defines the polarization of the FM electrodes is subject to shrink with increasing temperature, resulting in a less spin-polarized tunneling current and a lower TMR signal [64], iii) Opening of additional inelastic transport channels related to magnon and phonon-assisted tunneling under a temperature increase. The field of spin caloritronics treats the spin and charge properties of temperature-induced currents [65]. It was demonstrated that a gradient of

temperature-induced along the structure of an MTJ results in a spin-dependent Seebeck effect, hence, generating spontaneous voltages that gives rise to the tunneling magnetothermopower (TMTP) ratio. Yet in the following discussion thermo-currents are excluded since both electrodes are presumably at the same temperature. The literature on both epitaxial and sputtered MgO-based junctions is full of reports demonstrating the decrease of the spin-polarized transport with increasing temperatures, observed over the reduction of TMR. Drewello et al. [66] introduced a theoretical formalism that describes the thermal dependence of the junction's conductance as a function of thermal smearing and magnon-assisted tunneling. They were able to reach a good agreement between experimentally and theoretically predicted results on several experimental datasets [28]. Referring to Figure 4.3.a, the general temperature dependence on $\mathrm{R_P}$, $\mathrm{R_{AP}}$ and TMR is represented. The strong decrease of TMR under increasing temperature is mostly mediated by $\mathrm{R_{AP}}$. Furthermore, the temperature behavior of TMR is also related to the thickness of the dielectric spacer and to the tunneling transport taking place within the device. Ma et al. [67] investigated the temperature variation of TMR in epitaxial Fe/MgO/Fe junctions for several thicknesses of MgO $(\mathrm{t_{MgO}})$, see 4.3.b. This study has shown that thick MgO junctions have a sharper decrease with T. This originates from a stronger misalignment with T of their electrode's magnetizations. Furthermore, Teixeira et al. [68] demonstrated that the dominant mechanism determining T dependence of $\mathrm{G_P}, \mathrm{G_{AP}}$ and TMR is spin-polarized elastic tunneling. In this case, the thickness of the MgO spacer $(\mathrm{t_{MgO}} < 1.35\mathrm{nm})$ will define the T variation of the device's spintronic response. In neither of Drewello's or Ma's models were coherent/incoherent transport channels directly addressed. Khan et al. [69] successfully fitted thick $(2.1\mathrm{nm} < \mathrm{t_{MgO}} < 4\mathrm{nm})$ sputtered CoFeB/MgO junctions only once both polarized and unpolarized transport channels were considered.

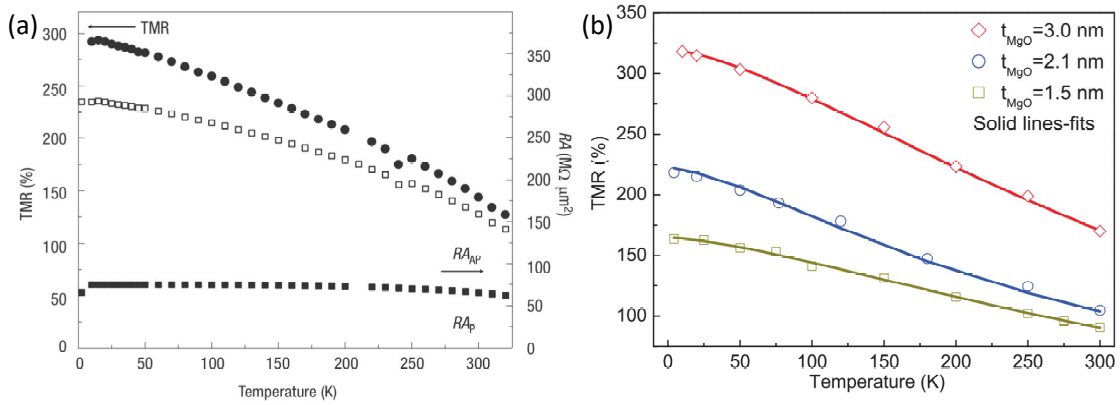

Figure 4.3: **Temperature variation of magnetotransport in sputtered and epitaxial MgO-based devices.** (a) Monotonous decrease of resistance-area product $\mathrm{RA_{AP}}$ and TMR within a sputtered CoFeB/MgO(3nm)/CoFeB junction whereas $\mathrm{RA_P}$ is quasi-constant, taken from ref [29]. (b) TMR decrease under increasing T in different MgO thicknesses epitaxial Fe/MgO/Fe junctions, taken from ref [67].

In section 5.2.4 we will discuss the active role of thermal addressing in the determination of localized states related transport features in MTJs. The next section briefly introduces the concept of localized states and their participation in the transport mechanism of spintronic devices.

4.2 Localized states in spintronics

In the scope of this thesis research project, we aimed to distinguish the effect of defects present within the insulating spacer. The next section briefly introduces several theoretical models on point defects in the MgO crystalline structure as well as their effect on the theoretically predicted TMR response in epitaxial systems.

4.2.1 Defects states in the MTJ's dielectric

Impurities and vacancies can appear in the dielectric spacer during its growth procedure or-and through the diffusion of intrinsic or extrinsic atomic species during the annealing procedure. There are two main categories of defect states in the insulator's potential: i) localized states – confined charges in the potential landscape of the dielectric. The wave function weakly overlaps with the surrounding atoms. Localized states assisted transport increases the conductance of the device and takes place through elastic or inelastic tunneling, ii) trap states – can both contribute to the reductions by of the conductance by charge trapping and to its increase by trap assisted tunneling. Elastic resonant tunneling (ERT) through a single localized state takes place when the Fermi energy of the tunneling electrons matches that of the defect state and is temperature independent [70]. When ERT takes place through two consecutive localized states, the conductance of this transport depends on temperature through $\mathrm{k_B T}$. Furthermore, inelastic resonant tunneling (IRT) is also prone to taking place through localized states when they are coupled to the phonon field of the dielectric. IRT increases the conductance of a simple elastic resonant tunneling and has a temperature of T_2 dependence [71]. Furthermore, if the concentration of defects is high enough, transport can take place through chains of localized states. If the discrete energy states are confined on a small energy scale, the electrons can cross through these chains by hopping. The conductance of hopping transport has a complicated temperature dependence T^{γ} where the γ is proportional to the chain's length. Temperature-dependent transport measurements are a powerful tool allowing to highlight transport through impurities in MTJs through a proper model fitting [72]. Several reports described transport through localized states as destructive for spin-polarized transport and judged it to be the main reason between theoretical and experimental TMR values. In the next section 4.2.2 the electronic structure and the resulting transport consequence of oxygen vacancies in MgO will be discussed. The coherent transport through this type of defect will be treated from in the theoretical and experimental frameworks.

4.2.2 Oxygen vacancies in MTJs

Oxygen vacancies are the most widespread species of defects in the family of oxide materials in consequence of the low formation energies. Historically, oxygen vacancies in magnesium oxide (MgO) were investigated for their intriguing optical properties [15,73–75]. In the field of spintronics the presence of defect states was always assigned to reduced TMR [76], incoherent transport [63] and a complex temperature-transport relationship [66]. The first part of this section presents the theoretical description of oxygen vacancies in MgO-based MTJs whereas the second part is devoted to their experimental observation in transport measurements.

4.2.3 Electronic structure of oxygen vacancies

When an oxygen cation (O^{2+}) is removed the rock-salt MgO crystalline structure is slightly deformed. The atomic orbitals of the defect states are confined in its vicinity forming localized electronic centers. Single (double) oxygen vacancies are denoted F centers (M centers). Velev et al. [77] studied transport in Fe/MgO/Fe MTJ in presence of F centers through first-principles calculations based on density functional theory. The calculated DOS of bulk MgO containing F centers have shown that occupied s states lay at -1eV from the fermi level whereas p states overlap with the conduction band thus are empty, see Figure 4.4.a. The calculated charge density of a single oxygen vacancy (F center), an F center forms an occupied localized s state and unoccupied resonant p state, see Figure 4.4.b-c. The s state has a strongly localized spherical shape that partially hybridizes exclusively with the first nearest oxygen atoms, as depicted in Figure 4.4.b. The p state also hybridizes strongly with the first nearest and weaker with all other oxygen atoms, as depicted in Figure 4.4.c.

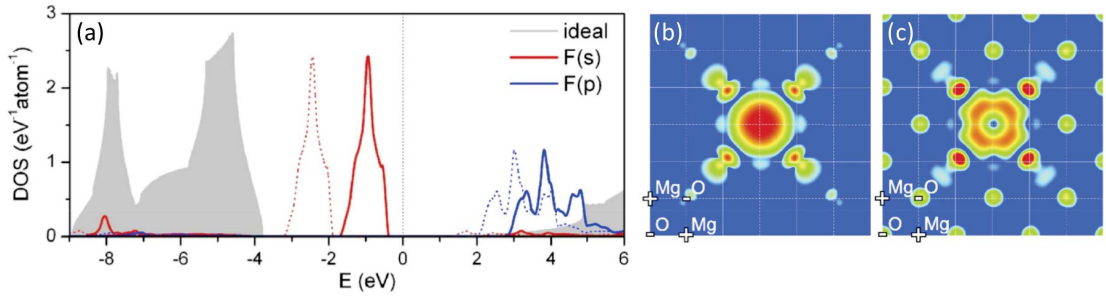

Figure 4.4: **Electronic structure of F centers in a crystallin bulk MgO.** (a) The density of states of defect-free bulk MgO crystal (solid gray), and in presence of F(s) and F(p) centers in red and blue respectively (solid line). The dashed line contains the self-interaction term. (b) - (c) Consequence of an individual F center on the calculated charge density in a perfect MgO structure in presence of a single s and p states respectively. Figure adapted from ref [77].

Furthermore, the authors have demonstrated that resonant tunneling through the F(s) states considerably increases the transmission of the Fe/MgO(5ML)/Fe(100) structure in-

creasing the conductance in both minority and majority P/AP configurations. Since s states are spherical in the *xy* plane they contribute to the Δ_1 symmetry transport channel. Out of resonance inelastic transport through collisions with oxygen vacancies reduces the overall transmission away from the defect level position, this induces higher attenuation rates and as result a lower conductance. This results in a reduced asymmetry between the P and AP conductances which causes a considerable reduction of the TMR ratio, from 1800% for an ideal structure to 800% in presence of single oxygen vacancies [77, 78]. The decrease of TMR is tightly related to the concentration of F centers in the MgO spacer of the junction's structure [79]. Furthermore, F centers can be populated by 0 electrons denoted F^0 centers(neutral), by 1 electron denoted F^{1+} centers (charged) and by 2 electrons denoted F^{2+} centers (charged). Reasonable the electron population defines the magnetic properties of these centers and may be critical for spintronics. In this manner, F^0 and F^{2+} centers are diamagnetic whereas F^{1+} centers are paramagnetic. The presence of F^{1+} centers can be revealed by electron spin resonance techniques [80]. The optical activity of charged and neutral F centers in MgO remained an enigmatic topic [15, 47, 81] till recent works revisiting the matter [73]. On the other hand, the electric participation of charged F centers in MgO-based spintronics remains a complicated scientific topic since their charged states induce dynamic processes.

At high concentrations of oxygen vacancies [82], the distance between the consecutive F centers is rather small and double oxygen vacancies or M centers tend to appear. McKenna and Blumberger [83] have predicted that as the distance between the single oxygen vacancies decreased, they were more likely to participate in a coherent charge transport between defect states rather than in an incoherent one. The footprint of M centers in the magnetotransport response of MTJs was elicited by a combination of electrical and thermal addressing [10–12].

Taudul et al. [12] calculated the density of states for MgO structure in presence of M centers. The later ones form two occupied states M_1 and M_2 below the fermi level and two unoccupied M_{1*} and M_{2*} states overlapping with the conductance band of MgO. Referring to Figure 4.5.a, the DOS of MgO is characterized by two sharp peaks M_1 and M_2 below the fermi level and two distinguishable peaks M_{1*} and M_{2*} in the conductance band. M_1 and M_2 both share a spherical shape (s-like character). M_1 (M_2) manifests a bonding (antibonding) state, see Figure 4.5.b-c. As in the case of F(s) centers, M centers hybridize with the first nearest oxygen atoms. From the same theoretical work, for an M center placed in the middle of a 7ML-MgO layer in presence of FeCo electrodes, the energy levels relative to the MTJ's $\mathrm{E_F}$ are -0.4eV for M_2 and -1.1eV for M_1. The experimental confirmation of the relative of M_1 and M_2 positions and the resulting defect-mediated transport will be discussed in the results Section 5.3.

As the next step, Taudul et al. [13] have compared the calculated conductances of Fe/MgO/Fe structure in presence of F centers, M centers and in their absence in the MgO layer. The conductances of each configuration were calculated as a sum of the transmission coefficient over the whole 2D (*xy*) Brillouin zone. This study has shown that: i) Naturally the conductances in the ideal (defect-free) structure are highly asymmetric leading to huge TMR values, ii) In presence of F centers the conductance in the P (spin-up) state is strongly reduced, leading to a tremendous decrease of conductance asymmetry

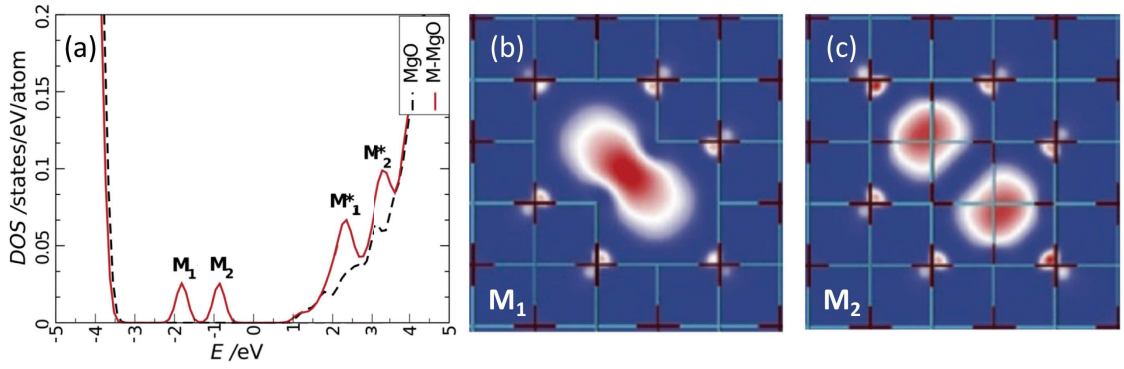

Figure 4.5: **Electronic structure of M centers in a crystallin bulk MgO.** (a) Density of state calculated for a pure MgO crystal (dotted line) and in presence of M centers (red line). M centers generate two occupied M_1 and M_2 states (sharp peaks) and two unoccupied M_{1*} and M_{2*} states in the low conduction band. Note that E=0 does not correspond to the E_F of a FeCo/MgO/FeCo MTJ, but rather to the chemical potential of bulk MgO with the M center. (b) - (c) Calculated charge density of the M_1 and M_2 states in MgO. Figure adapted from ref [12].

and very weak TMR, iii) In presence of M centers the conductance in G_P (spin-up) state that is higher than in the presence of F centers. Concurrently, the conductance G_P(spin-down) and G_{AP} undergo a very weak increase leading to a higher TMR when F centers are replaced by M centers. This result indicates that M centers contribute to more coherent transport channels than F centers, in line with Velev et al. [77] and as predicted by McKenna and Blumberg [83]. Table 4.1 summarizes the different calculated conductances and the resulting TMR ratio for a free, F centers and M centers Fe/MgO/Fe structure for two thicknesses of MgO 5 and 7ML.

	$G_P^{\uparrow}$	$G_P^{\downarrow}$	G_{AP}	TMR[%]
5 ML	79.0	0.46	1.0	7850
F (5ML)	7.21	0.63	3.2	145
M (5ML)	17.1	1.47	4.5	315
7 ML	5.3	0.003	0.03	15770
F (7ML)	0.12	0.006	0.03	304
M (7ML)	0.62	0.007	0.04	1624

Table 4.1: Calculated conductances and the resulting TMR. Conductances $G_P^{\uparrow}$, $G_P^{\downarrow}$ and G_{AP} and the resulting TMR [%] for a defect free, F centers and M centers Fe/MgO(x)/Fe structure, when x= 5ML and 7ML of MgO. Conclusion: M centers contribute to a more coherent transport and are much less ($\approx$ x2 to x5) destructive for the TMR response. Table taken from ref [13].

This study [13] predicts that spintronics of MgO based devices can benefit from a mind-

ful control over the species of oxygen vacancies, and especially its location within the barrier. Indeed, oxygen vacancies placed close to the MTJ interfaces promote recovery to TMR values closer to those predicted in an ideal case. It was experimentally concluded that the ratio of F to M centers in oxidized [84] dc-sputtered Mg spacer MTJs decreases when the sample's annealing temperature is increased from 200K to 300K [12]. Additionally, in the rf-sputtered MgO-MTJs process a dominant concentration of F centers to M centers [11]. Intriguingly, these observations fit rather well the fabrication protocol of the current most performing CoFeB/MgO/CoFeB devices. A relatively high $\mathrm{T_a} > 300$ annealing step is required to achieve high TMR values [40]. This leads to the proper recrystallization at the CoFe/MgO interfaces but can also reduce the ratio of F to M oxygen vacancies. Both the thickness (7ML) and the resulting 304% to 1624% TMR ratios for F and M centers-based structures fit rather well the experimentally observed high TMR signals 1100% with 2-2.5nm MgO spacers [40]. As of last, the combination of high TMR and low barrier heights in MgO MTJs can now be assigned to the presence of closely spaced oxygen vacancies (M centers) in the MgO barrier, preferably at its interfaces with the FeCoB electrodes [13]. This work revolutionizes the generally accepted detrimental effect of defects in spintronic devices. In the next chapter 5, the experimental evidence of oxygen vacancies-mediated transport in spintronic devices will be described in detail.

Chapter 5

Experimental Techniques and Results

The first objective of this research project was to identify defect states within the transport scheme of MgO based spintronic devices and to determine their origin through a combination of theoretical and experimental efforts. Upon this, the complete transport based potential landscape of a MgO layer embedded within an operating device can be determined. The first part of this section describes the fabrication details of the systems used in this study. The second part defines the experimental technique which allows us to experimentally measure the effective barrier heights felt by tunneling charge carriers. The third and last part summarizes a comparative study between two similar spintronic systems which enables us to consolidate the picture of tunneling spintronics across oxygen vacancies states in MgO.

5.1 Assembling magnetic tunnel junctions

The growth of the functional thin film stacks was performed by M. Hehn and coworkers from Institut Jean Lamour (IJL) in Nancy-France in the frame of our long-term collaboration. The three samples presented in this thesis manuscript (Chapter 5 and Part Part II) were grown on a commercial alliance concept DP850 magnetron sputtering system. The two samples presented in this section have been grown on a corning 1737 substrate and have the same composition differing only by the top FM electrode:
Ta(5)/Co(10)/IrMn(7.5)/CoFeB(4)/MgO(2.5)/FM(3)/Ta(1)/Pt(1), where FM stands for CoFeB or FeB top electrodes (numbers are in nm). The details description of the growth parameters can be found in Bernos et al. work [85]. These samples are annealed at $300°\mathrm{C}$ under an external in-plane magnetic field to set the exchange field between the antiferromagnetic IrMn layer and the bottom CoFeB ferromagnetic electrode. This step provides an achievable steady antiparallel magnetic configuration within the samples. The CoFeB alloy is characterized by the following concentrations: $\mathrm{Co_{40}Fe_{40}B_{20}}$, which corresponds well with the current most performant MgO-based devices and FeB stands for $\mathrm{Fe_{80}B_{20}}$. The fabrication process of MTJs on the grown wafer is performed at the STnano cleanroom class 100 facility through a UV lithography (365nm) process on a Süss MJB4 mask align setup. The patterning of 240 MTJs on a single die is performed through a standard 4 step lithography process summarized in Figure 5.1. Prior to the lithography procedure, a control quality is performed to avoid any possible contamination on the surface or during the lithography process. The unprocessed wafers are transported between institutes

covered by a protective photoresist. Through an acetone/ethanol cleaning in an ultrasonic bath, the photoresist is removed. The quality of the wafer's surface is controlled by a simple optical microscope, if any debris-contaminations are left other rounds of solution or plasma cleaning follow.

5.1.1 Lithography process of MTJs

Step I: Defining Pillars. The first step of lithography enables us to define 20 rows of 12 junctions (d = 20μm) in each and two adjacent pads for each row, see Figure 5.1.a for a single row. The pads serve for electrical access to the bottom electrode across a macroscopic area of the junction trilayer due to defects. A layer of commercial-grade positive photoresist (S1805) is deposited on the surface of the wafer by spin-coating and further soft baked. The sample is exposed to UV light for 2.6s through a shadow mask with the needed patterns in the contact aligner setup. Further, the sample is developed in AZ 726 MIF developer. Ar^+ ion beam etching (IBE) is used to transfer the pattern from the motif of photoresist onto the wafer's multilayer structure. In this step, the sample is etched till the bottom part of the MgO spacer, at 45° to avoid redeposition. The etching progress is controlled by Auger spectroscopy on the surface of the sample. The remaining photoresist is removed in an acetone bath. Each consecutive step of lithography is aligned to the previous one through special marks at all corners of the pattern. In such a way, a precision of $\pm 1\mu$m is achieved along with the whole structure.

Step II: Common bottom electrodes definition. Here again, the same protocol of positive photoresist is used to define a common bottom electrode for each of the 10 rows, see Figure 5.1.b. This step is followed by Ar^+ IBE etching till the glass substrate so that the 10 bottom electrodes and their respective junctions would be isolated on the surface of the sample. In this etching step redeposition of the etched material on the edges of the pillars is excluded since they are covered by the photoresist layer.

Step III: Passivation layer. Prior to the deposition of the dielectric SiO_2 material the surface of the pillars and bottom electrode's pads are covered with a negative photoresist (AZ 5214) which eases the lift-off step. The passivation layer allows us to decouple electrically the consecutive junctions and electrodes, see Figure 5.1.c. In that respect, a 150nm thick layer of SiO_2 is deposited by RF magnetron sputtering (Alliance Concept EVA300+) setup. Further, the sample undergoes a soft lift-off procedure in acetone and ethanol baths to remove the covering photoresist.

Step IV: Contact lines. To ensure easy electrical access for the patterned MTJs, conductive lines are deposited on top of the patterned pillars. Once again, through a negative photoresist lithography step opening stripes on top of each pillar are defined with a central photoresist motif covering the central part of the pillar to form an optical opening of d_o = 10μm, see Figure 5.1.d. A conductive Al(110nm)/Au(35nm) is deposited in a commercial e-beam thermal evaporation setup (Plassys MEB 550S). Then, the sample undergoes another soft lift-off step to remove the covering photoresist. To summarize, a 20μm diameter junction has a 12 μm opening in the SiO_2 passivation layer atop the pillar, and an annular 10 μm electrical contact associated with the top technological electrode layer. The resulting contact lines serve for ball or wedge wire-bonding of the sample's junctions to a

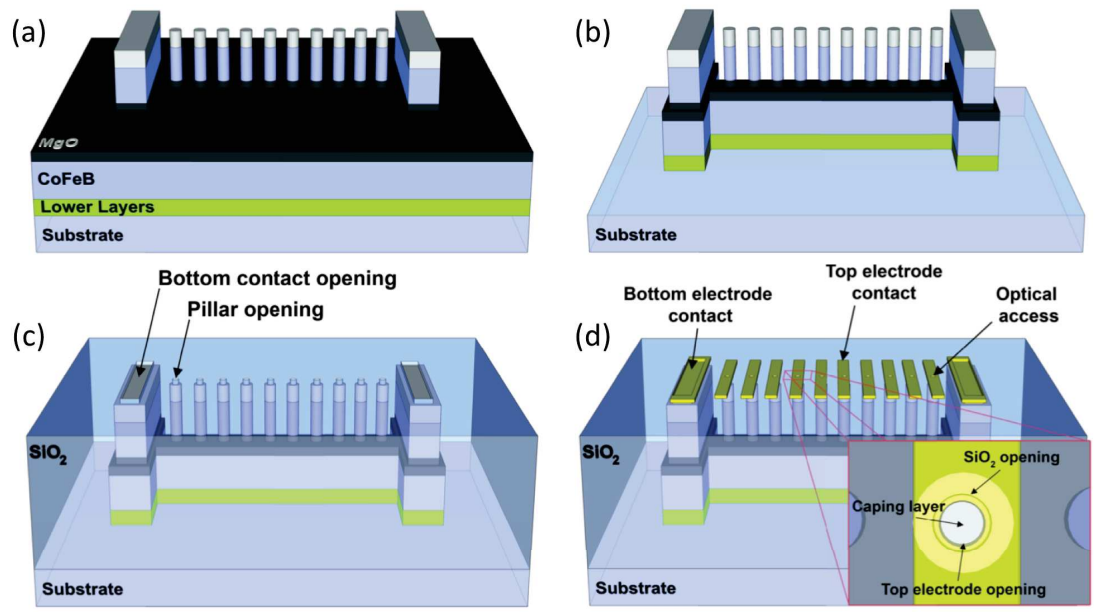

Figure 5.1: **Lithography process in fore steps.** (a) Pillar and bottom electrode's pads definition. (b) Definition of the common bottom electrode shared by 12 pillars. (c) Deposition of the SiO_2 passivation layer. (d) Deposition of the conducting pads for electrical connections. For more details see the description in the text. Figure taken from Ref [68].

custom-made sample holding chip.
Prior to the bonding step, the resistance properties of the resulting 240 MTJs of a processed sample are measured on a probing setup. This step enables us to determine the success rate of the lithography process and gather basic statistics on the system in question. The final step consists of cutting the processed wafer into two die pieces of 5x7mm and gluing them on custom-made chips for further wire bonding and electrical characterizations.

5.1.2 Statistics of lithography process

The standard lithography described in the previous Section 5.1.1 was applied to process $20\mu m$ in diameter MTJs for the CoFe (stack A) and FeB (stack B) systems. As the fabrication of MTJs is a sensitive process that relies on many external parameters, a careful examination of the lithography success rate may hint as to the origin of any possible failure. Referring to Figure 5.2, we present the statistical study of the resistance-area (RA) products for both stacks on samples with 120 junctions. The RA products on CoFeB (A) based junctions average around 1 * 108 $\Omega * \mu m^2$ and a 76% lithography success rate, while the FeB (B) devices average around 5 * 107 $\Omega * \mu m^2$ with 61% of success rate. The slight discrepancy in resistance between the two stacks is within the expected margin [39], noting that switching the top electrode material affects the spin-polarized states involved in

transport. The relatively high success rate and the small experimental variance suggest that the lithography and etching processes were properly performed.

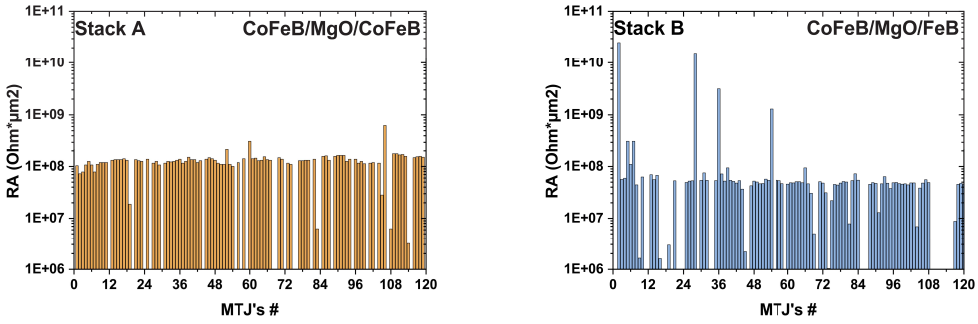

Figure 5.2: **Resistance-areas (RA) products for stacks A and B.** (a) & (b) RA product averages around $1 * 108\Omega * \mu m^2 (5 * 107\Omega * \mu m^2)$ for stack A (B). Both RA products were measured at V_{bias} = 5mV and no external magnetic field.

5.2 Magnetotransport characterization

The main goal of this section is to introduce to the reader the basic concepts of magnetotransport using the example of our two MTJ sets (that would be discussed in Section 5.2. Further, we shall define the not so well know I hat ($\hat{I}$) technique [10, 11, 22, 86] that can be used to determine the effective barrier heights generated by defect states within the spacer of an MTJ device. The comparison of experimentally extracted barrier heights for the FeB and CoFeB MTJs in conjunction with ab-initio calculations allows us to identify the species of defects involved in the transport and determine their position in the potential landscape of the dielectric barrier, Section 5.3. As a note of mention, the set of experimental datasets and their interpretation presented in this section led to the publication of an article - "Consolidated picture of tunneling spintronics across oxygen vacancy states in MgO" published recently [14]. My contribution to this work consisted of the MTJs processing, measurements, and analysis parts.

5.2.1 Magnetic properties

Magnetotransport measurements require a steady magnetism within the structure of the magnetic tunnel junction. In some rare cases, the magnetism of the pillars can be modified during the lithography and etching process steps. In that respect, we compare the magnetometry measurements of the unprocessed wafers with the respective resistance-field (RH) measurement of the processed MTJ. Referring to Figure 5.3.a, the room-temperature SQUID magnetometry measurement of the Ta/Co/IrMn/CoFeB/MgO(2.5)/CoFeB/Ta/Pt wafer (grown by M. Hehn, IJL Nancy) clearly indicates that both top and bottom CoFeB electrodes are magnetically decoupled, a sharp AP state is obtainable, and the respective

coercive field of each magnetic layer is detectable. Given that the exchange bias of IrMn underscores the magnetic decoupling here, this room-temperature measurement implies that, at lower temperatures, the decoupling shall also be ensured. The RH plot of the processed MTJ (same structure) in Figure 5.3.b indicates that both junction electrodes are decoupled. Since the MTJ's H_C fields match those from the raw SQUID measurement, we can confirm the magnetic properties weren't affected during the process steps.

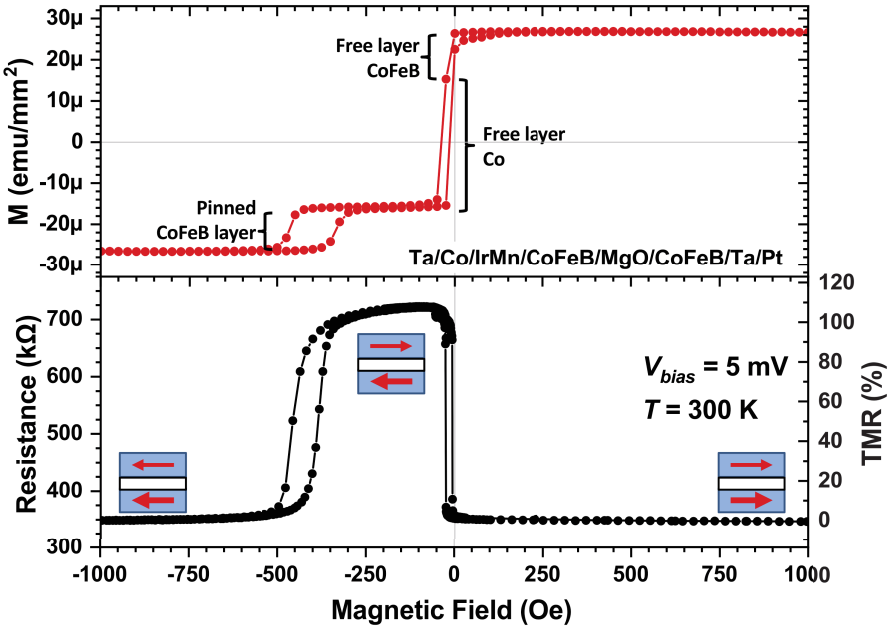

Figure 5.3: **Magnetic properties of samples before and after the process.** (a) Room-temperature SQUID measurement of the unprocessed wafer (see structure in the text). Both CoFeB ferromagnetic electrodes are properly decoupled. (b) Room-temperature resistance-field (RH) measurement performed on the processed MTJ. The magnetic properties of the grown stack are preserved during the lithography and etching steps.

5.2.2 Electrical characterization

All of the herein discussed transport measurements were performed on the custom-made multifunctional bench (BMF) assembled and automatized by M. Bowen, U. Halisdemir, and co-workers. A detailed description of the setup and its specific capabilities can be found by an interested reader in the Ph.D. manuscript of U. Halisdemir [22]. Nevertheless, the electrical measurement equipment needs to be specified for the coherence of the discussion about the experimental results. A Keithley 2636 Sourcemeter was used in a 4-point probe measurement mode (4pts) [87]. This mode is more sensitive than the standard 2-point probe mode and allows to eliminate of the current drop measurement along the connection lines and the electrodes material. Electrons (holes) are tunneling from the bottom (top) electrode to the top (bottom) one since V_- and I_- are connected to the bottom,

and V_+ and I_+ to the top, electrodes. Measurements of a calibrated $50k\Omega$ commercial resistance have shown that the maximum current (voltage) offset is 500pA (0.1mV), which very good for the investigation of the $[nA - \mu A]$ current range.

5.2.3 Comparing CoFeB and FeB MTJs

Since in this study we intend to compare and refine the defect-mediated transport properties of the previously reported [10–12, 22, 88] stack A and its slightly modified version stack B we begin by comparing their basic magnetotransport properties. In this section, we discuss the transport modification brought by altering the material of the top ferromagnetic electrode CoFeB ↔ FeB in the same MTJ structure. Referring to Figure 5.4, the current-voltage (IV) behavior at low T = 20K temperature in both P and magnetic configurations is presented for both MTJ's stacks A (Figure 5.4.a) and B (Figure 5.4.b) in the same exact current and voltage ranges. Replacing the top CoFeB electrode by FeB (MTJ Processing performed by F. Schleicher)yields to a flatter profile of IV of the latter case. This effect originates from the change in the symmetries available at the Fermi level and participating in transport. It was shown that the composition of the electrodes alloy is prone to alter its polarization and the resulting magnetoresistance response [89]. Removing Co atoms from the top electrodes layer provokes an additional majority conduction channels from $\Delta_{2'}$ and Δ_5 symmetries [46], see Figure 5.5. This latter effect reduces the P/AP conductances asymmetry, and hence provokes a TMR reduction.

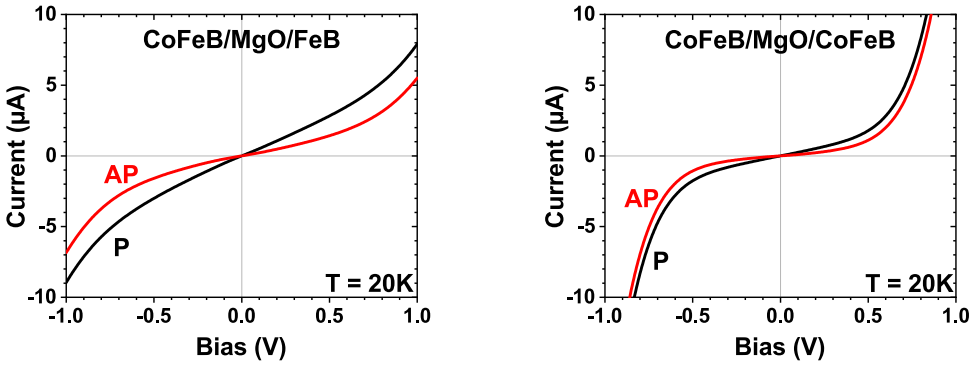

Figure 5.4: **Magnetotransport IV comparison between the CoFeB and FeB MTJs.** (a) and (b) share the same overall behavior, yet in the FeB case the IVs in both P and AP are flatter. This originates from the additional $\Delta_{2'}$ and Δ_5 symmetries-based transport in the spin-up channel when CoFeB is replaced by FeB [46], see Figure 5.5 and ref [89] for alloys concentration magnetoresistance comparative studies.

The other key effect of removing Co from one or both electrode's alloys is the chemical potential of the resulting structure, as it strongly affects the magnetotransport response of the device. Hence, by altering the alloy's composition we can tune the Fermi level and

alter the spintronics, this effect will be discussed on the basis of our experimental datasets in Section 5.3.

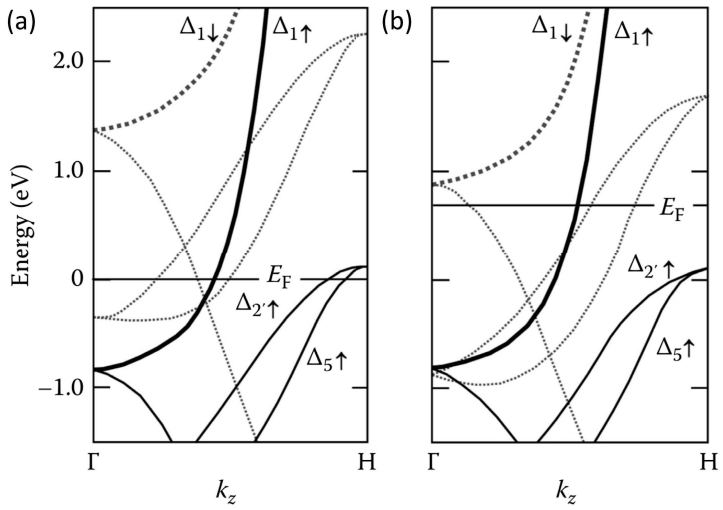

Figure 5.5: **Band structure of bcc Fe and Co along the [001]** (Γ **- H).** Solid (dotted) lines stand for the majority (minority) symmetries resolved band structure of Fe (a) and Co (b). Δ_5 and $\Delta_{2'}$ are present only in the minority bands of Co and at minority and majority of Fe. This leads to a higher spin-polarization of Co. Figure taken ref [16].

The direct consequence of the CoFeB → FeB switch can be seen within the TMR-voltage behavior of the two samples. Since both the band-structure and the Fermi level of the system are modified the resulting TMR(V) plot will be also different in both cases, see figure 5.6. At room temperature, both samples exhibit the sample TMR amplitude of 105% in the low bias range (dotted lines).

At low 20K temperature TMR reaches 205% for the CoFeB sample and 160% for the FeB sample. This discrepancy in TMR amplitudes is completely expected since the theoretically investigated epitaxial MgO/FeB interface is expected to less spintronically efficient [27], see Figure 5.5 and its caption. Butler and Zhang have estimated the TMR response of 34000% and 5400% in respectively FeCo/MgO(8ML)/FeCo and Fe/MgO(8ML)/Fe, thereby explaining the decrease of measured TMR between stacks A and B. The different slopes of TMR(V) for both structures at 20K are also a product of the altered band-structure. In conclusion, in both samples transport takes place through tunneling their spintronic properties aren't too far apart for a proper comparison of their defect-mediated transport.

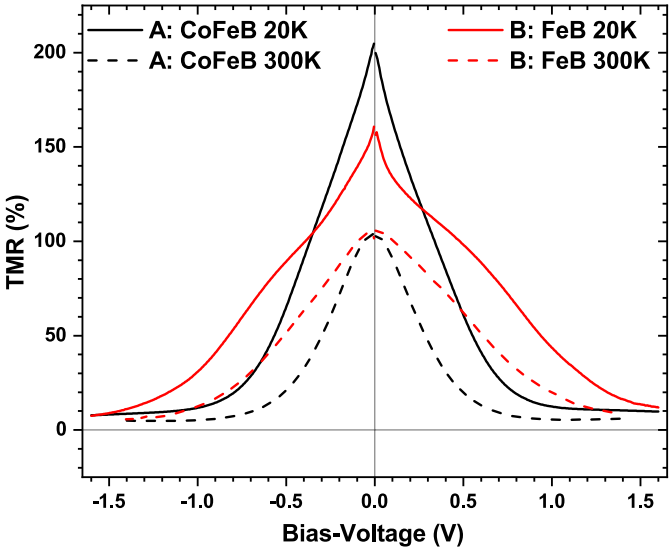

Figure 5.6: **Magnetotransport TMR comparison between stacks A and B.** (A) Stack A: Ta(5)/Co(10)/IrMn(7.5)/CoFeB(4)/MgO(2.5)/CoFeB(3)/Ta(1)/Pt(1). (B) Stack B: Ta(5)/Co(10)/IrMn(7.5)/CoFeB(4)/MgO(2.5)/FeB(3)/Ta(1)/Pt(1). Solid (dotted) lines stand for 20K (300K) temperature measurements. $\mathrm{TMR}_{\mathrm{A-LT}} = 205\%, \mathrm{TMR}_{\mathrm{B-LT}} = 160\%, \mathrm{TMR}_{\mathrm{A-B-RT}} = 105\%$, with LT = 20K and RT = 300K.

5.2.4 $\hat{\mathrm{I}}$ technique: Effective barrier heights

The defects species within the dielectric material of MTJs generate localized states in its band-gap, this results in the emergence of additional lower barrier heights. For instance, in the case of MgO whose band-gap is around 7.8eV and the pure barrier height Φ_{MgO} is estimated to be around 3.9eV [90] are never observed experimentally. The transport evaluation of MgO-based tunneling MTJs with unavoidably present defects reports sub 1eV effective barriers heights [10, 11, 47]. From a transport perspective, the localized states increase the overall device's current by lowering the effective barrier height felt perceived by tunneling charge carriers. Localized states mediated tunneling can be both elastic when electrons are directly tunneling through the states into the counter electrode without losing their energy or inelastic when electrons interact with the dielectric material and lose energy. Exploring the barrier heights perceived by incident charge carriers (electrons and holes) can give an insight into the potential landscape and the species of impurities present within the dielectric material. Brinkman's [18] and Simmon's [17] formulas are well known in the field of spintronics and are suitable only for perfect barrier steps and give only the averaged barrier height. Montaigne et al. [91] showed that the energetic sharpness of the interface must also be taken into account, even though this parameter is absent in the Brinkman and Simmons models.

To avoid the pitfalls of these phenomenological models [17, 18], we resort to a more physical approach. The formalism brought by Rottlander et al. [86] was further refined by my group members to extract the barrier heights from magnetotransport measurement [10]. The main principle of this spectroscopic technique consists of comparing the effect of additional thermal energy on the device's current at different bias-voltage values. Therefore, the IVs protocols are compared between two temperatures, $T_2 > T_1$ with $\Delta T = T_2 - T_1$. Thermal energy is used as a fine probing tool where ΔT defines the spectroscopic resolution. This so-called $\hat{I}$ or I_{rel} protocol is described by the following formula:

$$\hat{I} = \left(\frac{I(V, T_2)}{I(V, T_1)} - 1\right) * 100 \tag{5.1}$$

If at a given bias-voltage a defect state is within the vicinity of $\pm k_B \Delta T$ then additional current will flow through the barrier, the IV curve will change its slope. A peak in the $\hat{I}(V)$ plot corresponds to the 1.2 times the barrier height Φ [86] and therefore correlates with the position of the defect states. The schematic description of the $\hat{I}$ technique is represented in Figure 5.7.

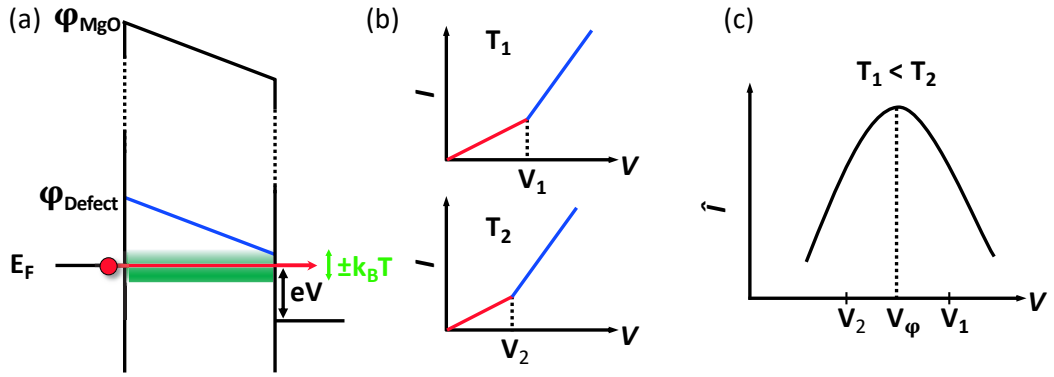

Figure 5.7: **Schematic representation of the $\hat{I}$ technique.** (a) Linear potential drop across the junction under an applied bias-voltage V. φ_{Defect} (φ_{MgO}) stands respectively for the barrier height of the localized defect (MgO dielectric). Current increases when the barrier is within $\pm k_B T$ of the Fermi level E_F of the injecting electrode. (b) IV slopes change sooner at T_2 ($V_2 > V_1$) than at T_1. Here we compare the bias-dependence of a thermally activated (ΔT) process. (c) The peak in $\hat{I}(V)$ corresponds to a thermally activated transport feature present in the barrier's potential landscape, that we logically attribute to defect states. Figure reworked from ref [22].

This technique was extensively applied to investigate the potential landscape of sputtered textured MgO-based MTJs due to oxygen vacancies [10, 11]. Furthermore, it can be applied to other tunneling spintronics systems to explore the eventual impurities present within their dielectric barriers. In the next section, we first apply the $\hat{I}$ technique for both device's structures. Afterward, we introduce TMR_{rel} method that enables us to increase

the signal-to-noise ratio and confidently extract the barrier heights. And at last, ab-initio calculations serve to explicitly confirm the Fermi level shift between the two systems. This enabled us to reattribute the barrier heights and conclude that, in these samples, defect-mediated transport is ensured by holes rather than electrons.

5.3 Mapping oxygen vacancies in MgO-based MTJs

In this section, we compare the $\hat{\mathrm{I}}(\mathrm{V})$ data for samples with a CoFeB and FeB top electrode. The comparison takes place at low temperature with T_1 = 23K (21K), T_2 = 45K (42K) and $\Delta\mathrm{T}$ = 22K (21K) respectively for CoFeB (FeB) sample. The temperature step $\Delta\mathrm{T}$ defines the resolution of the thermal probing and is proportional to the signal of $\hat{\mathrm{I}}$, yet a too high value of $\Delta\mathrm{T}$ would average the different thermally activated processes and isn't suited in this study. Mapping the MTJ's barrier heights consists in extracting the peaks positions of $\hat{\mathrm{I}}$ for T_2 and T_1, T_3 and T_2, ..., $\mathrm{T}_{\mathrm{N}+1}$ and T_N in the 20-300K temperature range. Referring to Figure 5.8.a, we overlay the I_P current at the two temperatures with the resulting $\hat{\mathrm{I}}_\mathrm{P}$ plot for the CoFeB sample. One can see that both currents are indistinguishable at this scale, yet the resulting $\hat{\mathrm{I}}_\mathrm{P}$ clearly has two peaks centered around $\pm 1\mathrm{V}$. The high amplitude in the vicinity of zero bias is due to the thermal activation of inelastic processes relating to the zero-bias anomaly.

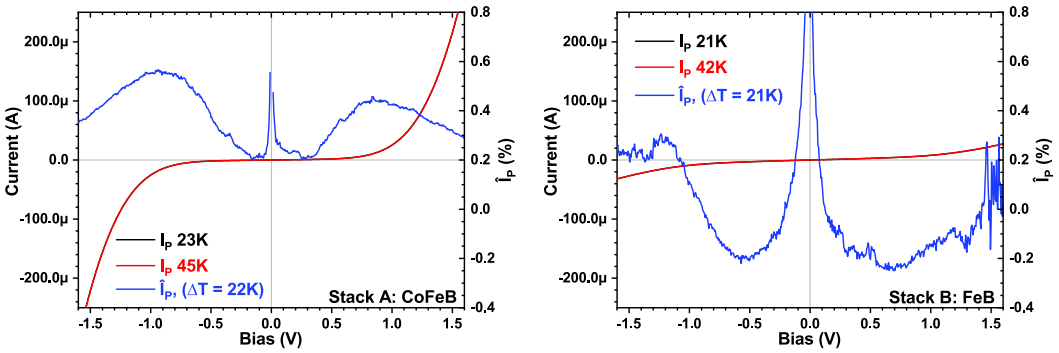

Figure 5.8: $\hat{\mathrm{I}}_\mathrm{P}$ **technique applied for** I_P **at low temperature.** Black, red, and blue stand for I_P at T $\approx$ 23K, I_P at T $\approx$ 45K, and the resulting $\hat{\mathrm{I}}_\mathrm{P}$ with $\Delta\mathrm{T} \approx$ 22K. (a) Stack A: CoFeB. The two $\hat{\mathrm{I}}_\mathrm{P}$ peaks centered around $\pm$ 1V corresponds to a thermally activated additional transport features. The position of these peaks is proportional to the position of a defect generated barrier height. (b) The same measurements were performed on the stack B: FeB. The $\hat{\mathrm{I}}_\mathrm{P}$ curve is noisier above (below) +1V (-1V). $\hat{\mathrm{I}}_\mathrm{P}$ strictly increases from the dips at +0.5V (-0.5V) towards higher (lower) values, we can envision that they are centered around the $\pm$ 1.6V marks which are more pronounced in $\mathrm{TMR}_\mathrm{rel}$ behavior, see Figures 5.9 and Figure 5.10.

Figure 5.8.b depicts the same measurements performed on the FeB sample. In this case,

the $\hat{\mathrm{I}}_{\mathrm{P}}$ curve is noisier and less pronounced above (below) +1V (-1V) bias values. Nevertheless, we see that $\hat{\mathrm{I}}_{\mathrm{P}}$ strictly increases from the dips at +0.5V (-0.5V) towards higher (lower) values and caps at below -1.3V and above +1.5V. According to the more pronounced thermally addressed features in $\mathrm{TMR}_{\mathrm{rel}}$ we estimate the $\hat{\mathrm{I}}_{\mathrm{P}}$ peaks to be centered around ± 1.6, see Figure 5.9 and following discussion. Measuring this device at higher bias values repeatedly led to more noise and irreproducibility. In both cases the $\hat{\mathrm{I}}_{\mathrm{P}}$ signal's amplitude range in the $0.2 - 0.4\%$ range with more noise in the FeB sample. Additionally, the amplitude of the $\hat{\mathrm{I}}_{\mathrm{P}}$ signal drastically increases at high T values which limits the proper LT and RT comparison of peak positions. The peak position is determined in a rather inaccurate manner, $\Delta \mathrm{V}_{\Phi} = \pm 0.2\mathrm{V}$, since the full width at half maximum (FWHM) is very large in these measured $\hat{\mathrm{I}}$ peaks. Here we presented only the $\hat{\mathrm{I}}_{\mathrm{P}}$ dataset, the $\hat{\mathrm{I}}_{\mathrm{AP}}$ dataset not presented here is characterized by the same features (peaks) with comparable amplitudes of the signal.

5.3.1 Thermal addressing of oxygen-vacancies

The same method can be applied for the TMR signal of the device, leading to the $\mathrm{TMR}_{\mathrm{rel}}$ protocol described by the following formula:

$$\mathrm{TMR}_{\mathrm{rel}} = \left(\frac{\mathrm{TMR}(\mathrm{V}, \mathrm{T}_2)}{\mathrm{TMR}(\mathrm{V}, \mathrm{T}_1)} - 1\right) * 100 \tag{5.2}$$

This approach consists in comparing the bias-voltage behavior of the device's TMR response between two temperatures T_1 and T_2 in search of thermally activated processes. $\mathrm{TMR}_{\mathrm{rel}}$ enables to circumvent the few limitations of $\hat{\mathrm{I}}$ and gives rise to higher amplitudes and more pronounced signals. These effects are depicted in figure 22.a in the case of a FeCoB top electrode. Both TMR signals at 23K and 45K are very similar in their shape and their resulting $\mathrm{TMR}_{\mathrm{rel}}$ clearly illustrated two pronounced dips centered around $\pm 1.2\mathrm{V}$. Both the amplitude and the precision (FWHM) are sharper in the case of $\mathrm{TMR}_{\mathrm{rel}}$ in comparison with the $\hat{\mathrm{I}}$ method. This result implies that the thermally activated defect mediated transport is detrimental for spin-polarized transport, since the $\mathrm{TMR}_{\mathrm{rel}}$ dips lead to a decrease in the TMR signal. Switching the top electrode from FeCoB to FeB leads to a broader $\mathrm{TMR}_{\mathrm{rel}}$ decrease, such that the peak now lies at least at 1.6eV, i.e. at the edge of our measurement range (NB: attempts to increase bias to witness the peak were unsuccessful due to the resulting junction instability).

Applying the $\mathrm{TMR}_{\mathrm{rel}}$ protocol $(\Delta \mathrm{T} \approx 20\mathrm{K})$ for the full available temperature range [20K- 300K] gives rise to a multitude of $\mathrm{TMR}_{\mathrm{rel}}(\mathrm{V})$ graphs for each $\Delta \mathrm{T}$ increment. An intuitive way to represent this experimental dataset is to use a 3Dmap with an x-axis for the temperature, y-axis for the bias-voltage, and z-axis for the amplitude of the $\mathrm{TMR}_{\mathrm{rel}}$ signal. Referring to Figure 5.10.a, the $\mathrm{TMR}_{\mathrm{rel}}$ map acquired on the CoFeB sample is represented. The color scale corresponds to the z-axis and the $\mathrm{TMR}_{\mathrm{rel}}$ amplitude of the measurements. The first strip of this $\mathrm{TMR}_{\mathrm{rel}}$ map is the $\mathrm{TMR}_{\mathrm{rel}}$ graph represented in Figure 5.9.a. Consequently, the $\mathrm{TMR}_{\mathrm{rel}}$ dips of Figure 5.9.a correspond here to the purple, blue and green colors. One can see that there are two main features, the first at $\pm 1.2\mathrm{V}$ in the 20K-80K temperature range and the second thicker one at $\pm 0.7\mathrm{V}$ in the 130K-300K

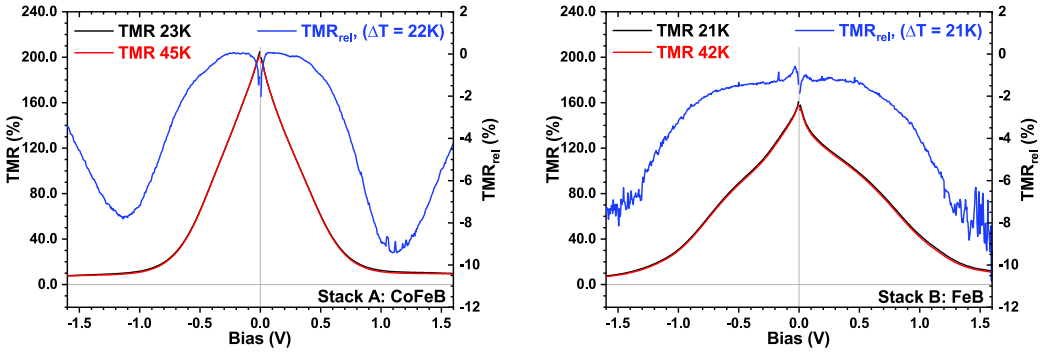

Figure 5.9: **TMRrel technique applied at low temperature.** Black, red and blue stand for TMR at T ≈ 23K, TMR at T ≈ 45K and the resulting $\mathrm{TMR_{rel}}$ with ΔT ≈ 22K. (a) Stack A: CoFeB. $\mathrm{TMR_{rel}}$ presents two sharp pronounced deeps centered around ± 1.2V. (b) Stack B: FeB. The $\mathrm{TMR_{rel}}$deeps move to higher bias-voltage values, seem to be centered around ± 1.6V. See Figure 24 for more details.

temperature range. And a switchover between these two features is observable at 80K-130K. This observation implies that there are at least two defect species at $\pm 1.2\mathrm{V}$ and $\pm 0.7\mathrm{V}$ that dominantly contribute to transport at two different temperature ranges. A more careful analysis of the high-temperature range backed up by ab-initio calculations (see Figure 5.11) indicates that it is composed out of two elements at $\pm 0.7\mathrm{V}$ and $\pm 0.4\mathrm{V}$. The latter feature is limited to the T > 250K temperatures. Overall, the $\mathrm{TMR_{rel}}$ map's major features are symmetric in bias-voltage. Furthermore, we associate the ± 1.2, $\pm 0.7\mathrm{V}$ and $\pm 0.4\mathrm{V}$ features to respectively $\mathrm{M_1}$, F and $\mathrm{M_2}$ oxygen vacancies states (See Figure 5.11 for the detailed description).

The same $\mathrm{TMR_{rel}}$ protocol performed on the FeB sample is represented in Figure 5.10.b. It is characterized by the same temperature dependence of the three main features as the CoFeB dataset, but in the FeB sample, they are shifted by 0.45V towards higher bias-voltages. To better understand the origin of this voltage shift, we performed a set of calculations demonstrating that the $\Delta\mathrm{V}$ shift takes its roots in the shift of the Fermi level of the whole sample's structure and consequently the shift of the oxygen vacancies positions in respect with the CoFeB case. The calculation of the central MgO's layer DOS in presence of F, $\mathrm{M_1}$, and $\mathrm{M_2}$ states was performed on the VASP code within the generalized gradient approximation (GGA). The position of the defect stats with respect to the Fermi level was adjusted with the Heyd-Scuseira-Ernzerhof (HSE03) method [92]. In this study, the MgO's DOS in presence of oxygen vacancies was compared for different sets of FM electrodes, namely Fe, CoFe, and Co. Figure 5.11 summarizes the most important results of this study. Swapping the FM both MTJ's electrodes from Fe to CoFe and finally to Co alters the Fermi level of the structure which results in the shift of oxygen vacancies states (sharp peaks in DOS) within the MgO spacer. From Fe(red) → CoFe(black) all states (F, $\mathrm{M_1}$ and $\mathrm{M_2}$) are shifted by 0.25eV, and from Fe(red) → Co(green) all three states are

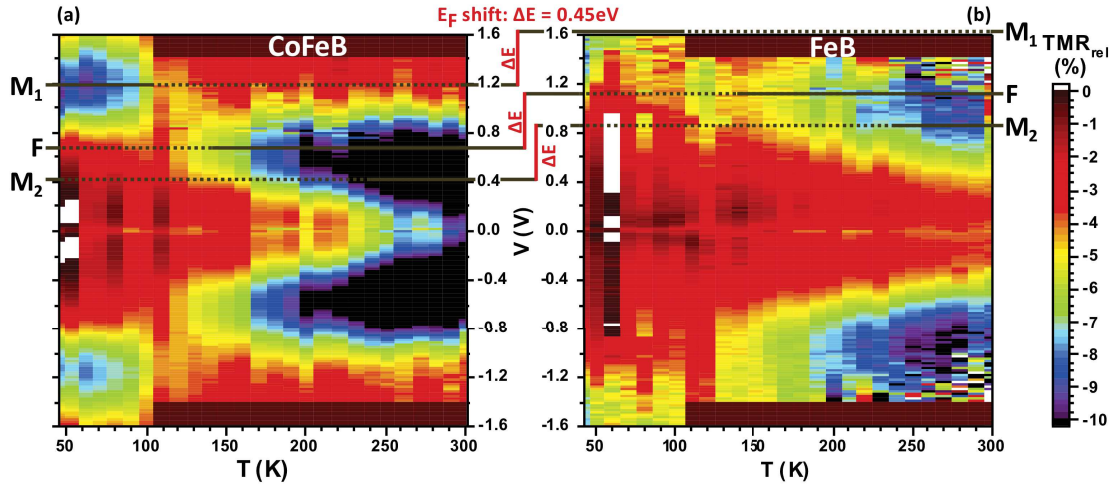

Figure 5.10: **Bias and temperature behavior of** $\mathrm{TMR_{rel}}$**.** Temperature and bias-voltage are along the x and y-axis; the color pallet represents the amplitude $(\%)$ of $\mathrm{TMR_{rel}}$. The solid (dotted) black lines correspond to the dominant presence (absence) of a feature at a given T range. (a) $\mathrm{TMR_{rel}}$. ($\Delta \mathrm{T} \approx 20\mathrm{K}$) map for the CoFeB sample. Three main thermally activated features are assigned to oxygen vacancies states $\mathrm{M_1}$ [±1.2V; 20K-80K], F [±0.7V; 130K-80K] and $\mathrm{M_2}$ [±0.4V; T > 250K]. (b) The same $\mathrm{TMR_{rel}}$. protocol performed on the FeB sample. A $\mathrm{TMR_{rel}}$ drop at ±1.6V is partially observable whereas the other two features at ±1.1V and ±0.8V are more pronounced. Both (a) and (b) share all the three features and have the exact same temperature dependence with the only difference between the two is a 0.45V bias offset. Figure taken from ref [14].

shifted by 0.4eV. Consequently, we associate the shift of thermally activated transport features which are basically defected states mediated transport manifestations with the shift of the structure's Fermi level between the CoFeB and FeB top electrode MTJs.

5.3.2 Redefined tunneling potential landscape

In conclusion single (F) and double (M) oxygen vacancies can be confidently attributed to the thermally activated features observed in the $\mathrm{TMR_{rel}}$ maps. Furthermore, the comparison between CoFeB and FeB samples both experimentally and theoretically indicates that the shift of the defects profile (Figure 5.10) originates from the Fermi level shift. The slight quantitative discrepancy between the theoretically predicted 0.25eV and the experimentally observed 0.45eV are to be considered within the experimental uncertainty (at least $\pm 0.05\mathrm{eV}$). Furthermore, we conclude that since it is occupied states that participate in the potential landscape, this implies that transport mediated by oxygen vacancies in these sputtered MgO-based MTJs is ensured by holes and not electrons. This idea originates from the fact that all three states F, $\mathrm{M_1}$, and $\mathrm{M_2}$ shift in the same direction when CoFeB

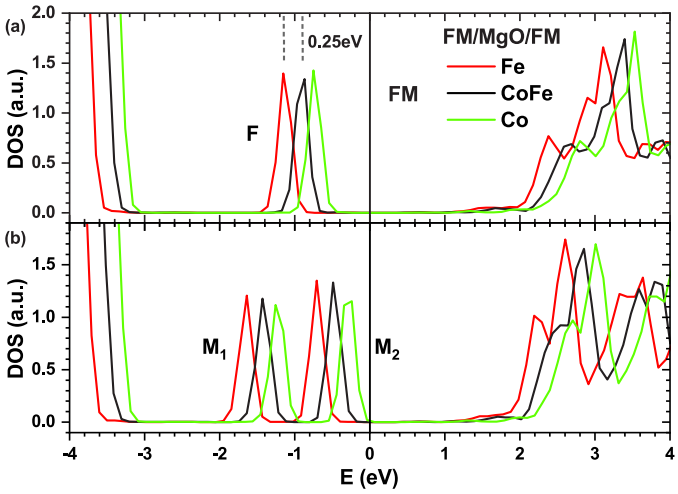

Figure 5.11: **Shifting MgO's density of state by altering its surrounding ferromagnetic electrodes.** Central MgO's DOS calculated for on a FM(001)/MgO(001)[7ML]/FM(001) structure, where FM is Fe(red), CoFe(black) and Co(green). In (a) and (b), F, M_1 and M_2 states are all shifted by 0.25eV for the Fe/CoFe replacement and by 0.4eV for the Fe/Co replacement. Figure taken from ref [14].

is replaced by FeB. This means that all three states lie from the same side of the Fermi level, and more precisely below it. This is all confirmed by the ab-inition calculations of Figure 5.11. This observation rewrites the commonly accepted picture of solely electron tunneling in commonplace MgO-based MTJs. The temperature-dependent potential landscape previously described [10] can be now revisited, and its schematic is represented in Figure 5.12. The black lines and the degraded gray color correspond to the central position and the respective spectral electronic resolution of the localized states taken from Figure 5.10. As we've seen before, each oxygen vacancy state is dominantly participating in transport only at a given temperature region. This effect is represented by filled/empty circles and their respective temperature ranges. All three states are found below the Fermi levels which are represented in green, black, and red dotted lines for the sets of electrode materials.

In conclusion, by thermally probing the bias dependence of the device's magnetotransport response we were able to determine the effective barrier heights felt by the tunneling charge carriers. Combining this study with an ab-initio theory we are able to assign each of these barrier heights to a specific specie of oxygen vacancies, namely M_1,M_2, and F/F^+ centers. The position and the electronic profile of these "additional" states close to the center of dielectric's band-gap are at the origin of the lower than expected TMR signals reported in the literature [13, 31, 40]. In the next section, we will demonstrate how the electronic portrait of oxygen vacancies in the MTJ's MgO-spacer can be used to optically address these devices and alter their spintronic properties, and in the process provide in-

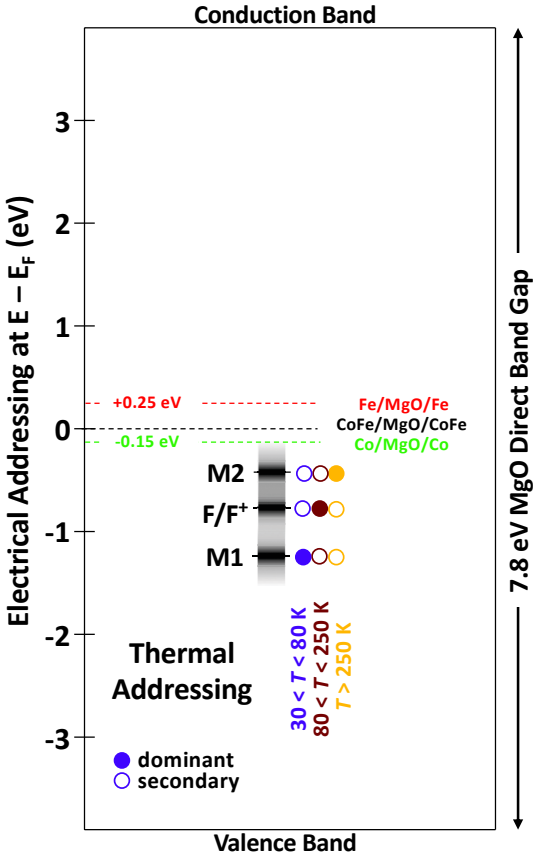

Figure 5.12: **Potential landscape of MTJ's MgO band-gap.** Schematic representation of oxygen vacancies states energy profile within the direct band-gap of MgO (7.8eV). All three M_2, F and M_1 states lie below the Fermi level for Fe, FeCo and Co electrodes. Each state is characterized by its dominant or secondary involvement into transport at given temperature ranges. Figure taken from ref [14].

operando insight into the nanotransport path they embody for the MTJ.

5.4 Addressing the nanotransport path in MgO spintronics using light

The optical activity of MgO crystals was vastly investigated in previous years, and the presence of optically active oxygen vacancies was defiantly demonstrated in several works [93–96]. The main motivation of this research project was to demonstrate that these optical mechanisms described in the literature on MgO crystals can serve to tune the spintronic properties of commonly used MgO-based MTJs, and in the process gain further insight into the device's actual nanotransport path. The main limitation of this concept is

that by shining a light on the MTJ it can increase its temperature by absorption. We note here that the generation of spontaneous thermovoltages within the device by addressing the MTJs surface with a focalized laser beam was recently demonstrated [97]. Moreover, the optically addressing of MTJs generated simultaneously two effects: i) it increases the device's temperature which in-turn alters the oxygen vacancy-driven transport as discussed in the previous Section 5.3, ii) it also promotes 'additional' populated oxygen vacancies states according to the Franck-Condon principle, which electronically alters the potential landscape and affects the tunneling scheme of the device. These effects can together modify its spintronic response. To separate the trivial thermal features from the optically activated electronic To separate the trivial thermal features from the optically activated electronic features, we inspected a relatively simple concept, which consists of comparing the device's pure thermal addressing with the optical one containing both possible thermal and electronic contributions. If shining light on the device doesn't provoke the exact thermal addressing trends we can conclude that an additional electronic component is involved and it can be quantified. Referring to Figure 5.13.a, we examined the optical absorption of a sputtered 50nm MgO crystal as a function of the optical wavelength (energy) at different temperatures. This study reveals a pronounced absorption peak centered around 3.2eV with substantial intensity between 3.5eV and 2.9eV, which has been attributed in the literature [74] to M centers. Note how the absorption strongly increases between 250K and 300K, i.e. in the same temperature range for which we find dominant thermal addressing of the $\mathrm{M_2}$ center in solid-state tunneling (see Figure 5.12). To promote optical absorption on the M centers of the MTJ's MgO barrier, we used a standard continuous-wave (CW) 405nm low power (70mW) laser source. The laser beam is characterized by a Gaussian profile with a diameter close to 200mum. Considering the $10\mu\mathrm{m}$ optical opening present on-top of each MTJ and the overall device's diameter (d $\approx 20\mu\mathrm{m}$; see Fig. 3.1(d)) the whole surface was addressed with photons. In Figure 5.13.b we compared the magnetoresistance response of the MTJ under purely optical (blue) and purely thermal (red) excitations. We utilize the term 'purely optical' since during these measurements the device remains at a given nominal temperature according to the cryostat, even though the laser is prone to heating the device and altering its temperature. In contrast, 'purely thermal' means that no light hit the device, and the temperature was varied from 25K to 100K. As a gauge of the MTJ's spintronic performance, we compare its TMR signal as a function of the current in the parallel configuration ($\mathrm{I_P}$), hence, we plot the TMR($\mathrm{I_P}$) dependence in the two cases. Since both TMR and $\mathrm{I_P}$ depend on temperature, TMR($\mathrm{I_P}$) as plotted for the 'purely thermal' and 'purely optical' experimental scenario should be identical if shining light on the MTJ generates a heating-only impact on the MTJ's transport. If both datasets differ, then shining light must also contain an electronic component relating to the absorption of light by M centers.

The measurements sequence is performed in the following way. The starting point of this experiments is at 25K at dark. We acquire 140 measurement points of the device's current response in its P and AP configurations at 10mV. We begin by performing the thermal addressing (red) by incrementally increasing the device's temperature from 25K - highest TMR($\mathrm{I_P}$) point to 100K - lowest TMR($\mathrm{I_P}$) point and back to 25K. All of this is done in the dark and in a 4-wire configuration. Then, while we remain at 25K, we

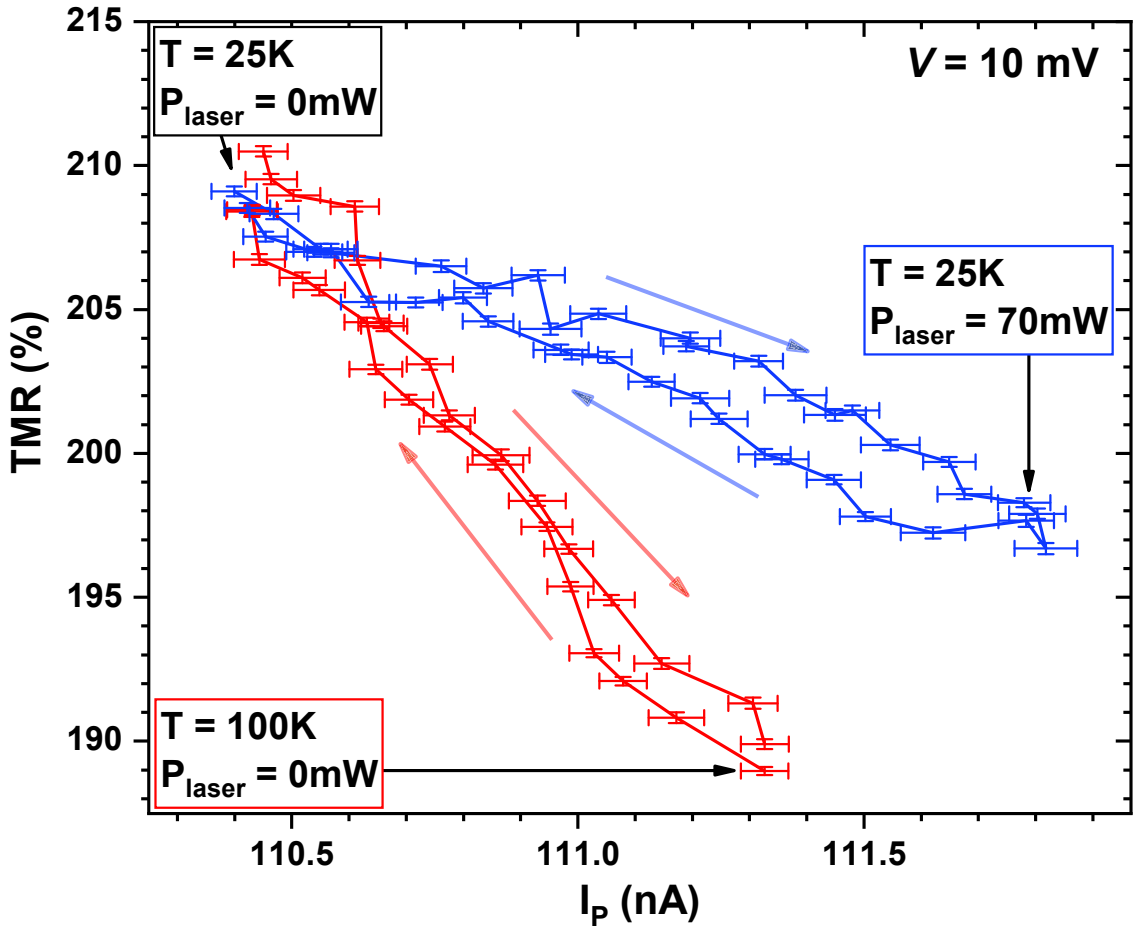

Figure 5.13: **Optical addressing of M-center mediated tunneling spintronics across MgO.** (a) Absorption spectrum acquired on a 2.5nm thick sputtered MgO, the 400nm sharp absorption peak is attributed to M centers. (b) Comparative study of a purely thermal (red) and a purely optical (blue) probing of the device's TMR(I_P) signal at 10mV highlighting the non-trivial heating effect of probing the MTJ's structure with photons at 405nm (3.06eV). Follow the discussion in the main text for more experimental and interpretation details.

address the device with the 405nm beam (blue) by progressively increasing the lasers power (i.e. photon flux) from 0mW - highest TMR(I_P) point to 70mW - lowest TMR(I_P) and back to 0mW. In both thermal and optical cases, we return to the same exact initial point. Moreover, the sweeps in and out are superimposed within the precision of error bars. This later observation precludes the presence of any experimental artefacts and implies that the MTJ's state doesn't drift during the measurement, and that we indeed compare the MTJ in the same state between the two 'purely optical' and 'purely thermal' scenario. As a note of mention, the error-bars are defined according to the averaging over the 140 points acquired at each device's configuration. In such manner, we are able to compare the purely thermal and a purely optical addressing. We observe an evident discrepancy between the

two behaviors: an electronic term is present in the device's response when it is shined upon with light. In other words, reducing the current $\mathrm{I_P}$ by the same proportion with temperature and light, the resulting TMR amplitude in these conditions isn't the same. Basically, we've confirmed that shining light on the MTJ doesn't only heat the device leading to a trivial thermal effect, but also generates an additional electronic modification to the tunneling potential landscape. At a given $\mathrm{I_P}$ amplitude generated using these two scenarios, we find that TMR is higher when M centers are absorbing light. This may be understood as a natural consequence of the role that M centers play in driving spintronic performance. Indeed, as described in Section 3.3, in the MTJ's P magnetic state, M centers promote a large conduction channel for Δ_1 states that are highly spin-polarized at $\mathrm{E_F}$ in the MTJ's FeCoB electrodes. This isn't the case in the MTJ's AP state, for which transport is dominated by the Δ_5 symmetry. Given that $\mathrm{TMR} = \mathrm{I_p}/\mathrm{I_{ap}} - 1$, it is natural that increasing Δ_1 conduction by generating photocarriers onto M centers will increase TMR, as observed experimentally.

5.5 Summary and perspectives

Since sputtered MgO-based magnetic tunnel junctions (MTJs) dominate the commercial market of spintronic devices, we oriented our research interests towards a refined understanding of their spintronic performance. The quality of the dielectric spacer (MgO) is essential for the spin and symmetry filtering and consequently to the tunneling magnetoresistance (TMR) effect observed in such devices. Oxygen vacancies are the most common defect species in the MgO material and therefore are the main agents altering its electronic properties. To better understand the current picture of defect mediated transport in such devices we've used an experimental spectroscopic technique, $\mathrm{I_{rel}}$ (or $\hat{\mathrm{I}}$), which allows to thermally probe the magnetotransport response of an MTJ device. In combination with ab-initio theory, this technique can give a mindful insight into the energy profile of the dielectric barrier's potential step, thus, to identify the localized oxygen vacancies states. In the first part of this chapter we have described the main origins of the TMR effect in epitaxial and sputtered MTJs. This step was necessary for the proper introduction of localized states within the dielectric spacer and their effects on transport, which was done in the second part. The last part of this chapter was devoted to the investigation of thermally activated transport features observed in both $\mathrm{I_{rel}}$ and $\mathrm{TMR_{rel}}$ spectra in two slightly different spintronic systems. Comparing the magnetoresponse response of two similar MTJs structures, namely a CoFeB/MgO/CoFeB and CoFeB/MgO/FeB, we've been able to clarify the energy position of the localized oxygen vacancies states therein involved. The shift of the Fermi level between the two systems is demonstrated by ab-initio theory [14]. Parallelly, the footprint of a unidirectional shift of all features in $\mathrm{TMR_{rel}}$ datasets indicates that single and double oxygen vacancies (F and $\mathrm{M_1}$ & $\mathrm{M_2}$) states lie on the same side of the Fermi level, contrary to the group's previous interpretation [10]. Ab-initio theory quantitatively attributes these features to the ground state of single and double oxygen vacancies, i.e. to occupied states. This result evidences that: i) oxygen vacancies participate in the transport of MgO-based MTJs by hole tunneling, ii) oxygen vacancies are lowering the ideal MgO's

barrier height and thus the RA product, thereby generating a higher current flow through the device. This last property points towards the intriguing combination of low RA products and high relatively high TMR signals in MgO-based spin-transfer-torque (STT) devices which are famously known for their MRAM applications. Moreover, in Section 5.4 we've addressed the nanotransport path in MgO spintronics using light. Comparing the 'purely thermal' and the 'purely optical' addressing of the MTJ, we demonstrated that M centers are driving the device's spintronic response, and that this response can be altered, indeed increased relative to a heating scenario when these M centers absorb photons. This factual proof that light can electronically alter the MTJ's nanotransport path will help us revisit the idea [47] of altering the symmetry-conserved channels of solid-state tunneling using the linear polarization of light. Furthermore,since the optical population/depopulation of excited states are function of time, the next step of this research would be to probe the dynamic time and energy dependent light generated effects arising MgO-based MTJs. Several key steps were performed during this thesis project towards such experiments. For instance we've managed to add a tunable pulsed light source to the current setup and perform few reference tests. A tunable pulsed 2 light source in combination with an ultra-fast (Ghz range) Keithley could enable the development of a dynamic-spectroscopic technique probing the defects species involved in the spin-polarized tunneling schemes of MTJs.

Traduction en Français:

Résumé et perspectives

Puisque les jonctions tunnel magnétiques (MTJ) à base de MgO pulvérisées dominent le marché commercial des dispositifs spintroniques, nous avons orienté nos intérêts de recherche vers une compréhension affinée de leurs performances spintroniques. La qualité de l'entretoise diélectrique (MgO) est essentielle pour le filtrage de spin et de symétrie et par conséquent pour l'effet de magnétorésistance tunnel (TMR) observé dans de tels dispositifs. Les lacunes en oxygène sont les espèces de défauts les plus courantes dans le matériau MgO et sont donc les principaux agents modifiant ses propriétés électroniques. Pour mieux comprendre l'image actuelle du transport par défaut dans de tels dispositifs, nous avons utilisé une technique spectroscopique expérimentale, Irel (ou I^), qui permet de sonder thermiquement la réponse de magnétotransport d'un dispositif MTJ. En combinaison avec la théorie ab-initio, cette technique peut donner un aperçu conscient du profil énergétique de l'étape de potentiel de la barrière diélectrique, ainsi, pour identifier les états de lacunes d'oxygène localisées. Dans la première partie de ce chapitre, nous avons décrit les principales origines de l'effet TMR dans les MTJ épitaxiales et pulvérisées. Cette étape était nécessaire pour la bonne introduction des états localisés dans l'entretoise diélectrique et leurs effets sur le transport, ce qui a été fait dans la seconde partie. La dernière partie de ce chapitre était consacrée à l'étude des caractéristiques de transport thermiquement activées observées dans les spectres Irel et TMRrel dans deux systèmes spintroniques légèrement différents. En comparant la réponse de magnétoréponse de deux structures MTJ similaires, à savoir un CoFeB / MgO / CoFeB et CoFeB / MgO / FeB, nous avons pu clarifier la position énergétique des états de lacunes d'oxygène localisés impliqués. Le

décalage du niveau de Fermi entre les deux systèmes est démontré par la théorie ab-initio [14]. Parallèlement, l'empreinte d'un décalage unidirectionnel de toutes les entités dans les ensembles de données TMRrel indique que les états des lacunes d'oxygène simples et doubles (F et M1 M2) se situent du même côté du niveau de Fermi, contrairement à l'interprétation précédente du groupe [10] . La théorie ab-initio attribue quantitativement ces caractéristiques à l'état fondamental des lacunes d'oxygène simples et doubles, c'est-à-dire aux états occupés. Ce résultat montre que: i) les lacunes d'oxygène participent au transport des MTJ à base de MgO par tunneling, ii) les lacunes d'oxygène abaissent les MgO idéaux la hauteur de la barrière et donc le produit RA, générant ainsi un flux de courant plus élevé dans l'appareil. Cette dernière propriété pointe vers la combinaison intrigante de produits à faible RA et de signaux TMR relativement élevés dans les dispositifs à couple de transfert de spin (STT) à base de MgO qui sont connus pour leurs applications MRAM. De plus, dans la section 4.4, nous avons abordé le chemin du nanotransport dans la spintronique MgO utilisant la lumière. En comparant l'adressage " purement thermique " et " purement optique " du MTJ, nous avons démontré que les centres M pilotent la réponse spintronique de l'appareil, et que cette réponse peut être altérée, voire augmentée par rapport à un scénario d'échauffement lorsque ces centres M absorbent des photons . Cette preuve factuelle que la lumière peut modifier électroniquement le chemin du nanotransport du MTJ nous aidera à revoir l'idée [47] de modifier les canaux conservés par symétrie du tunnel à semi-conducteurs en utilisant la polarisation linéaire de la lumière. De plus, étant donné que la population / dépeuplement optique des états excités est fonction du temps, la prochaine étape de cette recherche serait de sonder le temps dynamique et les effets générés par la lumière dépendant de l'énergie résultant des MTJ à base de MgO. Plusieurs étapes clés ont été réalisées au cours de ce projet de thèse vers de telles expériences. Par exemple, nous avons réussi à ajouter une source de lumière pulsée réglable à la configuration actuelle et à effectuer quelques tests de référence. Une source de lumière pulsée accordable 2 en combinaison avec un Keithley ultra-rapide (gamme Ghz) pourrait permettre le développement d'une technique spectroscopique dynamique sondant les espèces de défauts impliquées dans les schémas tunnel polarisés en spin des MTJ.

Part II

Power Generating Spintronics

Chapter 6

Power Generating Spintronics

Spintronics is usually strictly associated with the field of information storage since it's most known for applications in HDD read-heads and modern MRAM devices. In this research work, we investigate how spintronics can promote energy generation. This will be done through a careful analytical and experimental examination of a conceptual spintronic "spin-engine" embedded within a magnetic tunnel junction and capable of generating power by harvesting thermal energy. Developing novel energy harvesting techniques has a high impact factor since our society's well-being relies on the generation of renewable and clean energy. According to the Cambridge English dictionary, the term to "harvest" is associated with an action of collecting crops, information or any other type of goods at either no or a very small cost. At first glance harvesting energy from the surrounding medium seems to challenge the rules of thermodynamics and especially its 2^{nd} law. This law dictates that the entropy or the number of microscopic configurations of an isolated system can never decrease with time. In other words, the entropy of a system can only remain the same or increase. Consequently, completely free energy doesn't exist, but workarounds are possible since renewable sources exist. Geothermal, solar, gravitational and many other energies can be harvested i.e. converted into useful electrical power. In 1867 J.C. Maxwell mostly known for the classical electromagnetic radiation laws, imagined an entity, the "Maxwell's Demon" (MD), capable of challenging the 2^{nd} law of thermodynamics by locally generating a negative entropy. Its basic operation consists in controlling a gate between two gas reservoirs initially at the same temperature. Since the demon knows about the position and speed of each individual particle, he can sort the slow/fast particles between the two reservoirs by a well-timed opening and closing of the gate. Separating the particles into slow-moving and fast-moving moieties is equivalent to reducing the entropy of the system, hence, to generate energy for free. The field of quantum thermodynamics describes how thermodynamics laws are applicable in quantum mechanical systems. Recent advancements in this field have shown that the second law of thermodynamics can be violated only locally, giving in such way rise to a local negative entropy. Laundauer's principle [98] completes the initial MD operation scheme. It implies that the MD's entropy increases while the systems entropy decreases. It happens since the MD's operation dissipates heat through a memory erasure cycle required to avoid memory shortage. In the last decade multiple works reported about the realizations of MD harvesting energy in quantum systems both experimentally and theoretically [99–102, 102–108]. In our work we focus on a category of such energy-generating devices that utilize the mag-

netic and spin degree of freedom within spintronic device to harvest thermal energy from the surrounding medium. The key ingredients required for such an effect to take place are the following: i) A chain of discrete energy and spin states forming a specific energy profile within the dielectric layer. In our experiment we attribute the appearance of these states to oxygen vacancies within MgO [82] that capture diffused carbon atoms [109], thereby forming paramagenetic centers in the barrier with energy states whose spin splitting is lower than $\mathrm{k_B T}$, ii) A spintronic selector on each side of these paramagnetic centers. In our case its role is fulfilled by spinterface [110]. This effect arises from the interfacial mixture of spin states between the ferromagnetic electrode and the dielectric layers (see Section Section 9.6.1). The spintronic-selectors fulfill two key roles. Firstly they protect and preserve the central discrete energy and spin states from thermal smearing by the many degenerate states of the electrodes. And secondly, they are needed to efficiently alter the symmetry/asymmetry of the device's energy profile [100, 105]. If the system's energy profile is symmetric, charges carrier from left and right spintronic-selectors have the same spontaneous tunneling rates ($\Gamma_{\mathrm{left}} = \Gamma_{\mathrm{right}}$) onto the central discrete energy and spin states. In that case, the net spontaneous current in this symmetric system would be equal to zero, and this would preclude any energy harvesting prospect. Introducing an asymmetry into the system results in altering the spontaneous tunneling rates ($\Gamma_{\mathrm{left}} \neq \Gamma_{\mathrm{right}}$). When this property is coupled to a chain of discrete energy and spin states within the dielectric layer,thermal fluctuations and hence spin fluctuations can be rectified and transformed into a spontaneous voltage across the device [100, 105]. This spontaneous voltage is proportional to the splitting of central discrete states and leads to a spontaneous current flowing across the device [102]. The thermal fluctuation and therefore spin fluctuations on the central discrete states are rectified by asymmetrical spintronic rectifiers. This generates an imbalanced current flow in a preferential direction defined by the asymmetrical energy and spin profile of the device. This is the basic operation procedure of a spin-engine integrated within a spintronic device proposed in our recent work [109]. Two pioneering experimental realizations of such spintronic energy harvesting systems based on spin-asymmetry along the entire device's profile have been reported [99, 102]. In both cases, spontaneous voltages leading to non-zero currents, hence electrical power, were detected at low cryogenic temperatures in exotic materials. Concurrently, theoretical and experimental efforts unveiling the operation of autonomous quantum Maxwell demon were recently demonstrated [107, 108, 111]. Inspired by these recent advancements and the urgent need to attract pluri-disciplinary scientific interest to this useful topic, we propose here our model of a spin-engine capable of harvesting thermal fluctuations in order to generate electrical power at room-temperature that can be realized in a common-place MgO-based spintronic devices [109]. This chapter is divided in three main sections. The first section summarizes and references the most recent theoretical and experimental advancements in the field of quantum thermodynamics relevant for energy harvesting. In the second section, the analytical model of the energy harvesting spin-engine backed-up by ab-initio calculations and experiments is carefully examined. The analytical model is tightly related to a large number of experimental observations, it involves spin-polarized transport across highly asymmetrical energy and spin profile. The third main section contains two subsections. Firstly, an experimental dataset acquired on a single MgO-based MTJ generating 0.1nW

of electrical power at room-temperature will be presented. The simultaneous combination of a huge TMR signal at RT, and large spontaneous current dependent on the device's magnetic configuration strongly implies that a spintronics-driven electrical power generation is taking place in the device. Those results are highly reproducible on the same device, exceed any possible experimental offsets and are supported by both analytical and ab-initio theories. Secondly, the comparison of the experimental datasets and the spin-engine's analytical model gives a good qualitative agreement. Taken together, these results suggest that spinterfaces indeed exhibit a high transport spin polarization not only at low [54], but also at room temperature in agreement with spectroscopic studies [53]. Furthermore, we discuss the main ingredients required for a successful realization of such a spin-engine in spintronic devices. At last, we compare the efficiency of our spin-engine in current MgO-based MTJs densities with other renewable sources of energy.

Traduction en Français:

Introduction à la spintronique générant de l'énergie

La spintronique est généralement strictement associée au domaine du stockage des informations car elle est surtout connue pour les applications dans les têtes de lecture HDD et les dispositifs MRAM modernes. Dans ce travail de recherche, nous étudions comment la spintronique peut promouvoir la production d'énergie. Cela se fera à travers un examen analytique et expérimental minutieux d'un «spin-moteur» conceptuel spin-tronique intégré dans une jonction tunnel magnétique et capable de générer de l'énergie en récoltant de l'énergie thermique. Le développement de nouvelles techniques de récupération d'énergie a un impact important, car le bien-être de notre société repose sur la production d'énergie renouvelable et propre. Selon le dictionnaire anglais de Cambridge, le terme «moisson» est associé à une action de collecte de récoltes, d'informations ou de tout autre type de marchandises à un coût nul ou très faible. À première vue, récolter l'énergie du milieu environnant semble remettre en cause les règles de la thermodynamique et surtout sa 2e loi. Cette loi dicte que l'entropie ou le nombre de configurations microscopiques d'un système isolé ne peut jamais diminuer avec le temps. En d'autres termes, l'entropie d'un système ne peut que rester la même ou augmenter. Par conséquent, l'énergie totalement gratuite n'existe pas, mais des solutions de contournement sont possibles car des sources renouvelables existent. Les énergies géothermiques, solaires, gravitationnelles et bien d'autres peuvent être récupérées, c'est-à-dire converties en énergie électrique utile. En 1867, J.C. Maxwell surtout connu pour les lois classiques du rayonnement électromagnétique, imagina une entité, le «Démon de Maxwell» (MD), capable de contester la 2e loi de la thermodynamique en générant localement une entropie négative. Son fonctionnement de base consiste à contrôler une grille entre deux réservoirs de gaz initialement à la même température. Puisque le démon connaît la position et la vitesse de chaque particule individuelle, il peut trier les particules lentes / rapides entre les deux réservoirs par une ouverture et une fermeture bien chronométrées de la porte. Séparer les particules en fragments à déplacement lent et rapide équivaut à réduire l'entropie du système, par conséquent, à générer de l'énergie gratuitement. Le domaine de la thermodynamique

quantique décrit comment les lois de la thermodynamique sont applicables dans les systèmes de mécanique quantique. Des progrès récents dans ce domaine ont montré que la deuxième loi de la thermodynamique ne peut être violée que localement, donnant ainsi lieu à une entropie négative locale. Le principe de Laundauer [98] complète le schéma de fonctionnement initial du MD. Cela implique que l'entropie du MD augmente tandis que l'entropie du système diminue. Cela se produit car le fonctionnement du MD dissipe la chaleur à travers un cycle d'effacement de la mémoire nécessaire pour éviter un manque de mémoire. Au cours de la dernière décennie, de nombreux travaux ont rendu compte des réalisations de la MD captant l'énergie dans les systèmes quantiques à la fois expérimentalement et théoriquement [99–102, 102–108]. Dans notre travail, nous nous concentrons sur une catégorie de tels dispositifs générateurs d'énergie qui utilisent le degré de liberté magnétique et de spin dans le dispositif spintronique pour récolter l'énergie thermique du milieu environnant. Les ingrédients clés nécessaires pour qu'un tel effet se produise sont les suivants: i) Une chaîne d'énergie discrète et d'états de spin formant un profil d'énergie spécifique dans la couche diélectrique. Dans notre expérience, nous attribuons l'apparition de ces états à des lacunes d'oxygène au sein du MgO [82] qui capturent les atomes de carbone diffusés [109], formant ainsi des centres paramagénétiques dans la barrière avec des états d'énergie dont la division de spin est inférieure à kBT, ii) A sélecteur spintronique de chaque côté de ces centres paramagnétiques. Dans notre cas, son rôle est rempli par spinterface [110].. Cet effet résulte du mélange interfacial d'états de spin entre l'électrode ferromagnétique et les couches diélectriques (voir section Section 9.6.1). Les sélecteurs spintroniques remplissent deux rôles clés. Premièrement, ils protègent et préservent l'énergie discrète centrale et les états de spin de frottis thermique par le de nombreux états dégénérés des électrodes. Et deuxièmement, ils sont nécessaires pour modifier efficacement la symétrie / asymétrie du profil énergétique de l'appareil [100, 105]. Si le profil énergétique du système est symétrique, les porteurs de charges des sélecteurs spintroniques gauche et droit ont les mêmes taux de tunnel spontané ($\Gamma_{\mathrm{gauche}} = \Gamma_{\mathrm{droite}}$) sur l'énergie discrète centrale et les états de spin. Dans ce cas, le courant spontané net dans ce système symétrique serait égal à zéro, ce qui exclurait toute perspective de récupération d'énergie. L'introduction d'une asymétrie dans le système entraîne une modification des taux de tunneling spontanés ($\Gamma_{\mathrm{gauche}} = \Gamma_{\mathrm{droite}}$). Lorsque cette propriété est couplée à une chaîne d'énergie discrète et d'états de spin à l'intérieur de la couche diélectrique, les fluctuations thermiques et donc les fluctuations de spin peuvent être redressées et transformées en une tension spontanée aux bornes du dispositif [100, 105]. Cette tension spontanée est proportionnelle à la division des états discrets centraux et conduit à un courant spontané circulant à travers le dispositif [102]. La fluctuation thermique et donc les fluctuations de spin sur les états discrets centraux sont rectifiées par des redresseurs spintroniques asymétriques. Ceci génère un flux de courant équilibré dans une direction préférentielle définie par l'énergie asymétrique et le profil de spin du dispositif. Il s'agit de la procédure de fonctionnement de base d'un spin-engine intégré dans un dispositif spintronique proposé dans nos travaux récents [109]. Deux réalisations expérimentales pionnières de tels systèmes de récupération d'énergie spintronique basés sur l'asymétrie de spin le long du profil de l'appareil entier ont été rapportées [99, 102]. Dans les deux cas, des tensions spontanées conduisant à des courants non nuls, donc de la puissance électrique, ont été détectées à des températures

cryogéniques basses dans des matériaux exotiques. Parallèlement, des efforts théoriques et expérimentaux dévoilant le fonctionnement du démon quantique autonome de Maxwell ont été récemment démontrés [107, 108, 111]. Inspirés par ces avancées récentes et le besoin urgent d'attirer un intérêt scientifique pluridisciplinaire sur ce sujet utile, nous proposons ici notre modèle de spin-engine capable de capter les fluctuations thermiques afin de générer une puissance électrique à température ambiante réalisable dans un dispositif spintronique à base de MgO en lieu commun [109]. Ce chapitre est divisé en trois sections principales. La première section résume et fait référence aux avancées théoriques et expérimentales les plus récentes dans le domaine de la thermodynamique quantique pertinente pour la récupération d'énergie. Dans la seconde section, le modèle analytique du moteur de spin à récupération d'énergie, soutenu par des calculs et des expériences ab-initio, est soigneusement examiné. Le modèle analytique est étroitement lié à un grand nombre d'observations expérimentales, il implique un transport polarisé en spin à travers une énergie et un profil de spin hautement asymétriques. La troisième section principale contient deux sous-sections. Tout d'abord, un ensemble de données expérimentales acquises sur un seul MTJ à base de MgO générant 0,1 nW de puissance électrique à température ambiante sera présenté. La combinaison simultanée d'un énorme signal TMR à RT et d'un courant spontané important dépendant de la configuration magnétique de l'appareil implique fortement qu'une génération d'énergie électrique pilotée par la spintronique a lieu dans l'appareil. Ces résultats sont hautement reproductibles sur le même appareil, dépassent tous les décalages expérimentaux possibles et sont étayés par des théories analytiques et ab-initio. Deuxièmement, la comparaison des jeux de données expérimentaux et du modèle analytique du moteur de spin donne un bon accord qualitatif. Pris ensemble, ces résultats suggèrent que les spinterfaces présentent en effet une polarisation de spin de transport élevée non seulement à faible [54], mais aussi à température ambiante en accord avec les études spectroscopiques [53]. En outre, nous discutons des principaux ingrédients nécessaires pour une réalisation réussie d'un tel spin-engine dans des dispositifs spintroniques. Enfin, nous comparons l'efficacité de notre spin-engine en courant densités de MTJ à base de MgO avec d'autres sources d'énergie renouvelables.

Chapter 7

Theoretical Background: Harvesting Thermal Fluctuations

This section intends to describe several key examples of quantum energy harvesting systems, both to outline the development of quantum thermodynamics field and to discuss about their similarities and determine the main ingredients required to harvest energy from the surrounding medium on the quantum mechanical level.

The most used tools to generate energy are heat-engines, which convert the heat or thermal energy released from a given chemical reaction into a useful mechanical work. Thermal energy can also be converted directly into electricity through the well-known thermoelectric Seebeck effect [112]. Here, two reservoirs (2 terminal geometry) are held at different temperatures ($\mathrm{T_2} - \mathrm{T_1} = \Delta\mathrm{T}$). Where $\Delta\mathrm{T}$ consequently generates a thermovoltage, hence, a non-zero current at a zero applied voltage. Furthermore, this effect was experimentally observed in spintronics, thus, a gradient of temperature along a magnetic tunnel junction gives rise to a tunneling magnetic Seebeck effect (TMS) [113]. Böhnert et al. [114, 115] have experimentally observed the TMS effect in common-place CoFeB/MgO/CoFeB junction , with an output power $\mathrm{P_{out}} \approx 10\mathrm{pW}$ in a $12.6\mu\mathrm{m}^2$ device. The output power is evaluated by sourcing bias-voltage in association with a load resistance. As the main objective of this chapter is to describe the mechanics of converting thermal fluctuations into useful electrical power, the simple thermovoltage isn't relevant. In this respect, Thierschmann et al. [105] have experimentally implemented a proposal by Sanchez and Buttiker [100] a three terminal energy harvesting system capable of converting thermal fluctuations into an electric current, which is equivalent to electrical power. Referring to Figure 7.1.a, the system is composed of three main temperature and electron reservoirs coupled to two quantum-dots. The left (L) and right (R) reservoirs in blue are held at the same temperature T, whereas the central (H) reservoir is at a higher temperature T+ $\Delta\mathrm{T}$. The two QDs, $\mathrm{QG_C}$ and $\mathrm{QD_G}$ (yellow islands), are capacitively coupled (yellow wave): charge and energy can be exchanged between H and $\mathrm{QD_G}$ whereas $\mathrm{QD_C}$ is tunnel-coupled to the cold blue reservoirs L and R.

Harvesting thermal fluctuations, namely converting $\Delta\mathrm{T}$ into an electric current (J) is done in the following way. Referring to Figure 7.1.b, starting in (1) a low energy charge carrier is located in the left cold reservoir, then it can spontaneously tunnel with a given probability Γ_{L0} to the central $\mathrm{QD_C}$. Afterwards, in (2) a hot charge carrier can spontaneously tunnel onto the central $\mathrm{QD_G}$ with a probability Γ_{H1}. Since the two QDs are

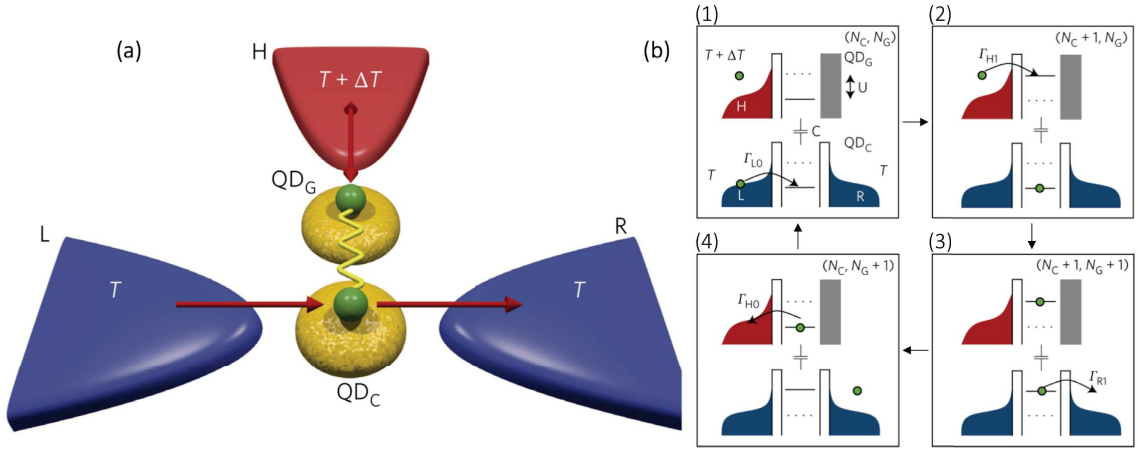

Figure 7.1: **Energy harvesting system and its operation schematics.** (a) Three terminal device converting thermal fluctuation into electrical current. Two reservoirs, left (L) and right (R) of a cold system in blue at a temperature T, a third central (H) hot reservoir in red at a temperature $\mathrm{T} + \Delta\mathrm{T}$. Two central yellow islands correspond to two capacitively coupled (yellow-wave) quantum-dots $\mathrm{QD_G}$ and $\mathrm{QD_C}$. The additional thermal energy $\Delta\mathrm{T}$ in the H reservoir can be converted into an electric current, red arrow from L into R. See description in the text. (b) Energy harvesting four-step cycle. 1) Spontaneous tunneling Γ_{L0} of L reservoir charge carrier to the central $\mathrm{QD_C}$. 2) Spontaneous tunneling Γ_{H1} of L reservoir charge carrier to the central $\mathrm{QD_G}$. 3) U energy exchange between $\mathrm{QD_C}$ and $\mathrm{QD_G}$, the cold charge carrier increases in energy. 4) The $\mathrm{QD_G}$ charge carrier relaxes since it gave its energy in (3) and spontaneously tunnels back to the hot reservoir at a rate Γ_{H0}. The excited charge carrier from $\mathrm{QD_C}$ spontaneously tunnels (rate of Γ_{R1}) to the R reservoir. The sequence of these four operations describes the thermal-fluctuations conversion into electrical current from L into R. See description in the text for the operation conditions. Figures taken from ref [105].

capacitively coupled, they can exchange thermal energy by packets (U). From 3 to 4, the hot charge carrier in $\mathrm{QD_G}$ transfers its energy to the cold charge carrier in $\mathrm{QD_C}$ .This is followed by the spontaneous tunneling Γ_{R1} and Γ_{H0}. As one can see, if the system is perfectly symmetric the current or energy flow will be the same in both directions, namely in (3) Γ_{R1} has the same probability as Γ_{L1} resulting in a zero-net current. If an asymmetry coefficient is introduced within the system, specifically in the tunneling probabilities between L, $\mathrm{QD_C}$ and R elements, a directed current flow, hence, energy is generated by the $\mathrm{T} + \Delta\mathrm{T}$ reservoir. Breaking the symmetry of this system is done by crafting a tunneling imbalance between L and $\mathrm{QD_C}$ and R and $\mathrm{QD_C}$. It is performed by a proper modification of the tunneling barriers perceived by the charge carriers in L and R reservoirs. This process is depicted in Figure 7.2. In panel (a), the barrier between L and $\mathrm{QD_C}$ is increased and therefore charge carriers are less prone to take the dotted path $\Gamma_{\mathrm{L0}}\Gamma_{\mathrm{R1}}$

than the solid $\Gamma_{L1}\Gamma_{R0}$ path. In this case the asymmetry of the system can be expressed as: $\Lambda = (\Gamma_{L0}\Gamma_{R1} - \Gamma_{L1}\Gamma_{R0})/(\Gamma_{L0}+\Gamma_{R0})(\Gamma_{R0}+\Gamma_{R1})$. Altering the sign of the asymmetry Λ results in altering the effective thermal fluctuations generated along the current path J, see Figure 7.2.a-b. The current sign linearly depends on J in the following way: $I_{TF} = e\Lambda J/U$. From this formula it is clear that in a symmetric system the thermal-fluctuation generated current I_{TF} is equal to zero. I_{TF} is negative(positive) if Λ is also negative(positive).

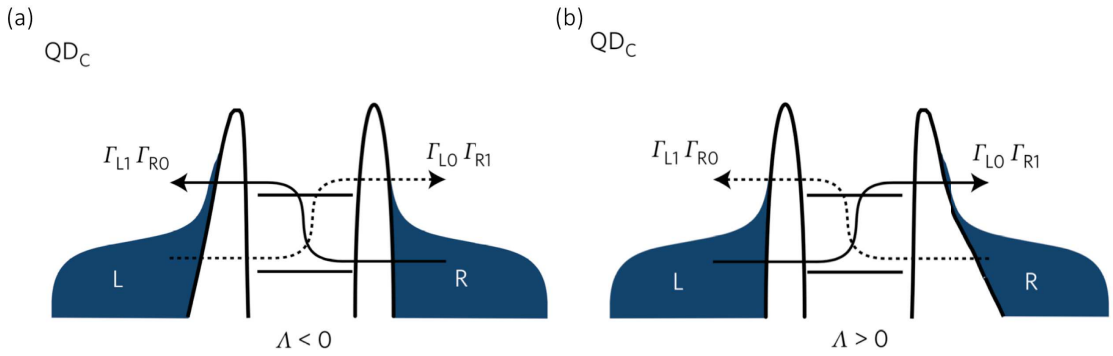

Figure 7.2: **Directing harvested-energy flow.** Introducing tunneling asymmetry Λ within the system allows to direct the thermally generated energy flow, hence, directs the current flow. (a) and (b) a negative asymmetry $\Lambda < 0$ and a positive asymmetry $\Lambda > 0$ give rise to different directions of current flow (solid arrow). Figure taken from ref [105].

To summarize, Thierschmann et al. [105] have experimentally demonstrated that introducing an asymmetry component enables the efficient harvesting of thermal fluctuations and their conversion into a directed current flow. As a note of mention, the authors have used bias-voltage on gates separating L and R reservoirs from QD_C to actively tune the barrier height felt by tunneling charge carriers. Hence, the system can be considered as a nonautonomous Maxwell's demon realization.

The recent rising interest towards quantum thermodynamics has given birth to multiple experimental and theoretical realizations of similar energy harvesting systems. Koski el al. [104] demonstrated the operation an autonomous Maxwell's demon system converting information (and not heat as in the case of Thierschmann et al. [105] into useful energy, and by that lowering locally the entropy of the system. Consequently, the temperature of the system decreases, and the demon becomes hotter,dissipating extracted heat. In this case, the asymmetry or that is to say the direction of the current is set by bias-voltage. A very similar effect of thermoelectric energy harvesting with quantum dots was theoretically predicted by Sothmann et al. [103]. Furthermore, this review article describes the role of the spin degree of freedom in heat engines harvesting thermal fluctuations. Recently, multiple other reports investigated the subject of harvesting thermal fluctuation by means of coupled quantum dots [101, 108, 111, 116, 117]. The efficiency of the thermal energy to electron flow was extensively discussed by Sanchez and Büttiker [100] almost a decade ago. The quantum system therein investigated is similar to the three terminal energy harvesting system recently presented by Thierschmann et al. [105] and is composed of cold

reservoirs (T_S) coupled by a conductive quantum dots in their turn capacitively couple to a QD of a hot reservoir. The heat to energy conversion mechanism is the same as described above and takes place by quantized packets from the hot reservoir (T_g) to the cold reservoir (T_s) one generating an imbalanced current flow (I), as represented in Figure 7.3. The authors have demonstrated that the maximum efficiency of heat to work conversion (Carnot efficiency [100]) is proportional to the tunneling asymmetry of the system. Interestingly, introducing additional conductive quantum dots, as represented in Figure 7.3, results in an increased efficiency by allowing only the "proper" transitions. In this case, the outer QDs act as energy-selectors by enabling only resonant tunneling between the left-lead/central QD and central QD/right-lead. The energy-selectors ban the direct transition from left to right lead by a single double state central QD.

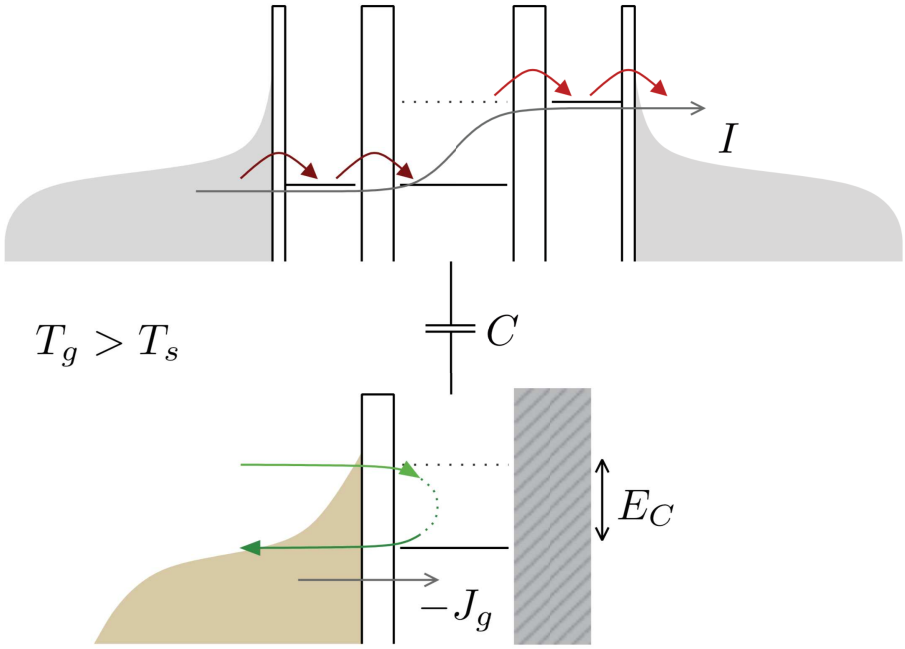

Figure 7.3: **Energy rectification – efficient heat to energy conversion.** The current flow I is represented by the solid gray arrow, it results from a sequential resonant tunneling through the central three QDs. The outer QDs act as energy-selector that blocks direct resonant tunneling through the central (double state) quantum dot and by this increase the overall efficiency of the heat-energy conversion. Figure taken from ref [100]. [Add Δ to the energy split, legend QDL, QDC, QDR]

To summarize, the two main ingredients evoked in the above referenced reports for a quantum heat to energy conversion are: i) A transport path along an energy-confined system (discrete energy states) assembled from a single or multiple quantum-dots along with a tunneling asymmetry between the left/right leads, ii) A high temperature reservoir that can exchange solely thermal energy with the colder transport section and not charge carriers, iii) The absorbed thermal energy E_C should be higher or at least equal to the energy split

Δ on the central$\mathrm{QD_C}, \mathrm{E_C} \geq \Delta$. As experimentally demonstrated [104, 105] the tunneling asymmetry is artificially introduced within the system by external bias-voltage on gates near the conductive QDs. A competing architecture utilizing magnetic tunnel junctions with an adjustable by an external magnetic field asymmetry will be demonstrated in section 8.1.1. In the next section 7.1 we will describe two concrete examples reported within the field of spintronics evidencing energy harvesting by rectifying thermal fluctuations on paramagnetic centers in magnetic tunnel junctions.

7.1 Harvesting energy within MTJs

Ten years ago, Hai et al. [99] unveiled an intriguing effect of generated magnetic energy features in the spintronic response of a magnetic tunnel junction. The device investigated by the authors is composed of GaAs/AlAs/GaAs/MnAs with MnAs nanoparticles in the GaAs barrier, as represented in Figure 7.4.b. In absence of external magnetic field, the IV response at low temperature of the device is centered around the zero point (I=0 at V=0), see Figure 7.4.a in black. Yet, once a magnetic field ($\mathrm{H_{ext}}$ = 10kG) is applied to the device the IV plot is shifted in voltage by 20mV. This voltage shift was assigned to the electromotive force (EMF) exerted on the tunneling electrons, hence, that they are acquiring additional energy when tunneling through the central superparamagnetic nanoparticles of MnAs. Yet, we associate this voltage-shift to energy harvesting effect by means of magnetic fields according to the previous description of heat-energy quantum engines and the section7.2 describing our analytical model of a spin-engine. The presence of an external magnetic field may lead to a spin-degeneracy lift on the central nanoparticles. Consequently, the naturally arising spin-fluctuations in the superparamagnetic MnAs nanoparticles are rectified by the asymmetrical spintronic profile of the junction leading to a current flowing in a preferred direction:see in Figure 7.4.a how the red curve is shifted to higher bias-voltages. The bias voltage shift therein observed is equivalent to a spontaneous voltage arising in the device as a direct consequence of the energy harvesting phenomena. Connecting a resistance load $\mathrm{R_L}$ and measuring the spontaneous voltage arising in the device the time relaxation of this effect can be determined. Referring to Figure 7.4.c, in presence of $\mathrm{R_L}$ the lifetime of the effect ranges in the $10^{2\sim}10^{3}\mathrm{s}$ range, the pink curve. On the other hand, when the connect resistance is infinite (open-circuit, see black curve) little relaxation is observed.

To better understand the origines of the spontaneous voltage arising in this and similar magnetic tunnel junctions and to provide a closer look into the role of spintronics in energy harvesting effects, we now discuss the recent scientific work of Miao el al. [102]. In this work, the authors assembled an asymmetric spin-profile MTJ device, with a set of specific properties (see 7.5.b for the $\mathrm{Al/EuS/Al_2O_3/Al/EuS/Al}$ structure): a) The magnetic insulator europium sulfide (EuS) layers are characterized by the spin-filtering effect [118]. Its magnetic orientation defines the spin dependent tunneling rates. b) The ultra-thin Al layer forms confined nanosized clusters leading to the formation of quantum dots with discrete, initially spin degenerate states. c) A huge exchange interaction that arises at the EuS/Al interface leads to the spin splitting of the confined Al islands, hence, generating

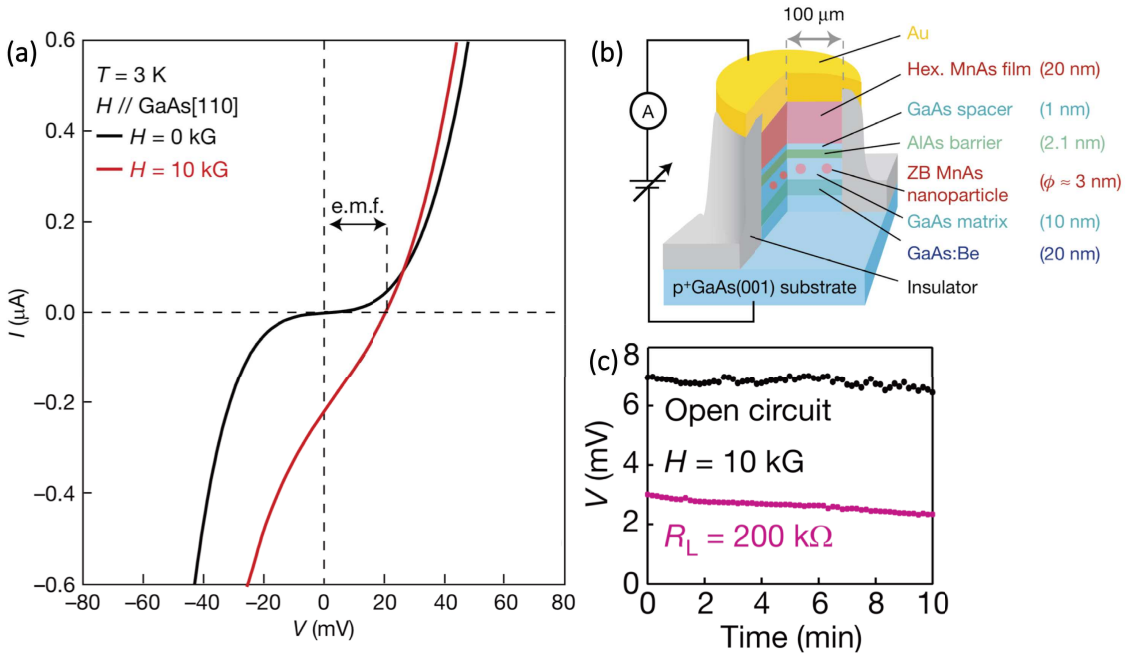

Figure 7.4: **Generating energy by rectifying spin-fluctuations: first report in 2009.** (a) The IV measurements performed at 3K, at zero field (black) and at H = 10kG (red). The shift of the red IV corresponds to spontaneous voltage that can originate from energy harvested by rectification of spin-fluctuation on the superparamagnetic MnAs nanoparticles. (b) Structure of the investigated MTJ device with the respective layers thicknesses and the measurement setup profile. (c) Open circuit (black) and connect load (pink) $\mathrm{R_L} = 200\mathrm{k}\Omega$ time evaluation of the spontaneous voltage (sourced bias V = 0 V). Figure taken from ref [99].

discrete spin split states, d) A thin Al_2O_3 insulating layer between Al and EuS prohibits the formation of a second interfacial exchange interactions field. This means that the spin splitting of the QD energy state is dominated by magnetism of one EuS barrier. Referring to Figure 7.5.a, the spintronic profile resulting from the above-mentioned multilayer structure is highly asymmetric. In this device current across the outer metallic Al electrodes is spin-unpolarized, whereas the magnetic orientation of the EuS spacers layers define its energy- and spin-dependent transport path leading to field dependent energy outputs ($\mathrm{E^P_{out}}$ and $\mathrm{E^{AP}_{out}}$). The magnetic configuration of the device defines the energy gap between the input energy and the output energy defined by the spintronic profile, as schematically visualized in Figure 7.5.a. The energy gap between the input and output energies in each of the magnetic configurations corresponds to the field dependent spontaneous voltages observed in these devices.

Referring to Figure 7.5.c, the spontaneous voltages detected in the device are strictly dependent on the applied magnetic field and are a direct consequence of energy profiles of P/AP states schematically represented in Figure 7.5.a. The maximum spontaneous voltage

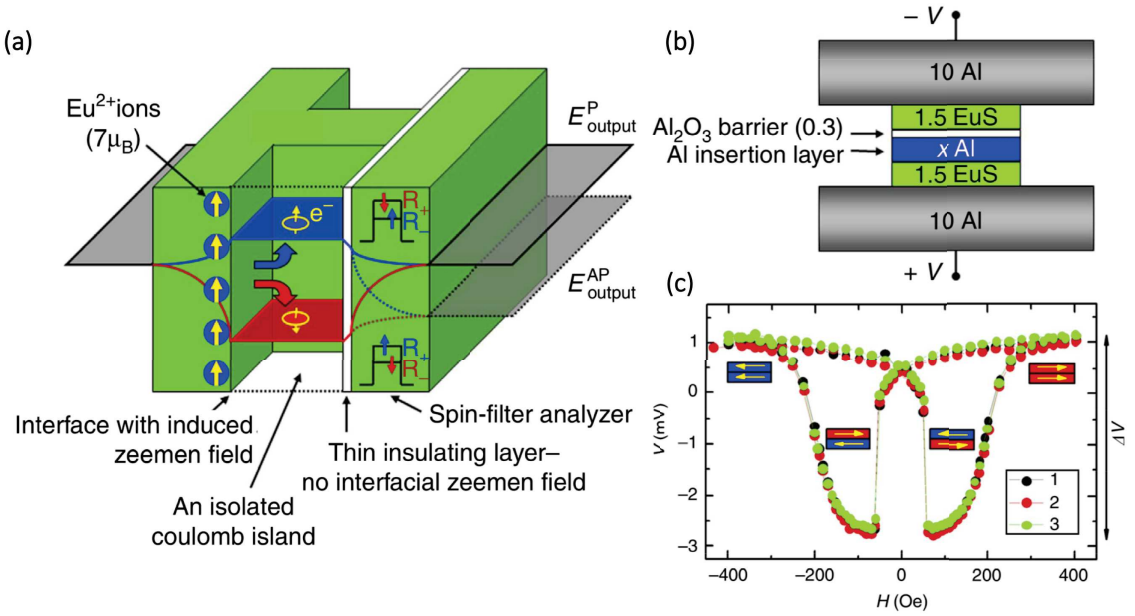

Figure 7.5: **Spin and energy profile of the MTJ and the resulting spontaneous-voltages.** (a) Electronic profile of the multilayer structure. Unpolarized Al leads generate continuous flat planes on both sides of the device. The EuS (green) filters the tunneling spins, leading to spin dependent attenuation rates, while a high interfacial exchange interaction splits the discrete energy levels of Al coulomb islands and the thin Al2O3 insulating layer ensures a perfect asymmetry. (b) Schematics representation of the MTJs structures with the respective layer thicknesses. (c) Magnetic field dependence of the measured spontaneous voltages acquired on three different samples (1, 2, 3), at 1K wihtout any driving bias-voltage or current. The change in spontaneous bias upon switching the relative orientation of EuS magnetizations demonstrates the spin-polarized origin of the harvested energy. Figures taken from ref [102].

of $\mathrm{V} \approx -2.6\mathrm{mV}$ in achieved in the AP configuration of the EuS layers. The amplitude of this effect $\Delta\mathrm{V}$ is proportional to the energy split of the Al islands and the spin-filtering efficiency of the EuS material. Additionally, the spontaneous voltage signal of the AP configuration relaxes upon $10^4\mathrm{s}$ time scale towards the more stable P configuration. The authors report about a 27pW of output power when a $6\mathrm{M}\Omega$ load resistance is connected to a $200\mathrm{x}200\mu\mathrm{m}^2$ device. Within the energy harvesting formalism discussed previously (section 7), the spin-filtering EuS layers act as spintronic-selectors constraining a spin-flip events for the tunneling electrons to cross the device, especially in the AP configuration. The thermal fluctuation induced by the environment (sample's temperature) on the central spin-split states are converted into spin fluctuations. These spin fluctuations are rectified by the outer EuS layers which set a preferential direction for the heat-generated current resulting in spontaneous current and voltage. The preferential direction is set by the unique combination of the asymmetric sample's profile $(\mathrm{Eu/Al/Al_2O_3/Eus})$ and the

spin-filtering properties EuS, thus by spin selection rules tunneling rates are higher in one direction than another. This mechanism is very similar to the one described by Sanchez and Büttiker [100], where the asymmetric energy profile of the confined transport path through QDs imposes a preferential direction to the thermally generated current, see Figure 7.3. The selection rules applied to the additional spin degree of freedom in this system establishes an efficient selectivity on both sides of the spin split central states and enables the harvesting of thermal fluctuation and the generating useful electrical power. In the next section 7.2, we will discuss in more details about the role of spintronic selectivity in energy harvesting mechanisms. This discussion will be held on the example of our conceptual spin-engine capable to convert spin fluctuations into a spontaneous current flow, hence, into useful electrical power. The requirements for its operation at room-temperature will be evoked thereafter. Additionally, we will examine in which manner such quantum mechanical structures can be routinely reproduced in commonplace sputtered MgO-based MTJs.

7.2 Analytical model of a Spin-Engine

Generating energy by means of quantum tunneling systems is astonishing because it seems to be counterintuitive at first glance, yet once the proper model is used to interpret such effects it becomes an inspiring field to investigate. As previously discussed, thermal fluctuations can be converted into an electron flow in a confined tunneling system when the two main elements are present: i) A central set of energy-split states dominantly participating in the transport that can be addressed ("mixed") by the surrounding thermal fluctuations, ii) A set of rectification elements on each side of the central states and also along the transport path. They will set asymmetric transmission rates on either side of the central main element, and in the spintronic focus that follows will be called spintronic selectors. Spinterfaces are highly spin-polarized electronic elements that tend to appear in spintronic devices at the interface between the ferromagnetic (FM) electrode and the insulating barrier [119, 120] and can fulfill the role of spintronic selectors. In the ideal case their polarization enables only one spin-channel of transport. Referring to Figure 7.6.a, a spin-engine is composed of two spin selectors L and R on either side of a paramagnetic (PM) center. The PM center is spin split and gives rise to two discrete spin states, spin up in red and spin down in blue. An electron's spin states on the PM center can be mixed by thermal fluctuations, as represented in purple arrows. Furthermore, if the spintronic selectors have ideal opposite polarization (AP configuration) only transmission rates $\Gamma_{\mathrm{L}\uparrow}$ and $\Gamma_{\mathrm{R}\downarrow}$ are allowed, whereas $\Gamma_{\mathrm{L}\downarrow}$ and $\Gamma_{\mathrm{R}\uparrow}$ are forbidden, as represented in Figure 7.6.a. This transport scheme is similar to the one described in Figure 7.3 of the previous section, but here the direction of the current flow is set by the spin selection rules.

The spin splitting in the PM center is prone to appear as a direct consequence of spin degeneracy lift on the PM center when its total spin is high ($\mathrm{S_{PM}} > 1/2$). It was demonstrated that when a high spin QD is brought in close vicinity to a ferromagnet to obtain tunneling an exchange field arises and splits the spin states, similar to the effect of spin-orbit coupling [121]. This spin splitting effect is especially important when high spin

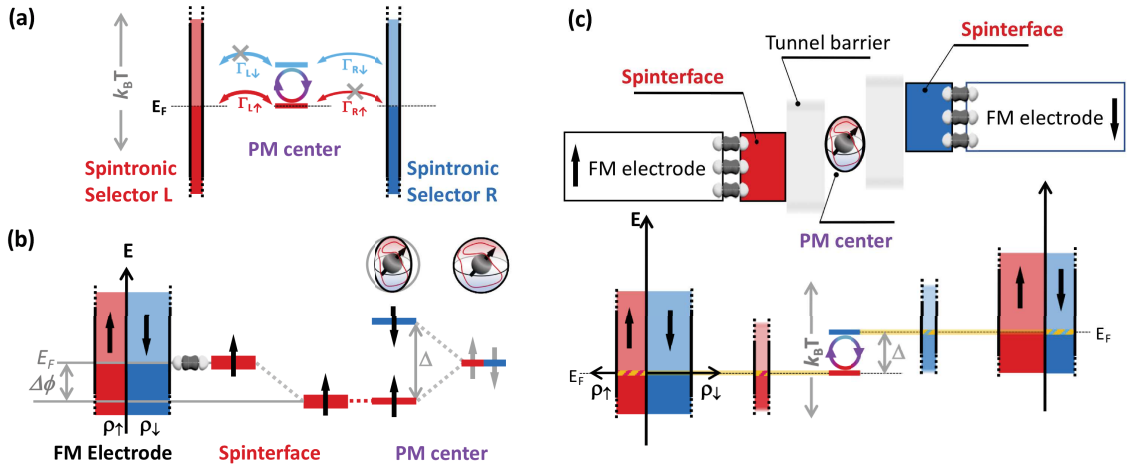

Figure 7.6: **Electronic structure of an energy-harvesting spin engine: example using spinterfaces.** Spin up (down) states are in red (blue). (a) Schematic representation of the main spin-engine's section composed of the left and right spintronic selectors in the antiparallel configuration and a paramagnetic (PM) center with one effectively spin-split energy state. Spin selection rules define spin-dependent transmission rates, $\Gamma_{L\downarrow} = \Gamma_{R\uparrow} = 0$ and $\Gamma_{L\uparrow} \neq 0$, $\Gamma_{R\downarrow} \neq 0$. An asymmetric spin profile is set within the system. Thermal fluctuations (purple) generate spin fluctuations on the central PM center. (b) Induced spintronic magnetic anisotropy on the PM center leading to a spin splitting (Δ) of the degenerate states. This effect is also illustrated by the deformation of the PM centers Bloch sphere. (c) Illustration of a spin-engine embedded with the spintronic structure of a magnetic tunnel junction. It is composed of two antiparallel ferromagnetic electrodes and respective spinterfaces with a central PM spin split QD-like element. A current (yellow line) is generated by thermal fluctuations $\mathrm{k_B T}$ on the PM centerand is flowing in the opposite to ΔV direction. See discussion in the text below for more details. Figure taken from ref [109].

polarizations (e.g. spinterfaces) are involved and tunneling is dominant. Referring to Figure 7.6.b, the induced spintronic magnetic anisotropy on the PM center is represented by the deformation of its Bloch sphere. The energy difference between the two PM center's spin states is defined by Δ. The low electronic density of the spinterfaces on both sides of the PM center protect the later from thermal broadening from the outer FM leads and preserve the discrete spin states, thereby enabling the engine to operate at RT. Furthermore, as the spinterface sets the preferential spin state and spatial orientation, it lowers the Fermi level of FM metal/spinterface by $\Delta\Phi$ towards the lower energy spin state in this direction [121, 122]. In a symmetric device, for instance in the P state, the "interfacial" Fermi level of both sample's sides will be aligned, and no spontaneous voltage will arise within the device, as previously discussed in section 7. The antiparallel configuration of electrodes and consequently of the spinterfaces is visualized in Figure 7.6.c: it results in

the formation of a spontaneous voltage ΔV since both interfaces are aligned with the respective levels of the PM center. The spontaneous voltage is proportional to the energy spin split Δ and the polarization amplitudes of both spinterfaces. In the ideal case of fully polarized spinterfaces (P = 100%) represented in Figure 7.6.c the spontaneous voltage is equal to $\Delta V = \Delta/e$. Since the thermal fluctuation expressed by $k_B T$ are higher than Δ, they induce the mixing of spin states on the PM center. These spin fluctuations are "directed" by spin selection rules on both sides of the PM center leading to an imbalanced flow of current i.e. spontaneous current flowing along the confined highly spin polarized transport path, as illustrated in Figure 7.6.c in yellow. In summary, the conceptual spin-engine herein described is capable of harvesting thermal fluctuations at room temperature by utilizing the magnetic energy of its elements and the asymmetric spintronic landscape along the transport path to generate a spontaneously flowing current. In the next Section 7.3 we will discuss about the already reported ingredients that can serve to assemble such an energy harvesting spin-engine. Furthermore, we will describe about the origins of the paramagnetic centers in sputtered MgO-based MTJs and in the process unveil the role of oxygen vacancies played in this energy generation effect.

7.3 Spin-engine's main ingredients

Electrical energy can be generated by spintronic selectors rectifying spin fluctuations. Therefore, the conversion efficiency of these elements is tightly related to their spin polarization. In an ideal case, a perfect polarization would provide the highest energy output. Several components in spintronics were reported to have high spin-polarization such as: a) Spinterfaces - generated at ferromagnetic/organic interfaces [54, 110]), b) Fe/MgO and FeCoB/MgO MTJs were reported to generate a high transport spin polarization thanks to symmetry filtering [31, 40], c) Magnetic semiconductors characterized by spin-filtering properties [102, 123], d) Half-metals [124–126]. As discussed previously, the second mandatory element for thermal spin fluctuations are discrete spin states. They can be generated by: a) Superconducting nanoparticles that are spin-split by exchange interactions [102], b) superparamagnetic nanoparticles [99], hence (a) & (b) can operate only at low cryogenic temperatures, c) Thermal fluctuations on spin-split discrete states [102,109]. Multiple elements can fulfil the role of spintronic selectors and spin fluctuators: the playground for power generation using spintronics is large.

7.3.1 Spintronic selectors

In order to demonstrate the spintronic energy generation effect at room temperature in a device that can be industrially deployed, we performed transport measurements on sputtered MgO-based magnetic tunnel junctions with thin carbon (C) layers inserted at the FM/MgO interfaces. The description of the MTJ's fabrication steps will be evoked in Section Section 5.1.1, whereas here we will describe the formation of highly polarized spinterfaces in FM/C bilayers. A recent work by Djeghloul et al. [110] completes the picture of carbon based spinterfaces. By utilizing spin-resolved X-ray photoemission

spectroscopy the authors were able to measure a nearly 100% polarization at the Fermi level of Cobalt/Carbon bilayers, see Figure 7.7 for more details. Note that this result is generic [127], and thus also describes Iron/Carbon interfaces used hereafter.

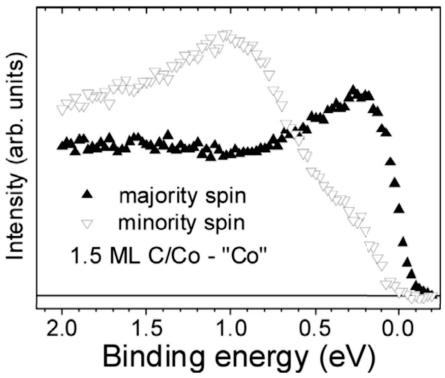

Figure 7.7: **Carbon based spinterfaces.** Spin-resolved X-ray photoemission spectroscopy on 1.5ML of Carbon deposited on Co layer, after a pure Co spectrum was subtracted. An almost complete spin imbalance is present between majority (filled triangles) and minority (empty triangles) spins at the Fermi level i.e. binding energy = 0 eV. Measurements performed at room temperature. Figure taken from ref [110].

7.3.2 Spin fluctuations

As discussed previously spin fluctuations take place when states that are spin-split by Δ are both populated thanks to thermal fluctuations $\mathrm{k_B T}$, i.e. when $\mathrm{k_B T} > \Delta$. We suggest that paramagnetic centers coupled to spinterfaces can play the role of spin split states owing to spintronic anisotropy [121]. In the framework of magnesium-oxide (MgO) dielectric material and carbon based spinterfaces paramagnetic centers can be formed by carbon-filled oxygen vacancies in MgO upon the diffusion of carbon atoms. Ab-initio theory has predicted that paramagnetic single (monomers) or double (dimers) centers are energetically prone to appear in C-doped MgO crystals [109, 128]. The distance between individual C impurities in the MgO crystalline structure characterizes their interactions. We have shown in our recent work [109] that C impurities are placed at the 4^{th} nearest-neighbor configuration (NNC) form antiferromagnetically (AFM) coupled paramagnetic dimers. This structural arrangement of C atoms can appear thanks to a low density of single F oxygen vacancies in MgO [10, 47]. In what follows we will see that only such entities (PM-dimer) are suited for the analytical model description of our experimental dataset in section 8.1.2.

Referring to Figure 7.8, the calculated spin-resolved density of states (DOS) of C-doped MgO (4^{th} - NNC) crystal is characterized by four discreet spin-degenerate energy states in the band-gap of MgO. The degeneracy lift responsible of spin split states is defined by the projection of the spinterfaces' spintronic magnetic anisotropy [121]. Most importantly,

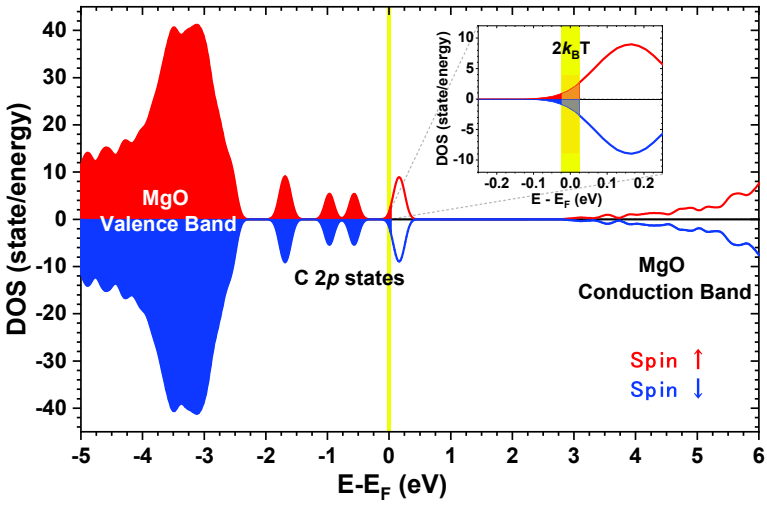

Figure 7.8: **Electronic structure of a PM dimer embedded into MgO.** Spin-resolved DOS of C-doped MgO in 4^{th} nearest-neighbor configuration characterized by six additional states in the MgO's band-gap. Inset – thermal fluctuations generate spin fluctuations at the Fermi level which intersects with a partially occupied PM-dimer state. See text above for more details. Figure taken from ref [109].

these calculations show that a partially occupied states are present at the Fermi level. The latter is defined to lay at 2.35eV above the valence band of MgO according to the computations performed on the whole Co/MgO/Co stack [109]. The inset of Figure 7.8 shows that thermal fluctuations $\pm k_B T (2k_B T$, with T=300K) indeed intersect a pair of C states. This theoretical demonstration fits the operational scheme of the spin-engine.

Chapter 8

Spin-driven electrical power generation at room temperature

As previously discussed, spintronic rectification of spin fluctuations is at the origin of spintronic-driven power generation using quantum thermodynamics. In this respect, we processed MTJs of $20\mu\mathrm{m}$ in diameter by means of photolithography of the following composition: Ta(5)/Co(10)/IrMn(7.5)/Co(4)/C(0.9)/MgO(2.5)/Co(10)/Pt(4) (numbers in nm). Samples were grown by M. Hehn of IJL Nancy, and processed by E. Urbain into micro-junctions. The lithography steps are described in Section Section 5.1.1. The stack was grown by sputtering on a Corning 1737 glass substrate [85]. To activate the pinning exchange bias at the IrMn/Co interface a $\mathrm{T_a} = 200°\mathrm{C}$ annealing step (1h) was performed prior to the lithography. This low temperature annealing sets a magnetically preferred direction of the bottom Co electrode, thereby enabling a steady antiparallel (AP) configuration, hence, a maximum spintronic asymmetry required for an efficient energy generation in the AP state. The low annealing temperature precludes the diffusion of Mn atoms [39], thus, excludes them from the defect states present in the MgO's band-gap. On the other hand, the low annealing temperature may be responsible for the diffusion of C atoms from the interface to the MgO spacer [32] and lead to the formation of both spinterfaces and PM dimers.

8.1 Spontaneous spin-driven transport

As a rare experimental event, we were able to discover a combination of transport features clearly indicating spintronics-driven power generation at room-temperature: i) The presence of spontaneous current and voltage, that are especially important in the AP configuration of the electrodes and much weaker in the P configuration. These spontaneous transport features are only detectable in the low bias-voltage range $\mathrm{V} < \pm 10\mathrm{mV}$ including zero-bias point. An important non-zero current $\mathrm{I} \neq 0$ can be measured at V = 0mV, ii) Spectroscopically sharp magnetoresistance features reaching 300% of TMR at room-temperature in a non-optimized MTJ's stack structure i.e. Co/MgO/Co sputtered structure with C-dusted interfaces annealed at low $200°\mathrm{C}$. These two properties suggest that highly spin-polarized transport channel through confined electronic objects is at the origin of spontaneous current flow and voltage. The main ambition of this section is to highlight the spin-engine formalism developed in the framework of quantum thermodynamics within

the experimental observations of sizable spontaneous transport in an MTJ device.

8.1.1 Experimental spin-engine's footprint

Referring to Figure 8.1, the current-field I(H) transport measurements at +5mV and +10mV indicate that stable magnetic P and AP configurations are achievable. At 10mV both currents I_P (-2000 Oe) and I_{AP} (+250 Oe) are positive and lead to a relatively low negative TMR = -17%. This result isn't much surprising since the presence of spinterfaces can change the interfacial polarization and by that lead to negative TMR in devices with nominally symmetric devices polarizations [54, 120].

The most intriguing effect takes place at 5mV. When the bias-voltage is lowered the induced current becomes smaller than the spontaneous current and this latter can be observed. This current is considered to be spontaneous since it flows in the opposite direction with respect to the sourced voltage, leading to an $I < 0 at V > 0$. Therefore, the combination of I_P (V = 5mV) = -20nA and I_{AP} (V = 5mV) = +35nA leads to a high negative TMR (V = 5mV) = -157%. The high currents measured in the nA range exclude any Keithley offset origins since it showed a maximum current offset of 500pA and maximum voltage offset of 0.1mV. All of the herein discussed transport measurement are performed in a 4-wire mode with V_+/I_+ connected to the top electrode. This mode eliminated any potentual thermovoltage artefacts along the device's contacts and leads. The time frame of these measurements further highlights their likelihood, since the I_P current is steadily negative ($I < 0 \,\&\, V > 0$) during the whole field sweep ($\approx$ 350s) and no drift of current-vs-time is observed.

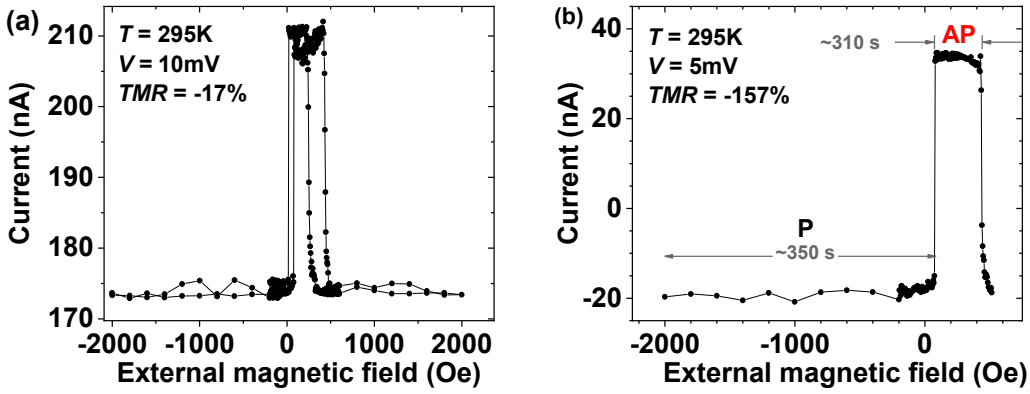

Figure 8.1: **Spontaneous current flow and high spintronic performance.** Field dependence of current - I(H) at room temperature at 10mV (a) and 5mV (b) respectively. Negative spontaneous current of -20nA at 5mV in the P configuration of electrodes leads to a huge -157% TMR signal. Figure taken from ref [109].

To examine in more details the transport properties of this device, we performed a bias-voltage dependence study of the currents I_P and I_{AP} their calculated conductances G_P

and G_{AP} and the resulting TMR. Figure 8.2 summarizes this study through the different panels. The current-voltage (IV) profile in the $\pm 10\mathrm{mV}$ range in panel (a) demonstrates that I_{AP} (red, H_{AP} = +250 Oe) and in a lesser extent I_P (black, H_P = -2kOe) intersect the forbidden quadrant $V > 0$ & $I < 0$ through all bias-voltage sweeps $(0 \longrightarrow +V_{max} \longrightarrow -V_{max} \longrightarrow +V_{max} \longrightarrow -V_{max} \longrightarrow 0)$. Overall the dataset is of high quality and reproducible within this single device. At V = 0 both $I_{AP} \neq 0$ and $I_P \neq 0$ currents are negative and exceed any experimental offset by 2 orders of magnitude. The resulting numerically derived conductance dI/dV in panel (b) is characterized by sharp features in both P (black) and AP (red) states. The conductance's spectral features range around 0.25meV of amplitude whereas the thermal smearing at RT is expected to confine features to at least 50meV ($\approx 2k_BT$). The TMR(V) resulting from these IVs in the MTJ's P and AP magnetic states (green) highlights the magnetic origin of these spontaneous currents. As seen in panel (a), altering the magnetic state P $\longleftrightarrow$ AP alters the amplitude and, in some cases, (5mV) the sign of the spontaneous current. Overall the current $I_P(V)$ and $I_{AP}(V)$ almost never overlap leading to a spectrally sharp TMR(V) in panel (c) characterized by three main features suggesting that the spontaneous current originate from highly spin polarized channels cutting through confined electronic objects such as QDs and spinterfaces:

i) A huge 300% TMR peak centered around -3.5mV defined by an 1.3meV full-width-half-max (FWHM) above any possible thermal smearing.Additionally, this high TMR cannot be explained by symmetry filtering as it is the case in current most performing CoFeB/MgO/CoFeB MTJs [40], since the Co electrodes utilized in this MTJ aren't bcc and don't have a high spin polarization of the Δ_1 states favored for tunneling transmission across MgO [31]. Therefore, we attribute the magnetoresistance features measured on this device to spinterface mediated transport within Julliere's framework [4].

ii) Negative TMR of -58% at V = 0 reinforces the notion of magnetically sensitive spontaneous currents indicating that it originates from spin-polarized electronic elements.

iii) The zone of highly negative $TMR < -100\%$(gray) centered around +5mV is related to the sign opposite signs of I_P and I_{AP}. As already seen in Figure 8.1.b an $TMR < -100\%$ amplitude is attained as a consequence of a negative I_P and positive I_{AP}.

If we attribute all of the above discussed features to artefacts related to the experimental measurements, then the following aspect should be considered. If both spontaneous currents arise from some kind of voltage or (and) current shift then one could correct both I_P and I_{AP} by the same amount to reproduce the standard IV properties of an MTJ. Yet, the is no single reasonable solution for this eventual correction of both P/AP since shifting both IVs by any $I_{corr}\mathrm{or(and)}V_{corr}$ wouldn't preclude IVs from entering the active device quadrants ($V > 0$ and $I < 0$, or $V < 0$ and $I > 0$). In this discussion reasonable values stand for values coherent with experimental offsets.

To summarize, herein we've presented an extended dataset acquired on a single Co/MgO/Co MTJ device that evidences a high spintronic performance in a non-optimized device. These key observations indicate that the transport is mediated by highly spin-polarized spinterfaces and confined electronic objects such as quantum dots or defect states. Additionally, the spectral sharpness in magnetotransport can't be explained easily since at RT thermal smearing in principle excludes features to be sharper that $2k_BT$. Therefore, we interpret the observed spontaneous currents and the resulting sharp magnetotransport as indications

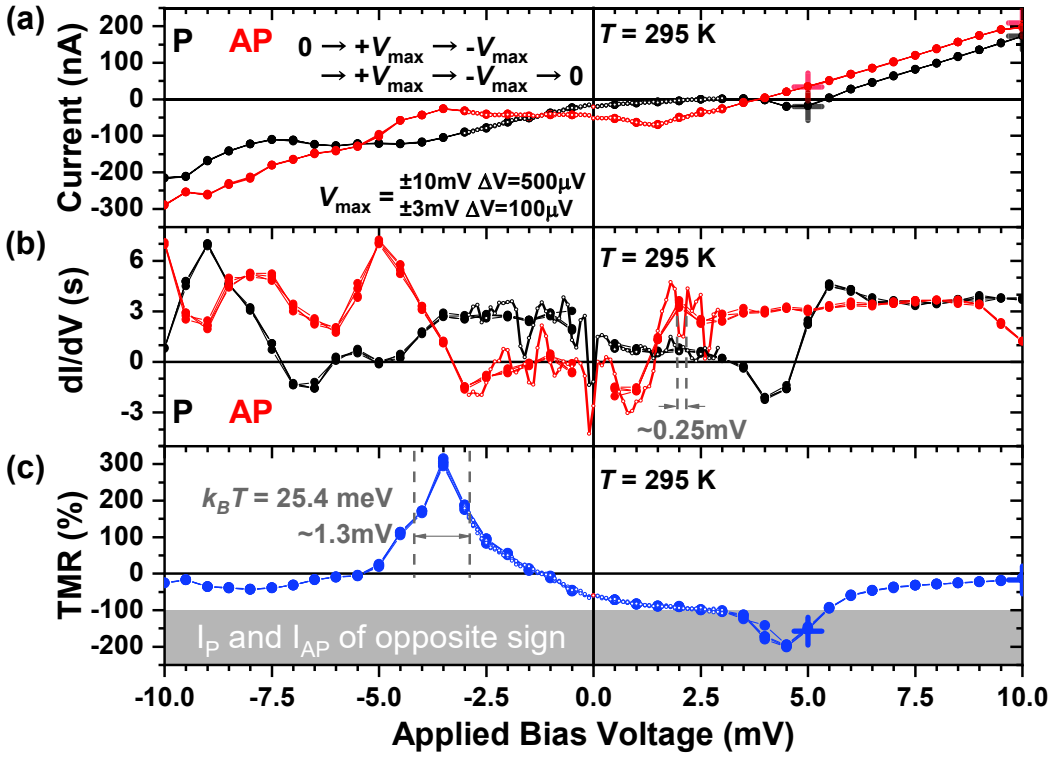

Figure 8.2: **Spintronics-driven power generation at room-temperature.** Magnetotransport measurements performed at T = 295K in the P (-2kOe) and AP (+250 Oe) magnetic configurations of the Co/C-MgO/Co MTJ device. (a) Current-Voltage (IV) measurements P (black) and AP (red) states upon several bias-sweeps. A spontaneous current whose amplitude depends on the MTJ's magnetic state is observed. (b) The resulting computed conductance (G = dI/dV) exhibits a tremendous energetic resolution ($\approx 0.25\mathrm{meV}$). (c) The resulting TMR(V) profile exhibits high sharp (≈ 1.3meV) magnetoresistance features, a peak at -3.5mV (TMR ≈ +320%) and a dip at +4.5mV (TMR ≈ −200%). More details are in the main text. Figure taken from ref [109].

of an operating spin-engine. To further examine this interpretation, we worked on an out-of-equilibrium analytical transport model idevelopped by J. Fransson from Uppsala university in Sweden [122]. In the next section 8.1.2, the formalism of this model will be described in few more details and will be used to fit the above-mentioned experimental dataset.

8.1.2 Analytical model transport

The main goal of our analytical model is to reproduce the experimental observations evoked in the previous section 8.1.1 by employing the main elements of a spin-engine described in section 7.2. The analytical model developped by J. Fransson from Uppsala University as derived from earlier work [122] to fit our understanding of the proposed transport path. I was tasked with exploring within the large parameter space how the model could be used to fit our data. As schematically illustrated in Figure 8.3, the electronic profile of the model consists of two ferromagnetic leads separated by four interconnected quantum dots. The two outer dots reproduce the spinterfaces (SP1 $\&$ SP2) while the two central ones mimic the PM-dimer center (PM1 $\&$ PM2). The individual QDs are modelled by discrete energy states to which localized spins are associated. Spin split states on the central PM dimer QDs are reproduced by considering several magnetic interactions, namely, Heisenberg, Ising and Dzyaloshinskii–Moriya interactions [122]. Each element in this model is electronically coupled to its neighbors by tunneling coefficients pL, T and pR (see schematics on Figure 9.11). Spin-polarized transport through the whole structure is evaluated by means of Greens functions. The polarization is defined by sp(L) and sp(R) parameters on the FM leads and by a unique SP parameter on the spinterfaces. Additionally, the position of the PM dimer and both spinterfaces with respect to the Fermi level of the structure is adjustable by e0 and E0 parameters respectively. The ASYM parameter defines the energy asymmetry between PM1 and PM2. As pointed previously, the spectral sharpness of magnetotransport features indicates that the inner QDs are shielded from the outer QDs. Therefore, in our analytical model PM1 and PM2 QDs are thermally shielded from the outer FM leads by spinterface QDs SP1 and SP2. By placing the localized states of the PM center into close vicinity with the chemical potential μ of the of the whole structure, thermal fluctuations are considered in the model, since $k_B T >> | \mu - E_0 |$. A detailed definition of the analytical model's formalism in term of the systems operators can be found in the supplementary information section of our recent work on this topic [109]. The spin polarization of the FM elements, hence, the magnetic configuration of the MTJ device, is defined by the sign of sp(L), SP and sp(R) parameters, with sp(R) = AP*sp(L). Referring to Figure 8.3, the parallel configuration of the MTJ is illustrated and the AP configuration is reproduced when SP on SP2 and sp(R) on the right lead are inverted in sign. In such manner, we are able to theoretically predict the spin-conserved tunneling transport along each of the spin-polarized channels.

Scrupulously exploring the analytical model's parameter space, we were able to reproduce all of the experimental magnetotransport features entailing energy harvesting at room-temperature, as depicted in Figure 8.2.a,c. This unique set of parameters reproduces the general trend of both $I_P(V)$ and $I_{AP}(V)$, with only minor alterations to the PM dimer's initial parameters e0 and ASYM when going from P to AP. In such manner for the P/AP states we used: sp(L)=8.4, SP=2, pL=pR=0.35, AP=0.3, E0=0, with pR and AP changing sign upon $P \longleftrightarrow AP$ transition, and e0(P)=-2.5 / ASYM(P)=0.5 while e0(AP)=0.85 / ASYM(AP) = -0.75. The bias-voltage dependence of the spin-resolved transport channels (IVs) along the device in P and AP configurations is represented in Figure 8.4.a. Spin-up ($\uparrow$) channel is pictured by solid red (AP) and black (P) lines, whereas the spin-down ($\downarrow$)

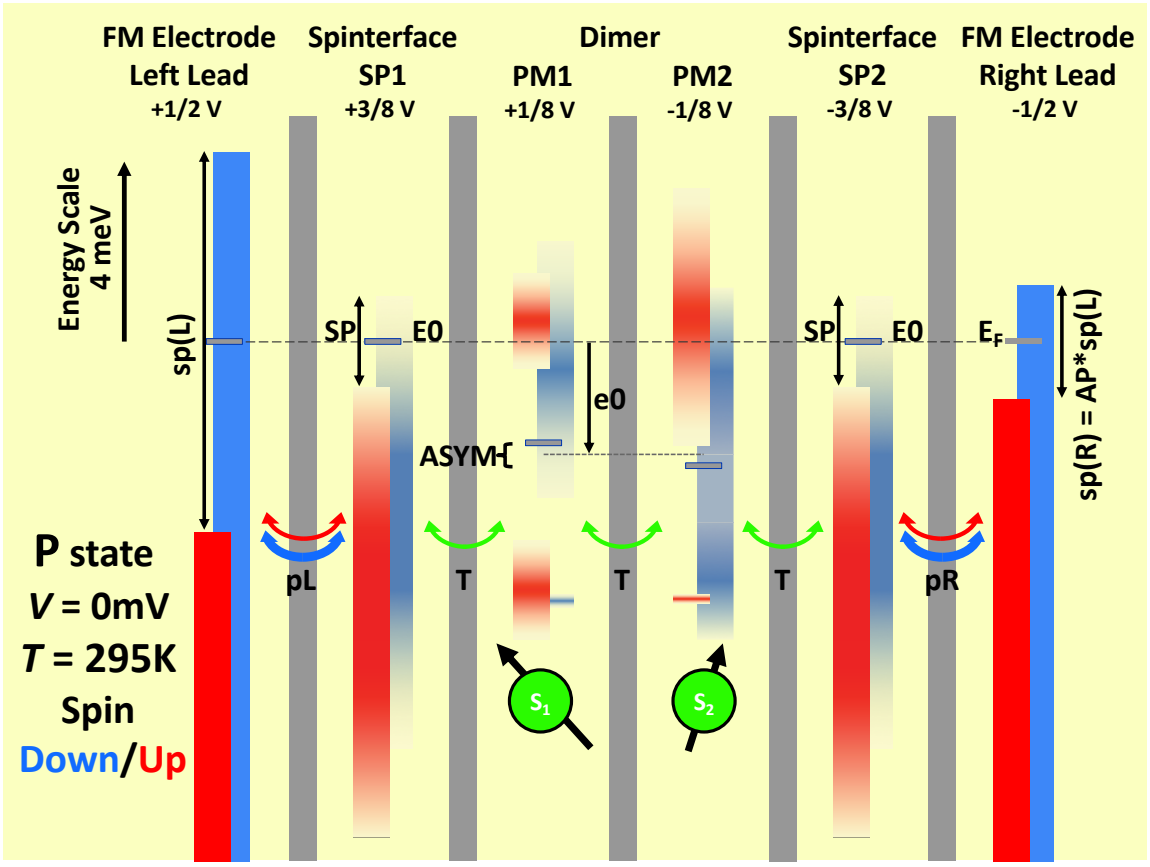

Figure 8.3: **Analytical model of the spin-engine's realization in an MTJ.** Electronic profile of QD-based MTJ enclosing a spin-engine in the P configuration of electrodes and zero-bias voltage. Two FM leads (Co) are separated by 4 tunneling coupled QDs. The outer ones SP1 and SP2 correspond to Co/C spinterfaces, and PM1 and PM2 to the PM dimer center. The physical meaning of the different parameters, sp(L), pL, SP, E0, ASYM, T, e0, pR, sp(R) is discussed in the text. Figure taken from ref [109].

channel is pictured by semi-transparent red (AP) and black (P) lines. We observe that spin up and down current channels are opposite in sign, hence, charge carriers of opposite spin flow in opposite directions. This later property seems to fit well the spin-engine's formalism evoked in section 7.3. Furthermore, a spontaneous current at V = 0 is present in both configurations P and AP since the polarization of spinterfaces and the PM center aren't total, and due to other spin-based asymmetries in the potential landscape. Summing the two spin currents, we obtain the theoretical $\mathrm{I_P(V)}$ and $\mathrm{I_{AP}(V)}$ and the resulting TMR(V) plotted in panel (b) of Figure 8.4. Comparing the experimental and theoretical datasets in panels (b) and (c) of Figure 8.4, we observe that the experimental features are rather well reproduced. Since theoretical and experimental IVs share the same behavior, the resulting TMR trends are also reproduced: a) the overall negative TMR, b) the sharp TMR peak at V < 0 even if its amplitude isn't the same, c) The zero voltage negative TMR and both

current, d) The TMR deep at V > 0 with a quite similar amplitude, e) Spontaneous current in P and AP at V = 0 V are in good agreement. As a note of mention, no direct tunneling between leads i.e. spinterfaces is taken into consideration within the analytical model's transport scheme. Therefore, once the sourced bias-voltage exceeds the electronic profile of the PM dimer, both theoretical currents $I_P(V)$ and $I_{AP}(V)$ asymptotically converge to the zero-current mark.

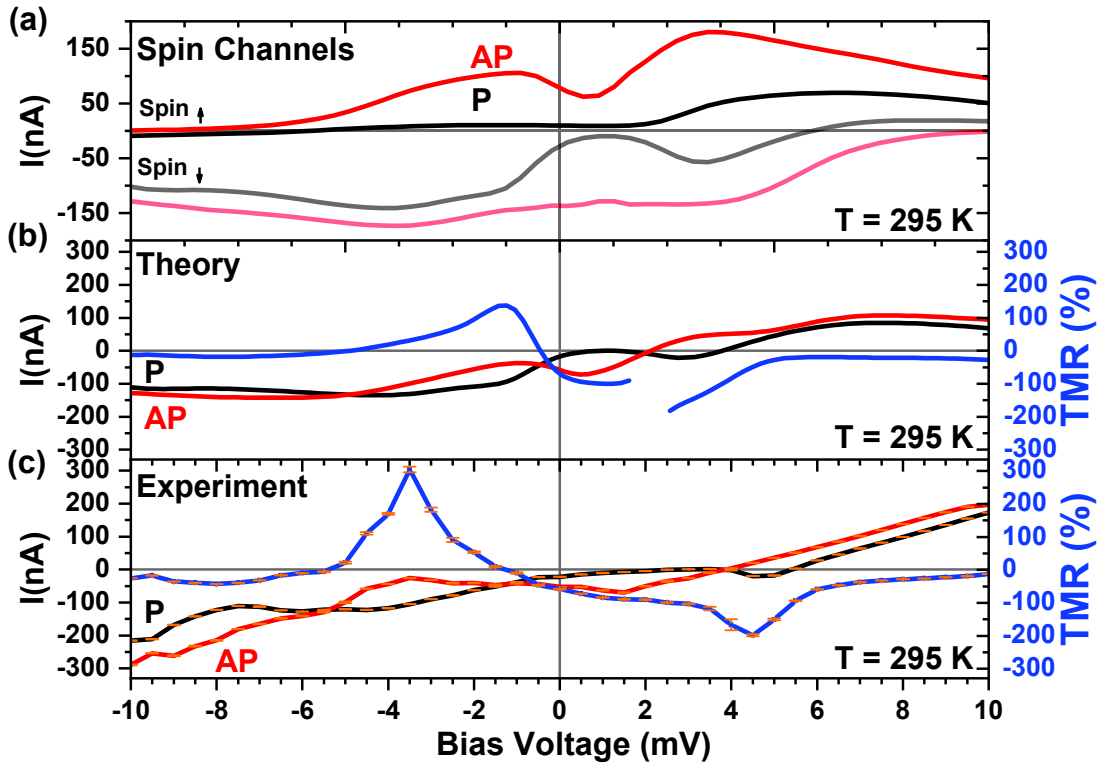

Figure 8.4: **Comparing theoretical and experimental magnetotransport datasets.** Theoretical results were modeled through the analytical model and the unique set of parameters described in the text. (a) Spin-resolved IVs for P (black) and AP (red) with solid lines for spin-up and semitransparent for spin-down. (b) Sum of the spin transport channels lead to I_P (black), I_{AP} (red) and TMR (blue). (c) Experimental dataset acquired on the Co/C-MgO/Co MTJ evoked in section 8.1.1. The orange error bars originate from the standard deviations of the respective mean values over the multiple bias sweeps. A good agreement between analytical model fit and experiment dataset is achieved. Figure taken from ref [109].

In conclusion, the analytical model closely replicates the experimental spontaneous currents and resulting magnetotransport features. This further enables to interpret their origin

in terms of a spintronics-driven pumping of electrons against the bias or even in its absence. The peculiar spintronic path enabling this effect to take place is composed of an antiferromagnetically coupled PM dimer center affiliated to spinterfaces at both sides. The spinterfaces arise in turn from the FM electrodes. These spinterfaces ensure firstly the rectifications by selection rules of spin fluctuation on the PM center and, secondly, the thermal shielding of the PM center's spin discrete state from the electronically broad FM electrodes. The theoretical formalism describing the autonomous operation of the quantum dots coupled to spin-polarized leads and setting a spontaneous current from could be brought by a recent theoretical work of Ptaszynski [107]. It depicts how two exchange-coupled quantum dots connected to spin-polarized leads can autonomously through a feedback-loop pump electrons against the bias, hence, generate a spontaneous current.

8.1.3 Generated power output

In this section we propose to evaluate the power output generated within the MTJ and to consider this value according to the currently know renewable sources of energy to evaluate its pertinence for potential industrial applications. Applying the power formula: $\mathrm{P} = \mathrm{V}^2/\mathrm{R}$ we can in a straightforward manner evaluate the power output Pout device. Referring to Figure 8.5, we evaluate the power output $\mathrm{P_{out}}$ dependence of bias-voltage in the forbidden-quadrant of Figure 8.2.a i.e. when V > 0 and I < 0. In both magnetic states P/AP the single MTJ device is generating up to 0.1nW of power at room-temperature. In the AP state: within the 1.4 < V(mV) < 2.4 output bias range the device's output resistance ranges between $20\mathrm{k}\Omega$ to $60\mathrm{k}\Omega$ providing the 0.1nW power output. In the P state: at $\mathrm{V} \approx 4.7\mathrm{mV}$ the output resistance is around $\mathrm{R} \approx 200\mathrm{k}\Omega$ and the device generates 0.1nW of power.

The power output is dynamically stable since no drift is observed in it, moreover, the averaging its value over the fore bias sweeps of Figure 8.2.a results in very narrow error bars in Figure 8.5. Overall, this unique in its properties MTJ device continuously expressed power generation features during the whole 90 minutes measurements acquisition timeframe. The spintronics footprint of the power out and the whole effect in general is expressed by the different power out variation in the MTJ's P and AP magnetic configurations. The low reproducibility of this effect in our MTJs originates most probably from the peculiar transport path required spin-engine to operate, thus, an atomic level control over the carbon filled oxygen vacancies in the MgO is required, yet this remains a very challenging task even with today's cutting edge technical tools. Assuming the spintronics-driven power generation discussed in this chapter can be routinely reproduced within industrial-grade densities of MTJs [129] and better understood novel energy-harvesting solutions could be designed. The next section presents some additional datasets and some experimental details confirming the non-artefact origin of the herein discussed power generation effects.

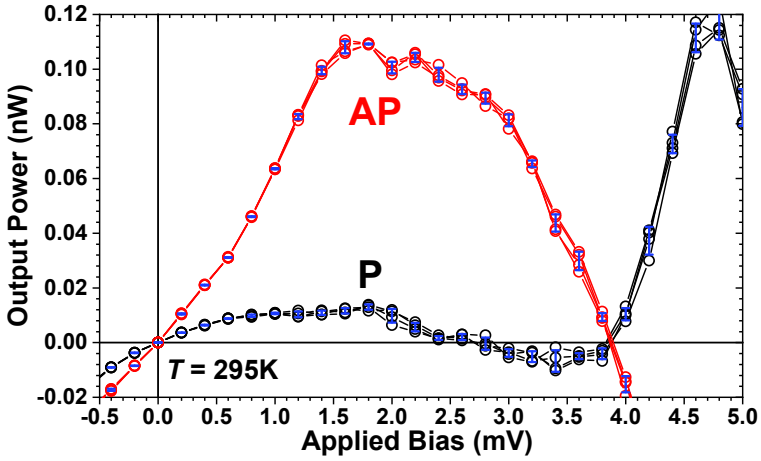

Figure 8.5: **Power output bias-voltage dependence in P and AP configurations.** In both magnetic states the single MTJ device can generate up to 0.1nW of power at room-temperature. The power output is dynamically stable in time, since the blue standard deviation error-bars are very small. Calculation performed over datapoints from Figure 8.2.a.

8.2 Experimental environment and additional datasets

Could all of the above discussed effects measured on a single MTJ device originate from artefacts related to our experimental technique? The additional magnetotransport datasets and an examination of the experimental environment can help answer this question. The magnetotransport dataset presented in Figure 8.2 was part of a 90min long continuous measurement of the device at room-temperature (295K). The measurements of I_P and I_{AP} at -2000 Oe and +250 Oe respectively were acquired for different bias-voltage steps (ΔV) and ranges. Figures 8.6 and 8.7 summarize this set of datapoint in an easy-to-compare form. Within each measurement each given individual IV point is defined by four measurements points, since we performed multiple bias-voltage sweeps: $0 \rightarrow +V_{max} \rightarrow -V_{max} \rightarrow +V_{max} \rightarrow -V_{max} \rightarrow 0$. As one can see within each of the seven measurement figures, almost all of the points perfectly overlap over the multiple bias sweeps. Furthermore, all of the magnetotransport features are reproduced in the panels of Figures 8.6 and 8.7 despite the differences in the measurement bias step ΔV and the maximum bias amplitude V_{max}.

The sharp resolution (ΔV=0.1mV) of panels (c) and (d) of Figure 8.7 clearly demonstrates the spintronic origin of the spontaneous currents at V=0, considering that its amplitude depends on the magnetic configuration of the device: I_P(V=0) = -22nA and $I_{AP}(V = 0)$ = -53nA resulting in TMR(V=0) = -58%. The more than two orders of magnitude difference between these values and the maximum current offsets (I_{off} = 500pA) of our setup reinforces the credibly of these results. Additionally, this effect is similar to the one observed IH(V+5mV) of Figure 8.1. The spontaneous current is strictly constant within

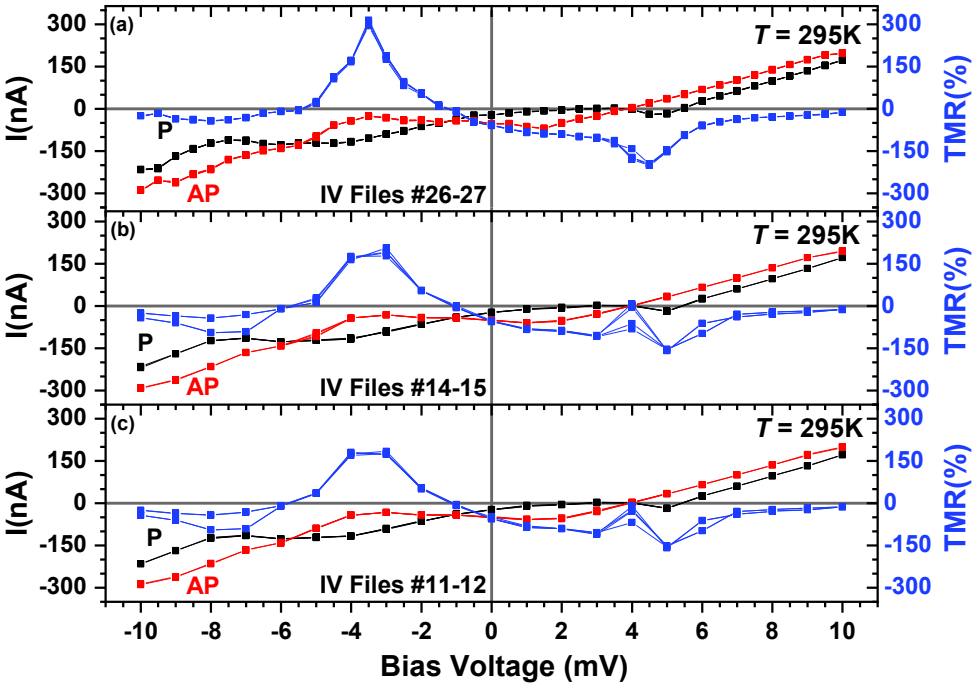

Figure 8.6: **Additional magnetotransport measurement - set 1.** 4-probe measurements of I_P (-2 kOe) and I_{AP} (+250 Oe) measured at room temperature (T = 295K) and their resulting TMR. (a) IV file #26-27, V_{max} = 10mV and ΔV= 0.5mV, (b) IV files #14-15, V_{max} = 10mV and ΔV = 1mV, (c) IV files #11-12, V_{max} = 10mV and ΔV = 1mV. Figure taken from ref [109].

the magnetic region of a given magnetic configuration P or AP and undergoes an abrupt change when the device's state is switched between P $\longleftrightarrow$ AP.

The experimental magnetotransport dataset testifying power generation at room temperature is an MTJ device is of very high quality and can't be easily interpreted in terms of trivial experimental artefacts. Yet, spontaneous currents can be generated by photovoltage-photocurrent [130, 131] or thermovoltage [114, 115]. Neither of these effects is likely to take place within our devices. Firstly, since the sample is placed in an optically sealed cryostat prohibiting any generation of photocurrent. Secondly, thermovoltage generated by simple Joule heating can be excluded since: a) we repeatedly detected field dependent non-zero currents at a zero sourced voltage, V = 0, b) Altering the bias-step (ΔV) during the current measurements would lead to a different heating rates, thus, to a different thermocurrent. Yet, the comparative study presented in Figures 8.6 and 8.7 clearly shows that ΔV doesn't distinguishably affects the device's transport response, c) The sharp electronic resolution (ε) present in the magnetotransport dataset and in the computed conductance (see Figure 8.2) is orders of magnitude higher than the expected thermal smearing at room-temperature ($k_B T$), ε = 0.25-1.3 meV << $k_B T$ = 26 meV, d) The bias-offset for which the

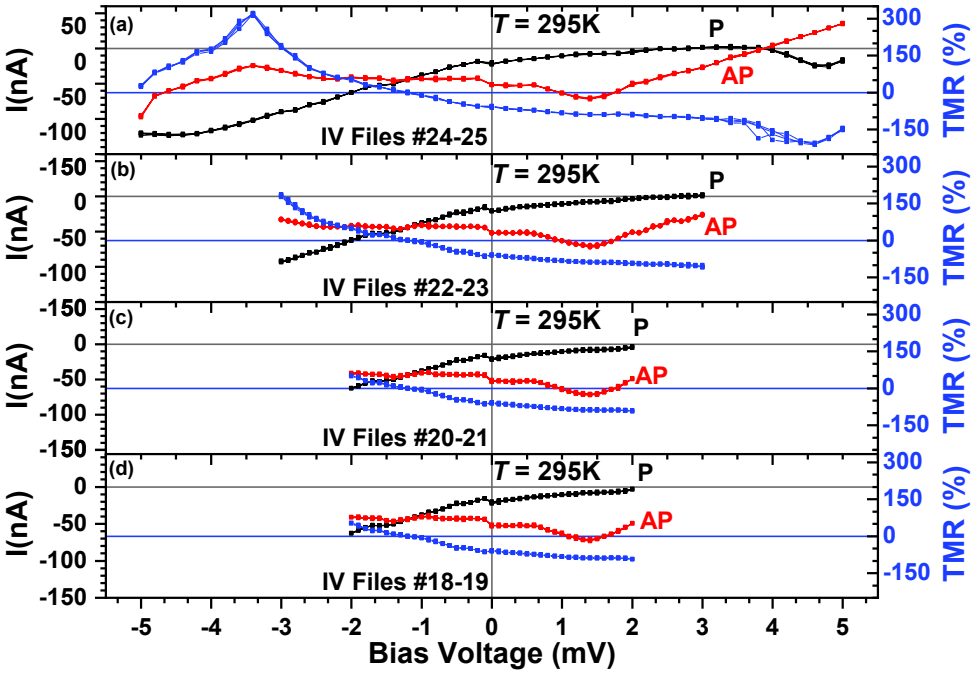

Figure 8.7: **Additional magnetotransport measurement - set 2.** 4-probe measurements of I_P (-2 kOe) and I_{AP} (+250 Oe) measured at room temperature (T = 295K) and their resulting TMR. (a) IV files #24-25, V_{max} = 5mV and ΔV = 0.5mV, (b) IV files #14-15, V_{max} = 3mV and ΔV = 0.2mV, (c) IV files #11-12, V_{max} = 2mV and ΔV = 0.1mV, (d) IV files #11-12, V_{max} = 2mV and ΔV = 0.1mV Figure taken from ref [109].

experimental current is zero is magnetic field independent, which excludes the spin Seebeck [112] origin of the spontaneous transport. Moreover, there are two bias offsets in the P state and a single one in the AP state, $V_{off1}(P) = V_{off1}(AP) = 3.75mV and V_{off2}(P) = 5.5mV$. This additional effect is hardly explainable by any artefact-driven bias-offset.

8.3 Summary and Perspectives

This manuscript's chapter focused on the recently discovered [102, 109] energy harvesting capabilities using spintronic devices and quantum thermodynamics. Firstly, we apply the basic principles of quantum thermodynamics to describe the mechanisms of harvesting thermal energy in confined quantum mechanical systems. The main principles of such systems rely on an asymmetric transport profile and spontaneous tunneling events enhanced by thermal fluctuations along the confined transport path. Basically, assembling the transport path in a proper asymmetric manner enables to pump electrons against an applied

bias, or even in the absence of an applied bias ,by utilizing thermal fluctuations. Such a device can output electrical power under a connected resistance load. Several key theoretical and experimental examples were revisited in section 7 and many other related works were referenced.

Secondly, the implication of the spintronic degree of freedom into the energy harvesting process was done on the example of our conceptual spin-engine. The spin state of the charge carriers can be utilized for their guided movement, thus the formation of a spontaneous current flow. Mainly inspired by the recent discovery of spintronics-driven power generation in MTJs containing magnetic insulators [102], we derived the main ingredients of an energy harvesting spin-engine in the framework of coherent tunneling: i) Spin-fluctuations – are at the center of the engine and can be generated by thermal-fluctuations on spin-split discrete energy states if they are split by $\Delta < \mathrm{k_B T}$, ii) Spintronic rectifications - spin dependent transmission rates on both sides of the spin-fluctuating central entity provide an imbalanced polarized current, hence, a spontaneous current flow along the spintronic path in the absence of, or against, the source bias. Furthermore, we proposed several candidates for the components of a spin-engine. For instance, the central spin-split entity can be established by nanoparticles or spin-degenerate states in the presence of a magnetic field [99, 102] or a spintronic magnetic anisotropy [109, 121]. The spintronic rectification can be ensured by spinterfaces [54, 110], spin-filters [102, 123], symmetry filtering within MTJs [40] and Half-metals [124–126].

Thirdly, we discussed about how spinterfaces and spin-split states may coexist in an Co/C-MgO/Co MTJ device, where C-MgO stands for an MgO dielectric with C-dusted interfaces and carbon filled oxygen vacancies in it. Our own ab-initio theory predicted the formation of paramagnetic (PM) centers by the carbon atoms within the MgO [109] and other works demonstrated the high spin polarization at the Fermi level of Co/C interfaces, hence, the presence of spinterfaces. We proposed that spintronic anisotropy generated by the spitnerface lift the degeneracy on the PM centers and generate discrete spin-split states. The successive examination of the magnetotransport dataset acquired on a single such MTJ at room-temperature revealed several features advocating for a spintronics-driven power generation: (A) Spontaneous current in the 10 nA range strictly related to the magnetic configuration of the MTJ. The P and AP current-bias IVs enter the energy-generating quadrant, when $\mathrm{V} > 0 \mathrm{and} \mathrm{I} < 0$, implying that electrons are flowing against the sourced bias. At $\mathrm{V} = 0, \mathrm{I} \neq 0$ the spontaneous current is field-dependent: $\mathrm{I_P}$(V=0) = -22nA and $\mathrm{I_{AP}}$(V=0) = -53nA, which strongly exceeds the maximum technical offset of 500pA. (B) Giant spintronics performance characterized by the tunneling magnetoresponse of the device, TMR (V = -3.5mV) = 315% and TMR (V = +4.5mV) = -200% and at RT. This effect can't be explained by symmetry filtering as in standard CoFeB/MgO/CoFeB MTJs. (C) Magnetotransport features described in (A) and (B) are defined by very sharp energetic resolutions between 0.25-1.3meV. This exceeds the expected thermal broadening $\mathrm{k_B T} (\approx 26 \mathrm{meV})$ by orders of magnitude. We interpret this discrepancy as thermal shielding of the PM centers by the low-density profile of spinterfaces on both sides. (D) Confident exclusion of both photocurrents and thermocurrents from the interpretation scheme, since all measurements were performed in the dark and that no thermocurrent features are observed.

Fourthly, we developed an analytical transport model based on Greens function transport

through FM leads, spinterfaces at both sides and a central spin split PM-dimer. A unique set of parameters leading to a proper agreement between the simulated and experimental magnetotransport features reinforces our initial attribution of these results to the room-temperature operation of a spin-engine within a common place MgO-based MTJ device. Therefore, this single $20\mu m$ wide MTJ device outputs 0.1nW of electrical power in both of its magnetic states. The reproducibility challenges of such power generating devices emerges from the rigid restrictions on the confined spintronic profile required for the efficient rectification and collection of spin fluctuations. In our system, the spatial distribution of oxygen vacancies in MgO and their "population" by diffused carbon atoms play a key role. Yet, these processes are almost impossible to control on the atomic level even with current cutting-edge technologies. Future development in the field of spintronics would answer whether magnetic tunnel junctions can be used as spin-batteries in integrated circuits or in larger scale applications. An interesting materials strategy to achieve energy generation reproducibility could be: i) to utilize the PM centers of molecules within junctions similar to those described in Chapter 10, ii) to utilize directly CoFeB electrodes for their symmetry filtering properties as an alternative to spinterfaces and explicitly position PM centers in the MgO barrier.

Traduction en Français:

Résumé et perspectives

Le chapitre de ce manuscrit s'est concentré sur les capacités de récupération d'énergie récemment découvertes [102, 109] à l'aide de dispositifs spintroniques et de thermodynamique quantique. Premièrement, nous appliquons les principes de base de la thermodynamique quantique pour décrire les mécanismes de récolte de l'énergie thermique dans des systèmes de mécanique quantique confinés. Les grands principes de ces systèmes reposent sur un profil de transport asymétrique et des événements de tunnel spontanés accentués par des fluctuations thermiques le long du trajet de transport confiné. Fondamentalement, l'assemblage du chemin de transport d'une manière asymétrique appropriée permet de pomper des électrons contre une polarisation appliquée, ou même en l'absence d'une polarisation appliquée, en utilisant des fluctuations thermiques. Un tel dispositif peut fournir une puissance électrique sous une charge de résistance connectée. Plusieurs exemples théoriques et expérimentaux clés ont été revisités dans la section 7 et de nombreux autres travaux connexes ont été référencés. Deuxièmement, l'implication du degré de liberté spintronique dans le processus de récupération d'énergie a été faite sur l'exemple de notre moteur de spin conceptuel. L'état de rotation du des porteurs de charge peuvent être utilisés pour leur mouvement guidé, donc la formation d'un flux de courant spontané. Principalement inspirés par la découverte récente de la production d'énergie axée sur la spintronique dans les MTJ contenant des isolants magnétiques [102], nous avons dérivé les principaux ingrédients d'un moteur de spin à récupération d'énergie dans le cadre d'un tunneling cohérent: i) Les fluctuations de spin - sont à le centre du moteur et peuvent être générés par des fluctuations thermiques sur des états d'énergie discrets à spin-split s'ils sont divisés par $\Delta < k_B T$, ii) Redressements spintroniques - taux de transmission dépendant du

spin des deux côtés de l'entité centrale à rotation de spin fournissent un courant polarisé déséquilibré, d'où un courant spontané le long du trajet spintronique en l'absence ou contre la polarisation de la source. De plus, nous avons proposé plusieurs candidats pour les composants d'un spin-engine. Par exemple, l'entité centrale de division de spin peut être établie par des nanoparticules ou des états dégénérés de spin en présence d'un champ magnétique [99,102] ou d'une anisotropie magnétique spintronique [109,121]. La rectification spintronique peut être assurée par des spinterfaces [54,110], des filtres de spin [102,123], un filtrage de symétrie au sein des MTJs [40] et des demi-métaux [124–126]. Troisièmement, nous avons discuté de la façon dont les spinterfaces et les états de division de spin peuvent coexister dans un dispositif Co / C-MgO / Co MTJ, où C-MgO représente un diélectrique MgO avec des interfaces en poussière de C et des lacunes en oxygène rempli de carbone. Notre propre théorie ab-initio a prédit la formation de centres paramagnétiques (PM) par les atomes de carbone dans le MgO [109] et d'autres travaux ont démontré la polarisation de spin élevée au niveau de Fermi des interfaces Co / C, d'où la présence d'interfaces spatiales. Nous avons proposé que l'anisotropie spintronique générée par la face crachée lève la dégénérescence sur les centres PM et génère des états discrets de spin-split. L'examen successif de l'ensemble de données de magnétotransport acquis sur un seul tel MTJ à température ambiante a révélé plusieurs caractéristiques préconisant une génération d'énergie entraînée par la spintronique: (A) courant spontané dans la gamme 10 nA strictement liée à la configuration magnétique de le MTJ. Les IV de polarisation de courant P et AP entrent dans le quadrant générateur d'énergie, lorsque $\mathrm{V} > 0 \mathrm{and} \mathrm{I} < 0$, ce qui implique que les électrons circulent à contre-courant de la polarisation d'origine. À $\mathrm{V} = 0, \mathrm{I} \neq 0$, le courant spontané est dépendant du champ: $\mathrm{I_P}$(V=0) = -22nA et $\mathrm{I_{AP}}$(V=0) = -53nA ce qui dépasse fortement le décalage technique maximal de 500pA. (B) Performances de la spin- tronique géante caractérisées par la magnétoréponse tunnel de l'appareil, TMR (V = -3,5mV) = 315% et TMR (V = + 4,5mV) = -200% et à RT. Cet effet ne peut pas être expliqué par le filtrage de symétrie comme dans les MTJ CoFeB / MgO / CoFeB standard. (C) Les caractéristiques de magnéto-transport décrites en (A) et (B) sont définies par des résolutions énergétiques très nettes entre 0,25-1,3 meV. Cela dépasse le kBT d'élargissement thermique attendu ($\mathrm{k_B T} (\approx 26 \mathrm{meV})$) de plusieurs ordres de grandeur. Nous interprétons cet écart comme un blindage thermique des centres PM par le profil de faible densité des interfaces sp des deux côtés. (D) Exclusion sûre des photocourants et des thermocourants du schéma d'interprétation, puisque toutes les mesures ont été effectuées dans l'obscurité et qu'aucune caractéristique de thermocourant n'est observée. Quatrièmement, nous avons développé un modèle de transport analytique basé sur le transport de la fonction Greens à travers des dérivations FM, des interfaces sp des deux côtés et un dimère PM à spin central. Un ensemble unique de paramètres conduisant à un accord approprié entre les caractéristiques de magnétotransport simulé et expérimental renforce notre attribution initiale de ces résultats au fonctionnement à température ambiante d'un moteur de spin dans un dispositif MTJ à base de MgO. Par conséquent, ce dispositif MTJ unique de $20 \mu \mathrm{m}$ de large produit 0,1 nW d'énergie électrique dans ses deux états magnétiques. Les défis de reproductibilité de tels dispositifs de production d'électricité émerge des restrictions rigides sur le profil spintronique confiné requis pour la rectification efficace et la collecte des fluctuations de spin. Dans notre système, la distribution spatiale des la-

cunes d'oxygène dans le MgO et leur «population» par les atomes de carbone diffusés jouent un rôle clé. Pourtant, ces processus sont presque impossibles à contrôler au niveau atomique même avec les technologies de pointe actuelles. Le développement futur dans le domaine de la spintronique permettrait de déterminer si les jonctions tunnel magnétiques peuvent être utilisées comme batteries de spin dans des circuits intégrés ou dans des applications à plus grande échelle. Une stratégie intéressante pour les matériaux pour atteindre la reproductibilité de la production d'énergie pourrait être: i) d'utiliser les centres PM des molécules dans des jonctions similaires à celles décrites au chapitre Chapter 10, ii) d'utiliser directement des électrodes CoFeB pour leurs propriétés de filtrage de symétrie comme alternative aux spinterfaces et positionner explicitement les centres PM dans la barrière MgO.

Part III

Bias controllable magnetoresistance effect in phthlocyanine-based magnetic tunnel junctions

Chapter 9

Introduction to organic spintrnonics

In this chapter the reader is invited to familiarize himself with the young field of organic spintronics and discover the spintronic mechanisms we've experimentally unveiled in such novel systems. We begin by presenting the basic notions of organic materials. This is followed by an intuitive description of magnetic molecular compounds further we explain why they are suited for spintronic applications. Then, we describe how organic magnetic junctions can be assembles with these magnetic molecules. At last we describe how the magnetoresistance effects arising in such molecular spintronic devices can be actively controlled by bias voltage.

Traduction en Français:

Introduction à la spintrnonique organique

Dans ce chapitre, le lecteur est invité à se familiariser avec le jeune domaine de la spintronique organique et à découvrir les mécanismes spintroniques que nous avons expérimentalement dévoilés dans ces nouveaux systèmes. Nous commençons par présenter les notions de base des matières organiques. Ceci est suivi d'une description intuitive des composés moléculaires magnétiques, nous expliquons plus en détail pourquoi ils sont adaptés aux applications spintroniques. Ensuite, nous décrivons comment les jonctions magnétiques organiques peuvent être assemblées avec ces molécules magnétiques. Enfin, nous décrivons comment les effets de magnétorésistance apparaissant dans de tels dispositifs spintroniques moléculaires peuvent être activement contrôlés par la tension de polarisation.

9.1 Background to Organic electronics

The field of electronics was restricted to inorganic materials until the discovery of semiconducting properties of doped polymers by A.J. Heeger et. al in the 70s [132]. This discovery brought up the concept of utilizing organic materials in electronic compounds due to their semiconducting properties. Within the field of organic electronics, many different technologies have emerged. For instance, within consumer electronics, organic light emitting diodes (OLEDs) are commonly used as high-quality screens [133]. In energy generation, organic photovoltaic cells (OPVs) could in a perspective to shrink the manufacturing costs of transparent and flexible solar panels [134, 135]. In electronic circuits,

organic field effect transistors (OFETs) were developed [136]. Organic materials utilized in electronics can already in some cases compete with their inorganic counterparts and bring new assets such as lightweight, flexibility, and low costs. Spintronics mostly relies on the manipulation of the electron spin-state. In the most efficient inorganic systems, this effect is based on the combination of the symmetry and consequently spin-filtering properties of the inorganic semiconducting (ISCs) spacers and the spin-polarization properties of ferromagnetic electrodes that encapsulate them. The physics of organic semiconductors (OSCs) is very different from their inorganic counterparts and the rest of this chapter will describe in which manner OSCs can be beneficial for spintronic applications.

9.2 Electronic properties

9.2.1 Single molecule

A molecule is a group of two or more atoms linked together by chemical bonds. There are two types of chemical bonds, i) ionic bonds - a purely electrostatic attraction between ions of opposite charge, a single electron is shared between the two atoms. ii) covalent bonds - the overlap of atomic orbitals when an electron is shared between a pair of atoms. Due to the different geometry of the orbital overlap, there exist two subtypes of covalent bonds, a) σ - bonds - a frontal overlap characterized by a strong bond and highly confined electrons. b) π -bonds - a lateral overlap of p (or d) of orbitals, therefore a weaker bonding and therefore more delocalized electrons. This later property of π -bonds gives them the main role in the charge carrying properties of molecules.

Referring to Figure 9.1, the molecular orbital theory dictates that the a π - bond between two $\mathrm{p_z}$ atomic orbitals forms two $\mathrm{p_z}$ molecular orbitals, a low energy π bonding orbital and a high energy π^* antibonding molecular orbital. The π - bonds lead to the formation of delocalized electrons, which can be either delocalized on a portion of the molecule or the whole molecule depending on its chemical structure. Therefore, the molecular orbitals which are involved into charge transport are the highest occupied molecular orbital (HOMO) and the lowest unoccupied molecular orbital (LUMO). The energy levels of those molecular orbitals are respectively equivalent to the conduction and valence bands in inorganic semiconductors.

9.2.2 Molecular layers: transport properties

Organic semiconductors composed of molecular layers usually have no precise lattice structure. Therefore, the cohesion between electrically neutral molecules is ensured by relatively weak van der Waals or London forces. The weak molecular interactions result in a small overlap of molecular orbitals, which almost excludes the formation of free delocalized electrons in the bulk molecular material and therefore limits charge transport. The morphology of molecular layers can be crystalline, polycrystalline or amorphous, depending on the molecule's geometry and its deposition methods. In each of these states the electronic structure will be different and will affect the transport mechanisms in OSCs.

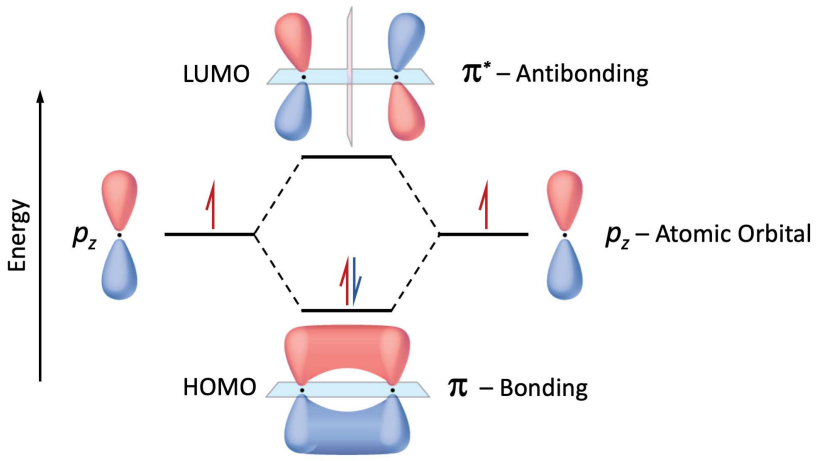

Figure 9.1: **Energy diagram of two interacting p_z atomic orbitals and the resulting π - bonding and π^* - antibonding orbitals.** The energy level of the π - bonding orbital lies below the p_z orbital's level and forms the highest occupied molecular orbital (HOMO). The π^* - antibonding orbital is of higher energy and forms the lowest unoccupied molecular orbital (LUMO).

The injected charge carriers can follow two conduction scenarios: (i) **Band Transport** - the strong overlap of π-orbitals generates quasi continuous energy bands [137], which transport the injected charge carriers, as represented in Figure 9.2.a. As a note of mention, this type of transport is much less likely to take place in OSCs as they hardly form perfect crystalline structures. (ii) **Hopping** - the electron consecutively hops through localized pi-orbitals. This mechanism takes place in disordered systems with a weak overlap of molecular orbitals [138], see Figure 9.2.b. Hopping transport strongly depends on the temperature, electric field, presence of traps and carrier's density in the material. In this type of transport, the traveling electron may lose some of its energy and quantum state.

Historically, the first molecular spintronic devices were assembled of thick 40 - 200nm molecular spacers [139–141], hence they were characterized by a strong hopping transport. This led to a relative puzzling interpretation of the molecular transport results [142]. Molecular spintronics reached an important milestone when the molecular spacer was substantially reduced and tunneling transport was reported in organic spin-valve devices [54, 143]. This breakthrough brought on the concept of utilizing molecular spacer to tune the polarization properties at the ferromagnetic-molecular interfaces rather than for their purely transport properties. The following sections of this chapter depicts in detail the current state of the art of the molecular spintronics.

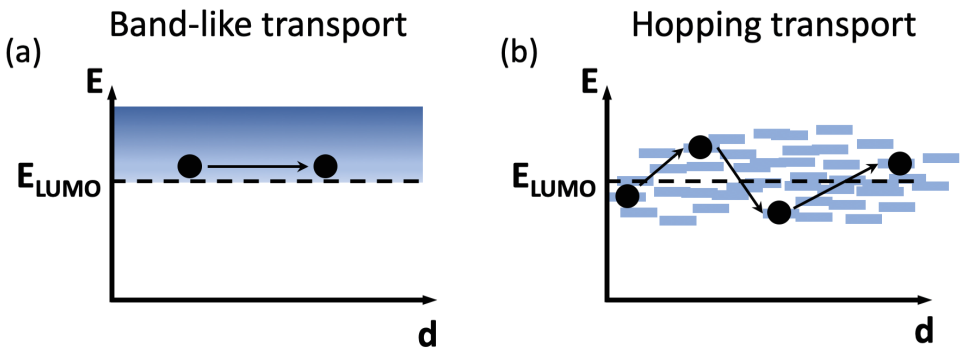

Figure 9.2: **Schematic representation of band-like and hopping transport regimes.** a) Band-like transport arises in strongly ordered molecular structures and weakly depends on the temperature. b) Hopping transport arises in amorphous molecular layers and in the presence of a weak orbital overlap. It is characterized by a complicated temperature dependence.

9.3 Molecular Spin-chains: magnetic ordering of molecules

Developing organic spintronic applications for today's and future societal solutions such as organic memory elements [144, 145], organic solar-cells [135, 146], and even logic units [147, 148] implies a thoughtful understanding and efficient manipulation of the spin-polarized transport taking place across the device. The unique way to actively manipulate spin-polarized currents is through an external magnetic field. The chemistry community reports about nine million know organic compounds. Some of these organic spintronic candidates have magnetic properties as it is the case of transition-metal phthalocyanine molecular complexes (TMPc). The major advantage of utilizing such magnetic molecules in spintronic devices is the additional degree of freedom they enable to manipulate the spin-polarized currents. This chapter is entirely devoted to the detailed description of the effects arising in such hybrid molecular systems. The journey towards magnetic molecular spintronics starts with the description of these magnetic molecular elementary bricks. Afterward, the structures that can be assembled with these molecular bricks are characterized. And at last, an overview of these structures and their implementation in molecular spintronic devices is described.

9.3.1 Elementary bricks

Transition-metal phthalocyanine molecules

The history of phthalocyanine molecules starts at the beginning of the 20^{th} century when the first metal-free hydrogen-phthalocyanine molecules ($\mathrm{H_2Pc}$) were discovered. Phthalocyanine (Pc) molecules are square planar $(\mathrm{C_8H_4N_2})^4$ single decker macrocyclic organic compound. These molecules are composed of four isoindole units held by the

pyrrole nitrogen atoms, hence their four-fold axis of symmetry. The molecule has a two-dimensional geometry and a broad ring of 18 π-electrons that are mainly responsible for the charge carrier mobility. The metal-Pc compounds are characterized by a metallic ion that forms covalent bonds with two of the central N-atoms, whereas the other two central N - atoms form coordinate covalent bonds. In such a way, there are around 70 different phthalocyanine based compounds discovered up-to-date. Whenever the central point of a Pc molecule is occupied by a transition metal, for instance a Cobalt Co^{2+} cation, the resulting cobalt-phthalocyanine (CoPc) compound acquires magnetic properties. The schematic structure of a CoPc molecule is visualized in Figure 9.3.

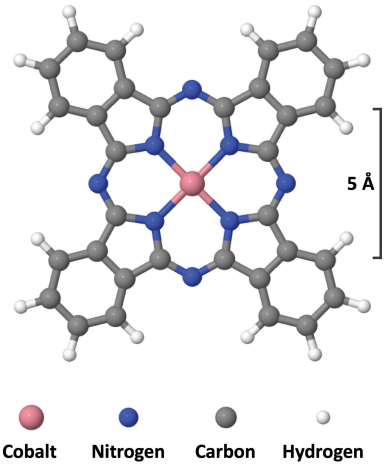

Figure 9.3: **Single cobalt-phthalocyanine molecule.** The central Co^{2+} cation forms two covalent bonds and two coordinate bonds with the central ring nitrogen atoms. The molecule has a very confined lateral dimension of the typical single atom length, and it is considered as quasi-two-dimensional compound.

Molecular orbitals

It is well known that both the electric and magnetic properties of any material are defined by its electronic properties, hence can be described by the atomic orbitals of the material. In quantum mechanics, atomic orbitals are mathematical functions defining the space region in which a single or a pair of electrons can be found with a given probability. For instance, transition metals exert high electric conductivity and magnetism in part due to their unfilled *d* electron sub-shells. The *d*-orbitals of a single transition metal atom are denoted as $d_{xy}, d_{xz}, d_{yz}, d_{z2}$ and $d_{x^2-y^2}$. These five *d*-atomic orbitals are visualized in Figure 9.4.

The metal-phthalocyanine compounds are classified under coordination complexes as they are composed of an electron pair acceptor (metallic cation) and electron pair donors (ligands). Furthermore, the interactions between metal ions and molecule ligand orbitals in coordination complexes are described by the ligand field theory (LFT). When ligands

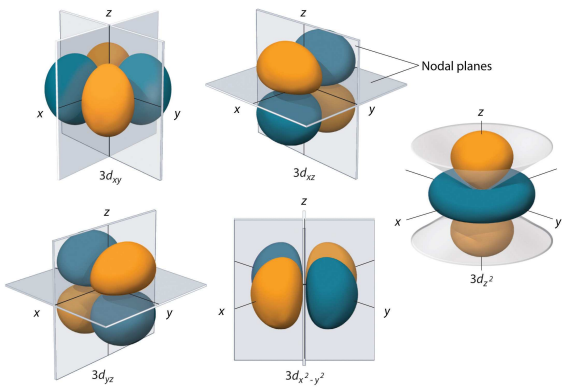

Figure 9.4: **The spatial orientations of transition metals d atomic orbitals.** The five orbitals denoted $\mathrm{d_{xy}}, \mathrm{d_{xz}}, \mathrm{d_{yz}}, \mathrm{d_{z2}}$ and $\mathrm{d_{x^2-y^2}}$are degenerate and the yellow color stands for spin-down whereas green for spin-up. Figure taken from ref [149].

surround the metal ion, the degeneracy of its orbitals is lifted through electrostatic interactions. The geometry and spatial orientation between the interacting metal-ligand orbitals dictate the energy split of the *d* orbitals energy levels. The electrostatic field generated by ligands raises all of the *d* orbitals on the metallic center. In $\mathrm{D_{4h}}$ symmetry the d orbitals are split into molecular orbitals that are labeled according to their symmetry (within the irreducible representation. As in this manuscript $\mathrm{D_{4h}}$ symmetry group (central metal ion interacts with 4 molecular sites in the same plan) CoPc complexes are of our main interest we describe here only this scenario of ligand field interactions applied to a metal with a 3d, 4s and 4p atomic orbitals. Ligand field theory describes the energy splitting of 3d, 4s and 4p metals orbitals into the $\mathrm{b_{1g}(d_{x^2-y^2}), b_{2g}(d_{xy}), a_{1g}(d_{z^2})and e_g(d_{xz}and d_{yz})}$ subsets, as depicted in Figure 9.5.

The electronic structure of MPs molecules

The material's density of states (DOS) characterizes the number of accessible states to be occupied and unoccupied by the system. As in the scope of this thesis we investigate CoPc based spintronic devices, this section evokes merely the DOS of this MPc species. The electronic and magnetic properties of CoPc molecules are dictated by the spin-splitting of molecular orbitals (MO), hence the uncompensated spin-population. Brede et al. reported the spin and orbital resolved density of state of a free CoPc molecule through ab-initio calculations [151]. Figure 9.6 visualizes the theoretical results of this report. The magnetic behavior is mostly mediated by the metallic molecular orbitals emerging at the molecule through the insertion of the central Cobalt atom. At the Fermi level, exclusively the $\mathrm{d_{z2}}$ MO situated at the central Co ion is present at spin-down DOS and not at spin-up DOS. The SP-DOS of a free CoPc molecule is highly asymmetric near the Fermi level and this results in the magnetism of these molecular compounds.

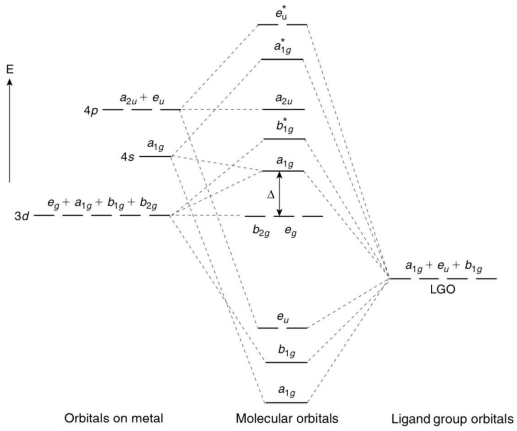

Figure 9.5: **A molecular orbital energy level diagram for a square planar complex.** Left - 3d, 4s and 4p metal orbitals. Right - molecular ligand orbitals. Center - Hybridization through ligand field interactions of the metal and ligand orbitals. The band without (with) the star (*) correspond respectively to the bonding (antibonding) subsets, and Δ represents the energy gap between $\mathrm{d_{xy}}$ and $\mathrm{d_{x2-y2}}$ subsets. Diagram taken from ref [150].

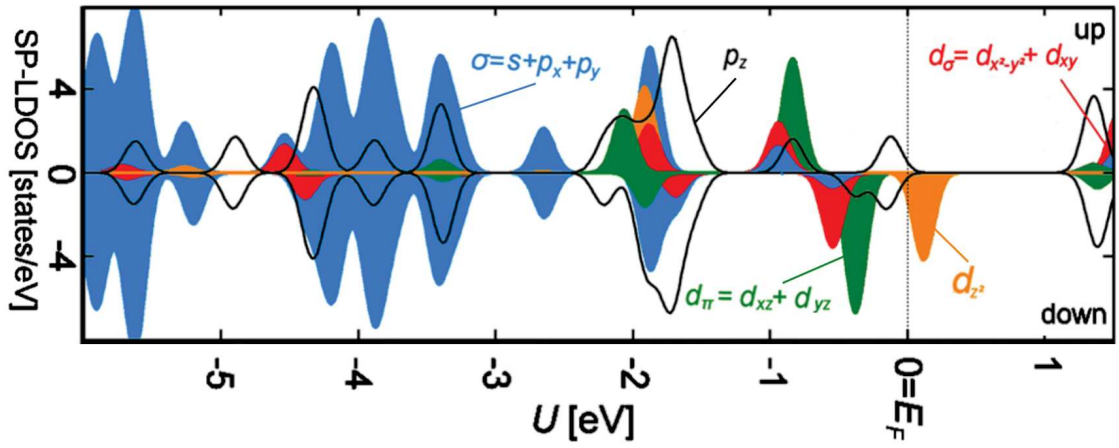

Figure 9.6: **The geometry and the calculated density of states for a free CoPc molecule.** Spin resolved-DOS (SP-DOS) of a free CoPc molecule resulting from **ab-initio** calculations. The color of the SP-DOS stands for the molecular orbital symmetry, black outline for $\mathrm{p_z}$, blue for $\sigma(\mathrm{s+p_x+p_y})$, green for $\mathrm{d_\pi(d_{xz}+d_{yz})}$, orange for $\mathrm{d_{z^2}}$ and red for $\mathrm{d_\sigma(d_{x^2-y^2}+d_{xy})}$ molecular orbitals. Figure adapted from ref [151].

9.3.2 Elementary constructions: assembled molecular layers

Single molecule spintronics have known some strong interest [152,153] and could be the ultimate step in the miniaturization of the technological node. Nonetheless, in the scope of this work we focused on molecular magnetic tunnel junctions, which implies working

with molecular layers. It turns out that the crystallographic structure of MPc molecules makes them into ideal candidates for organic spintronic applications. MPcs can naturally form two different polycrystalline structures, the α and β phases. The polymorphism of MPc molecules is characterized by a column-like structure along the b axis and forms vertical pillars of MPc molecules. The α and β phases differ by the stacking tilt angle and between the consecutive molecules in the column. Figure 9.7 represents the ideal $\alpha(65.8°)$ and $\beta(42.9°)$ polycrystalline phases with their characteristic tilting angles [154].

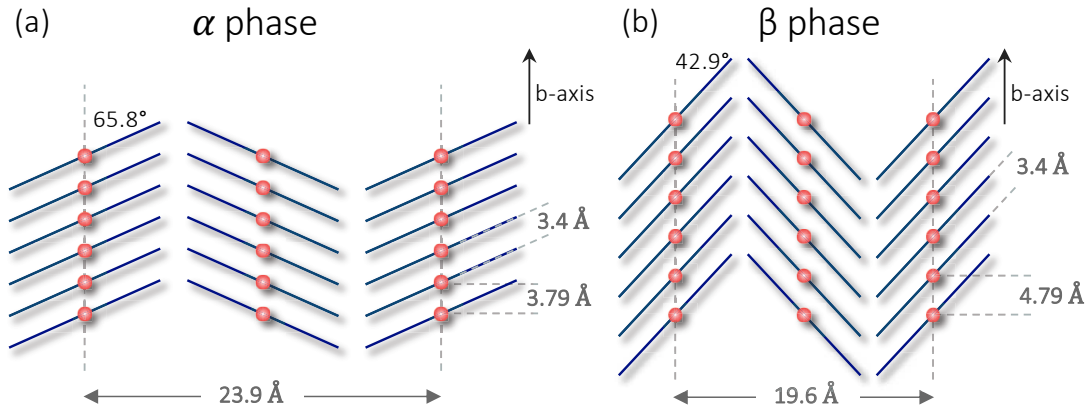

Figure 9.7: **Polymorphism of MPc stacks.** Stacking arrangement of CoPc molecules along the b-axis. At the left, α phase (left) with a $65.8°$ tilt between the b-axis and the molecular plane. At the right β phase with a $42.9°$ tilt. Figure adapted from ref [155].

The stacking phase of the MPcs can be defined through the molecular layer's deposition process. The polycrystalline α phase of MPc films arise when the molecules are evaporated onto a substrate which is at room temperature [156]. The β phase is achievable if the deposition is performed on a higher-temperature substrate or upon annealing and α phase at $200°C$ [157]. The high crystalline structure along the b-axis of MPc molecular layers plays a key role in their implementation within vertical hybrid organic junctions. The phase type defines the distance between two vertically adjacent metal ions; thus, it defines the overlap of metallic orbitals and dictates both the electronic and magnetic properties of the MPc molecular layers. It was reported that the α phase of MPcs stacks give rise to an antiferromagnetic (AFM) coupling between the vertically adjacent molecules of a single column [158–161]. Additionally, it was reported that the β phase stacking structure gives rise to FM magnetic order [162]. In the following section, a more detailed description of the magnetic interactions arising in CoPc molecular layers will take place.

9.3.3 Spin-chains: antiferromagnetic order in molecular layers

As discussed previously the magnetism of each MPc molecule is triggered by the central transition metal atom. Therefore, the stacking geometry of MPc complexes and the mag-

netism individual molecule implies the presence of magnetic interactions within between single molecules originating in the naturally arising vertical pillars of MPc. Experimentally Chen et al investigated the long-range superexchange interactions in molecular layers of CoPc complexes [163]. The coupling of each spin moment with its neighbors was probed by means of spin-flip inelastic electron tunneling spectroscopy (IETS) (see Section 9.4 for a description). The authors demonstrated the arrangement of CoPc molecules in one-dimensional CoPc-chains and that an antiferromagnetic ordering occurs in these structures. Superexchange interactions hence antiferromagnetic (AFM) order in the molecular chains arises when an electron from the pyrrole N $\mathrm{E_g}$ orbital of the Pc hops on the cobalt's $\mathrm{d_{z2}}$ orbital, the remaining unpaired electron interacts with $\mathrm{d_{z2}}$ orbital of the Co center of the molecule beneath it, see Figure 9.8 below. This superexchange mechanism was further confirmed by ab-initio calculations by Serri et al. [162]. These aforementioned interactions at both sides of each CoPc molecular plane bound the vertical structure and established the one-dimensional spin-chain (as each of the molecules carry a spin-moment).

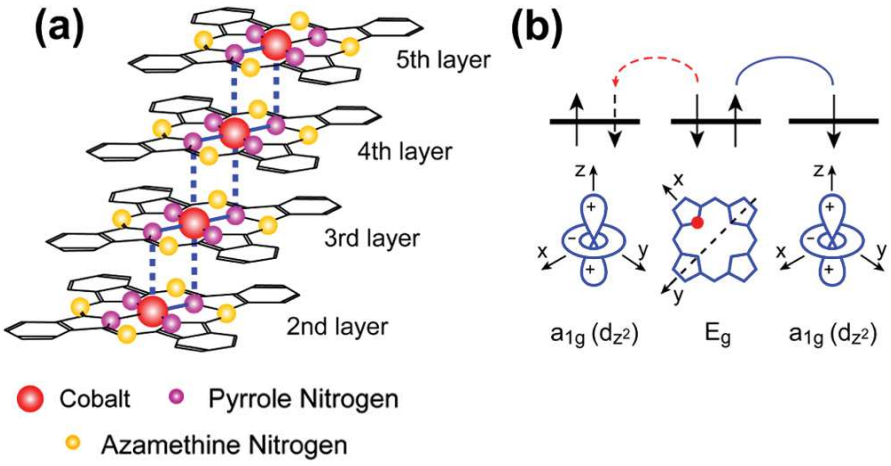

Figure 9.8: **Spin-chains and superexchange mechanism.** a) Superexchange mechanism between consecutive CoPc molecules. The dashed red (change color) line represents the interaction between the unpaired electron of the Eg orbital of the pyrrole N and the $\mathrm{d_{z2}}$ orbital of the cobalt beneath it. The solid blue line (left and right) corresponds to the transferred electron from the $\mathrm{E_g}$ orbital to the $\mathrm{d_{z2}}$ orbital above it. b) Schematic representation of a 1D CoPc spin-chain. Figure taken from ref [163].

Chen et al. [163] have experimentally observed the presence of an AFM spin-chain in CoPc molecular layers with an $60^\circ \pm 3^\circ$ tilt angle, which is in good agreement with the ideal polymorph α phase at 65.8° tilt angle. Independently, Serri et al. have demonstrated through magnetic susceptibility experiments that the α phase powder exhibits a strong AFM coupling, whereas the β phase is prone to exhibit a much weaker AFM coupling. The magnetic order discrepancy originates from the structural stacking difference, hence, in the orbital overlap in each the two phases. In the α phase, the $\mathrm{d_{z2}}$ orbitals experience an overlap whereas in the β phase knows no overlap of incident $\mathrm{d_{z2}}$ orbitals. The strength of the

magnetic coupling within the spin-chain is characterized by the exchange energy between two consecutive centers. The experimentally reported α phase exchange energies range between 70K to 106K according to Serri et al. [162] and close to 200K according to Chen et al. [163]. In both cases the AFM exchange energy measured experimentally in CoPc spin-chains remains lower than room-temperature. It turns out that the exchange energy of the spin-chains depends not only on the stacking geometry of the molecular layer but also on the magnetic properties of the hosting substrate. Furthermore, it was demonstrated that the magnetic order of a spin-chain can be mediated by the magnetic hosting substrate. This effect takes place when the end-member of a spin-chain is magnetically coupled to a FM substrate. The room-temperature MnPc spin-chain's AFM order reported by Gruber et al. [156] doesn't originate from an α phase structure of the molecules but is rather dictated by the substrate's magnetism. The authors grew few molecular layers on a ferromagnetic Co substrate. By comparing standard magnetometry with an element sensitive studies by X-ray magnetic circular dichroism (XMCD) authors were able to observe a ferromagnetic (FM) interaction between the Co substrate and the 1st ML of MnPc.

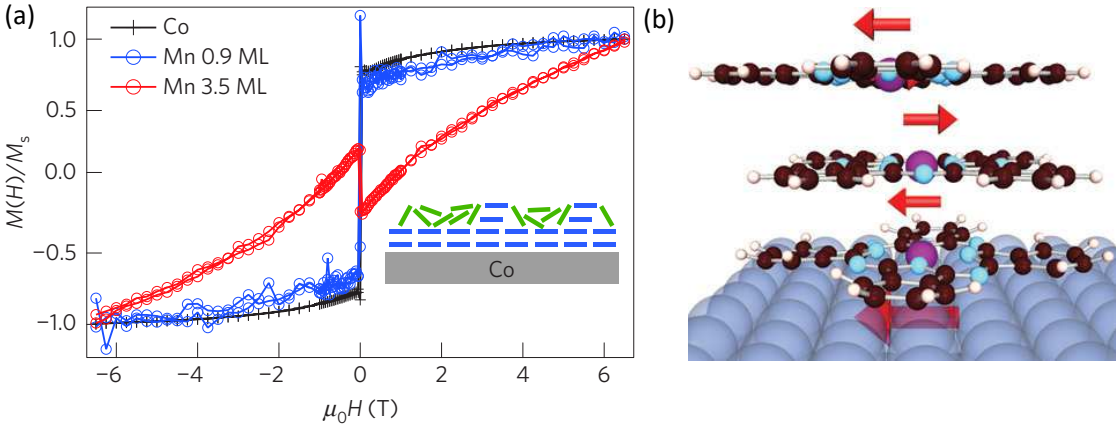

Figure 9.9: **Antiferromagnetic ordering of the MnPc molecules and the spin-chain geometry.** a) Normalized magnetization plots for the pure Cobalt substrate (black), 0.9ML (3.5ML) of MnPc deposited on the cobalt substrate in blue (red). b) Visualization of a trilayer MnPc spin-chain sitting in a Co substrate. The red arrows correspond to the direction and amplitude of the local spin moments. Figure taken from ref [156] .

In this respect, Figure 9.9.a demonstrates FM interaction between the Co substrate and the first monolayer of absorbed MnPc molecules, as previously reported [164, 165]. One can see that both the two curves in black and blue share the exact same magnetization behavior, hence an FM coupling is necessarily present. Further through XMCD measurements the AFM interactions between the 1^{st} and the 2^{nd} ML of CoPc was determined. Referring to Figure 9.9.b, the formation of an MnPc spin-chain on a Co substrate is visualized with their respective magnetic moments. At the interface between Co and 1^{st} CoPc ML FM interactions take place, whereas afterwards the discrete magnetic moments of each MnPc molecule are coupled in an AFM manner. In such a way, the development

of an MnPc spin-chain on a Co substrate was demonstrated at room-temperature. In this manner, a major corner stone of molecular spintronics was reached, and the development of MPc-based spintronic devices operating at room-temperature is foreseeable. The next section of this chapter describes the excitation mechanisms of spin-chains and in what manner these excitations may affect the transport through such systems once implemented in spintronic devices.

9.4 Spin-flip spectroscopy

The main mechanism of exciting a spin-chain is to alter one or more of its discrete spin-states by overcoming the exchange parameter J that defines the interaction between two consecutive spin-states within the spin chains. The Heisenberg Hamiltonian describes well the interaction between the spin states of the molecules:

$$\mathrm{H_{int}} = -\mathrm{J} \sum_{\mathrm{i}=1 \rightarrow \mathrm{N}-1} \mathrm{S_i} * \mathrm{S_{i+1}} \tag{9.1}$$

Where $\mathrm{S_i}$ is the spin of the $\mathrm{i^{th}}$ site, J is the exchange parameter and N the number of sites in the chain. A negative J corresponds to an antiferromagnetic coupling whereas a positive J defines a ferromagnetic interaction. Experimentally the exchange parameter of a spin-chain can be determined by performing an inelastic electron tunneling spectroscopy (IETS). To achieve a submolecular resolution IETS is usually performed on scanning tunneling microscope (STM) setup. In this study the electron tunnels from the STM tip through the CoPc layers to the conducting substrate. The tunneling electron can undergo two different schemes: i) an elastic tunneling, where both the spin angular momentum and the energy of the electron are preserved and, ii) an inelastic tunneling, where the electron interacts with the tunneling environment and exchanges energy. If this exchanged energy is higher than the exchange parameter J the spin-chain can be excited. Inelastic electron tunneling spectroscopy (IETS) enables to measure the energy of discrete excitations to investigate the electronic states within the tunneling barrier. Here we describe the mechanisms of IETS using the simple example of a 3-layer long CoPc molecule deposited on a metal substrate. In this case, the electron is tunneling through the molecules from(to) an STM tip to(from) the substrate. The total spin of a single CoPc molecule has a spin of S = 1/2 from the singly occupied $\mathrm{d_{z2}}$ orbital. The IETS excitation of a single free molecule corresponds to the spin moment transition of $\mathrm{m} = \mid +1/2 > \rightarrow \mathrm{m} = \mid -1/2 >$, hence, dubbed a spin-flip excitation. The 3-layer long AFM CoPc spin chain has a total spin moment $\mathrm{S_C}$ = 0 (the first molecule is completely absorbed by the substrate and loses its spin state [163], following the selection rules can only become $\mathrm{S_C}$ = 1 upon the transition. The exchange parameter J corresponds to the energy of the transition: $\mathrm{S_C} = 0 \rightarrow \mathrm{S_C} = 1$ as depicted in Figure 9.10.

As in this thesis manuscript we will examine the spin-flip excitations of a molecular spin-chains embedded in a magnetic junction, see Section 10.4.3, the next Section 9.4.1 depicts the general spin-chain's spin-flip transitions formalism.

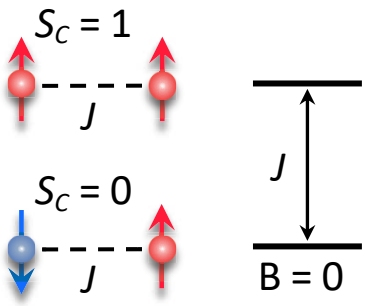

Figure 9.10: **Schematic of a singlet state spin-flip excitation.** The total spin S_C = 0 at the ground state of the 3-center long spin-chain. The excited state is defined by a total spin S_C = 1 as both the spin point in the same direction. A single down spin spin-flips into an up spin. The transition energy corresponds to the exchange parameter J that defines the strength of the AFM order within the spin-chain. This transition takes place at a zero external magnetic field, which can split the singlet state into a triplet state.

9.4.1 Spin-flip excitations of spin-chains

The elastic tunneling from the tip towards the metal substrate is represented in Figure 9.11.a.1-a.2. When the energy of the incident electrons is lower than the exchange parameter J the excitation transition is forbidden. In terms of the IETS this can is equivalent to the bias voltage being lower than the threshold voltage V_{th} = ± J/e (with e the electron's charge and J the exchange parameter). In this case the conductance dI/dV curve obtained from IETS is characterized by a flat line for both polarities of voltage (V_+ and V_-) as represented in Figure 9.11.c. Once the sourced bias voltage reaches thresholds at V_{th} the energy of the incident tunneling electrons that can be lost by interaction with the surrounding environment is equal or higher than the exchange energy between the two spins. Hence, the transition $S_C = 0 \rightarrow S_C = 1$ through an inelastic excitation is achievable. During this inelastic excitation transition the spin moment of the tunneling electron undergoes the following transition $m = |+1/2> \rightarrow m = |-1/2>$ (Δm = -1) and the total spin moment of the 3 center long spin-chain (but only two are really have spin-moments, the first layer is quenched) undergoes a transition of $S_C = 0 \rightarrow S_C = 1$ as depicted in Figure 9.10. Therefore, the opening of an additional inelastic channel corresponds to a spin-flip excitation of the spin-chain.

The opening of an additional inelastic channel increases the tunneling current, hence, a jump in the conductance dIdV plot appears at the threshold V_{th} voltage, see Figure 9.11.c. At bias voltages superior to the threshold value both tunneling channels coexist as represented on the left dI/dV graph (Figure 9.11.c). The allowed transition on the spin-chain defines the population of tunneling charge carriers that can participate in its spin-flip excitation. Within the example described herein, only one spin-channel (spin-up electrons) can ensure the transition on the spin-chain $S_C = 0 \rightarrow S_C = 1$. This simplified description

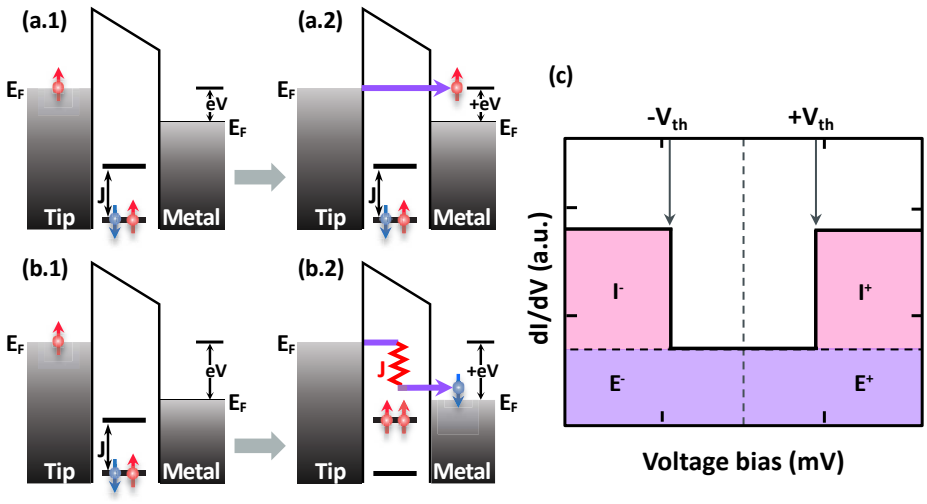

Figure 9.11: **Elastic and Inelastic tunneling and the respective conductance.** (Left) Schematic representation of the energy profile of an IETS-STM measurement performed on a 3-center long spin-chain. The two states within the tunneling barrier correspond to the spin states of the spin-chain depicted in Figure 9.10. (a.1) Sourced voltage is lower than $\mathrm{V_{th}} = \pm \mathrm{J/e}$, (a.2) Elastic tunneling: the tunneling electron doesn't have enough energy to excite the spin-chain, hence break its exchange interaction. The spin moment of the electron is preserved. Corresponds to the low voltage flat section of the conductance in (c). (b.1) Sourced voltage is higher than $\mathrm{V_{th}}$, (b.2). Inelastic tunneling: the tunneling electron has enough energy to excite the spin-chain, its spin-moment undergoes $\mathrm{m} = \mid +1/2 > \mathrm{m} = \mid -1/2 >$ spin-flip transition. $\mathrm{V} > \mathrm{V_{th}}$ and the spin-chain can be excited and also undergo a spin-flip. (c) Conductance plot, at $-\mathrm{V_{th}} < \mathrm{V} < +\mathrm{V_{th}}$ the conductance is flat - elastic tunneling. Opening of the inelastic channel at $\mathrm{V} = \mid \mathrm{V_{th}} \mid$ corresponds to a jump in dI/dV. Figure adapted from refs [166, 167].

of IETS-STM spin-flip excitations along a spin-chain portrays the experimental technique used by Chen et al. [163] to determine the exchange parameter J and therefore the strength of the spin-chains structure. Spin-flip excitations along the molecular spin-chain demonstrates their sensitivity to the most easily accessible external stimuli as is bias voltage. The enhancements that can be brought by molecular spin-chains to the interfacial properties of the hosting magnetic substrate will be discussed in the following subsection. The contribution of spin-chains to the magnetism of the hosting ferromagnetic substrates will be discussed in the next section while the spin-chain mediated transport will be introduced and examined in Chapter 10.

9.5 Tailoring interfacial magnetism: Exchange Bias

One of the fundamental properties of a ferromagnet (FM) is its ability to maintain its magnetic order under an external magnetic field, this effect is defined by the FM's coercivity ($\mathrm{H_C}$). It was demonstrated that the interfacial coercivity of a FM material can be altered in FM/AFM bilayers through the exchange bias ($\mathrm{E_B}$) effect [168, 169]. The first subsection presents the simplified model of $\mathrm{E_B}$, whereas the manifestation of the molecular spin-chain mediated $\mathrm{E_B}$ effect in hybrid FM/AFM(molecular) bilayers is detailed in the second subsection and at last the thermal stability of this the $\mathrm{E_B}$ effect is discussed in the third part.

9.5.1 Exchange-Bias

The effect of exchange bias can be demonstrated using the example of an FM/AFM bilayer. The temperature (T) of the magnetic bilayer defines its magnetic order. If the temperature is below the Curie temperature ($\mathrm{T_C}$) of the FM layer, then its FM order is maintained. The AFM order of the AFM layer is preserved if the temperature is held below the Néel temperature ($\mathrm{T_N}$). In Figure 9.12 below we visualize the sequence of steps generating an $\mathrm{E_B}$ at the FM/AFM interface. Referring to Figure 9.12, (1) the system is initially at an intermediate temperature between the Curie and Néel characteristic temperatures: $\mathrm{T_N} < \mathrm{T_1} < \mathrm{T_C}$, hence the FM layer is stable whereas the AFM layer is disordered. The magnetization loop along the easy axis of the FM layer in the initial state (1) is symmetric around the zero-field mark. The coercive field $\mathrm{H_C}$ of the FM layer in both reversal directions is equal, $\mathrm{H_{C1}} = \mathrm{H_{C2}}$. The two main components required to generate $\mathrm{E_B}$ within the system are, i) the coexistence of AFM and FM magnetic order within the bilayer - the temperature should be below $\mathrm{T_N}$ and $\mathrm{T_C}$ ($\mathrm{T} < \mathrm{T_N} < \mathrm{T_C}$), ii) an induced magnetic reference to the system - applied external magnetic field $\mathrm{H_{FC}}(\mathrm{H_{FC}} > \mathrm{H_{C1,2}})$, denoted field cooling magnetic field. To carry the system from its initial state (1) to ensure the two above conditions, we need to perform a field cooling ($\mathrm{F_C}$) procedure. It consists in continuously applying a strong external magnetic field $\mathrm{H_{FC}}(\mathrm{H_{FC}} > \mathrm{H_{C-FM}})$ along the easy axis of the FM layer and cooling the system down below $\mathrm{T_N}$ and $\mathrm{T_C}$.

Referring to Figure 9.12, in (2) state the magnetic moments at the FM/AFM interface are FM coupled and pointing in the direction of the $\mathrm{H_{FC}}$ applied during the $\mathrm{F_C}$ procedure. When the external magnetic field is progressively swept from a positive value in Figure 9.12.2 to a negative one in Figure 9.12.4 the magnetization of the FM layer undergoes a rotation. The interfacial spins of the AFM layer are aligned with the magnetization of the FM layer and remain pinned in the direction of the field cooling by AFM interactions of the layer. In such manner a unidirectional exchange anisotropy is induced into the system (i.e. with a 2π symmetry). The coercive field of the FM layer in the opposite direction of $\mathrm{F_C}$ (here $\mathrm{H_{C-}}$) is increased as a result of the AFM pinning. As represented in Figure 9.12, the magnetization loop of the bilayer shifts by an amount of the exchange bias field HEB. $\mathrm{H_{EB}}$ is proportional to new coercive fields: $\mathrm{H_{EB}} = (\mathrm{H_{C+}} + \mathrm{H_{C-}})/2$, where $\mathrm{H_{C+}}$ and $\mathrm{H_{C-}}$ are coercive fields at positive and negative field. In most cases the exchange bias field $\mathrm{H_{EB}}$ has an opposite sign to the field cooling field $\mathrm{H_{FC}}$, yet in some systems the

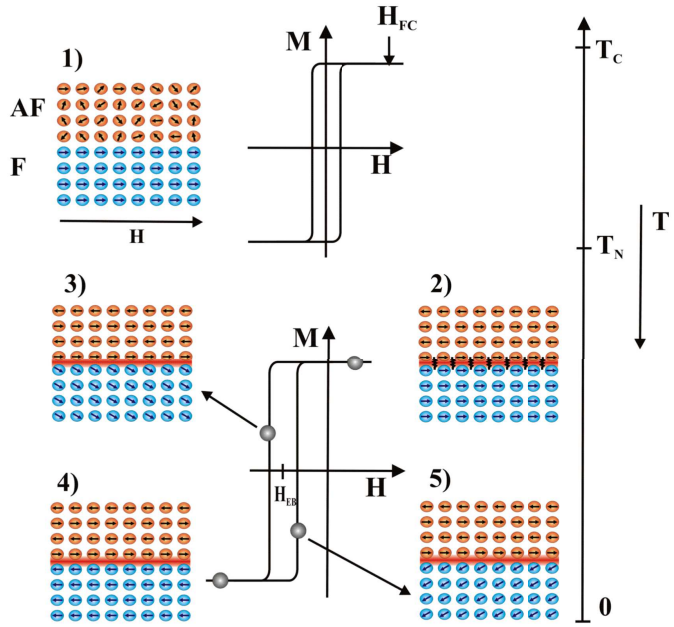

Figure 9.12: **Introduction of unidirectional exchange bias in a FM/AFM bilayer.** Simplified model of E_B with uniform magnetizations, arrows within the circles correspond to magnetic moments. Temperature scale of the system on the left, with the characteristic T_1, T_C and T_N temperatures. Initial state (1) - Magnetically ordered (disordered) FM (AFM) layers leading to a symmetric magnetization loop. The transition from (1) to (2) state is performed through a field cooling procedure (see detailed described in text). In the (2) state at $T < T_N < T_C$ the magnetic exchange interaction between FM/AFM reinforces the coercive field by H_{EB}. The figure is taken from ref [170].

two share the same sign [171].

9.5.2 Exchange bias generated by spin-chains

As discussed in Section 9.4.1 MnPc molecules were reported to form a stabilized AFM spin-chain when deposited on a cobalt substrate. The same AFM spin-chains can exert an exchange bias on the hosting FM substrate after a field cooling procedure as described in the previous subsection, see Figure 9.12. Gruber et al. [156] were able to observe a large exchange bias effect in a Co(20ML)/MnPc(25ML) bilayer. Figure 9.13 unveils the magneto-optical kerr effect (MOKE) measurements performed on this bilayer at different temperatures. The room temperature (RT) magnetization curve in red is symmetric around the origin as $T_N < T < T_C$ and no exchange bias is present at the interface. At RT the MnPc layer is mostly disordered magnetically and exerts no detectable pinning strength on the Co FM substrate. Once a field cooling is performed to $T < T_N$ at $H_{FC} = +0.2T$ (in-plane) the magnetization of the bilayer is altered. The blue magnetization curve is asymmetric and shifted towards negative fields by the exchange bias field. Increasing the

temperature to 58K in green reduces the E_B amplitude.

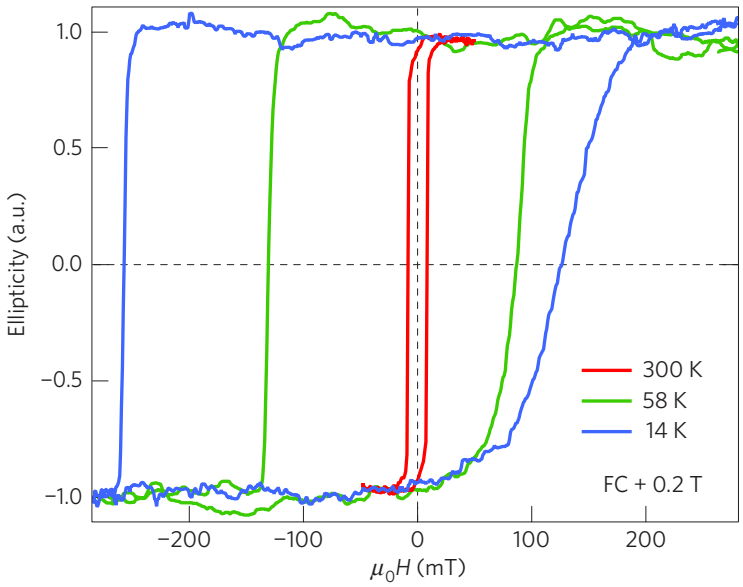

Figure 9.13: **Spin-chain origin of exchange bias in a hybrid FM/AFM bilayer.** Magnetization-field measurement of a Co(20ML)/MnPc(25ML) bilayer at room temperature (red), at 58K (green) and at 14K (blue) upon an H_{FC} = +200mT field cooling. The asymmetrical shifter magnetization at 14K originates from an interfacial exchange bias. Figure taten from ref [156].

9.5.3 Blocking temperature of molecular exchange bias

Gruber et al. [156] reported that the exchange bias effect reached its maximum amplitude at 14K (≈ -60mT) and decreased progressively with an increasing temperature before completely vanishing at 100K its blocking temperature (T_B), as shown in Figure 9.14. Above 100K the unidirectional anisotropy induced by the AFM molecular spin-chains vanishes, yet a fraction of the spin-chain maintains a certain AFM order even at room temperature as discussed in the same paper. A proper manipulation of these effects within a molecular magnetic tunnel junction requires a further understanding of the tight link between the blocking temperature of E_B and the above discussed exchange parameter J of the AFM molecular spin-chains. Remarkably the E_B blocking temperature of 100K is in an almost perfect agreement with Serri's 106K [162] exchange energy (J/k_B) extracted from magnetic susceptibility experiments on alpha 200nm CoPc film on silicon substrate.

Exchange bias in inorganic compounds were reported to have much higher T_B, temperatures well above room-temperature were reported [172, 173]. The current record of T_B in hybrid molecular-ferromagnet systems doesn't exceed 150K [174], hence a room-temperature demonstration of the effect is still lacking. To overcome this complication a more complete understanding of the interfacial AFM/FM exchange bias is needed [175].

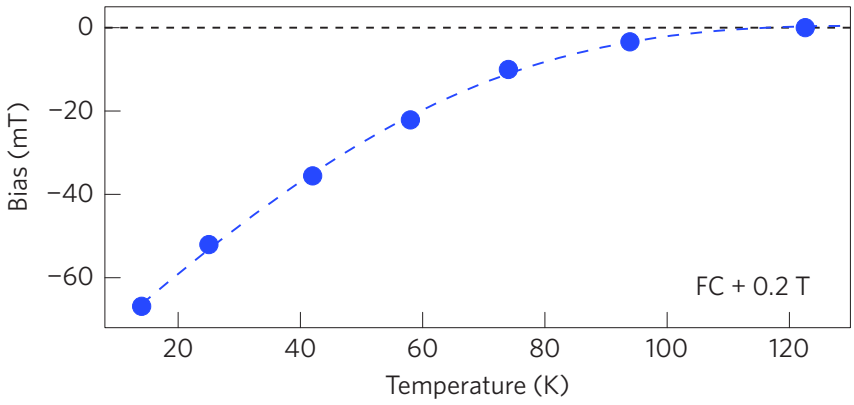

Figure 9.14: **Temperature dependence of Exchange bias generated by MnPc spin-chains.** Each exchange bias value was extracted from a MOKE magnetization measurement after a system reset at 150K. Exchange bias vanished at 100K, its blocking temperature. Field cooling performed in plane to the sample at H_{FC} = +200mT. Figure taken from ref [156].

Mastering and engineering the hybrid interface at the molecular scale could pave the way towards room-temperature molecular exchange bias.

In this section we described the formation of one-dimensional spin-chains out of magnetic transition-metal-phthalocyanine molecules. Thereafter, the antiferromagnetic order governing in these molecular spin-chains was characterized. The generation of an exchange bias field the hybrid ferromagnet-molecular spin-chain interface was also mentioned in detail. The next section describes a more general consequence interfacial interactions taking place in metallic-molecular bilayers, namely the modification of the interfacial spin-polarization and the formation of a new effective interface titles spinterface.

9.6 The rise of spinterface science

The high spintronic performances achievable in fully inorganic magnetic tunnel junctions originate from the spin-selectivity of the tunneling transport channels. This useful property in most cases is ensured by the combination of spin-polarization of ferromagnetic electrodes, the symmetry filtering efficiency of the semiconducting barrier and the proper continuity of wavefunctions at the interface [26]. In this respect, utilizing molecular semiconductors as the spacer of devices enables to overcome this constraint through interfacial absorption of molecular compounds.

9.6.1 Spinterfaces: ferromagnet-molecule interface

When a single molecule is deposited on an inert substrate, for instance gold-Au, the weak interaction regime of physisorption emerges through van der Waals interactions [119]. The interfacial hybridization strength is defined by $\Delta E = | E_F - \varepsilon_{eff} |$, where

$\varepsilon_{\mathrm{eff}}$ is the energy amplitude of shifted molecular energy level and $\mathrm{E_F}$ the Fermi level of the substrate, see Figure 9.15. The physisorption regime is characterized by very low $\Delta\mathrm{E}$, typically in the range of 100meV. In the case of physisorption the electronic structure of the molecule is barely frustrated, $\varepsilon_{\mathrm{eff}} \approx \varepsilon_0$($\varepsilon_0$ is the isolated molecular energy state). On the other hand, when a single molecule is deposited on a highly reactive metallic substrate, the interfacial interactions generates chemical bonds. The molecular orbitals hybridize with the large electronic bands of the metallic substrate, hence, the molecular electronic structure is strongly modified. The chemisorption regime is defined by large hybridization strengths $\Delta\mathrm{E}$, typically $\Delta\mathrm{E} > 1\mathrm{eV}$. The discreate molecular levels are energetically broadened to a finite width $\Gamma \approx \hbar/\tau$, where ($\hbar$) is the reduced Planck constant and τ the lifetime of the hybridized state. In a first approximation, the energy width of the hybridized level Gamma is proportional to the density of state (DOS) of the metal. In FM metals the density of states is spin-dependent ($\mathrm{DOS}^{\uparrow} \neq \mathrm{DOS}^{\downarrow}$), therefore the hybridization of molecular levels will depend on their spin state. As a result, the level broadening and the energy shift are respectively different for each spin population, i.e. $\varepsilon^{\uparrow}_{\mathrm{eff}} \neq \varepsilon^{\downarrow}_{\mathrm{eff}}$ and $\Gamma^{\uparrow}_{\mathrm{eff}} \neq \Gamma^{\downarrow}_{\mathrm{eff}}$, see Figure 9.15.

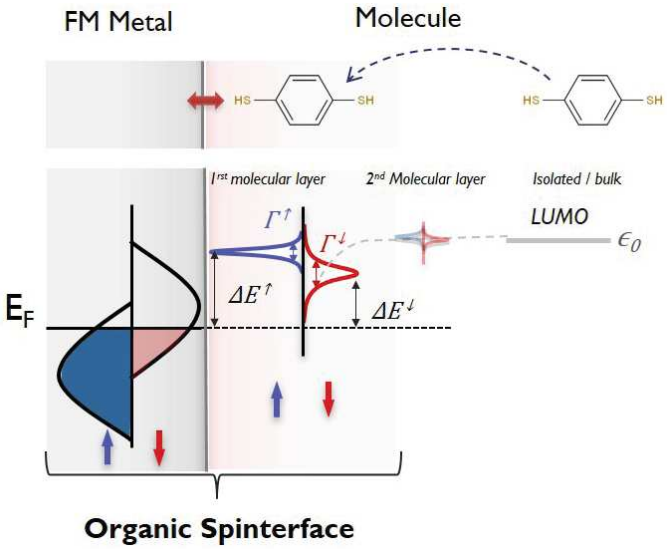

Figure 9.15: **Organic spinterface: spin-dependent interfacial hybridization.** (top) Schematic representation of a free molecule far away from the FM metallic substrate and in contact. (bottom) The respective energy diagram of a free molecule is a discrete the energy state (ε_0. Chemisorption regime between a FM substrate and a single molecule on it. The energy diagram depicts the spin-dependent broadening $\Gamma^{\uparrow} \neq \Gamma^{\downarrow}$, and the hybridization strength $\Delta^{\uparrow} \neq \Delta^{\downarrow}$. The absorbed molecule forms a new effective interface with a new effective spin-polarization, namely a spinterface. Figure adapted from ref [120].

Spinterfaces: ferromagnet-molecule interface

The molecular-ferromagnet hybridization alters the interfacial spin-polarization properties and hence generates a new effective interface entitled "spinterface" [176]. The emergence of a spinterface may entail two opposite effects, i) Enhancement of the raw ferromagnet's interfacial polarization P_{FM} up to P_{int}, resulting in $P_{int} > P_{FM}$, ii) Or the inversion of the interfacial ferromagnet's polarization, resulting in $P_{int} = -P_{FM}$. The mathematic formalism describing these the two effects was first introduced by Barraud et al. [54] and further developed by their group members [120, 177].

In this subsection we summarize the main ingredients of spinterfacial spin-polarization. The inversion of Pint takes place when the energy broadening Γ is much higher than the coupling strength ΔE, i.e. $\Gamma >> \Delta E$, see Figure 9.16.b. This condition is fulfilled when Γ strongly depends ($\Gamma^{\uparrow}_{eff} \neq \Gamma^{\downarrow}_{eff}$) on the spin state whereas ε_{eff} doesn't ($\varepsilon^{\uparrow}_{eff} \approx \varepsilon^{\downarrow}_{eff}$). In this case, the induced molecular DOS has an opposite spin-polarization sign with respect to the FM's SP and is almost in resonance with E_F, see Figure 9.16.a.

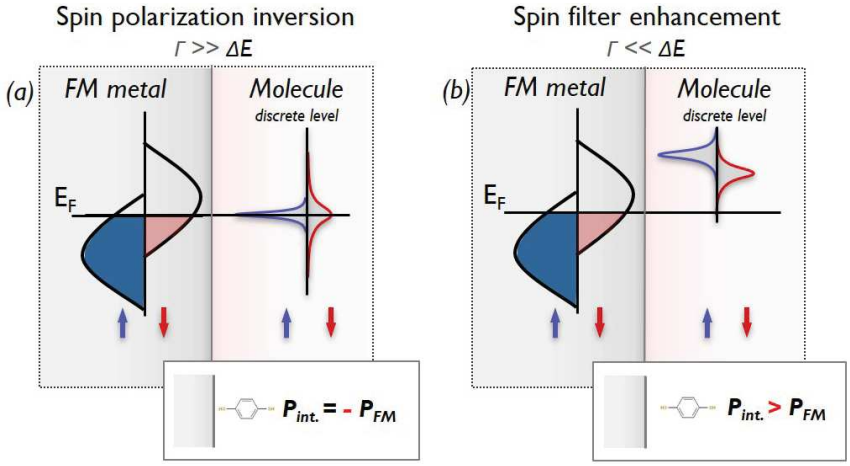

Figure 9.16: **Inversion and Enhancement of the interfacial spin polarization.** (a) $\Gamma >> \Delta E$ - results in the inversion of the raw FM's polarization, hence, $P_{int} = -P_{FM}$. (b) $\Gamma << \Delta E$ - results in the enhancement of the raw FM's polarization, hence $P_{int} > P_{FM}$. Figure reproduced from ref [120].

The enhancement of the SP occurs when the energy broadening Γ is much lower than the coupling strength ΔE, i.e. $\Gamma << \Delta E$. This condition is fulfilled when ε_{eff} strongly depends ($\varepsilon^{up}_{eff} \neq \varepsilon^{down}_{eff}$) on the spin state whereas the Γ doesn't ($\Gamma^{up}_{eff} \approx \Gamma^{down}_{eff}$). In this case, the molecular DOS is positioned above E_F, and can enhance the interfacial spin-polarization by filtering (passing) a single spin-population (spin-filtering effect).

The modification of the interfacial spin-polarization, thus, the appearance of a spinterface is tightly related to the contact geometry, the metal-molecule distance, and the materials of the system with their respective electronic orbitals involved in the hybridization on both sides. The high flexibility of chemical compounds potentially allows to tune the above-mentioned properties and enables the chemical engineering of desired spintronic performances within molecular spintronic devices.

9.6.2 Measuring a Spinterface

A few years after the first demonstration of the organic spin-valve effect [139,140] which is considered as the birth of the organic spintronic field Sanvito et al. [178] predicted from a theoretical standpoint the generation of spinterfaces in FM-Molecular bilayers. The authors performed standard density function theory (DFT) calculation to simulate the spin-resolved interfacial density of states of Nickel-Tricene bilayer as a function of their separation distance. They've observed a progressive spin-split and broadening of the Tricene's molecular orbital states as the distance was decreased, hence the interfacial polarization was modified. The extent and the time frame of this novel work catalyzed the scientific community and paved the way towards the young but very rich field of organic spintronics. The footprint of a spinterface generation in a molecular spin-valve was missing for several years due to the low quality of those early devices. As the processing of organic spin-valves precludes the use of standard solvent-photoresist photolithography, other techniques should be adopted. The first prototypical (vertical) organic spin-valve devices were tailored with simple shadow-masking, hence were pretty large ($\approx 50\mathrm{x}50\mu\mathrm{m}^2$). The low quality of the interfacial molecular-ferromagnet hybridization and the weak homogeneity of the molecular layers ruled out the observation of the spinterface effect within magneto-transport. The interdiffusion of the top electrode within the soft organic material was another limiting factor: this pushed scientists to work with thick organic spacers, which complicated the investigation of spin injection. In 2010, Barraud et al. [54] were able to achieve a tremendous advancement in the miniaturization of organic magnetic tunnel junctions (OMTJs). The vertical miniaturization of devices allowed to shrink the organic spacer and hence achieve a tunneling regime through the organic spacer. The authors utilized the previously reported technique proposed by Bouzehouane et al. [179]. It consists in using an atomic force microscope (AFM) tip to indent the bottom electrode-organic spacer-photoresist stack and deposit therein a nanometer-size top contact. The typical OMTJ processed within the nanoindentation technique is represent in Figure 9.17.a. The authors were able to observe a giant 300% TMR at low 2K temperature in a nanometer size $\mathrm{LSMO}/\mathrm{Alq_3}(2\mathrm{nm})/\mathrm{Co}$ organic MTJ, represented in Figure 9.17.b. The half-metallic manganite $\mathrm{La_2}/3\mathrm{Sr_1}/3\mathrm{MnO_3}$ (LSMO) was used for its almost perfect spin-polarization at low temperatures [180], whereas the 8-hydroxy-quinoline aluminum $(\mathrm{Alq_3})$ molecule was used as it was the most famous organic candidate in the early years of the field. This result is monumental because the high 300% TMR amplitude experimentally observed can't be achieved without the molecular spacer. As tunneling is the dominating transport regime the TMR ratio is proportional, according to Julliere's formalism [4] , to the product of electrodes polarizations. Assuming that the LSMO's polarization is quasi total the cobalt's polarization required to ensure 300% of TMR is much higher than the experimentally reported value [20] Such high polarizations at the cobalt side can only be reached as a consequence of the molecular-ferromagnet hybridization, thus by the presence of a highly polarized a spinterface. This work manifested the high importance of spinterface mediated transport and triggered a further interest to the field.

Over the following few years, momentum began to rise around the direct measurements of organic spinterfaces [151,181–183], especially the ones involving phthalocyanine

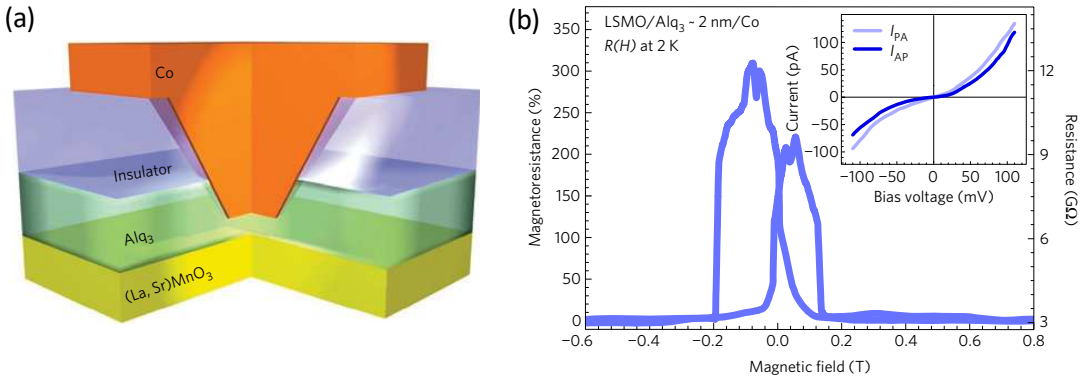

Figure 9.17: **Nanoindentation processes organic MTJ and the resulting giant 300% TMR signal at 2K.** (a) Nanosized $La_2/3Sr_1/3MnO_3/Alq_3/Co$ organic magnetic tunnel junction. (b) Butterfly shape TMR curve provided by magnetotransport measurements at 2K. The high amplitude of the TMR signal evidences a highly spin-polarized transport through a spinterface at least on the Alq_3/Co interface. (Inset) 2K IV transport plots in P and AP configurations as a result of different coercivities of both FM electrodes. Figure taken from ref [54].

molecules. The main weakness of Alq_3 spinterfaces is the geometrical form of this small molecule and the resulting interfacial dipole fluctuations [184]. In this respect, metal-phthalocyanine molecules are more suited to form homogeneous layers, hence facilitate the detection of a more uniform spinterface.

The experimental advancements of Lach et al. [182] on the understanding of the spinterface generation on the atomic level confirmed the previous pioneering works of Iacovita [183] and Brede [151] Referring to Figure 9.18.a, the spin and atom resolved DOS calculations (DFT+Coulomb) of a CoPc-Co spinterface manifests the role of the carbon atoms ring (blue spheres) that forms covalent bonds (blue lines) with the Co substrate. The central molecular Co atom plays a key role in the spinterface's magnetism. A strong ferromagnetic coupling appears between the Co-substrate and the Co molecular center, whereas the ligands form weak AFM coupling with the Co substrate.

In 2013 the direct observation of a highly polarized molecular spinterface at room temperature was reported by Djeghloul et al with Manganese-phthalocyanine (MnPc) molecules56. The authors used spin-resolved photoemission (SRPE) spectroscopy to directly measure the spin-resolved band structure of the Co/MnPc interface. Incorporating ab initio calculations, the authors were able to attribute the high asymmetry of PE spectra at E_F to the presence of a highly polarized spinterface, $P_{int} \approx +80\%$ at Co/MnPc(2-2.6ML), see Figure 9.18.b. The growing number of scientific reports consolidating the understanding of phthalocyanine-based spinterfaces confirmed the pioneering forecasts of Sanvito [176] and Barraud [54] that spinterfaces may arise on hybrid interfaces and can play a key role in organic spintronic devices. The next subsection presents the current state of the art on the magnetoresistance arising in phthalocyanine based organic magnetic tunnel junctions.

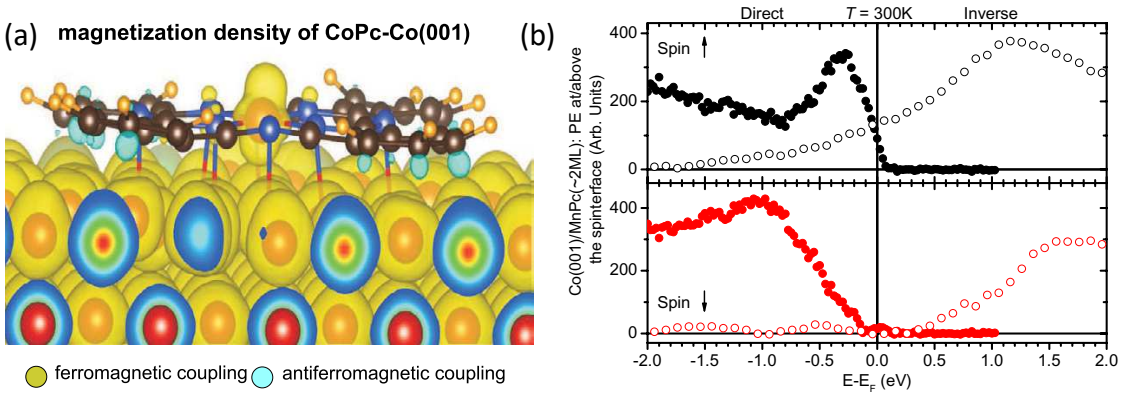

Figure 9.18: **Ab-initio calculations of a CoPc-Co spinterface and the photoemission confirmation of an MnPc-Co spinterface.** (a) Atom and spin resolved DOS calculation (DFT + coulomb interaction - U) of a CoPc molecule atop of Co(001). Ferromagnetic coupling arises between the Co substrate and the central molecular Co-center, ligands form weak AFM coupling. (b) Direct photo-emission (PE) spectra of a MnPc-Co spinterface, closed (open) symbols stand for the direct (inverse) PE spectra. The interfacial band-structure is dominated by the majority channel, leading to $\mathrm{P} \approx +80\%$. Figure taken from refs [53, 182].

9.7 Phthalocyanine based magnetotransport

In 2015 Barraud et al reported nanosized MTJs with a thin CoPc spacer and Co electrodes [185] employing the previously described nanoindentation technique. A unidirectional magnetic anisotropy generating a tunneling anisotropy magnetoresistance (TAMR) effect was observed upon field cooling in these devices. A careful examination of these results is very useful for the proper description and interpretation of our experimental results on similar phthalocyanine based devices.

9.7.1 Unidirectional tunneling anisotropy magnetoresistance

The low temperature transport measurements indicate that tunneling is the dominating transport regime. Therefore, the magnetoresistance signal of these devices is described within the two-current formalism of Julliere [4]. The low T (2K) magneto-transport measurements performed at the direction of $\mathrm{F_C}$ ($0°$) emphasize the induced anisotropy present in the system. Referring to Figure 9.19.a, the saturation resistances at $\pm 1\mathrm{T}$ in the parallel configurations $\mathrm{P_1}$ in same direction as $\mathrm{H_{FC}}$ and $\mathrm{P_2}$ opposite in direction to $\mathrm{H_{FC}}$ are respectively different at $32\mathrm{G}\Omega$ and $30\mathrm{G}\Omega$. As the transport mainly takes place through spin-polarized tunneling this asymmetry of $\mathrm{P_1}$ and $\mathrm{P_2}$ resistances originates from the induced anisotropy of the spinterface. As a consequence it was attributed to an TAMR effect. This effect originates from the $\mathrm{F_C}$ procedure, when a spin-reference is established within the CoPc layers. Under the imposed unidirectional spin reference i.e. external magnetic

field the fraction of ordered CoPc spin-chains are aligned.

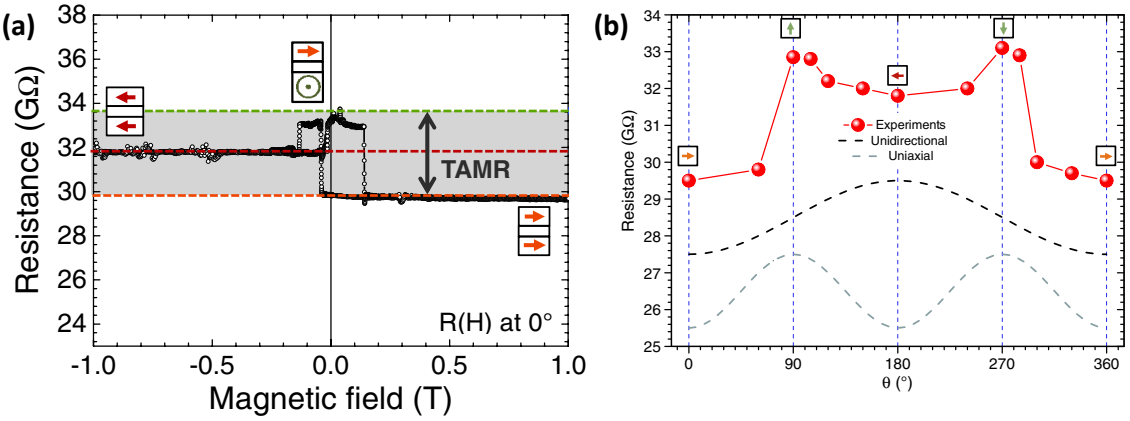

Figure 9.19: **Anisotropy term within low temperature magnetoresistance measurement and its angular dependence.** (a) Low T = 2K magnetotransport measurement at Vbias = -200mV and $0°$ of external field, upon a +0.1 T ($0°$) FC procedure. The parallel resistances P_1 and P_2 are different (description in the text). TAMR effect is defined between the two extremum resistance states at $0°$ and $90°$ ($R90°$ green dotted line, dataset not presented here). (b) Angular dependence of the P_2 resistance state - unveils the combination of a unidirectional and uniaxial anisotropy terms in the TAMR effect (description in the text). Figure taken from ref [185].

The angular dependence of the device's resistance in P state at +2T unveils its anisotropic behavior containing two main components, see Figure 9.19.b, i) Uniaxial term - attributed by the authors to the magnetization of Co electrode, ii) Unidirectional term - attributed to the unidirectional anisotropy of hybrid interfacial states, thus similar to the footprint of a spinterface. The assignment of the unidirectional anisotropy term to an interfacial origin requires a temperature study, since analysing its blocking temperature can reveal its interfacial (by exchange bias) or spin-chain (structural order) origins. A careful comparison of the temperature behavior of the unidirectional term to the blocking temperature of the interfacial exchange bias effect reported by Gruber et al. [156] could reinforce its interfacial attribution. In the results Chapter 10 we discribe a temperature study of similar unidirectional magnetoresistance effects. Barraud et al. [185] discuss the spin polarization of the two spinterfaces $SP_{Co/CoPc}$ and $SP_{CoPc/Co}$ In their Co/CoPc/Co nanopillar in terms of the TMR signal detected at $90°$ magnetoresistance curve (not shown here). A TMR signal of -20% indicates that the hybridization taking place at the two phenomenologically equivalent interfaces is different to the point of generating opposite spin-polarization at $SP_{Co/CoPc}$ and $SP_{CoPc/Co}$ (within Julliere's formalism). As discussed previously the SP developed on the spinterface is tightly related to the interfacial hybridization and the contact properties, hence the two interfaces should be of different quality (this issue is well-known in the community of organic spintronics).

9.7.2 Spin-flip excitations in phthalocyanine devices

The electrical excitation of molecular chains was reported by Barraud et al. a year later [186]. Spin-flip excitations along molecular spin-chains were observed in MnPc based MTJs. Using the same nanoindentation technique Barraud et al. were able to craft a nanoscale junction of the following structure $\mathrm{Co/H_2Pc/MnPc/Co}$. The insertion of a thin (1 nm) layer of $\mathrm{H_2Pc}$ at the bottom interface enables a magnetic decoupling while maintaining a molecular hybridization. Having a top MnPc/Co interface gives eventually rise to both a spinterface formation and magnetic interaction such as exchange bias.

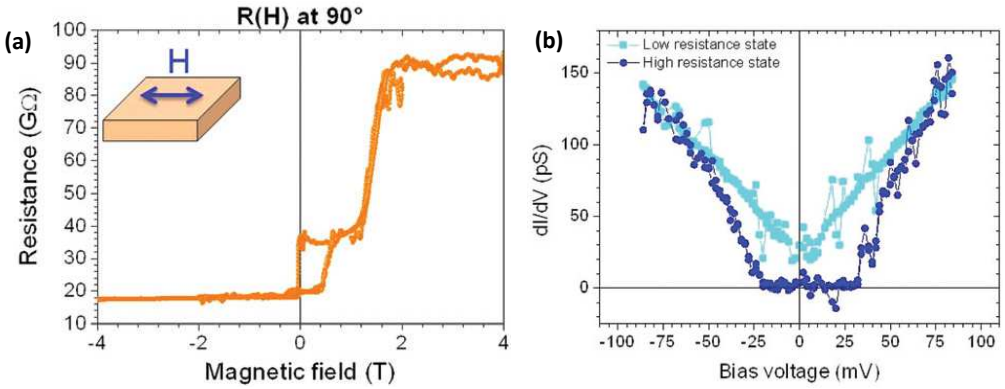

Figure 9.20: **Magnetoresistance at the corresponding conductance.** (a) Magnetoresistance measurement performed at $90°$ (upon an $0°$ FC). (b) Conductance curve for the low and high resistance states. Figure taken from ref [186].

In such a way, this hybrid molecular MTJ with a single magnetically interacting interface serves as a 'simpler' example to apprehend the different physical effects arising in such novel devices. Upon field cooling, at low temperature (2K) the magnetotransport measurement reveal two resistance states for the two opposite parallel configurations: a low resistance state at negative fields and a high resistance state at positive fields, referring to Figure 9.20.a. As discussed previously in Section 9.4, the conductance measurement of the device can inform about the opening of additional inelastic channels. Referring to Figure 9.20.b, the conductance the low resistance state is of a "V" shape and doesn't present any noticeable features, whereas the conductance in the high resistance state demonstrates a "jump" at around $\pm 25\mathrm{mV}$. This jump is interpreted as corresponding to the opening of a spin-flip excitations channel along the MnPc spin-chains. The threshold value of 25mV is in good agreement with the value of 17meV reported by Hirjibehedin et al. measured on a trimer AFM chain of Mn atoms [187]. Comparing the threshold value of STM experiments on single spin-chain with the threshold values extracted from transport measurements on junctions enveloping thousands of inhomogeneous chains has to be done in a careful manner.

From a theoretical standpoint, the opening of the spin-flip excitations channel above the threshold voltage $\mathrm{V_{th}}$ should act as a spin-filter [152, 187, 188]. The spin-population that can execute the spin-excitation on the spin-chain is dictated by the transition's selection

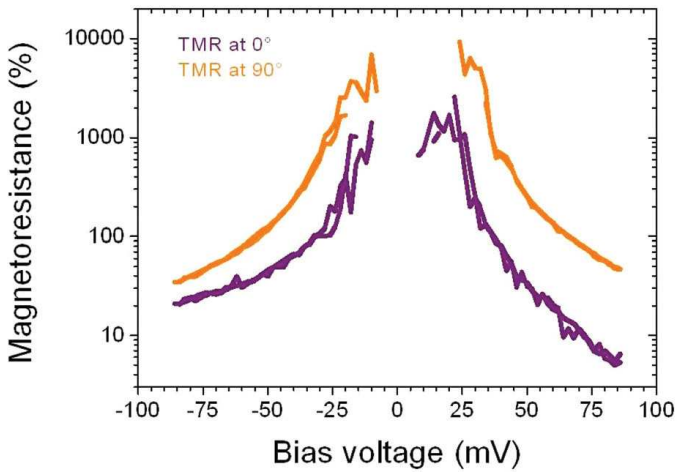

Figure 9.21: **Magnetoresistance-bias voltage evolution at 2K for both magnetic field directions.** Figure taken from ref [186].

rules. Within a two-current model, the inelastic channel can be opened only by one spin population, hence, should lead to a high spin-polarized transport channel which enhances the spintronic performances of the organic device. Barraud et al. [186] observed a huge MR effect in their sample, as represented in Figure 9.21. Yet alone, the opening of the inelastic channel above $\pm 25\mathrm{mV}$ doesn't seem to increase the TMR signal, hence increase of the effective spin-polarization of the tunneling current. A clearer picture of the spin-flip excitations effect on the magnetoresistance in phthalocyanine based junctions will be depicted in the following results section.

Chapter 10

Spin-flip excitations driven magnetoresistance

10.1 Research motivations

In the previous introductory section, we've introduced phthalocyanine molecules, both their magnetic and electric properties and the magnetotransport effect they elicit. This section is entirely devoted to our experimental efforts to disclose the physical phenomena in MPc-based magnetic tunnel junctions. The main goal of this project was to broaden the current understanding of phthalocyanine-based organic devices [185, 186, 189–192], demonstrate their potential and catalyzer the interest towards the field organic spintronics.

Herein, we propose a description of an effect that enables an active control over the magnetoresistance response of the device through an electric field. We observe that a spin-polarized current flowing through the spin-chains embedded in a magnetic tunnel junction is able to excite the chain, perturb the AFM order within the chain and therefore change the magnetic interactions within the sample. The footprint of this latter effect is observed in the magnetoresistance response of the molecular-based MTJ device, and its operation will be discussed in details in this chapter.

10.2 Thin Hybrid Films

10.2.1 Growth of thin layers

The fabrication of ultra-thin structures begins with a high quality, smooth and clean substrate. In that respect, we've used commercial grade Si/SiO_x substrates that were cleaned by acetone, ethanol and isopropanol in an ultra-sonic resonator. A further cleaning is performed by "soft O_2" + plasma. The preliminary procedure gives a clean and smooth surface of 0.2nm RMS roughness. Substrates are then introduced into our team's hybrid multichamber cluster. The deposition of the whole functional junction's stack on the Si/SiO_x wafer, namely "Cr(5)/Fe(50)/CoPc(20)/Co(10)/Cr(5)" (numbers in nm) is performed through a shadow mask that patterns the shape of a common bottom electrode for all of the future junctions. The fabrication of ultra-thin structures was carried out by PhD colleague E. Urbain. The architecture of the multiple junctions sharing the similar common bottom electrode is described in the lithography Section 5.1.1. All of the metallic layers of Cr, Fe and Co are deposited by custom made DC magnetron sputtering with the wafer held at room temperature. The thickness of the deposited layers is calibrated with a a quartz microbalance, cross-checked by grazing incidence x-ray reflectometry, while the morphology was inspected by atomic force microscopy (AFM) measurements [193]. The deposition of CoPc molecular layers is performed by thermal sublimation in an organic molecular beam epitaxy (OMBE) setup which is connect in-situ with the sputtering chamber. Prior to the deposition the commercial CoPc powder is purified by sublimation and re-condensation by several cycles. Cross-section measurements on a reference not patterned wafer follow-up the deposition of the multilayer structure. For instance, conductive tip AFM studies on the molecular layers give insight into the holes present in the organic layers upon thermal sublimation. An interested reader may question about the nominal 20nm thickness of CoPc used in our devices: it was defined according to the AFM surface studies (not shown here) indicating holes up to 5-8nm deep. Therefore, to avoid shot-circuited junctions the thickness of CoPc was increased up to 20nm. An efficient approach to further miniaturize the organic spacer is to decrease the diameter of the pillar so as to to minimize the chances of retaining holes within the surface of the junction's pillar, or by changing the deposition protocol of the top electrode [194]. Magnetometry studies performed on the same reference wafer give an insight on the magnetic and therefore structural quality of the deposited thin multilayer structure.

10.2.2 Magnetic characterization of thin films

Magnetotransport measurements require sharp parallel (P) and anti-parallel (AP) magnetic configurations. The choice of different materials and their respective thicknesses was dictated by the decoupling requirement; hence this property of the Fe/CoPc/Co stack was confirmed through low temperature (2K) SQUID magnetometry measurements, presented on the Figure 10.1. The two ferromagnetic electrodes Fe(50nm) and Co(10nm) are magnetically decoupled and exert the respective coercive field $H_C \approx 850Oe$ and $H_C \approx 30Oe$.

As a note of mention, no detectable E_B is observed within these measurements since

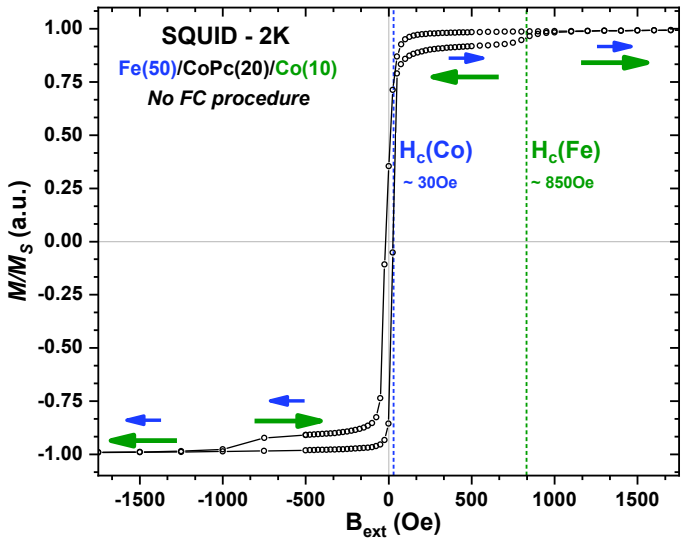

Figure 10.1: **Low temperature SQUID measurement on the Fe/CoPc/Co hybrid trilayer.** Both of the FM-electrodes are decoupled and have different coercive field, Fe (blue) ≈ 850 Oe and Co (green) ≈ 30 Oe. No external magnetic field was applied during the cooling procedure preceding to these measurements. Measurements performed at 2K.

the cooling was performed without an external magnetic field. In Section 10.4.1 the effect of field cooling on this structure in processed MTJs will be discussed. The decoupling of the FM electrodes informs us that this multilayer thin stack can serve to define magnetic tunnel junctions as we describe in the next section.

10.3 Nanosphere lithography process

Processing molecular MTJs is a challenging task considering the rational restriction to use solvents and photoresist as they may degrade the molecular layers, hence the standard photolithography process cannot be used. The field has thus been almost entirely restricted to the study of macroscale junctions. As an exception that was discussed previously, the nanoindentation technique, is a dry process technology which allows the manufacture of nano-scale junctions without solvents. Yet, the technique tends to be complicated to set up and to further obtain reproducible junctions as a result of structural damage to organic layer and exposure of ultrathin layer to air. Inspired by Wang et al. [195] who presented a novel a nanosphere lithography process overcoming these technological issues, our PhD colleague E. Urbain adapted the technic to craft organic MTJs [193]. It consists in using nanospheres as shadow masks to tailor the nanopillars, thereby bypassing the utilization of photoresists or solvents. In order to tailor molecular MTJs, we've used a combination of standard shadow mask depositions for the multi-layer structure and nanosphere shadow masking for the definition of pillars, the lithography steps are represented on Figure 10.2.

The main steps of the nanosphere lithography process of molecular MTJs:

I. Deposit the nanospheres on the surface of the sample (*) and cover the square pads of the bottom electrode with kapton tape. Figure 10.2.b **II.** Use ion etching to tailor the nanopillars protected by the shadow-masking nanospheres. Figure 10.2.c **III.** Deposit a passivation layer of SiO_2. The passivation layer serves to electrically decouple the parallel pillars with the same common bottom electrode. Figure 10.2.d **IV.** Remove the nanospheres with an N_2 gun, and the kapton tape. Figure 10.2.e **V.** Deposit through a proper shadow mask the top metallic contact of Al/Au serving as pads for wire bonding, hence electrical measurements. Figure 10.2.f

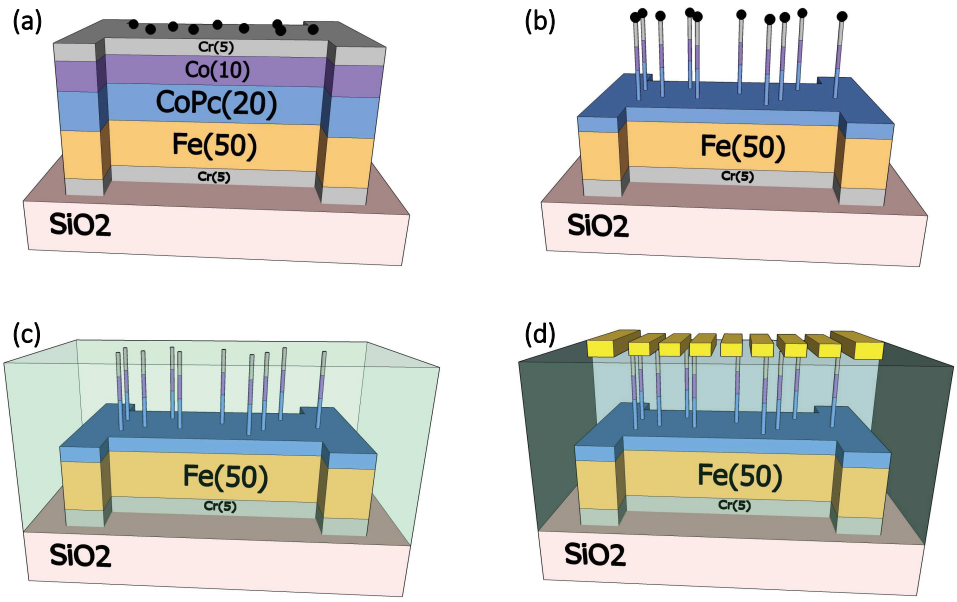

Figure 10.2: **Nanosphere lithography process of molecular submicronic molecular MTJs.** The consecutive process steps (a) to (d) are described in the text above.

In such a way, a single common bottom electrode (step.1) can incorporate up to 20 pillars, and this number is solely limited by the size of the top contacts deposited through a shadow mask too (step.6). The lateral size on pillars is tightly related to the size of the nanospheres used for the patterning of pillars and the geometry of the ion etching. The experimental results on molecular MTJs were acquired on pillars of approximatively 500nm width.

The two main challenges of this technique are: i) to deposit the nanospheres in a controlled manner on the surface of the sample (step.2). ii) to align the top contacts with respect to the tailored pillars. The first prototypical depositions of spheres were performed by simple mechanical manner(using vibrations), thus were rather uncontrolled. The current upgraded version of the nanosphere deposition setup incorporates a x, y, z-axis controlled nano-pipette tool enabling the depositing of nano-droplets of a highly diluted nanosphere solution, hence a single sphere deposition can be achieved.

10.4 Low temperature magnetotransport of Fe/CoPc/Co submicronic junctions

The most important aspect of any transport measurements studies is a proper definition of the main transport mechanisms taking place in the device. A temperature and (or) thickness study of the device's transport may give insight on the transport mechanisms taking place through the semiconducting spacer of the junctions. Nominally the molecular CoPc layer is of 20 nm thick. Yet, this thickness is nominal as a result of the unavoidable interdiffusion of the top electrodes heavy atoms within the soft molecular layers. This is a well-known issue of organic spin-valves fabrication. To determine the transport mechanism, we therefore rely purely on experimental observations. The magnetotransport effects discussed in this chapter were acquired on a single Fe/CoPc/Co MTJ device, yet they were repeatedly reproduced with different degrees of similarity in same and similar structures of CoPc-based MTJs. To retain a clean and complete discussion we deviced to restrain to this dataset, it is characterized by all of the observed magnetotransport features and is of good quality excluding any trivial artefacts. The topic of molecular spintronics continuous to be investigated in our group, and more details could be found on this topic in the following years. At room-temperature the resistance of this junction is relatively small ($\mathrm{R_{300K}} = 32\mathrm{k}\Omega$), whereas at low 17K the resistance increased by an order of 10^4 and reached $\mathrm{R_{17K}} = 10\mathrm{G}\Omega$. Such a huge temperature dependent increase of resistance implies that the main transport mechanism is thermally assisted hopping, which is in principle destructive for spin-polarized transport through the 20nm CoPc spacer. The observation also hints that most likely the magnetoresistance signals detected in this junction originate from the hybrid FM-Molecular interface rather than from a standard injection-detection of spin-polarized current between FM electrodes.

10.4.1 Field cooling: crafting the junction's magnetism

The measurement schematics is depicted in the inset of Figure 10.3. Therein a bias voltage is sourced to the measured junction and the current drop is measured by a Keithley amperemeter. In such a way, at a positively sourced voltage, electrons are traveling from the bottom Fe electrode towards the top Co electrode, through the CoPc layers. An interested reader can find a brief description of the transport setup used during these measurements in the complementary Chapter 11.

As discussed previously, the field cooling procedure crafts the interfacial magnetism of FM electrodes and the molecular in contact with them. The field cooling procedure is performed within the sample plane and parallel to the bottom electrode (long stripe) at $\mathrm{H_{FC}} = -1\mathrm{T}(0^\circ)$, see the Figure 10.3. The field cooling procedure starts at room-temperature and finishes at low 17K, In Figure 10.3, we the temperature dependence of R, which indicates a mostly linear increase of R when T goes down. As we will see in the following Section 10.4.2, the singularity of device's transport at $\mathrm{V_{bias}}$ = 100mV complicated the interpretation of its temperature-resistance dependence represented in Figure 10.3. A complete FC study on nominally the same junction (Fe/CoPc/Fe) can be found in the

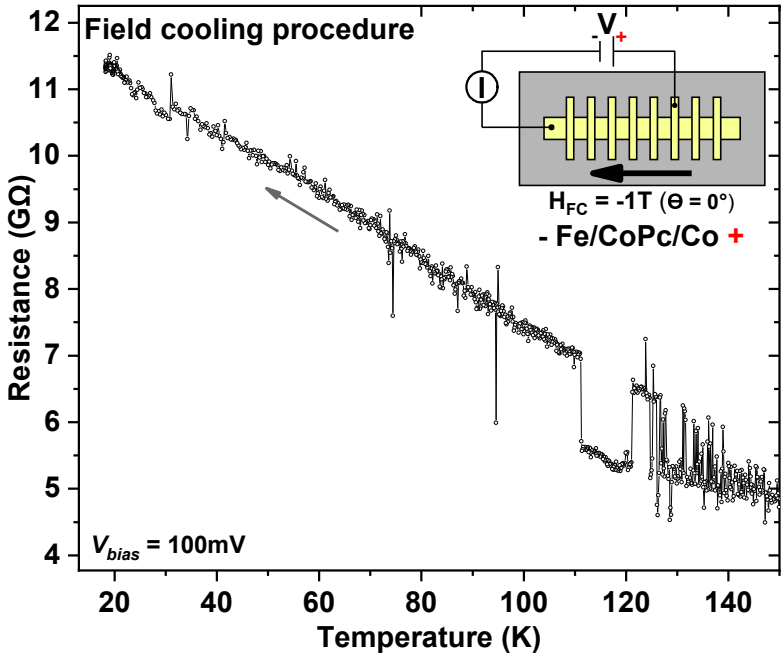

Figure 10.3: **Field cooling of the Fe/CoPc/Co junction.** Linear increase of the resistance with decreasing temperature performed at $\mathrm{V_{bias}} = +100\mathrm{mV}$ and $\mathrm{H_{FC}}$ = -1T (0°). Inset: Schematics of the measurement setup, bias voltage sourced, and current drop measured along the device. At $\mathrm{V} > 0$, electrons flow from bottom to top.

complementary Section 11.8, it indicates that the thermal hopping is likely to dominate transport and that the device undergoes a magnetic rearrangements during FC procedure.

10.4.2 Two-channels transport

Upon field cooling, the first transport measurement performed at low 17K temperature are characterized by three main features, see Figure 10.4: i) the raw measured IV (black) isn't centered at the origin of the graph, characterized by a current offset, $\mathrm{I_{offset}} \approx -4.35\mathrm{pA}$ (blue). The offset has a purely technical origin and is related to the low-resolution of the lowest 100pA range of our 2636 Keithley. Therefore, we can shift remove $\mathrm{I_{corr}}$ from all measurements, and obtain the corrected current $\mathrm{I_{corr}}$ curve in red. ii) The raw IV has an opening that is related to the charging and discharging of the device and to voltage-heating, hence changing the bias voltage step changes the opening in IVs. iii) Both the raw (black) and corrected (red) IVs have two slopes, the first one at the low $\pm 50\mathrm{mV}$ bias zone, and second one appearing above this threshold values. The first two features (i) and (ii) will be omitted in the results interpretation, and solely the third (iii) feature of the two IV slopes will be carefully examined. In what follows, all of the presented experimental dataset will be corrected by the same current offset, $\mathrm{I_{corr}}$.

To further analyze the two slopes observed in the transport measurements we calculate

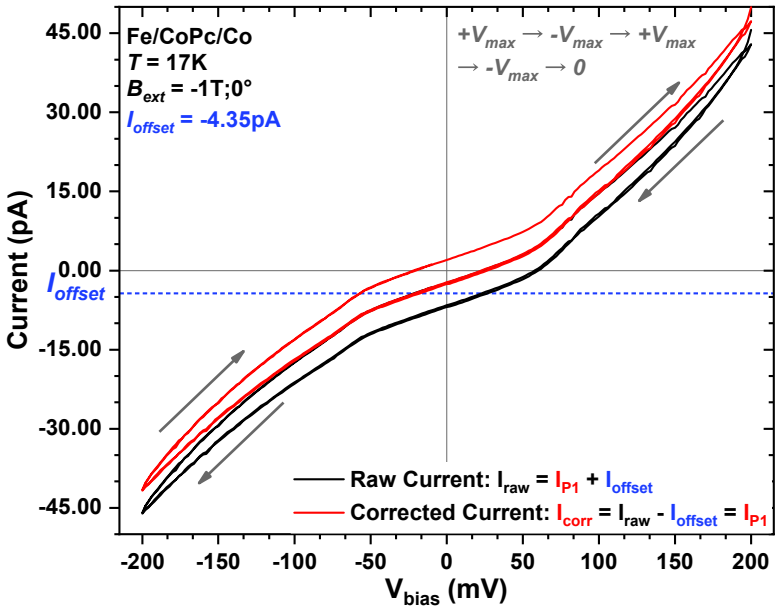

Figure 10.4: **Current vs bias voltage (IV) measurements at 17K and at -1T field** ($0°$). Black - raw IV measurement containing a current offset (blue) of around -4.35pA. Red - corrected IV measurement without the current offset. The consecutive $+\mathrm{V_{max}} \rightarrow -\mathrm{V_{max}} \rightarrow +\mathrm{V_{max}} \rightarrow -\mathrm{V_{max}} \rightarrow 0$ bias voltage swipes overlap, with $\mathrm{V_{max}} = 200\mathrm{mV}$.

the conductance dIdV based on the corrected IV measurement $\mathrm{I_{corr}}$. The conductance dIdV represent in Figure 10.5 clearly indicates an opening of an inelastic channel at voltage threshold value $\mathrm{V_{th}}$ of approximatively $\pm 55\mathrm{mV}$. The red dIdV is the raw derivative of the IV curve at -1T, whereas the blue curve corresponds to the smoothed dIdV with a 5-point moving-average.

Taking into consideration the IETS-STM experiments performed on molecular chains of CoPc [163] and on other atomic chains [187] we recognize the footprint of spin-chains excitations effects described in Section 9.4. In the low bias region, $-\mathrm{V_{th}} < \mathrm{V_{bias}} < +\mathrm{V_{th}}$, the transport takes place though the ground state of the spin-chains, as in this specific region the conductance dIdV almost perfectly increases linearly Figure 10.5. As soon as the bias voltage reaches the threshold value ($\mathrm{V_{th}} \approx \pm 55\mathrm{mV}$) a sharp increase in current provokes a prompt dIdV increase. The "jump" is interpreted as the opening of an additional inelastic transport channel corresponding to the spin-flip excitation the spin-chain. The inelastic channel's opening i.e. the dIdV sharp slope is pretty much symmetric in voltage and $\mathrm{V_{th}}$ is the same for both voltage polarities. However, the amplitude of the dIdV's jump is rather asymmetric: it is lower for $\mathrm{V} < 0$ (dIdV $\approx$ 200pS) and higher for $\mathrm{V} > 0 (\mathrm{dIdV} \approx$ 250pS). This may arise from the different spin injection at both sides of the junction, since both electrodes are composed of different ferromagnetic materials and the structural quality of the interfaces may also differ. In what follows we will refer to the low-bias transport channel as the ground-state and respectively the high-bias (inelastic channel,

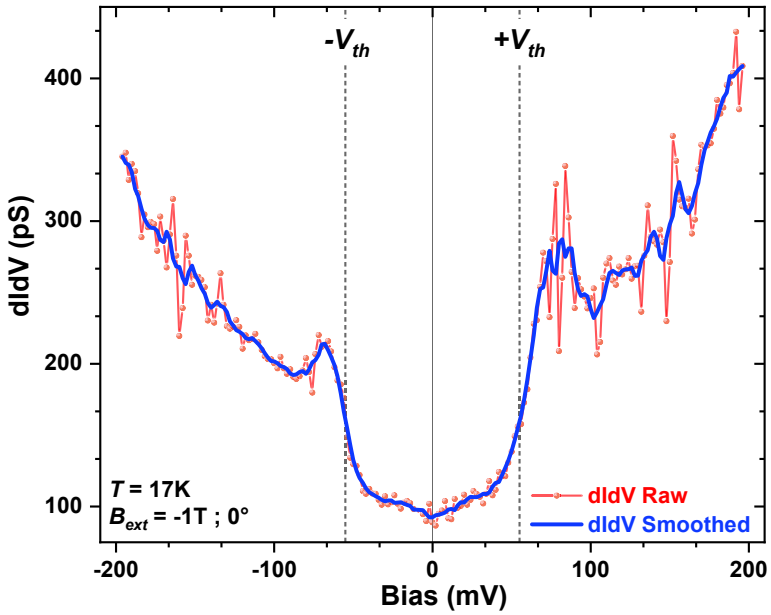

Figure 10.5: **Calculated conductance dIdV at 17K.** Red dIdV is directly calculated derivative of IV, whereas the blue dIdV is smoothed with a 5-point moving average. Flat low bias region: $-\mathrm{V_{th}} < \mathrm{V_{bias}} < +\mathrm{V_{th}}$, the conductance is flat. Above the threshold bias voltage $\mathrm{V_{th}}$, $\mathrm{V} > \mid \mathrm{V_{th}} \mid$ a jump in dIdV corresponds to the opening of an inelastic channel.

$\mid \mathrm{V} \mid > \mathrm{V_{th}}$) as the excited-state channel. In the ground state the different spin-chains of CoPc maintain a natural AFM order, whereas once the spin-chain's excited state is attained the AFM order is frustrated at one or more magnetic centers. The next section describes in detail the different spin-flip excitations that can take place along molecular spin-chains in a nano-scale device.

10.4.3 Spin-flip excitations of CoPc spin-chains

Taking into consideration the lateral size of the junction, $\mathrm{d_{pillar}} \approx 500\mathrm{nm}$ and the 20nm thickness of the CoPc layer the length of CoPc spin-chains isn't necessarily homogeneous. Within a simplified system there may be three types of CoPc molecular chains with their respective transition rules:

1) Single "free" CoPc molecules, with a total spin $\mathrm{S_C} = 1/2$ (ground-state). The spin-flip event on the Co-atom corresponds to the transition: $\Delta\mathrm{s}$ = +1 and $\Delta\mathrm{m}$ = -1 that can be ensured performed only by spin-down electrons. Here $\Delta\mathrm{s}$ and $\Delta\mathrm{m}$ correspond respectively to the spin-state and to the spin-moment transitions on the CoPc's Co atom.

2) Even chains of CoPc molecules are reduced to the same spin-flip scenario as single free CoPc molecules, thus can only be excited by the spin-down electrons .

3) Odd chains of CoPc molecules, with the total chain's spin-moment $\mathrm{S_C}$ = 0 (ground-state). The spin-flip excitation event on the Co atom corresponds to the transition: $\Delta\mathrm{s}$ =

+1 and $\Delta m = +1$. This excitation can be ensured only by spin-up electrons.

According to the CoPc spin-chain length (odd or even), the spin-selection rules are different therefore the spin population allowed to participate in the spin-flip excitation is different. A peculiar IETS-STM study on the same exact molecular stack, and a further control over the spin-chains on a molecular level is required to identify the exact spin-flip transition taking place in such molecular junctions. Omitting the unknown exact spin-flip transition along the molecular CoPc chains and which spin population is involved, the magnetotransport measurements reveal an effect on the spin-excitation of the magnetoresistance of the molecular device. The description of this intriguing effect will be done in the following section.

10.5 Magnetoresistance controlled by spin-flip excitations of molecular spin-chains

The magnetotransport description will be done within the framework of the previously evoked transport channels, namely the ground and excited spin-chain state transport channels. Magnetotransport measurements in the low voltage bias region, in the ground state of the spin-chains are characterized by a low negative MR signal, as represented in Figure 10.6.

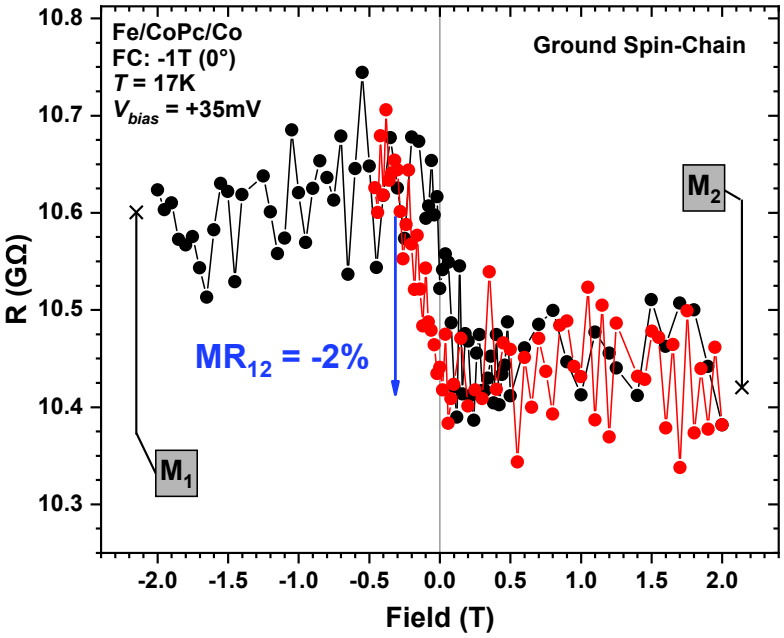

Figure 10.6: **Magnetotransport measurement performed at V_{bias} = 35mV (17K).** Low signal of $MR \approx -2\%$. Spin-chains of CoPc are in their ground-state at $V < V_{th}$.

The device's resistance response in its prepared by $H_{FC} = -1T$ M_1 magnetic config-

uration state is higher than the reciprocal saturation resistance in$\mathrm{M_2}$ at +2T. The weak negative $\mathrm{MR_{12}} = -2\%$ (in blue) is defined between the resistances levels of $\mathrm{M_1}$ and $\mathrm{M_2}$ configuration states. The relatively low amplitude of the $\mathrm{MR_{12}}$ signal implies that the charge carrier transport taking place through the CoPc spacer isn't highly spin-polarized or (and) that the interfacial spin-polarizations are weak. The latter is less probable since the spinterface's presence was widely reported in similar systems [53, 156, 186, 196]. A note of mentio to clarify the future MR terms discussion: i) The MR signal between the two resistance levels in the spin-chain's ground level ($-\mathrm{V_{th}} < \mathrm{V} < +\mathrm{V_{th}}$) will be always denoted $\mathrm{MR_{12}}$ since we compare the resistance between the device's $\mathrm{M_1}(-2\mathrm{T} < \mathrm{B_{ext}} < 0)$ and $\mathrm{M_2}(0 < \mathrm{B_{ext}} < +2\mathrm{T})$ magnetic configurations, ii) In the excited spin-chain's state at $|\ \mathrm{V}\ | > \mathrm{V_{th}}$ as we will see in Section 10.5.3 $\mathrm{M_{12}}$ won't be discussed anymore since other effects therein discussed would appear. The remaining unanswered question is whether or not molecular spin-chains play a role in this low MR signal. In what follows a detailed angular study of this MR effect will clarify this aspect.

10.5.1 Unidirectional magnetic anisotropy

As we've discussed previously, upon field cooling the AFM spin-chains introduce a unidirectional anisotropy into the system, and according to the angular dependence of the MR term it is mediated by a unidirectional component, see Figure 10.7.

The MR signal exhibits a unidirectional behavior which hints towards an interfacial origin. The $\mathrm{p_z}$ orbitals of the CoPc molecules undergo a strong hybridization with the d-states of the Fe-atoms, the hybrid molecule-metal states are anisotropic which is at the origin of the MR term we detect in the Fe/CoPc/Co junction. The two main arguments that are in favor of the interfacial MR origin are:

1. The linear device's IV response in the $-\mathrm{V_{th}} < \mathrm{V_{bias}} < +\mathrm{V_{th}}$ bias-range, and the huge increase of resistance under a decreasing T, $\mathrm{R_{17K}}/\mathrm{R_{300K}} \approx 10^4$, implies that thermally activated hopping is the dominant transport mechanism rather than tunneling. Therefore we propose to exclude spin-polarized transport through the device at first glance out of the MR interpretation and tend towards an interfacial interpretation.

2. When one of the ferromagnetic electrodes is replaced by diamagnetic Copper electrode a single magnetic molecular-ferromagnet interface is present within the device the same unidirectional MR detected in the devices magnetotransport. See Figure 10.8 describing magnetotransport measurements on a Cu/CoPc/Fe molecular junction. This effect has also been seen on a Co/CoPc/Cu junction [120].

Interfacial magnetoresistance (IMR) effect was reported in hybrid molecular-ferromagnetic systems [144, 185, 186, 197]. The first CoPc molecular layer is completely absorbed on the Fe surface and the second CoPc molecular layer acts as a spin-filter [118, 152, 188]. The spin-filtering molecular layer is seen by the incident charge carriers as a spin-dependent energy barrier that gives rise to an interfacial spin-dependent resistance. In this respect, the magnetic reversal of the Fe layer will provoke a resistance change which defines the IMR effect.

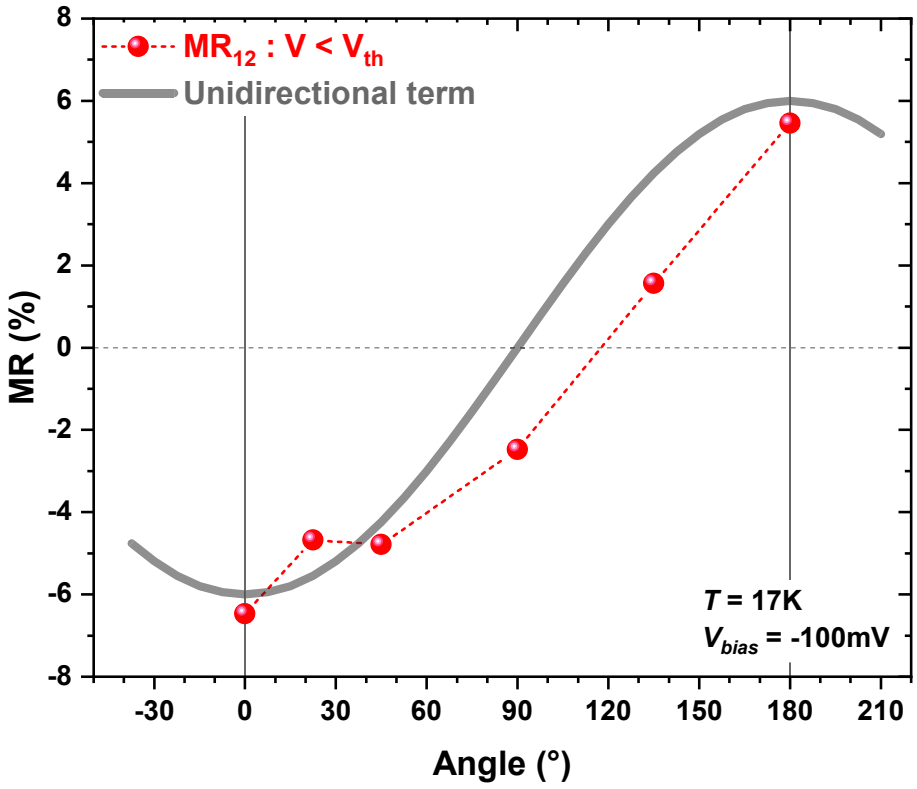

Figure 10.7: **Angular variation of MR** ($\mathrm{V} < \mathrm{V_{th}}$) **and a typical unidirectional term.** Each point was extracted from an RH measurement at the respective angle of applied external magnetic field.

Magnetic anisotropy of Cu/CoPc/Fe devices

Moreover, upon replacing one of the FM electrodes by a diamagnetic copper electrode, we still detect the same IMR effect, but this time with a single magnetic interface embedded within the device. Referring to Figure 10.8, low temperature magnetotransport upon -1T field cooling in a Cu(50)/CoPc(16)/Fe(10) (numbers in nm) junction exhibit a weak negative $\mathrm{IMR} \approx -0.85\%$.

The change in the resistance between $\mathrm{M_1(B_{ext} < 0)}$ and $\mathrm{M_2(B_{ext} > 0)}$ device's magnetic configurations can only originate from the reversal of the top Fe-electrode as visualized in the insets of Figure 10.8. In $\mathrm{M_1}$ state the magnetization of Fe-atoms is pointing in the same direction as the interface's magnetization, whereas in $\mathrm{M_2}$ state the two are antiparallel. The reversal of the magnetic molecular layer is totally possible, yet it is tough to describe by solely considering magneto-transport measurement and a more detailed study is required. Yet, we suppose that the magnetic layer doesn't rotate in the ground-state of the spin-chains. The rotation of the interfacial magnetic layer englobing the first ML of CoPc and the interfacial Fe-atoms will be discussed in the next sub-section.

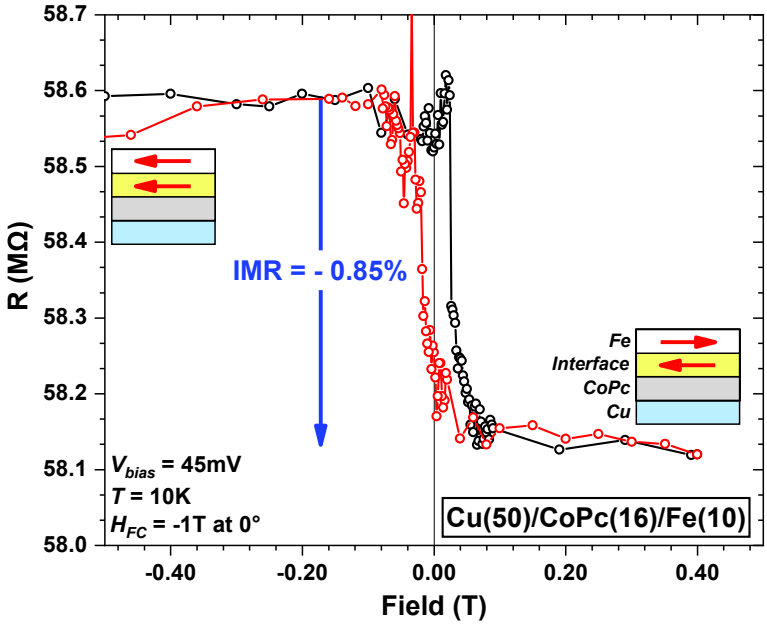

Figure 10.8: **Magnetoresistance measurement of a Cu/CoPc/Fe junction at 10K.** The RH measured at 45mV and 10K upon an -1T (0°) FC. Low amplitude IMR signal of -0.85% eventually originates from the interfacial spin-filtering and the magnetic reversal of the Fe-electrode.

10.5.2 Low bias magnetoresistance effect

Returning to the double FM-electrode junction of Fe/CoPc/Co, both of the interfaces can potentially develop a strong chemisorption at the interface and hence generate IMR effects. One way of untangling the role of each interface in the MR signal of this device is to compare the IMR at $V_{bias} < 0$ and $V_{bias} > 0$. This comparison is represented in Figure 10.9.

The red MR_{12} is calculated from IVs in the $M_1(B_{ext} = -1T)$ and $M_2(B_{ext} = +1T)$ states whereas the black MR_{12} is extracted out of RH measurements at each V_{bias} value. We considered that the magnetic configurations are identical at $B_{ext} = \pm 1T$ and $B_{ext} = \pm 2T$, since we observe the same resistance values, hence, we can compare the RHs and IVs (extract) MR terms. The low signal-to-noise ratio and the low amplitude of the IMR signal prevents us from discerning with confidence the MR bias polarity dependence. Taking into account the presence of the same MR term in a single magnetic interface in Cu/CoPc/Fe and the bias symmetry of the MR signal in Fe/CoPc/Co with two magnetic interfaces, we consider that in this structure analogous effects arise at both hybrid-interfaces Fe/CoPc and CoPc/Co. This implies that the resulting IMR can originate from a single magnetic interface. Additionally, the unidirectional nature of the MR signal advocates for its interfacial origin, hence the presence of an IMR effect. The further discussed field cooling effect in Section 10.6.1 on IMR and its temperature dependence strongly reinforces the interfacial interpretation of the MR detected in the ground state of the spin-chains. The following discussion will now focus on the magnetotransport response of the device in the excited

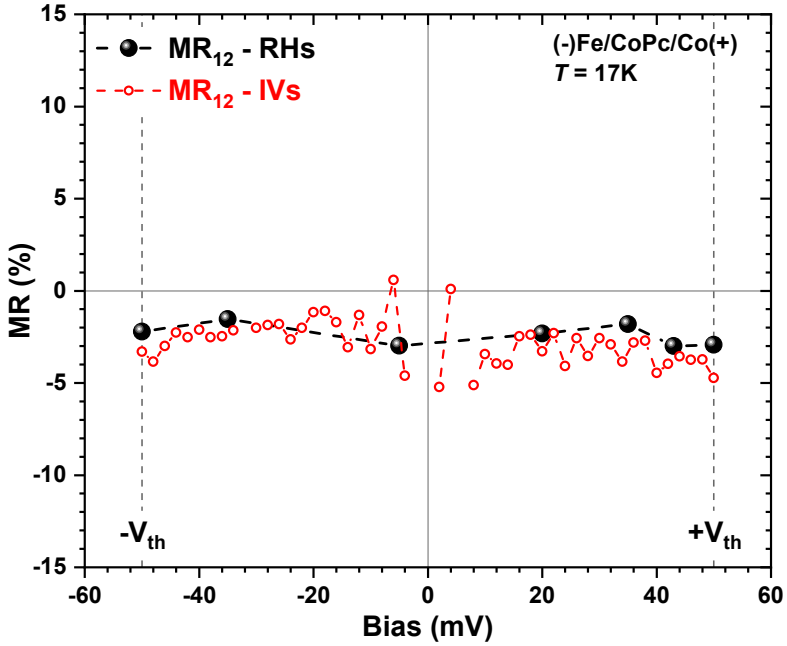

Figure 10.9: **Bias dependence of IMR at 17K.** Black - MR_{12} extracted out of RHs, Red - MR_{12} extracted out of IVs at $\pm 1\mathrm{T}$. The amplitude of IMR doesn't allow to distinguish between the two interface Fe/CoPc $(\mathrm{V}_{\mathrm{bias}} > 0)$ and CoPc/Co $(\mathrm{V}_{\mathrm{bias}} < 0)$.

state of the spin-chains i.e. at bias voltage above the threshold V_{th} voltage.

10.5.3 Spin-flip excitations driven magnetoresistance

The above discussed spin-flip excitations of the CoPc spin-chains takes place at a bias voltage higher than $\pm\mathrm{V}_{\mathrm{th}}$. Within a simplified description of such molecular spin-chains, each molecule's atomic center is characterized by a discrete magnetization. Upon spin-flip excitations a single or multiple magnetizations along the chain are altered, hence the total spin-chain's magnetic AFM order is frustrated. Once the bias voltage is decreased below V_{th} the spin-chain relaxes to its ground state and the AFM structure is reestablished. The frustration of the AFM spin-chains at $\mathrm{V} > \mathrm{V}_{\mathrm{th}}$ reduces the coercivity of a strong magnetic element within the device that can now be reversed at high positive magnetic fields. This mechanism can be seen in Figure 10.10 below, which shows that at $\mathrm{V} > \mathrm{V}_{\mathrm{th}}$ an additional MR term appears in RHs and that it is characterized by a huge coercive field $\mathrm{H}_{\mathrm{C}} \approx 1.4\mathrm{T}$. This effect takes place at both bias polarities. Here for the clarity of the effect's description, only $\mathrm{V} > 0$ is presented. The negative bias voltage dataset is briefly presented in the supplementary information Section 11.1.

The opening of the spin-flip excitations channel starts at $\pm 50\mathrm{mV}$ and smoothly increases before reaching its maximum at $\pm 75\mathrm{mV}$ and the same exact progressive growth of the additional MR term is observed in RHs between ± 50 and $\pm 75\mathrm{mV}$, as depicted in Fig-

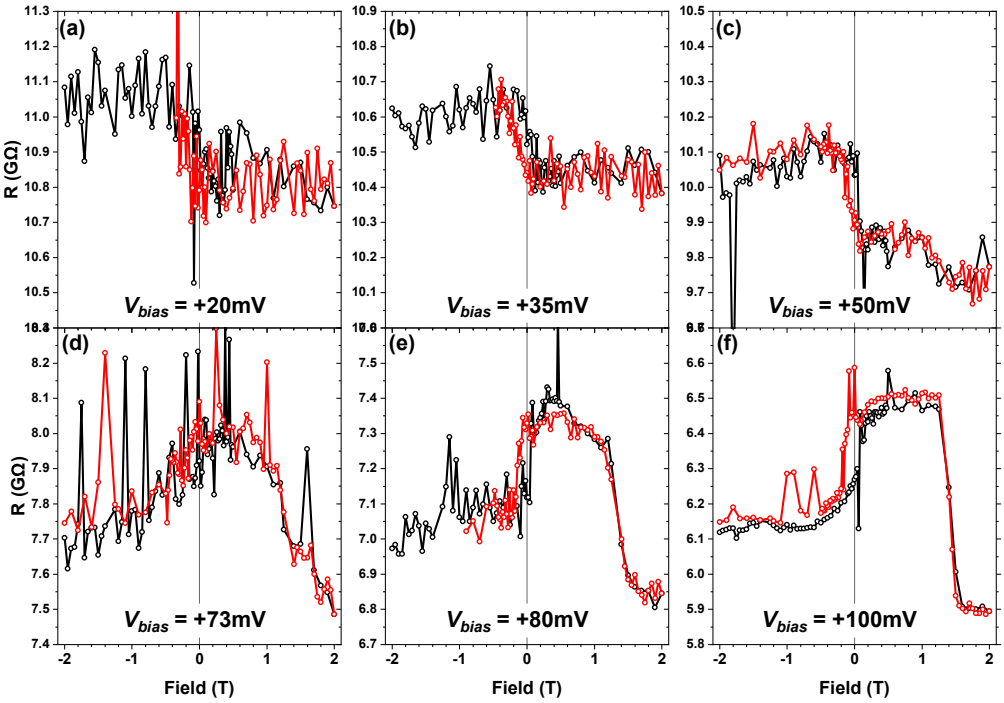

Figure 10.10: **Magnetoresistance measurements performed at consecutive incrementations of bias voltage at 17K.** Black curves stand for the -2T → +2T measurements, whereas the red one's red for +2T → -2T measurements. The progressive opening of the inelastic channel from the starting point of 50mV gives rise to the appearance of an additional MR term that saturates at 100mV. The same effect takes place for $-\mathrm{V}_{\mathrm{bias}} < -\mathrm{V}_{\mathrm{th}}$ but isn't presented here for simplicity.

ure 10.10.b. and Figure 10.10.c. In the spin-chain ground-state, at 20mV and 35mV solely the previously discussed IMR effect is discernable in the RHs curves characterized by a resistance change at the low field region. At $\mathrm{V} < \mathrm{V}_{\mathrm{th}}$, the system is magnetically stable and solely the soft FM electrodes can rotate at their respective coercive fields. Yet, the signal-to-noise ratio precludes the observation of an soft-electrodes AP configuration magnetoresistance feature. The resistance difference between the negative and positive fields resistance is attributed to the alignment of the electrodes and the blocked upon field-cooling set of spinterfaces and spin-chains. Starting from 50mV and above an additional MR effect is detectable and the RH is characterized three resistance levels, the previously evoked M_1 at -2T ($\mathrm{B}_{\mathrm{ext}} < 0$), M_2 at +1T and a new M_{AP} state at +1T (see Figure 10.11.a). The resistance of the M_2 state increases compared to the respective resistances in M_1 and M_{AP} with the increase of the inelastic channel in dIdV above $\mathrm{V}_{\mathrm{th}} \approx 50\mathrm{mV}$. The measured RHs above 100mV indicate that the MR effect saturates at 100mV and remains stable up to 150mV exactly as the dIdV plots. To further unveil the origins and mechanisms of the new MR term we represent the RH performed at 100mV, Figure 10.11.a and define the

three resistance states M_1, M_2, M_{AP} and the respective MR terms, MR_{1AP}: M_1 vs M_{AP} and MR_{AP2}: M_{AP} vs M_2 and the huge coercive field $H_C \approx 1.4T$. The choice of names M_1, M_2 and M_{AP} of the resistance levels will be clarified in Section 10.9 through the description of the magnetic reversals taking place in this sample.

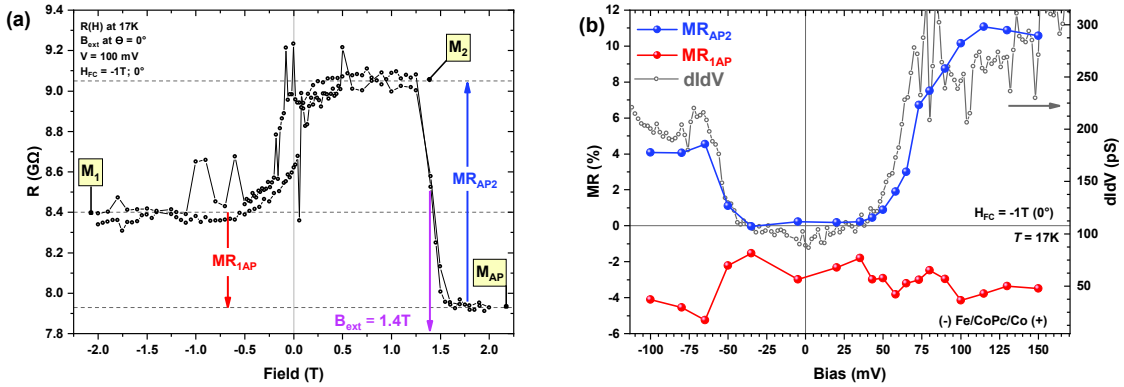

Figure 10.11: **Magnetoresistance measurement at 100mV and the bias dependence of the two MR effects.** (a) RH at V_{bias} = +100mV, M_1 defined for negative magnetic fields, M_{AP} defined as the lowest resistance state at high positive magnetic fields and M_2 defined according to the highest resistance state for positive fields below $B_{ext} \approx 1.4T$. The respective MR terms. (b) Bias dependence extracted out of RHs at each consecutive bias voltage value. In red - MR_{1AP}: M_1 vs M_{AP} and in blue MR_{AP2}: M_{AP} vs M_2 and in dark gray the conductance dIdV (right axis).

Referring to Figure 10.11.b, the bias dependence of MR_{1AP} seems to be relatively constant in the range [-100mV; +150mV] within the signal-to-noise ratio. Whereas, MR_{AP2} tracks the conductance plot dIdV. At this level of interpretation, we ignore how MR_{1AP} appears to track dIdV for $V < -50mV$. In the low bias region $-V_{th} < V < +V_{th}$, MR_{AP2} is non-existing, but starts to progressively grow with the smooth opening of the inelastic channel from V_{bias}± 50mV. The asymmetry of dIdV for positive and negative bias most probably originates from the material difference in the top Co/CoPc and bottom Fe/CoPc interfaces, hence a different spin-polarization available for the inelastic processes to take place along the CoPc spin-chains. The other origin could be related to the structural differences, and hence a difference chemisorption at the two interfaces. Remarkably, the dIdV asymmetry is also observed in the bias dependence of MR_{AP2}. The same behavior of dIdV and MR_{AP2} implies that this MR effect is mediated by the inelastic transport that takes place in the device. Yet, the mostly linear shape of the IV measurement, Figure 10.4. hints that elastic tunneling isn't the dominant mechanism in neither the ground-state nor the excited-state (inelastic channel). Therefore, the spin-polarized transport origin of MR_{AP2} is less likely than an interfacial source as is already the case of MR_{1AP}.

The huge coercive field H_C separating the M_2 and M_{AP2}resistance states results from the rotation of a strongly pinned magnetic element within the transport path of the device. The detailed examination of H_C would allow to further examine the MR_{AP2} term

appearing along the spin-flip excitation of the CoPc spin-chains.

10.6 Strong Spinterface's magnetism

Extracting the bias dependence of H_C field out of the consecutive RHs reveals that this huge field is quasi-constant within the uncertainty of our measurement and is symmetric in bias. Figure 10.12. summaries the bias dependence of H_C (pink) and illustrates its association with the conductance dIdV (gray). One can see that H_C appears at the opening of the inelastic channel in the conductance and remain at the same value during the growth and saturation of the inelastic channel. For $| V |< V_{th}$, no H_C is measured. The sharp appearance of H_C once the inelastic transport channel is achieved ($V > V_{th}$) may indicate that the rotating magnetic entity (set of spinteraces adn spin-chain's) is strongly coupled at low T.

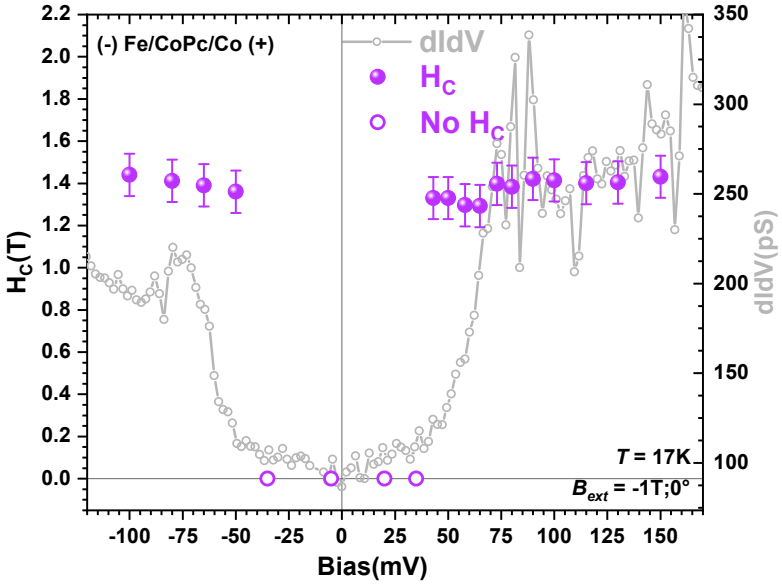

Figure 10.12: **Bias dependence of the huge magnetic field HC and the conductance dIdV plot.** In pink - H_C was extracted out of RHs measured at the respective bias voltages; the error bars are defined with respect to the magnetic step in RHs of $\approx$ 500 Oe (graph scale on the left). In the low bias region, no H_C is detectable. In black - the conductance dIdV, graph scale on the right.

The characteristic coercive fields of the Fe and Co FM electrodes are two order of magnitude smaller than the huge $H_C \approx 1.4T$ detected in RHs. The reported exchange bias effect [156, 196] arising at the hybrid molecular-ferromagnet interface is also one to two orders of magnitude smaller than H_C. These observations indicate that H_C emerges from the rotation of a strongly pinned magnetic element, such as for instance the magnetically frustrated molecular spin-chain.

10.6.1 Effect of field cooling

The unidirectional spin-reference is implemented within the spin-chains during the field cooling procedure. Therefore, we've compared the effect of FC on the RHs in the excited state of the spin-chains i.e. the effect of FC on the huge coercive field H_C. The previously discussed $H_C \approx +1.4T$ was extracted out of RHs performed upon an H_{FC} = -1T field cooling. Referring to Figure 10.13, we compare a negative FC (H_{FC} = -1T) and a positive FC (H_{FC} = +2T (0 Oe)) and observation that the respective coercive field H_C strictly depends on the orientation of the FM electrodes upon or during the cooling, hence, a negative FC gives a positive $H_C \approx +1.4T$ and the positive FC gives a negative $H_C \approx -1.4T$. As a note of mention, the positive FC was done in the following way: +2T field was applied at +120K, then turned off and the cooling was done at $H_{FC} = 0Oe$, since both RHs are similar to the extent of an inverted H_C we concluded that the effect resetting the system at 120K under +2T is permanent at remains during the cooling procedure. Both RHs measurements were acquired under the exact same external parameters and can be used unveil the dependence of H_{FC} and H_C. The small resistance offset of $R_{offset} \approx 0.5G\Omega$ between the two RHs probably originates from the wear of the junction after consecutive FC procedures and one week of around-the-clock measurements.

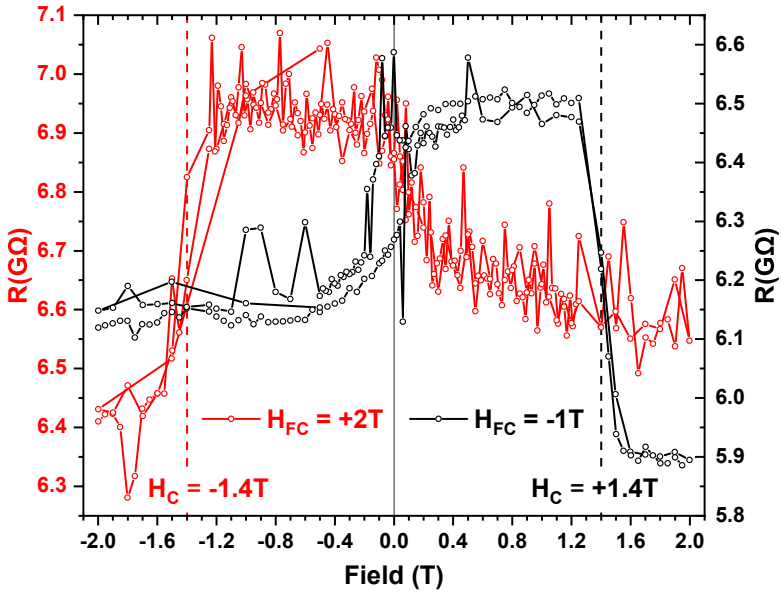

Figure 10.13: **Magnetotransport measurements upon opposite field FC procedures.** Black - RH performed upon $H_{FC} < 0$ (-1T). Red - RH performed upon $H_{FC} > 0$ (+2T). The huge coercive field's amplitude doesn't depend on H_{FC}, whereas its sign is opposite to the sign of H_{FC}. Both measurements are performed in the exact same conditions and differ solely by the FC procedure.

The field dependence of H_C observed in Figure 10.13 strongly hints towards the spin-chain origin of H_C. During the field cooling procedure, the spin-reference is introduced

within the AFM order of the spin-chains, hence the easy axis this magnetic entity is defined along this direction i.e. H_C is defined by the sign of H_{FC}. Generally speaking, magnetotransport measurements are sensitive only to the fraction of magnetic entities participating in the transport of charge carriers and can't be considered as standard magnetometry measurements. Yet, one can inspect the origin of magnetotransport features through multifunctional temperature, angular and bias voltage studies. The next subsection describes the temperature behavior of the different MR features and H_C to further investigate their origins and intrinsic origins.

10.7 Temperature behavior of magnetoresistance

We compared the temperature dependence of the huge coercive field H_C and the two MR terms to further clarify the mechanism of their appearance. Upon a field cooling at H_{FC} = -1T, RH measurements were performed at consecutive incrementations of temperature from 17K up to 120K. All of the measurements were done at V_{bias} = +100mV and H_C and the MR terms were extracted out of each RH curve. Figure 10.14 presents the temperature dependence of MR_{AP2} (black), MR_{1AP} (red) and the huge coercive field H_C.

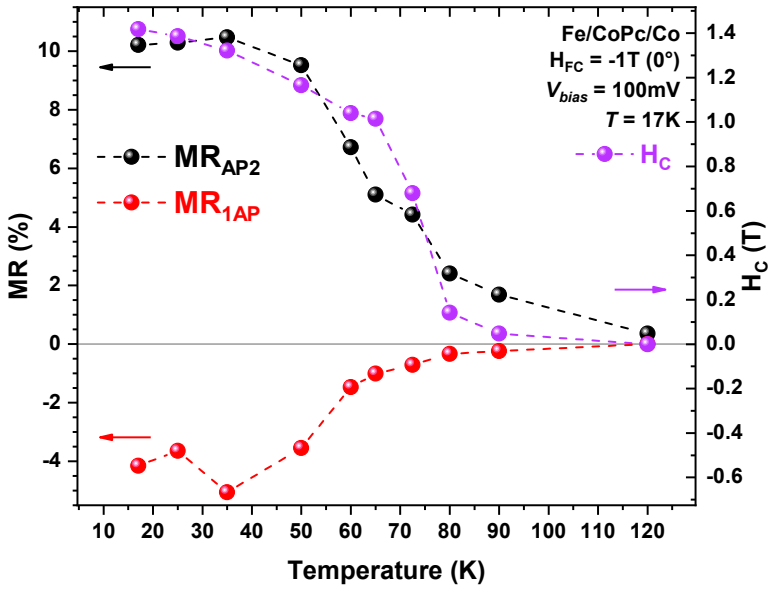

Figure 10.14: **Temperature dependence of magnetoresistance ratios and the huge coercive field H_C.** In black - MR_{AP2} : M_{AP}vsM_2, in red - MR_{1AP} : M_1vsM_{AP} and in pink - H_C. Data-points extracted out of RH measurements acquired after H_{FC} = -1T cool down to 17K as temperature was iteratively increased (17K $\longrightarrow$ 120K).

Remarkably, both MR terms and H_C share the same exact temperature behavior, summarized in the following: All three signals reach their maximum amplitude at 17K, it remains quasi-constant till 50K, then all three amplitudes begin to sharply decrease till they

reach their lowest detectable amplitude at 90K, further they completely vanish at 120K. Somehow this temperature resembles to the exchange bias blocking temperature of $\mathrm{T_B}$ = 100K of reported by Gruber et al. [156] on a Co/MnPc interface and the antiferromagnetic coupling exchange energy in CoPc spin-chains reaching 100K reported by Serri et al. [162]. Note that the temperature dependence of the $\mathrm{E_B}$ reported by Gruber et al has a different trend for $\mathrm{T} < 50\mathrm{K}$ (see Figure 9.14). There are two possible sources for the 100K blocking temperature at which the MRs and $\mathrm{H_C}$ vanish in our samples: i) the two MR terms and the huge $\mathrm{H_C}$ originate from the CoPc spin-chains present in the bulk of the spacer, hence the 100K blocking temperature corresponds to the exchange energy of CoPc-chain, or (and), ii) those features originate from the point of attachment at the interface, hence to the interfacial exchange bias that fades at 100K leading to the disappearance of MRs and $\mathrm{H_C}$. In any of those cases, the spin-chain origin of the MR terms and $\mathrm{H_C}$ is quasi-certain at this point.

10.8 Breaking the huge magnetic pinning

A remarkable event takes place in the 100mV RHs by when the measurement temperature is increased. At 17K, the RH is highly asymmetric (see Figure 10.15). This asymmetry endures up to T=58K. At 65K the RH becomes symmetric and is characterized by two huge coercive field at $\mathrm{H_C} \approx \pm 1\mathrm{T}$, as well as by an almost similar resistance in $\mathrm{M_1}$ and $\mathrm{M_{AP}}$. A symmetric RH at 65K indicates that the strong magnetic entity being reversed by the external magnetic field undergoes full magnetization reversal at 65K. The presence of two $\mathrm{H_C}$ fields at both field signs indicates that the previously pinned magnetic entity is loosened by the additional thermal energy. One way of depicting this effect is the following: upon field cooling, the strong magnetic entity is blocked in the prepared direction, therefore its reversal at 17K at fields of $\mathrm{H_{ext}} > \mathrm{H_C}$ isn't complete, and it aims to rotate back which generates an asymmetric RH characterized by a single $\mathrm{H_C}$ = 1.4 T. Note how this magnetic entity must be prepared electrically, i.e. for $\mid \mathrm{V} \mid > \mathrm{V_{th}}$. Once the temperature increases the additional thermal energy brought to the system overcomes the magnetic pinning.

In the last subsection of this chapter we combine all of the experimental observation to crystalize a model describing the nature rotating magnetic entity and the role of spin-flip excitations along the molecular spin-chains on the interfacial magnetoresistance effect observed in this junction.

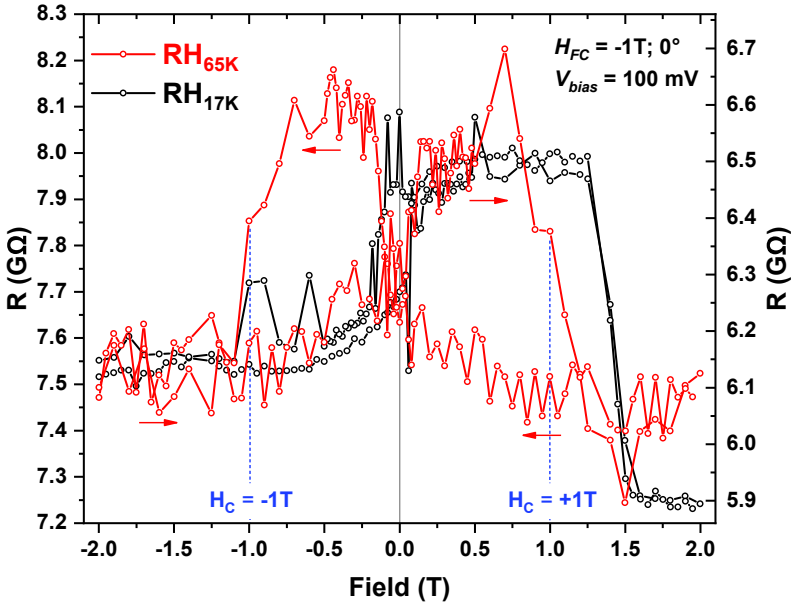

Figure 10.15: **Magnetotransport asymmetry breakage at 65K.** In red - a nearly symmetric RH measurement at 65K and 100mV, in gray - an asymmetric, pinned RH measurement at 17K and 100mV. At 65K two huge coercive field at $\pm 1\mathrm{T}$ are detectable.

10.9 Spin-chains driven magnetoresistance

Taking into consideration all of the previously discussed magnetotransport measurements and their observations-based interpretations, we propose a model describing the role of spin-chains in the bias-controllable unidirectional magnetoresistance signal of cobalt phthalocyanine based magnetic tunnel junctions. This model relies on the main hypothesis that the dominant transport ingredient is thermally activated i.e. thermal hopping [198, 199] or consecutive multi-step tunneling [200]. Both of these effects can take place in molecular spintronic devices and their inorganic counterparts. The dominant hopping transport interpretation in our sample relies on fore strong experimental observations: 1) The thermal dependence of the devices resistance is huge, $\mathrm{R_{17K}/R_{300K}} \approx 10^4$ (at V = 10mV)11.8, 2) Linear IV response in the $-\mathrm{V_{th}} < \mathrm{V_{bias}} < +\mathrm{V_{th}}$ bias-range at low T giving rise to an almost linear conductance dIdV in this region rejects elastic tunneling, 3) the $\mathrm{MR_{AP}} : \mathrm{M_2 vs M_{AP}}$ term is directly related to the bias-polarity of the devices conductance dIdV and transport IV implying a strong interfacial component in the device's magnetoresistance response, 4) The nominal thickness of the CoPc spacer is of 20nm, which is higher than the standard tunneling spacer's thicknesses [185, 186]. Rejecting these observations and treating the magnetotransport dataset under spin-polarized transport formalism [4] requires considering both FM electrodes and their respective spinterfaces in the interpretation of the device's magnetotransport response. In the herein discussed model we focus only on the hybrid FM/Molecular interface in the treatment of the device's magnetotransport properties avoiding the consideration of the spin "analyser" electrode/spinterface.

The field cooling procedure sets the spin-references within the system, namely, the actively participating in mangetotransport bottom device's interface coupled to the FM electrode. As a result both magnetic entities are aligned along the direction of the external field generating a unidirectional magnetic anisotropy within the structure. As we assume only it actively participates in magnetotransport for $V > 0$, i.e. when electrons transport from the bottom to the top electrode. The bias control over the magnetotransport response of this molecular MTJ is achieved by the opening of an additional inelastic spin-flip transport channel above a given threshold voltage. The opening of this spin-flip excitations channel is associated with introduction of spin-frustrations along the molecular spin-chains which alters its magnetic structure and consequently shrinks the coercivity of the pinned FM electrodes it sits on. This leads to two strictly different magnetoresistance signals below and above the bias threshold schematically depicted in Figure 10.16.

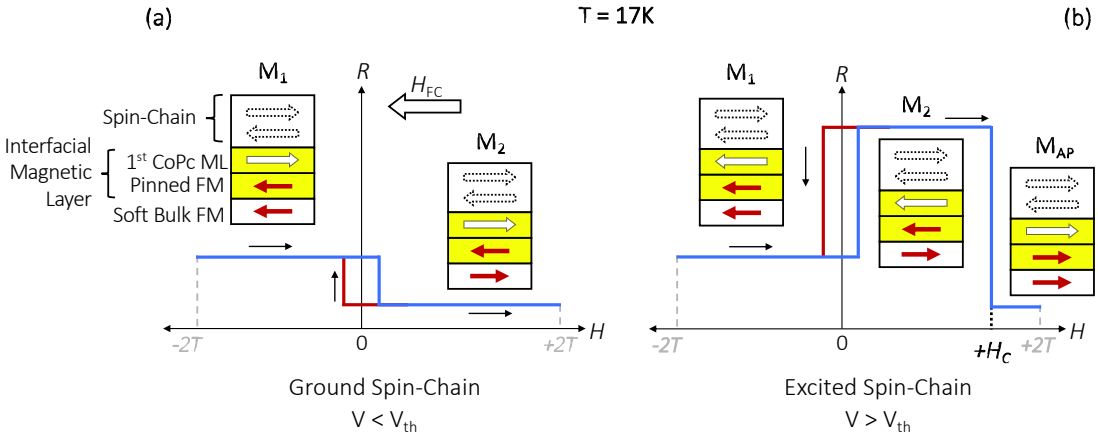

Figure 10.16: **Magnetoresistance manipulation through spin-flip excitations model.** Resistance and the respective magnetic configuration schematics, arrows in rectangles correspond to magnetization orientation of each respective element defined in the legend. Only the bottom interface is considered as we assume only it actively participates in magnetotransport for V>0, i.e when electrons transport from the bottom to the top electrode. (a) spin-chain in its ground state, $V < V_{th}$, The AFM spin-chain is within its unfrustrated AFM order and the magnetic interface is pinned. The interfacial magnetoresistance (IMR) effect originates solely from the rotation of the bottom Fe-electrode. (b) spin-chain in its excited state, $V > V_{th}$, the spin-flip excitations frustrate the AFM order of the spin-chain. The rotation of the spin-chain and the interfacial magnetic layer is possible. The high resistance state corresponds to the additional inelastic transport channel in the antiparallel configuration of the Fe-electrode and the interfacial magnetic layer. The low resistance state achieved at $H > H_C$, arises from the rotation of the magnetic molecule and the 2^{nd} molecular layer.

Referring to Figure 10.16, we represent only the actively participating in mangetotrans-

port bottom device's interface since at $V > 0$ electrons are tunneling from the bottom electrode of the sample to the top electrode. In panel (a) - below the bias threshold $V < V_{th}$ the spin-chain is in its ground state and retains its magnetic orientation upon the field sweep between $\pm 2T$. In this case neither the spin-chain nor the bottom pinned FM interfacial layer undergo a magnetization reversal, only the bottom unpinned (soft) FM bulk layer rotates at its characteristic low coercivity fields. Therefore, two magnetic configurations M_1 and M_2 are achievable upon field sweeps, M_1 resulting in a higher resistance and M_2 leading to a lower resistance state, the respective magnetization configurations are schematically depicted in Figure 10.16.a. Finally, the unidirectional MR term originates from the interfacial alignment of the FM bulk electrode and the rest of the pinned elements (the interfacial pinned elements and the spin-chain). In panel (b) - above the bias threshold $V > V_{th}$ the tunneling electrons have enough energy to excite the spin-chain's ground state and alters its magnetic order. In this case, an additional inelastic spin-flip channel is opened, moreover this channel should be highly spin-polarized according to the spin-selection rules defined by the spin-flip transition on the spin-chain's centers. Since the additional transport channels generates spin-frustration along the spin-chain the resulting coercive fields are decreased. Consequently, in panel (b) we observe three magnetic configurations (M_1, M_2 and M_{AP}), M_1 defined only by an inversion of a single (for simplicity) spin-chain's center leading to an intermediate resistance state, M_2 corresponds to the excited spin-chain's center and the inversion of the bulk FM (magnetically soft) layer at low magnetic field leading to a high resistance state and M_{AP} which appears upon the huge coercive field H_C that defines the rotation of the interfacial spin-chain's element and the pinned interfacial FM layer but not the whole spin-chain. Therefore, M_{AP} doesn't correspond to a complete reversal and leads to the lowest resistance state, $R(M_{AP}) < R(M_1)$. A complete symmetric reversal would eventually require both resistances at $\pm 2T$ to be the same $R(M_{AP}) = R(M_1)$.

RH plots acquired at 60K demonstrate simultaneously the presence of the same resistance levels at $\pm 2T$ and the presence of an intermediate M_{AP} state giving rise to a the lowest resistance state, see Section 11.7 for this data-set. Moreover, Figure 10.16 illustrates the case of the magnetically pinned structure. This can be seen by the overall asymmetric profile of the RHs in both cases, but especially at $V > V_{th}$. The magnetic field (H) sweep-in ($-2T \rightarrow +2T$) represented in blue is followed by the same sweep-out ($+2T \rightarrow +2T$) highlighting the magnetic pinning implement during FC procedure and present in this state of the device. As we've seen in Section 10.7, the temperature dependence of the device's magnetotransport effects turns out to be crucial for its proper interpretation. Therefore, Figure 10.17 continues the schematic description of our device and visualizes the effects taking place upon the asymmetry breakage at 65K. Increasing the temperature from low (17K) to an intermediate value (65K) breaks the asymmetry and gives rise to an almost perfectly symmetry RH illustrated in Figure 10.17. This effect originates from the additional thermally mediated spin-frustrations along the molecular magnetic structure. Consequently, the spin-chain's magnetic reference implemented during the FC procedure is depressed by these spin-frustrations. In the spin-chain's excited-state ($V > V_{th}$) the reversals are complete leading to the same resistance response of the device in its magnetic configurations at $\pm 2T$ and $\pm 0.5T$, as schematically represented in Figure 10.17.

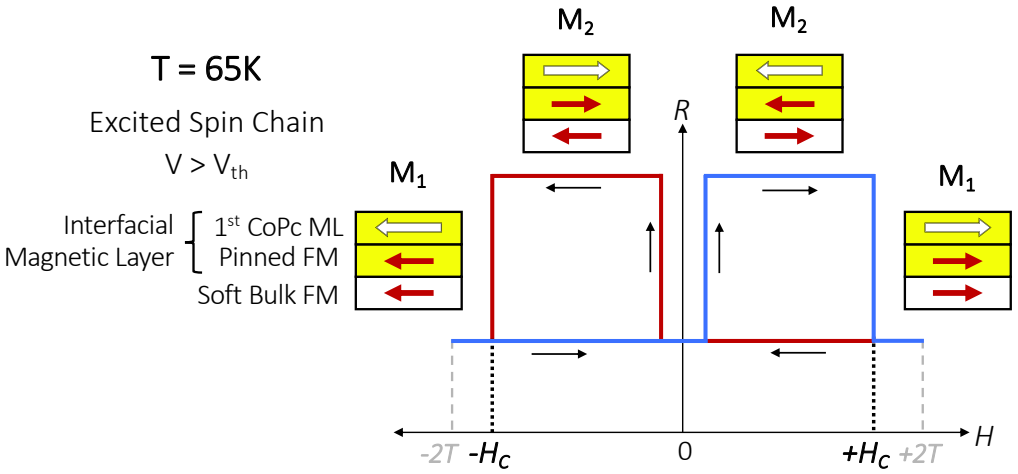

Figure 10.17: **Magnetotransport asymmetry breakdown at 65K.** Resistance and the respective magnetic configuration schematics, arrows in rectangles correspond to magnetization orientation of each respective element. For simplicity of the schematics the spin-chain magnetization isn't represented.

The symmetric butterfly-shape of the RH at 65K is characterized by two coercive fields $H_C = \pm 1$ highlighting the complete reversal of all magnetic entities, namely the bulk soft FM layer, the interfacial FM pinned layer and the first spin-chain's element upon the magnetic $\pm 2T$ sweeps. As we have previously seen, increasing the temperature reduces H_C and the MR terms. The MR_{1AP} term is almost indiscernible at 65K and solely MR_{AP2} is still present but will a diminished amplitude, see Sections 10.7. Increasing further the temperature completely cancels the molecular magnetic order and the resulting from its device's magnetoresponse at around 100K. This blocking temperature is in coherent agreement with the previous reports on CoPc spin-chains. The magnetic molecular origin of these bias-controllable magnetoresistance effects is especially clear when we compare the thermal dependence of H_C, MR terms and the device's overall resistance. According to Sections 10.4.1 and 10.7, the device's resistance remains mostly unchanged in the 17K-100K region whereas H_C and the MR signals undergo a strong decrease and completely vanishes around 100K, which is confirmed by previous studies [156]. This implies that the magnetic structure of the device is much more sensitive to increasing temperatures rather than the transport mechanisms, such temperature sensitivity is characteristic for molecular magnetism known for its rather limited thermal stability. This is a good example of the advantages and tunability molecular/organic spintronics could bring once it attracts the attention of the industry sector. Since, to achieve similar effects of pinning in inorganic devices several additional functional magnetic layers need to be implemented within the MTJs structure, herein it's achieved purely by tailoring the magnetic molecular structure of the device.

10.10 Summary and perspectives

In this chapter, we introduced the transition-metal - phthalocyanine (TMPc) molecular compounds as well as their electronic and magnetic properties. The structural aspects of TMPc molecules were evoked, hence, the formation of vertically arranged molecular complexes called spin-chains. Furthermore, we discussed the main interests of their adoption in spintronic devices. We in particular emphasized how hybrid molecular-ferromagnetic interfaces can alter, enhance or even invert the interfacial spin-polarization through orbital hybridizations or charge projection, and hence generate spinterfaces. Additionally, these interfacial mechanisms can alter the magnetism at the interfacial layer. Therefore, the two main elements of spintronics, namely spin-polarization and magnetism, can be enhanced at such hybrid molecular-ferromagnetic interfaces.

Firstly, the deep-rooted bottleneck of the magnetic tunnel junction fabrication with organic spacers was addressed. We presented a novel nanosphere lithography technique enabling to overcome most of the issues of using molecules as the main spacing material in junctions. This followed up with the demonstrated operation of sub-micronic junctions processed with this nanosphere lithography technique.

Secondly, we probed the magnetotransport arising in such CoPc-based magnetic junctions through transport, temperature, angle, and field cooling multifunctional measurements. The resistance-temperature correlation evidences that the main transport mechanism through the device is thermally assisted hopping. The opening of an additional inelastic transport channel above a voltage threshold value detected through conductance measurements turned out to alter the magnetoresistance response. It appears that the inelastic channel is responsible for a spin-flip excitation along the molecular spin-chains and that these excitations alter the magnetism of the device, therefore, its magnetoresistance signal. This experimental study manifests that the unidirectional anisotropy interfacial magnetoresistance effect can be tuned by addressing the CoPc molecular spin-chains embedded between ferromagnetic electrodes at the correct bias voltage.

Our experimental achievements and their coherent interpretation can be considered as the benchmarking of organic spintronics capabilities at the scale of hybrid magnetic junctions. Once the process protocol of organic junctions is established and routinely mastered the capabilities of organic spintronics are enormous, much richer and tunable than fully inorganic spintronics.

The journey towards future-proof organic memory solutions is just at its starting point, and a interdisciplinary physical and chemical studies must be conducted, yet the field of organic spintronics remains a very exciting field to explore.

Traduction en Français:

Résumé et perspectives

Dans ce chapitre, nous avons présenté les composés moléculaires métal de transition-phtalocyanine (TMPc) ainsi que leurs propriétés électroniques et magnétiques. Les aspects structuraux des molécules TMPc ont été évoqués, d'où la formation de complexes moléculaires disposés verticalement appelés chaînes de spin. De plus, nous avons discuté des

principaux intérêts de leur adoption dans les dispositifs spintroniques. Nous avons en particulier souligné comment les interfaces hybrides moléculaires-ferromagnétiques peuvent modifier, améliorer ou même inverser la polarisation de spin interfaciale par hybridation orbitale ou projection de charge, et donc générer des spinterfaces. De plus, ces mécanismes interfaciaux peuvent modifier le magnétisme au niveau de la couche interfaciale. Par conséquent, les deux éléments principaux de la spintronique, à savoir la polarisation de spin et le magnétisme, peuvent être améliorés à de telles interfaces hybrides moléculaires-ferromagnétiques. Premièrement, le goulot d'étranglement profondément enraciné de la fabrication de jonction tunnel magnétique avec des espaceurs organiques a été abordé. Nous avons présenté une nouvelle technique de lithographie par nanosphère permettant de surmonter la plupart des problèmes liés à l'utilisation de molécules comme matériau d'espacement principal dans les jonctions. Cela a suivi le fonctionnement démontré des jonctions submicroniques traitées avec cette technique de lithographie par nanosphère. Deuxièmement, nous avons sondé le magnétotransport se produisant dans ces jonctions magnétiques à base de CoPc par des mesures multifonctionnelles de transport, de température, d'angle et de refroidissement de champ. La corrélation résistance-température montre que le principal mécanisme de transport à travers le dispositif est le saut assisté thermiquement. L'ouverture d'un canal de transport inélastique supplémentaire au-dessus d'une valeur de seuil de tension détectée par des mesures de conductance s'est avérée modifier la réponse de magnétorésistance. Il apparaît que le canal non élastique est responsable d'une excitation de spin-flip le long des chaînes de spin moléculaires et que ces excitations altèrent le magnétisme du dispositif, donc son signal de magnétorésistance. Cette étude expérimentale montre que l'effet de magnétorésistance interfaciale à anisotropie unidirectionnelle peut être réglé en adressant les chaînes de spin moléculaires CoPc intégrées entre les électrodes ferromagnétiques à la tension de polarisation correcte. Nos réalisations expérimentales et leur interprétation cohérente peuvent être considérées comme le benchmarking des capacités de spintronique organique à l'échelle des jonctions magnétiques hybrides. Une fois que le protocole de processus des jonctions organiques est établi et régulièrement maîtrisé, les capacités de la spintronique organique sont énormes, beaucoup plus riches et réglables que la spintronique entièrement inorganique. Le voyage vers des solutions de mémoire organique à l'épreuve du futur n'en est qu'à son point de départ, et des études physiques et chimiques interdisciplinaires doivent être menées, mais le domaine de la spintronique organique reste un domaine très passionnant à explorer.

Chapter 11

Supplementary datasets

This chapter is entirely devoted to the complementary experimental datasets acquired on the single Fe(50)/CoPc(20nm)/Co(10) submicronic hybrid magnetic junction. This strategical choice was done to preserve a continuous comprehensive "story" in the main section of the manuscript and to leave all of the supplementary information in an additional section. The figures presented in this section are to be considered within the iterative description held in the main sections of the manuscript. Therefore, to avoid redundancy each plot is only briefly introduced and contains a detailed caption.

11.1 Negative voltage magnetotransport comparison

The molecular magnetic junction is electrically connected in the following way: at positive sourced voltage electrons are traveling from the bottom Fe-electrode through the CoPc spacer into the top Co-electrode, whereas for negatively sourced voltage in the respective opposite direction. This section presents the comparison of magnetotransport at both voltage polarities. Referring to Figure 11.1, the MR effects are entirely symmetric in bias at $\pm 35\mathrm{mV}$ and $\pm 50\mathrm{mV}$, thus the magnetotransport is unchanged by bias voltage polarity in the ground-state of the spin-chain ($\mathrm{V} < \mathrm{V_{th}}$).

At $\pm 50\mathrm{mV}$ the transport channel is close enough to the ground-state since the inelastic channel is just got accessible. Interestingly, at $\pm 100\mathrm{mV}$ both RHs aren't similar in the AP resistance states. This discrepancy most probably originates from the bias voltage asymmetry of the conductance, as the amplitude of the inelastic channel is proportional to the generation of the AP state (see the next Section 10.5.3).

11.2 Magnetoresistance voltage dependence

The voltage behavior of $\mathrm{MR_{1AP}}$ and $\mathrm{MR_{AP2}}$ was discussed in the main sections of the manuscript based on RHs data. Here, we present the complementary comparison between the extracted MR signal and the raw MR obtained from IVs in the respective magnetic states. The raw MR plots are in perfect agreement with the extracted MR terms and the conductance dIdV, as one can see in Figure 11.2. The single tiny discrepancy can be seen in the low voltage $-\mathrm{V_{th}} < \mathrm{V_{bias}} < +\mathrm{V_{th}}$ region in which the raw MR terms are pretty noisy but still follow the general trends of extracted MR terms.

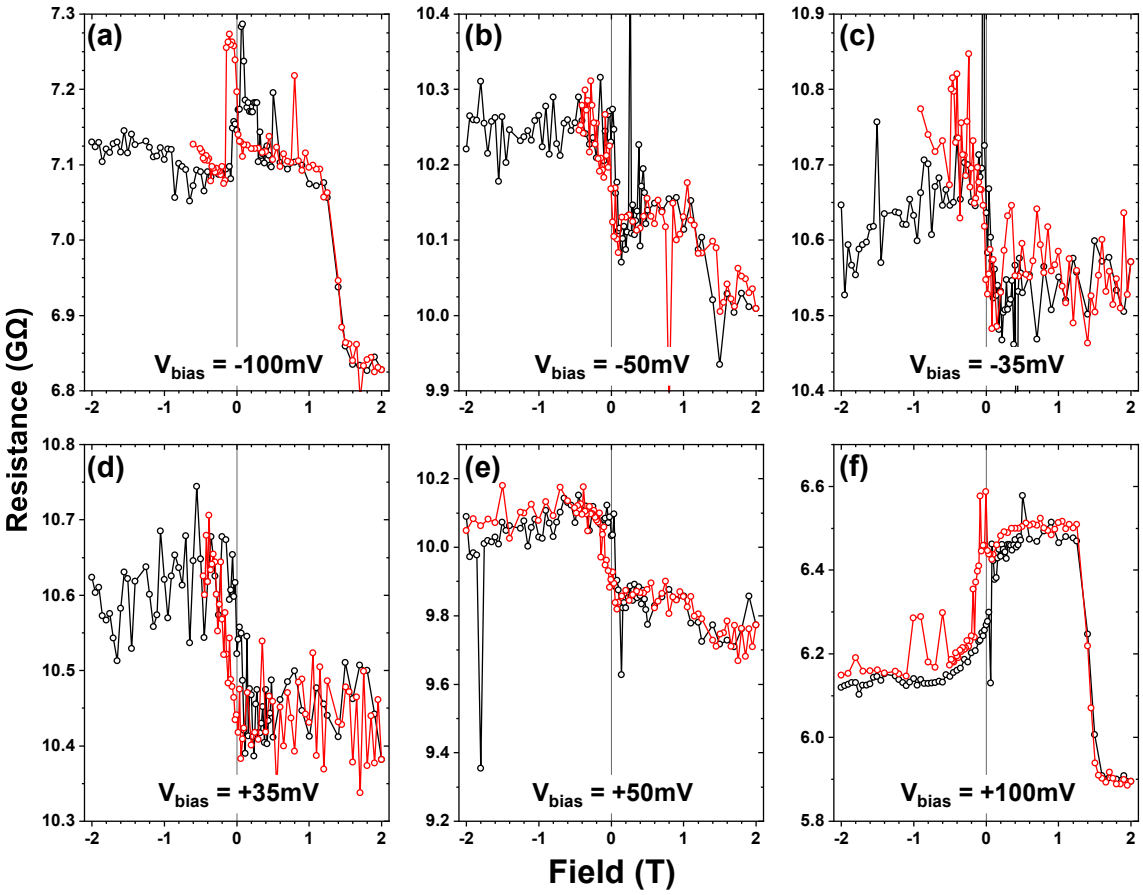

Figure 11.1: **Bias voltage dependence of magnetoresistance at low temperature upon field cooling.** All of the RHs were performed consecutively from negative to positive voltages, $-100\mathrm{mV} \rightarrow +100\mathrm{mV}$. Field cooling was done at -1T (hence, $\mathrm{H_C} > 0$). Measurements performed at 17K, $\mathrm{V} < 0$: $\mathrm{e^-}$ flow through Co/CoPc/Fe and for $\mathrm{V} > 0$: $\mathrm{e^-}$ flow through Fe/CoPc/Co. The black curves correspond to the sweep-in and red corresponds to the sweep-back. RHs are entirely symmetric in voltage at $\pm 35\mathrm{mV}$and $\pm 50\mathrm{mV}$. The asymmetry at $\pm 100\mathrm{mV}$ originates from the asymmetry in dIdV and from the differences at the two interfaces Fe/CoPc and CoPc/Co.

These experimental observations implies that junction charging effects discussed in the main Section 10.4.2 aren't affecting at first glance the magnetoresistance response of the device. Note how the dynamical IV measurements and the static RH measurements lead to the same $\mathrm{MR_{AP2}}$ and $\mathrm{MR_{1AP}}$ signals.

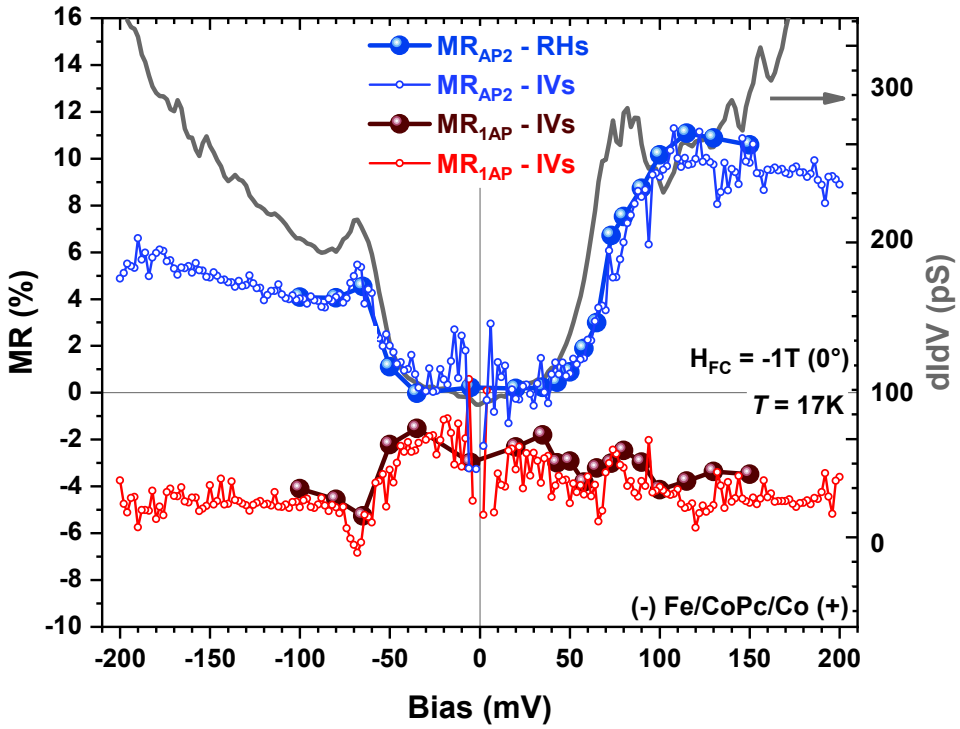

Figure 11.2: **Magnetoresistance-voltage behavior and the conductance dIdV.** Low temperature MR terms extracted from RHs in dark blue & red, raw MR terms calculated of respective IVs in bright blue & red and the calculated conductance in dark gray.

11.3 Unidirectional anisotropy magnetoresistance effect

As discussed in the main section of the manuscript both of the magnetoresistance terms are tightly related to the magnetic anisotropy implemented within the system during the field cooling procedure. Previously, we demonstrated only the angular dependence of the negative MR term in the low bias region. The amplitude of MR: $V < V_{th}$ feature undergoes a progressive switch from -6.2% at $0°$ into $+5.8\%$ at$0°$, as one can see in Figure 11.3.

This mirror symmetry of the MR signal implies that it is regulated by a unidirectional magnetic anisotropy, as previously reported by Barraud et al. In this supplementary section we present the angular dependence of the MR terms in the excited state of the spin-chains, hence performed at $V > V_{th}$. The MR: $V > V_{th}$ also follow the trend of a unidirectional anisotropy terms which implies a sign change in the effect's amplitude between $0°$ and $180°$ configurations. Yet, we see that the MR at $[45° - 135°]$ range is more complex. This arises from the AP resistance state that we probe at this angle values. Therefore we decided not to consider these points. Consequently, the MR in both of the spin-chain's ground and excited states is mediated by a uniaxial magnetic anisotropy present in the

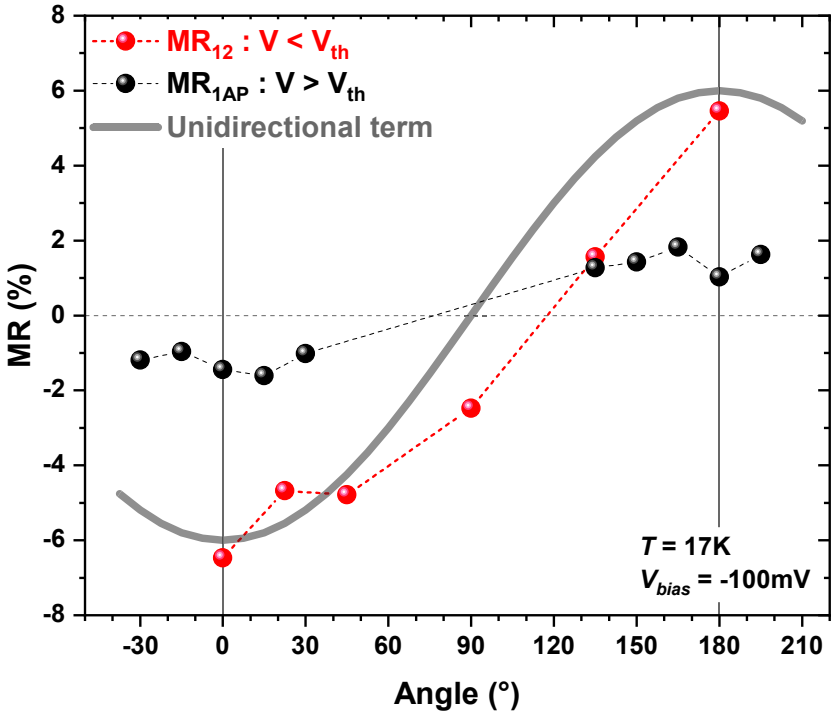

Figure 11.3: **Unidirectional magnetic anisotropy in the ground and excited states of the spin-chains MR terms.** Extracted out of RHs MR terms at $\mathrm{V} < \mathrm{V_{th}}$ (red) and at $\mathrm{V} > \mathrm{V_{th}}$ (black) as a function of externally applied magnetic field at consecutive angle values. The MR terms are defined between $\mathrm{R(B_{ext} = -2T)}$ and $\mathrm{R(B_{ext} = +2T)}$ states. The amplitude of both MR terms is opposite between $0°$ and $180°$. The red MR term follows a smooth transition and corresponds perfectly to a unidirectional behavior in dark gray. The black MR term is also following a unidirectional trend, yet in the $[45° - 135°]$ range we probe the high resistance $\mathrm{M_2}$ state; hence, these points shouldn't be considered.

system. Considering the temperature studies (Sections 10.7) and the field cooling studies (Section 10.6.1, the unidirectional anisotropy is attributed to the molecular antiferromagnetic order implemented during the field cooling procedure.

11.4 Complementaty angular study

In the last Section 10.9 of the main manuscript we brought up a model describing the magnetoresponse of the device through the rotation of magnetic elements at one of the interfaces, namely the pinned by exchange bias bottom electrode, the first layer of magnetized molecules and the spin-excited frustrated AFM spin-chain. This description is fully justified by the experimental observations presented in this manuscript, yet it's not impossible that our model is too simplified. Therefore, here we present the raw magnetotransport data acquired at different angles of magnetic field that can bring some additional information about the rotation of different magnetic ingredients within the device. Most likely in the M_1 state the ferromagnetic electrode and the absorbed first molecular layer are in parallel, as a direct consequence of the field cooling procedure. On the other hand, the exact magnetic orientation is hard to determine only through magnetotransport measurements. Referring to Figure 11.4, one can see that the resistance in the AP state is at the same level as the resistance of the RH performed at $90°$ (in blue) and the low resistance state M_{AP} at $0°$ lays on the level of the RH performed at $120°$ (in purple). Taking into consideration these similarities in the resistance levels, one can deduce that in the $0°$ - AP state the electronic and magnetic configurations are similar to the $90°$ configuration case. Similarly, the low resistance M_{AP}state eventually corresponds to the $120°$ configuration case.

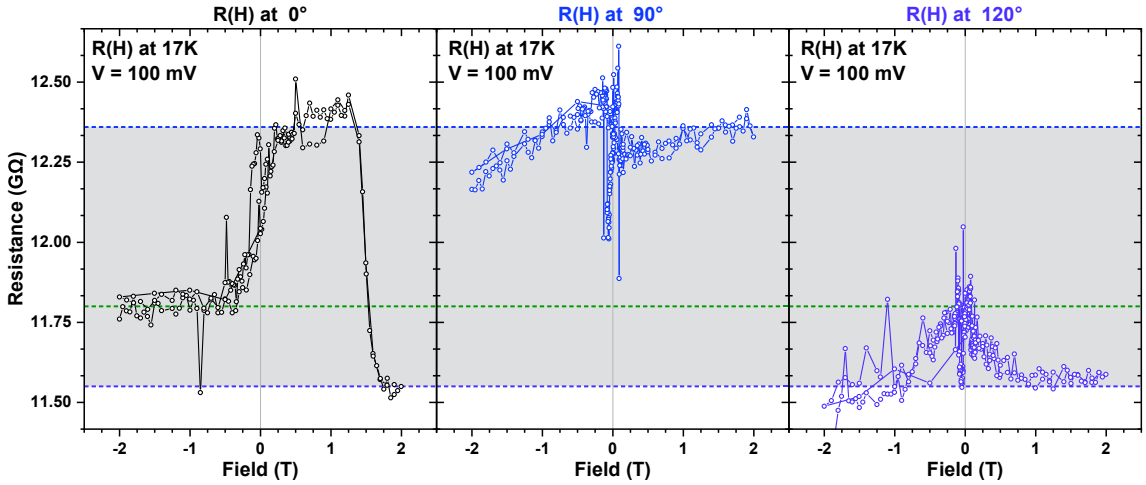

Figure 11.4: **Low 17K temperature magnetoresistance RH measurements at $0°$, $90°$ and $120°$ of externally applied magnetic field.** The angular behavior of the main resistance states $M_1(B_{ext} = -2T)$, $M_2(B_{ext} = +1T)$ and $M_{AP}(B_{ext} = +2T)$ can be attributed to the respective $0°$, $90°$ and $120°$ magnetic configurations between the bottom Fe electrode and the magnetic interfacial layers.

11.5 Temperature dependent magnetotransport

The temperature dependence of magnetoresistance was discussed in the main section in terms of temperature dependent molecular order and interfacial exchange bias. In Section 3.6. the temperature effect on magnetotransport is assigned to the thermal softening of the pinning CoPc spin-chains which can undergo a full reversal at 65K. Figure 11.5 visualizes the key RH plots acquired at the same exact conditions and differing solely on the temperature of the measurements.

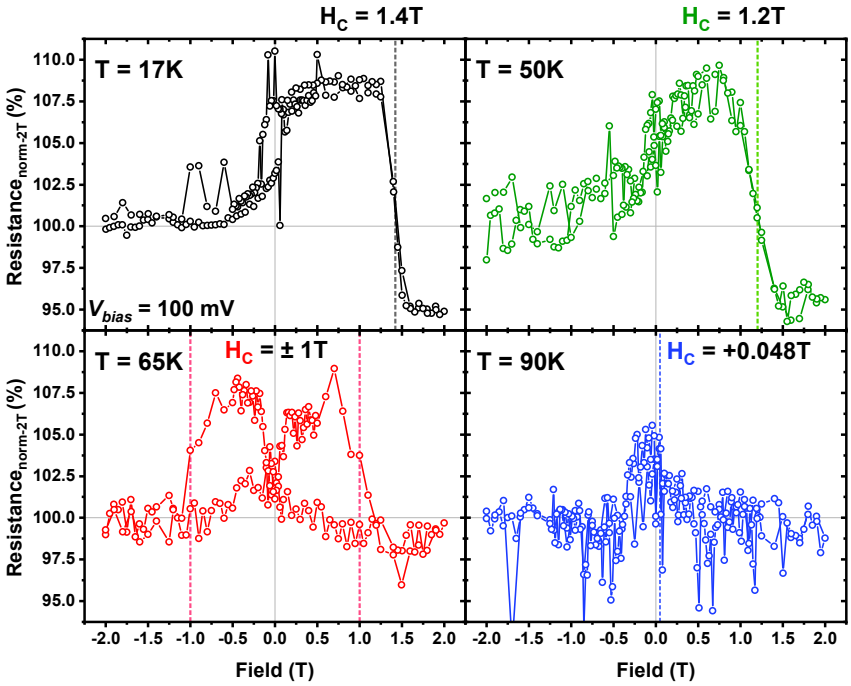

Figure 11.5: **Temperature dependence of magnetotransport measurements between 17K and 90K.** Normalized to $\mathrm{R(M_1)}$ magnetoresistance measurements were consecutively performed from 17K, 50K, 65K and 90K, at $\mathrm{V_{bias}}$ = +100mV and upon $\mathrm{H_{FC}}$ = -1T (0°) field cooling procedure. The extracted $\mathrm{H_C}$ values are indicated at each respective RH plot.

One can see that at both 17K and 50K the RH is asymmetric in field, has a single coercive field $\mathrm{H_C}$ in the opposite direction to the field cooling procedure, whereas the 65K RH is symmetric in field and contains two $\mathrm{H_C}$ values at $\mathrm{H_C}$ =±1T. This return to a symmetric RH implies that magnetic pinning is overcome by thermal energy at 65K, hence $\mathrm{R(M_1)}$ is quasi-equal to $\mathrm{R(M_{AP})}$. At 90K the MR signal is completely undetectable. The blocking temperature of 90K may originate from the exchange interactions within the molecular spin-chains or (and) the exchange energy between the molecular spin chain and the FM electrode, namely the exchange bias effect that was reported to vanish around 100K in such systems [156].

11.6 Thermally assisted molecular chain's spin-flip excitations

In the main section of the manuscript the jump in conductance was attributed to the opening of an additional inelastic channel. When this feature was compared with the multitude of reports in literature [163, 186] on CoPc spin-chains it seems coherent that it corresponds to the spin-flip excitations of the molecular spin-chains. Therefore, the threshold voltage (V_{th} = 50mV at 17K) of this channel's opening corresponds to the exchange coupling energy characterizing the spin-chain. In this supplementary section we further confirm this interpretation we compared the temperature behavior of the conductance plots. Referring to Figure 11.6, the conductance dIdV plots acquired at 17K, 50K, 72K and 90K were shifted for simplicity and indicate three main things: i) The threshold voltage V_{th} decreases from 50mV at 17K to 30mV at 50K and further decreases under an increasing temperature, ii) the quality of the signal deteriorates when T increases and is indistinguishable at 90K, iii) the effect is asymmetric with the bias polarity and the negative threshold voltage ($-V_{th}$) disappears already at 50K. This may indicate that the two interfaces Fe/CoPc and CoPc/Co have different properties.

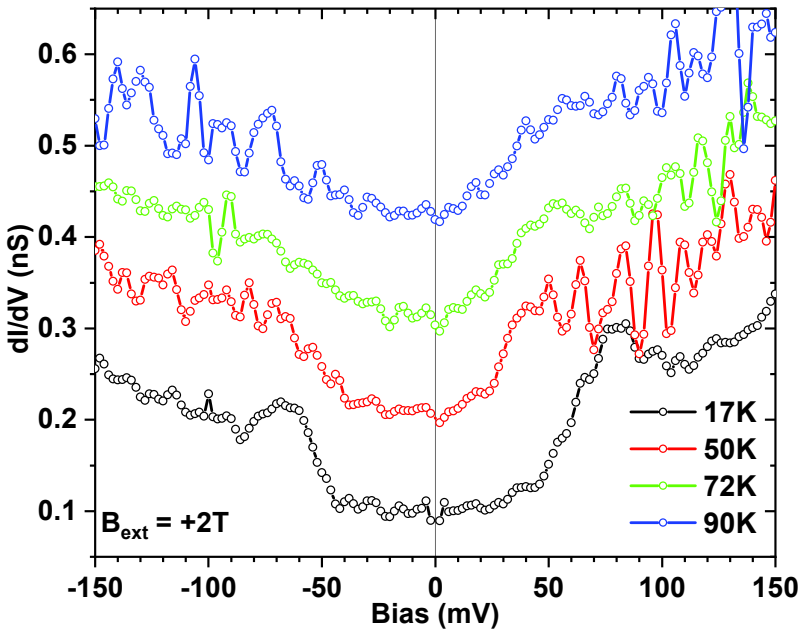

Figure 11.6: **Temperature dependence of the conductance dIdV at a +2T field.** The conductance measurements are calculated out of consecutively measured IVs in the respective temperature values. Plots are smoothed with 5 points moving average and shifted for simplicity.

As a note of mention, the conductance is independent to the magnetic field, thus these dIdV plots are in good agreement with the previously discussed in the main section IVs at ±1T.

11.7 Minor magnetoresistance loops

An interesting set of measurements was acquired at T = 60K and $V_{bias} > V_{th}$ (+58mV). We were able to capture both the huge coercive field of magnetic molecular interface H_C and the huge retention field H_{ret} which characterizes the unidirectional pinning of the system. Referring to Figure 11.7, fore loops of RHs with different field sweeps showcase the different magnetic rotations with the junction. As a note of mention, the consecutive RHs are shifter in resistance for clarity.

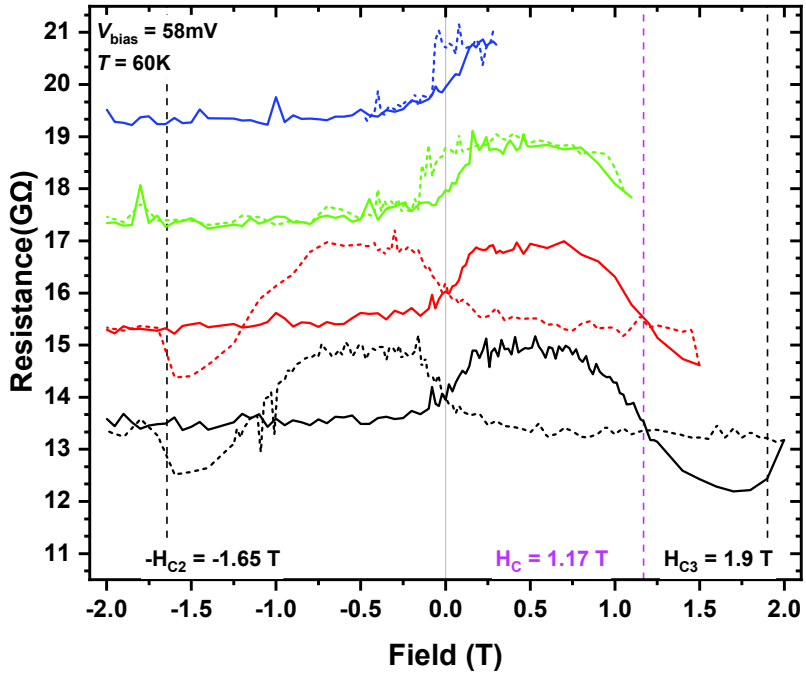

Figure 11.7: **Minor magnetoresistance loops at 60K in the excited state of the spin-chains.** Black, red, green and blue are loops measured between -2T and respectively +2T, +1.5T, +1.1T and +0.3T. Continuous line is the sweep-in and the dotted line corresponds to the sweep-back. For clarity of representation the RH loops where shifted. The resistance level of the sweep-in defines the sweep-back and therefore the shape of the RH plot, see description in the text.

The reversal of the magnetic molecular layer and the coupled to it spin-chain characterized by H_C and H_{ret} can undergo two scenarios, i) in blue and green the resistance R(H) doesn't go below $R[M_1](-2T)$ and therefore the sweep-back (dotted line) is the same as the sweep-in (continuous line). Consecutively, the RH profile is asymmetric, ii) Once the resistance R(H) reaches the low resistance state, in red and black, the sweep-back takes a different path which results in a symmetric RH profile with two H_C and H_{ret} values (black RH). In pink - H_C is the field defining the transition between $R[M_2](+0.5T)$ and $R[M_{AP}](+1.75T)$. In black - H_{ret} defines the transition between $R[M_{AP}](+1.75T)$ and $R[M_1](+2T)$ =$R[M_1]$(-2T). At low temperatures (17K) H_{ret} is much higher than the maximum 2T field achievable on our setup, hence it was only observed at 60K once it was

reduced through additional thermal energy to detectable fields. At 65K the retention field if lower that H_C, hence the reversal of the interfacial magnetic layers is complete, and the low resistance opening at high fields ($H_{ext} > H_C$) disappears.

11.8 Complementary field coolings

This section summarizes a full temperature range [300-10K] field cooling study on Fe/CoPc(16nm)/Fe junctions. The field cooling was performed twice to check the reproducibility of these observations. These junctions were processed with the same nanosphere lithography technique and are nominally of the same size as the ones discussed in the main part (Fe/CoPc/Co). The FC process was performed at $V_{bias} = 10mV$, $B_{ext} = -1$ at $0°$. At room-temperature (300K) the device's resistance is equal to $2.3k\Omega$ and it grows to $1.05G\Omega$ at 12K, the resistance increase ratio is around, $R_{12K}/R_{300K} = 10^5$. Referring to Figure 11.8, such huge increase in the device's resistance indicates: i) That thermal hopping is most probably the dominant transport mechanism, ii) That the molecular MTJ undergoes a magnetic restructurization, this effect is especially observable in the low temperature range, when the resistance "jumps" from $10M\Omega$ to $1G\Omega$ between 25K and 12K. We believe that the same effects take place in the discussed Fe/CoPc/Co junctions in the main part of this chapter.

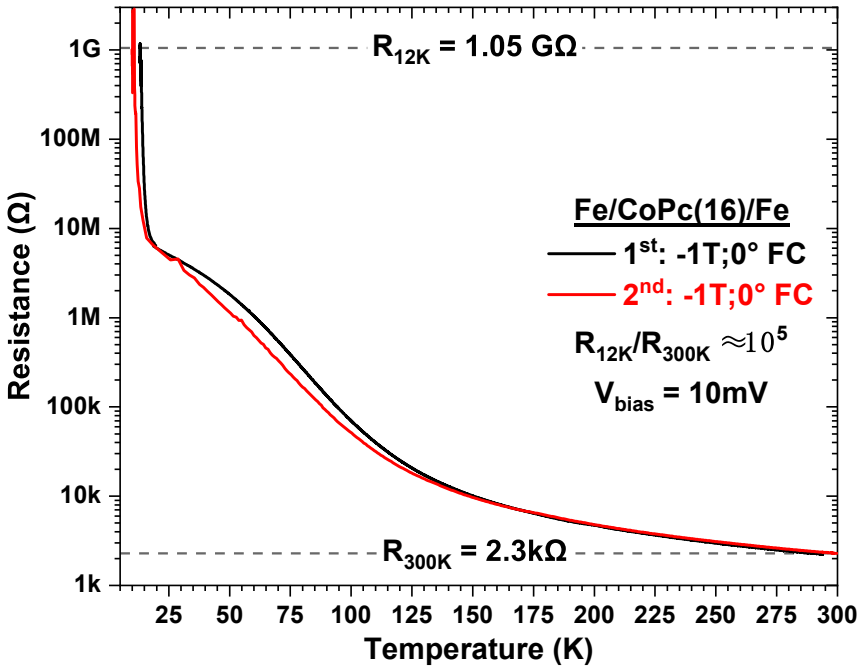

Figure 11.8: **Field cooling procedure applied to an Fe/CoPc/Fe MTJ device.** Two consecutive field coolings from 300K(RT) down to 12K(LT) under $B_{ext} = -1T$ at $0°$ and $V_{bias} = 10mV$. See for a description in the text.

Chapter 12

General conclusion

In this research work, we've highlighted the role of confined nanotransport paths in spintronic devices and the spectacular capabilities they can bring once thoughtfully crafted. We've seen in Part I that oxygen vacancies generate a particular temperature- and energy-dependent profile in the MgO band gap that alters the commonly accepted magnetotransport scheme of common-place sputtered MgO-based MTJs. Addressing these localized states with a continuous photon flux alters the tunneling symmetry-dependent potential landscape and consequently modifies the spintronic performances of the device. In Part II we've seen how the confined asymmetric profile of nanotransport paths is suited to rectify thermal fluctuations on paramagnetic centers and convert them into a current flow. This is the precise definition of an energy harvesting engine that converts thermal fluctuations of the surrounding medium into a useful electrical power. In Part III, we've seen that nanotransport paths formed by molecular spin-chains give the possibility or alter the magnetoresponse of such devices in a controllable manner. These scientific results remain highly perspective and some of the herein presented efforts are performed by our group to further investigate this subjects. For instance, during my PhD several synchrotron runs were completed to establish a novel in-operando spectroscopical technique with focalized X-rays. Shinning highly energetic element sensitive X-rays on an operating MTJ device can reveal the role of nanotransport paths in spintronic devices [88]. Our groups scientific interests are oriented towards the development and optimization of this in-operando technique to further to expand our current understanding of nanotransport paths in spintronic devices and further bring quantum physics to real-world devices.

Traduction en Français:

Conclusion général

Dans ce travail de recherche, nous avons mis en évidence le rôle des chemins de nanotransport confinés dans les dispositifs de spin-tronique et les capacités spectaculaires qu'ils peuvent apporter une fois conçus de manière réfléchie. Nous avons vu dans la partie I que les lacunes d'oxygène génèrent un profil particulier dépendant de la température et de l'énergie dans la bande interdite MgO qui modifie le schéma de magnétotransport communément accepté des MTJ à base de MgO pulvérisés en lieu commun. L'adressage de ces états localisés avec un flux de photons continu modifie le paysage potentiel dépendant de la symétrie tunnel et par conséquent modifie les performances spintroniques du

dispositif. Dans la deuxième partie, nous avons vu comment le profil asymétrique confiné des chemins de nanotransport est adapté pour recréer les fluctuations thermiques sur les centres paramagnétiques et les convertir en flux de courant. C'est la définition précise d'un moteur de récupération d'énergie qui convertit les fluctuations thermiques du milieu environnant en une puissance électrique utile. Dans la partie III, nous avons vu que les chemins de nanotransport formés par des chaînes de spin moléculaires donnent la possibilité ou modifient la magnétoréponse de tels dispositifs de manière contrôlable. Ces résultats scientifiques restent très en perspective et certains des efforts présentés ici sont réalisés par notre groupe pour approfondir ces sujets. Par exemple, au cours de mon doctorat, plusieurs essais de synchrotron ont été réalisés pour établir une nouvelle technique spectroscopique in-operando avec des rayons X focalisés. Faire briller des rayons X sensibles aux éléments hautement énergétiques sur un appareil MTJ en fonctionnement peut révéler le rôle des chemins de nanotransport dans les dispositifs spintroniques [87]. Les intérêts scientifiques de nos groupes sont orientés vers le développement et l'optimisation de cette technique in-operando afin d'élargir davantage notre compréhension actuelle des chemins de nanotransport dans les dispositifs spintroniques et d'amener davantage la physique quantique aux dispositifs du monde réel.

Bibliography

[1] Borexino Collaboration. Neutrinos from the primary proton–proton fusion process in the Sun. *Nature*, 512(7515):383–386, August 2014.

[2] P. Pavan, R. Bez, P. Olivo, and E. Zanoni. Flash memory cells-an overview. *Proceedings of the IEEE*, 85(8):1248–1271, Aug./1997.

[3] J. Bardeen. Tunnelling from a Many-Particle Point of View. *Physical Review Letters*, 6(2):57–59, January 1961.

[4] M. Julliere. Tunneling between ferromagnetic films. *Physics Letters A*, 54(3):225–226, 1975.

[5] M. N. Baibich, J. M. Broto, A. Fert, F. Nguyen Van Dau, F. Petroff, P. Etienne, G. Creuzet, A. Friederich, and J. Chazelas. Giant Magnetoresistance of (001)Fe/(001)Cr Magnetic Superlattices. *Physical Review Letters*, 61(21):2472–2475, November 1988.

[6] G. Binasch, P. Grünberg, F. Saurenbach, and W. Zinn. Enhanced magnetoresistance in layered magnetic structures with antiferromagnetic interlayer exchange. *Physical Review B*, 39(7):4828–4830, March 1989.

[7] J. S. Moodera, Lisa R. Kinder, Terrilyn M. Wong, and R. Meservey. Large Magnetoresistance at Room Temperature in Ferromagnetic Thin Film Tunnel Junctions. *Physical Review Letters*, 74(16):3273–3276, April 1995.

[8] Saied Tehrani. Status and Outlook of MRAM Memory Technology (Invited). In *2006 International Electron Devices Meeting*, pages 1–4, San Francisco, CA, USA, 2006. IEEE.

[9] A V Khvalkovskiy, D Apalkov, S Watts, R Chepulskii, R S Beach, A Ong, X Tang, A Driskill-Smith, W H Butler, P B Visscher, D Lottis, E Chen, V Nikitin, and M Krounbi. Basic principles of STT-MRAM cell operation in memory arrays. *Journal of Physics D: Applied Physics*, 46(7):074001, February 2013.

[10] F Schleicher, U Halisdemir, D Lacour, M Gallart, S Boukari, G Schmerber, V Davesne, P Panissod, D Halley, H Majjad, Y Henry, B Leconte, a Boulard, D Spor, N Beyer, C Kieber, E Sternitzky, O Cregut, M Ziegler, F Montaigne, E Beaurepaire, P Gilliot, M Hehn, and M Bowen. Localized states in advanced dielectrics from the vantage of spin- and symmetry-polarized tunnelling across MgO. *Nature communications*, 5:4547, 2014.

[11] F Schleicher, U Halisdemir, E Urbain, D Lacour, M Gallart, S Boukari, F Montaigne, E Beaurepaire, P Gilliot, M Hehn, and M Bowen. MgO magnetic tunnel junctions of enduring F-type upon annealing. *Journal of Physics D: Applied Physics*, 48(43):435004, November 2015.

[12] Beata Taudul, Elmer Nahuel Monteblanco, Ufuk Halisdemir, Daniel Lacour, Filip Schleicher, François Montaigne, Eric Beaurepaire, Samy Boukari, Michel Hehn, Mébarek Alouani, and Martin Bowen. Tunneling Spintronics across MgO Driven by Double Oxygen Vacancies. *Advanced Electronic Materials*, 3(7):1600390, July 2017.

[13] Beata Taudul, M. Bowen, and M. Alouani. Impact of single and double oxygen vacancies on electronic transport in Fe/MgO/Fe magnetic tunnel junctions. *arXiv:1904.02554 [cond-mat]*, April 2019.

[14] F Schleicher, B Taudul, U Halisdemir, K Katcko, E Monteblanco, D Lacour, S Boukari, F Montaigne, E Urbain, L M Kandpal, J Arabski, W Weber, E Beaurepaire, M Hehn, M Alouani, and M Bowen. Consolidated picture of tunnelling spintronics across oxygen vacancy states in MgO. *Journal of Physics D: Applied Physics*, 52(30):305302, July 2019.

[15] G. H. Rosenblatt, M. W. Rowe, G. P. Williams, R. T. Williams, and Y. Chen. Luminescence of F and F+ centers in magnesium oxide. *Physical Review B*, 39(14):10309–10318, 1989.

[16] Evgeny Y Tsymbal and Igor Žutić. *SPIN TRANSPORT AND MAGNETISM*. CRC Press, 2012.

[17] John G. Simmons. Generalized Formula for the Electric Tunnel Effect between Similar Electrodes Separated by a Thin Insulating Film. *Journal of Applied Physics*, 34(6):1793–1803, June 1963.

[18] W. F. Brinkman, R. C. Dynes, and J. M. Rowell. Tunneling Conductance of Asymmetrical Barriers. *Journal of Applied Physics*, 41(5):1915–1921, April 1970.

[19] R. Meservey and P.M. Tedrow. Spin polarization of tunneling electrons from films of Fe, Co, Ni, and Gd. *Solid State Communications*, 11(2):333–336, 1972.

[20] R Meservey and P M Tedrow. Spin-polarized electron tunneling. *Physics Reports*, 238(4):71, 1994.

[21] LeClair PR (Patrick). *Fundamental Aspects of Spin Polarized Tunneling : Magnetic Tunnel Junctions and Spin Filters*. PhD thesis, Technishe Universiteit Eindhoven, 2002.

[22] Halisdemir Ufuk. Probing the impact of structural defects on spin dependent tunneling using photons. *Thesis*, 200, 2016.

[23] Xiu-Feng Han, Mikihiko Oogane, Hitoshi Kubota, Yasuo Ando, and Terunobu Miyazaki. Fabrication of high-magnetoresistance tunnel junctions using Co75Fe25 ferromagnetic electrodes. *Applied Physics Letters*, 77(2):283–285, July 2000.

[24] Yu Lu, X. W. Li, G. Q. Gong, Gang Xiao, A. Gupta, P. Lecoeur, J. Z. Sun, Y. Y. Wang, and V. P. Dravid. Large magnetotunneling effect at low magnetic fields in micrometer-scale epitaxial La 0.67 Sr 0.33 Mn O 3 tunnel junctions. *Physical Review B*, 54(12):R8357–R8360, September 1996.

[25] J. M. De Teresa. Role of Metal-Oxide Interface in Determining the Spin Polarization of Magnetic Tunnel Junctions. *Science*, 286(5439):507–509, October 1999.

[26] Guo-Xing Miao, Markus Münzenberg, and Jagadeesh S Moodera. Tunneling path toward spintronics. *Reports on Progress in Physics*, 74(3):036501, March 2011.

[27] X.-G. Zhang and W. H. Butler. Large magnetoresistance in bcc Co / Mg O / Co and Fe Co / Mg O / Fe Co tunnel junctions. *Physical Review B*, 70(17), November 2004.

[28] M. Klaua, D. Ullmann, J. Barthel, W. Wulfhekel, J. Kirschner, R. Urban, T. L. Monchesky, A. Enders, J. F. Cochran, and B. Heinrich. Growth, structure, electronic, and magnetic properties of MgO/Fe(001) bilayers and Fe/MgO/Fe(001) trilayers. *Physical Review B*, 64(13):134411, September 2001.

[29] Stuart S. P. Parkin, Christian Kaiser, Alex Panchula, Philip M. Rice, Brian Hughes, Mahesh Samant, and See-Hun Yang. Giant tunnelling magnetoresistance at room temperature with MgO (100) tunnel barriers. *Nature Materials*, 3(12):862–867, December 2004.

[30] S Yuasa and D D Djayaprawira. Giant tunnel magnetoresistance in magnetic tunnel junctions with a crystalline MgO(0 0 1) barrier. *Journal of Physics D: Applied Physics*, 40(21):R337–R354, 2007.

[31] W. H. Butler, X.-G. Zhang, T. C. Schulthess, and J. M. MacLaren. Spin-dependent tunneling conductance of Fe/MgO/Fe sandwiches. *Physical Review B*, 63(5):054416, 2001.

[32] C Tiusan, F Greullet, M Hehn, F Montaigne, S Andrieu, and A Schuhl. Spin tunnelling phenomena in single-crystal magnetic tunnel junction systems. *Journal of Physics: Condensed Matter*, 19(16):165201, April 2007.

[33] Ph. Mavropoulos, N. Papanikolaou, and P. H. Dederichs. Complex Band Structure and Tunneling through Ferromagnet / Insulator / Ferromagnet Junctions. *Physical Review Letters*, 85(5):1088–1091, July 2000.

[34] P.H. Dederichs, Ph. Mavropoulos, O. Wunnicke, N. Papanikolaou, V. Bellini, R. Zeller, V. Drchal, and J. Kudrnovský. Importance of complex band structure

and resonant states for tunneling. *Journal of Magnetism and Magnetic Materials*, 240(1-3):108–113, February 2002.

[35] William H Butler. Tunneling magnetoresistance from a symmetry filtering effect. *Science and Technology of Advanced Materials*, 9(1):014106, January 2008.

[36] X-G Zhang and W H Butler. Band structure, evanescent states, and transport in spin tunnel junctions. *Journal of Physics: Condensed Matter*, 15(41):R1603–R1639, October 2003.

[37] Shinji Yuasa, Taro Nagahama, Akio Fukushima, Yoshishige Suzuki, and Koji Ando. Giant room-temperature magnetoresistance in single-crystal Fe/MgO/Fe magnetic tunnel junctions. *Nature Materials*, 3(12):868–871, December 2004.

[38] David D Djayaprawira, Koji Tsunekawa, Motonobu Nagai, Hiroki Maehara, Shinji Yamagata, Naoki Watanabe, Shinji Yuasa, Yoshishige Suzuki, and Koji Ando. 230% room-temperature magnetoresistance in CoFeB/ MgO/ CoFeB magnetic tunnel junctions. *Appl. Phys. Lett.*, 86(092502):3, 2005.

[39] J. Hayakawa, S. Ikeda, Y. M. Lee, F. Matsukura, and H. Ohno. Effect of high annealing temperature on giant tunnel magnetoresistance ratio of CoFeB/MgO/ CoFeB magnetic tunnel junctions. *Applied Physics Letters*, 89(23):232510, December 2006.

[40] S. Ikeda, J. Hayakawa, Y. Ashizawa, Y. M. Lee, K. Miura, H. Hasegawa, M. Tsunoda, F. Matsukura, and H. Ohno. Tunnel magnetoresistance of 604% at 300 K by suppression of Ta diffusion in CoFeBMgOCoFeB pseudo-spin-valves annealed at high temperature. *Applied Physics Letters*, 93(8):7–10, 2008.

[41] T Miyazaki and N Tezuka. Giant magnetic tunneling effect in Fe/Al2O3/Fejunction. *Journal of Magnetism and Magnetic Materials*, page 4, 1995.

[42] J. Faure-Vincent, C. Tiusan, E. Jouguelet, F. Canet, M. Sajieddine, C. Bellouard, E. Popova, M. Hehn, F. Montaigne, and A. Schuhl. High tunnel magnetoresistance in epitaxial Fe/MgO/Fe tunnel junctions. *Applied Physics Letters*, 82(25):4507–4509, June 2003.

[43] M. Bowen, V. Cros, F. Petroff, A. Fert, C. Martıńez Boubeta, J. L. Costa-Krämer, J. V. Anguita, A. Cebollada, F. Briones, J. M. de Teresa, L. Morellón, M. R. Ibarra, F. Güell, F. Peiró, and A. Cornet. Large magnetoresistance in Fe/MgO/FeCo(001) epitaxial tunnel junctions on GaAs(001). *Applied Physics Letters*, 79(11):1655–1657, September 2001.

[44] Shinji Yuasa, Akio Fukushima, Taro Nagahama, Koji Ando, and Yoshishige Suzuki. High Tunnel Magnetoresistance at Room Temperature in Fully Epitaxial Fe/MgO/Fe Tunnel Junctions due to Coherent Spin-Polarized Tunneling. *Japanese Journal of Applied Physics*, 43(No. 4B):L588–L590, April 2004.

[45] Shinji Yuasa, Toshikazu Katayama, Taro Nagahama, Akio Fukushima, Hitoshi Kubota, Yoshishige Suzuki, and Koji Ando. Giant tunneling magnetoresistance in fully epitaxial body-centered-cubic Co/MgO/Fe magnetic tunnel junctions. *Applied Physics Letters*, 87(22):222508, November 2005.

[46] Shinji Yuasa, Akio Fukushima, Hitoshi Kubota, Yoshishige Suzuki, and Koji Ando. Giant tunneling magnetoresistance up to 410% at room temperature in fully epitaxial CoMgOCo magnetic tunnel junctions with bcc Co(001) electrodes. *Applied Physics Letters*, 89(4):042505, July 2006.

[47] U. Halisdemir, F. Schleicher, D. J. Kim, B. Taudul, D. Lacour, W. S. Choi, M. Gallart, S. Boukari, G. Schmerber, V. Davesne, P. Panissod, D. Halley, H. Majjad, Y. Henry, B. Leconte, A. Boulard, D. Spor, N. Beyer, C. Kieber, E. Sternitzky, O. Cregut, M. Ziegler, F. Montaigne, J. Arabski, E. Beaurepaire, W. Jo, M. Alouani, P. Gilliot, M. Hehn, and M. Bowen. Oxygen-vacancy driven tunnelling spintronics across mgo. page 99310H, San Diego, California, United States, September 2016.

[48] F. Bonell, S. Andrieu, F. Bertran, P. Lefevre, A.T. Ibrahimi, E. Snoeck, C.-V. Tiusan, and F. Montaigne. MgO-Based Epitaxial Magnetic Tunnel Junctions Using Fe-V Electrodes. *IEEE Transactions on Magnetics*, 45(10):3467–3471, October 2009.

[49] S.G. Wang, G. Han, G.H. Yu, Y. Jiang, C. Wang, A. Kohn, and R.C.C. Ward. Evidence for FeO formation at the Fe/MgO interface in epitaxial TMR structure by X-ray photoelectron spectroscopy. *Journal of Magnetism and Magnetic Materials*, 310(2):1935–1936, March 2007.

[50] X.-G. Zhang, W. H. Butler, and Amrit Bandyopadhyay. Effects of the iron-oxide layer in Fe-FeO-MgO-Fe tunneling junctions. *Physical Review B*, 68(9):092402, September 2003.

[51] F. Bonell, S. Murakami, Y. Shiota, T. Nozaki, T. Shinjo, and Y. Suzuki. Large change in perpendicular magnetic anisotropy induced by an electric field in FePd ultrathin films. *Applied Physics Letters*, 98(23):10–13, 2011.

[52] C Tiusan, M Sicot, J Faure-Vincent, M Hehn, C Bellouard, F Montaigne, S Andrieu, and A Schuhl. Static and dynamic aspects of spin tunnelling in crystalline magnetic tunnel junctions. *Journal of Physics: Condensed Matter*, 18(3):941–956, January 2006.

[53] F. Djeghloul, F. Ibrahim, M. Cantoni, M. Bowen, L. Joly, S. Boukari, P. Ohresser, F. Bertran, P. Le Fèvre, P. Thakur, F. Scheurer, T. Miyamachi, R. Mattana, P. Seneor, A. Jaafar, C. Rinaldi, S. Javaid, J. Arabski, J. P Kappler, W. Wulfhekel, N. B. Brookes, R. Bertacco, A. Taleb-Ibrahimi, M. Alouani, E. Beaurepaire, and W. Weber. Direct observation of a highly spin-polarized organic spinterface at room temperature. *Scientific Reports*, 3(1), December 2013.

[54] Clément Barraud, Pierre Seneor, Richard Mattana, Stéphane Fusil, Karim Bouzehouane, Cyrile Deranlot, Patrizio Graziosi, Luis Hueso, Ilaria Bergenti, Valentin Dediu, Frédéric Petroff, and Albert Fert. Unravelling the role of the interface for spin injection into organic semiconductors. *Nature Physics*, 6(8):615–620, August 2010.

[55] Xeniya Kozina, Siham Ouardi, Benjamin Balke, Gregory Stryganyuk, Gerhard H. Fecher, Claudia Felser, Shoji Ikeda, Hideo Ohno, and Eiji Ikenaga. A nondestructive analysis of the B diffusion in Ta–CoFeB–MgO–CoFeB–Ta magnetic tunnel junctions by hard x-ray photoemission. *Applied Physics Letters*, 96(7):072105, February 2010.

[56] A. A. Greer, A. X. Gray, S. Kanai, A. M. Kaiser, S. Ueda, Y. Yamashita, C. Bordel, G. Palsson, N. Maejima, S.-H. Yang, G. Conti, K. Kobayashi, S. Ikeda, F. Matsukura, H. Ohno, C. M. Schneider, J. B. Kortright, F. Hellman, and C. S. Fadley. Observation of boron diffusion in an annealed Ta/CoFeB/MgO magnetic tunnel junction with standing-wave hard x-ray photoemission. *Applied Physics Letters*, 101(20):202402, November 2012.

[57] H. Kurt, K. Rode, K. Oguz, M. Boese, C. C. Faulkner, and J. M. D. Coey. Boron diffusion in magnetic tunnel junctions with MgO (001) barriers and CoFeB electrodes. *Applied Physics Letters*, 96(26):262501, June 2010.

[58] Toyoo Miyajima, Takahiro Ibusuki, Shinjiro Umehara, Masashige Sato, Shin Eguchi, Mineharu Tsukada, and Yuji Kataoka. Transmission electron microscopy study on the crystallization and boron distribution of CoFeB/MgO/CoFeB magnetic tunnel junctions with various capping layers. *Applied Physics Letters*, 94(12):122501, March 2009.

[59] H. Sato, E. C I Enobio, M. Yamanouchi, S. Ikeda, S. Fukami, S. Kanai, F. Matsukura, and H. Ohno. Properties of magnetic tunnel junctions with a MgO/CoFeB/Ta/CoFeB/MgO recording structure down to junction diameter of 11nm. *Applied Physics Letters*, 105(6):2012–2016, 2014.

[60] Zhaoqiang Bai, Lei Shen, Qingyun Wu, Minggang Zeng, Jian-Sheng Wang, Guchang Han, and Yuan Ping Feng. Boron diffusion induced symmetry reduction and scattering in CoFeB/MgO/CoFeB magnetic tunnel junctions. *Physical Review B*, 87(1):014114, January 2013.

[61] Zhongming Zeng, Giovanni Finocchio, Baoshun Zhang, Pedram Khalili Amiri, Jordan A. Katine, Ilya N. Krivorotov, Yiming Huai, Juergen Langer, Bruno Azzerboni, Kang L. Wang, and Hongwen Jiang. Ultralow-current-density and bias-field-free spin-transfer nano-oscillator. *Scientific Reports*, 3(1):1426, December 2013.

[62] H Meng, R Sbiaa, S Y H Lua, C C Wang, M A K Akhtar, S K Wong, P Luo, C J P Carlberg, and K S A Ang. Low current density induced spin-transfer torque

switching in CoFeB–MgO magnetic tunnel junctions with perpendicular anisotropy. *Journal of Physics D: Applied Physics*, 44(40):405001, October 2011.

[63] J. M. Teixeira, J. Ventura, J. P. Araujo, J. B. Sousa, P. Wisniowski, S. Cardoso, and P. P. Freitas. Resonant Tunneling through Electronic Trapping States in Thin MgO Magnetic Junctions. *Physical Review Letters*, 106(19):196601, May 2011.

[64] Chang He Shang, Janusz Nowak, Ronnie Jansen, and Jagadeesh S. Moodera. Temperature dependence of magnetoresistance and surface magnetization in ferromagnetic tunnel junctions. *Physical Review B*, 58(6):R2917–R2920, August 1998.

[65] Gerrit E. W. Bauer, Eiji Saitoh, and Bart J. van Wees. Spin caloritronics. *Nature Materials*, 11(5):391–399, May 2012.

[66] V. Drewello, J. Schmalhorst, A. Thomas, and G. Reiss. Evidence for strong magnon contribution to the TMR temperature dependence in MgO based tunnel junctions. *Physical Review B*, 77(1):014440, January 2008.

[67] Q. L. Ma, S. G. Wang, J. Zhang, Yan Wang, R. C. C. Ward, C. Wang, A. Kohn, X.-G. Zhang, and X. F. Han. Temperature dependence of resistance in epitaxial Fe/MgO/Fe magnetic tunnel junctions. *Applied Physics Letters*, 95(5):052506, August 2009.

[68] J. M. Teixeira, J. Ventura, J. P. Araujo, J. B. Sousa, P. Wisniowski, and P. P. Freitas. Tunneling processes in thin MgO magnetic junctions. *Applied Physics Letters*, 96(26):262506, June 2010.

[69] Ayaz Arif Khan, J. Schmalhorst, G. Reiss, G. Eilers, M. Münzenberg, H. Schuhmann, and M. Seibt. Elastic and inelastic conductance in Co-Fe-B/MgO/Co-Fe-B magnetic tunnel junctions. *Physical Review B*, 82(6):064416, August 2010.

[70] T. V. Shahbazyan and M. E. Raikh. Two-channel resonant tunneling. *Physical Review B*, 49(24):17123–17129, June 1994.

[71] Yizi Xu, D. Ephron, and M. R. Beasley. Directed inelastic hopping of electrons through metal-insulator-metal tunnel junctions. *Physical Review B*, 52(4):2843–2859, July 1995.

[72] Y. Lu, M. Tran, H. Jaffrès, P. Seneor, C. Deranlot, F. Petroff, J-M. George, B. Lépine, S. Ababou, and G. Jézéquel. Spin-Polarized Inelastic Tunneling through Insulating Barriers. *Physical Review Letters*, 102(17):176801, April 2009.

[73] Patrick Rinke, André Schleife, Emmanouil Kioupakis, Anderson Janotti, Claudia Rödl, Friedhelm Bechstedt, Matthias Scheffler, and Chris G. Van de Walle. First-Principles Optical Spectra for F Centers in MgO. *Physical Review Letters*, 108(12):126404, March 2012.

[74] Y. Uenaka and T. Uchino. Photoexcitation, trapping, and recombination processes of the F -type centers in lasing MgO microcrystals. *Physical Review B*, 83(19):195108, May 2011.

[75] R. González, M. A. Monge, J. E. Muñoz Santiuste, R. Pareja, Y. Chen, E. Kotomin, M. M. Kukla, and A. I. Popov. Photoconversion of F-type centers in thermochemically reduced MgO single crystals. *Physical Review B*, 59(7):4786–4790, February 1999.

[76] G. X. Miao, Y. J. Park, J. S. Moodera, M. Seibt, G. Eilers, and M. Münzenberg. Disturbance of Tunneling Coherence by Oxygen Vacancy in Epitaxial Fe / MgO / Fe Magnetic Tunnel Junctions. *Physical Review Letters*, 100(24):246803, June 2008.

[77] J. P. Velev, K. D. Belashchenko, S. S. Jaswal, and E. Y. Tsymbal. Effect of oxygen vacancies on spin-dependent tunneling in FeMgOFe magnetic tunnel junctions. *Applied Physics Letters*, 90(7):2–5, 2007.

[78] J. P. Velev, M. Ye. Zhuravlev, K. D. Belashchenko, S. S. Jaswal, E. Y. Tsymbal, T. Katayama, and S. Yuasa. Defect-Mediated Properties of Magnetic Tunnel Junctions. *IEEE Transactions on Magnetics*, 43(6):2770–2775, June 2007.

[79] Youqi Ke, Ke Xia, and Hong Guo. Oxygen-Vacancy-Induced Diffusive Scattering in Fe / MgO / Fe Magnetic Tunnel Junctions. *Physical Review Letters*, 105(23):236801, November 2010.

[80] Lawrence A. Kappers, Roger L. Kroes, and Eugene B. Hensley. F + and F ′ Centers in Magnesium Oxide. *Physical Review B*, 1(10):4151–4157, May 1970.

[81] Y. Chen, V. M. Orera, R. Gonzalez, R. T. Williams, G. P. Williams, G. H. Rosenblatt, and G. J. Pogatshnik. Effect of substitutional hydride ions on the charge states of oxygen vacancies in thermochemically reduced CaO and MgO. *Physical Review B*, 42(2):1410–1416, July 1990.

[82] D. J. Kim, W. S. Choi, F. Schleicher, R. H. Shin, S. Boukari, V. Davesne, C. Kieber, J. Arabski, G. Schmerber, E. Beaurepaire, W. Jo, and M. Bowen. Control of defect-mediated tunneling barrier heights in ultrathin MgO films. *Applied Physics Letters*, 97(26):1–4, 2010.

[83] Keith P. McKenna and Jochen Blumberger. Crossover from incoherent to coherent electron tunneling between defects in MgO. *Physical Review B - Condensed Matter and Materials Physics*, 86(24):1–5, 2012.

[84] Faiz Dahmani. Effect of Seed Layer on Room Temperature Tunnel Magnetoresistance of MgO Barriers Formed by Radical Oxidation in IrMn-Based Magnetic Tunnel Junctions. *Japanese Journal of Applied Physics*, 51:043002, March 2012.

[85] J. Bernos, M. Hehn, F. Montaigne, C. Tiusan, D. Lacour, M. Alnot, B. Negulescu, G. Lengaigne, E. Snoeck, and F. G. Aliev. Impact of electron-electron interactions induced by disorder at interfaces on spin-dependent tunneling in Co-Fe-B/MgO/Co-Fe-B magnetic tunnel junctions. *Physical Review B - Condensed Matter and Materials Physics*, 82(6):1–4, 2010.

[86] P. Rottländer, M. Hehn, and A. Schuhl. Determining the interfacial barrier height and its relation to tunnel magnetoresistance. *Physical Review B*, 65(5), January 2002.

[87] F M Smits. Measurement of Sheet Resistivities with the Four-Point Probe, 1957.

[88] Michał Studniarek, Ufuk Halisdemir, Filip Schleicher, Beata Taudul, Etienne Urbain, Samy Boukari, Marie Hervé, Charles-Henri Lambert, Abbass Hamadeh, Sebastien Petit-Watelot, Olivia Zill, Daniel Lacour, Loïc Joly, Fabrice Scheurer, Guy Schmerber, Victor Da Costa, Anant Dixit, Pierre André Guitard, Manuel Acosta, Florian Leduc, Fadi Choueikani, Edwige Otero, Wulf Wulfhekel, François Montaigne, Elmer Nahuel Monteblanco, Jacek Arabski, Philippe Ohresser, Eric Beaurepaire, Wolfgang Weber, Mébarek Alouani, Michel Hehn, and Martin Bowen. Probing a Device's Active Atoms. *Advanced Materials*, 29(19):1606578, May 2017.

[89] Christian Kaiser, Alex F. Panchula, and Stuart S. P. Parkin. Finite Tunneling Spin Polarization at the Compensation Point of Rare-Earth-Metal–Transition-Metal Alloys. *Physical Review Letters*, 95(4):047202, July 2005.

[90] M. Bowen, A. Barthélémy, V. Bellini, M. Bibes, P. Seneor, E. Jacquet, J.-P. Contour, and P. H. Dederichs. Observation of Fowler–Nordheim hole tunneling across an electron tunnel junction due to total symmetry filtering. *Physical Review B*, 73(14):140408, April 2006.

[91] F. Montaigne, M. Hehn, and A. Schuhl. Tunnel barrier parameters and magnetoresistance in the parabolic band model. *Physical Review B*, 64(14):144402, August 2001.

[92] Jochen Heyd, Gustavo E. Scuseria, and Matthias Ernzerhof. Hybrid functionals based on a screened Coulomb potential. *The Journal of Chemical Physics*, 118(18):8207–8215, May 2003.

[93] David Domínguez-Ariza, Carmen Sousa, Francesc Illas, Davide Ricci, and Gianfranco Pacchioni. Ground- and excited-state properties of M-center oxygen vacancy aggregates in the bulk and surface of MgO. *Physical Review B*, 68(5):054101, August 2003.

[94] Biswajit Choudhury and Amarjyoti Choudhury. Microstructural, optical and magnetic properties study of nanocrystalline MgO. *Materials Research Express*, 1(2):025026, May 2014.

[95] D O O'Connell, B Henderson, and J M Bolton. UNIAXIAL STRESS AND POLARISATION STUDIES OF F2 CENTRE LUMINESCENCE IN MgO. *Solid State Communications*, 38(4):3, 1980.

[96] J D Bolton, B Henderson, and D O O'Connell. PHOTOLUMINESCENCE OF F2(2+) CENTERS IN ADDITIVELY COLOURED MAGNESIUM-OXIDE. *Solid State Communications*, 38(4):4, 1980.

[97] U. Martens, J. Walowski, T. Schumann, M. Mansurova, a. Boehnke, T. Huebner, G. Reiss, a. Thomas, and M. Münzenberg. Pumping laser excited spins through MgO barriers. *Journal of Physics D: Applied Physics*, 50(144003):1–12, 2017.

[98] R Landauer. Irreversibility and Heat Generation in the Computing Process. *IBM Journal*, page 9, 1961.

[99] Pham Nam Hai, Shinobu Ohya, Masaaki Tanaka, Stewart E. Barnes, and Sadamichi Maekawa. Electromotive force and huge magnetoresistance in magnetic tunnel junctions. *Nature*, 458(7237):489–492, March 2009.

[100] Rafael Sánchez and Markus Büttiker. Optimal energy quanta to current conversion. *Physical Review B*, 83(8):085428, February 2011.

[101] Andrew N. Jordan, Björn Sothmann, Rafael Sánchez, and Markus Büttiker. Powerful and efficient energy harvester with resonant-tunneling quantum dots. *Physical Review B*, 87(7):075312, February 2013.

[102] Guo-Xing Miao, Joonyeon Chang, Badih A. Assaf, Donald Heiman, and Jagadeesh S. Moodera. Spin regulation in composite spin-filter barrier devices. *Nature Communications*, 5, April 2014.

[103] Björn Sothmann, Rafael Sánchez, and Andrew N Jordan. Thermoelectric energy harvesting with quantum dots. *Nanotechnology*, 26(3):032001, January 2015.

[104] J. V. Koski, A. Kutvonen, I. M. Khaymovich, T. Ala-Nissila, and J. P. Pekola. On-Chip Maxwell's Demon as an Information-Powered Refrigerator. *Physical Review Letters*, 115(26), December 2015.

[105] Holger Thierschmann, Rafael Sánchez, Björn Sothmann, Fabian Arnold, Christian Heyn, Wolfgang Hansen, Hartmut Buhmann, and Laurens W. Molenkamp. Three-terminal energy harvester with coupled quantum dots. *Nature Nanotechnology*, 10(10):854–858, October 2015.

[106] Giuliano Benenti, Giulio Casati, Keiji Saito, and Robert S. Whitney. Fundamental aspects of steady-state conversion of heat to work at the nanoscale. *Physics Reports*, 694:1–124, June 2017.

[107] Krzysztof Ptaszyński. Autonomous quantum Maxwell's demon based on two exchange-coupled quantum dots. *Physical Review E*, 97(1), January 2018.

[108] Rafael Sánchez, Peter Samuelsson, and Patrick P. Potts. Autonomous conversion of information to work in quantum dots. *arXiv:1907.02866 [cond-mat, physics:quant-ph]*, July 2019.

[109] K. Katcko, E. Urbain, B. Taudul, F. Schleicher, J. Arabski, E. Beaurepaire, B. Vileno, D. Spor, W. Weber, D. Lacour, S. Boukari, M. Hehn, M. Alouani, J. Fransson, and M. Bowen. Spin-driven electrical power generation at room temperature. *Communications Physics*, 2(1):116, December 2019.

[110] F. Djeghloul, G. Garreau, M. Gruber, L. Joly, S. Boukari, J. Arabski, H. Bulou, F. Scheurer, A. Hallal, F. Bertran, P. Le Fèvre, A. Taleb-Ibrahimi, W. Wulfhekel, E. Beaurepaire, S. Hajjar-Garreau, P. Wetzel, M. Bowen, and W. Weber. Highly spin-polarized carbon-based spinterfaces. *Carbon*, 87:269–274, June 2015.

[111] G. Jaliel, R. K. Puddy, R. Sánchez, A. N. Jordan, B. Sothmann, I. Farrer, J. P. Griffiths, D. A. Ritchie, and C. G. Smith. Experimental realization of a quantum dot energy harvester. *arXiv:1901.10561 [cond-mat]*, January 2019.

[112] K. Uchida, S. Takahashi, K. Harii, J. Ieda, W. Koshibae, K. Ando, S. Maekawa, and E. Saitoh. Observation of the spin Seebeck effect. *Nature*, 455(7214):778–781, October 2008.

[113] T Kuschel, M Czerner, J Walowski, A Thomas, H W Schumacher, G Reiss, C Heiliger, and M Münzenberg. Tunnel magneto-Seebeck effect. *Journal of Physics D: Applied Physics*, 52(13):133001, March 2019.

[114] Tim Böhnert, Roberta Dutra, Rubem L. Sommer, Elvira Paz, Santiago Serrano-Guisan, Ricardo Ferreira, and Paulo P. Freitas. Influence of the thermal interface resistance on the thermovoltage of a magnetic tunnel junction. *Physical Review B*, 95(10):104441, March 2017.

[115] T. Böhnert, E. Paz, R. Ferreira, and P.P. Freitas. Magnetic tunnel junction thermocouple for thermoelectric power harvesting. *Physics Letters A*, 382(21):1437–1440, May 2018.

[116] Shinya Kano and Minoru Fujii. Conversion efficiency of an energy harvester based on resonant tunneling through quantum dots with heat leakage. *Nanotechnology*, 28(9):095403, March 2017.

[117] Paolo Andrea Erdman, Francesco Mazza, Riccardo Bosisio, Giuliano Benenti, Rosario Fazio, and Fabio Taddei. Thermoelectric properties of an interacting quantum dot based heat engine. *Physical Review B*, 95(24):245432, June 2017.

[118] Jagadeesh S Moodera, Tiffany S Santos, and Taro Nagahama. The phenomena of spin-filter tunnelling. *Journal of Physics: Condensed Matter*, 19(16):165202, April 2007.

[119] Mirko Cinchetti, V. Alek Dediu, and Luis E. Hueso. Activating the molecular spinterface. *Nature Materials*, 16(5):507–515, April 2017.

[120] Sophie Delprat, Marta Galbiati, Sergio Tatay, Benoît Quinard, Clément Barraud, Frédéric Petroff, Pierre Seneor, and Richard Mattana. Molecular spintronics: The role of spin-dependent hybridization. *Journal of Physics D: Applied Physics*, 51(47):473001, November 2018.

[121] Maciej Misiorny, Michael Hell, and Maarten R. Wegewijs. Spintronic magnetic anisotropy. *Nature Physics*, 9(12):801–805, October 2013.

[122] Jonas Fransson, Jie Ren, and Jian-Xin Zhu. Electrical and Thermal Control of Magnetic Exchange Interactions. *Physical Review Letters*, 113(25), December 2014.

[123] Guo-Xing Miao and Jagadeesh S. Moodera. Spin manipulation with magnetic semiconductor barriers. *Physical Chemistry Chemical Physics*, 17(2):751–761, 2015.

[124] J. S. Parker, S. M. Watts, P. G. Ivanov, and P. Xiong. Spin Polarization of CrO 2 at and across an Artificial Barrier. *Physical Review Letters*, 88(19):196601, April 2002.

[125] Georg M. Müller, Jakob Walowski, Marija Djordjevic, Gou-Xing Miao, Arunava Gupta, Ana V. Ramos, Kai Gehrke, Vasily Moshnyaga, Konrad Samwer, Jan Schmalhorst, Andy Thomas, Andreas Hütten, Günter Reiss, Jagadeesh S. Moodera, and Markus Münzenberg. Spin polarization in half-metals probed by femtosecond spin excitation. *Nature Materials*, 8(1):56–61, January 2009.

[126] M. Bowen, A. Barthélémy, M. Bibes, E. Jacquet, J.-P. Contour, A. Fert, F. Ciccacci, L. Duò, and R. Bertacco. Spin-Polarized Tunneling Spectroscopy in Tunnel Junctions with Half-Metallic Electrodes. *Physical Review Letters*, 95(13):137203, September 2005.

[127] Fatima Djeghloul, Manuel Gruber, Etienne Urbain, Dimitra Xenioti, Loic Joly, Samy Boukari, Jacek Arabski, Hervé Bulou, Fabrice Scheurer, François Bertran, Patrick Le Fèvre, Amina Taleb-Ibrahimi, Wulf Wulfhekel, Guillaume Garreau, Samar Hajjar-Garreau, Patrick Wetzel, Mebarek Alouani, Eric Beaurepaire, Martin Bowen, and Wolfgang Weber. High Spin Polarization at Ferromagnetic Metal–Organic Interfaces: A Generic Property. *The Journal of Physical Chemistry Letters*, 7(13):2310–2315, July 2016.

[128] Hua Wu, Alessandro Stroppa, Sung Sakong, Silvia Picozzi, Matthias Scheffler, and Peter Kratzer. Magnetism in C- or N-doped MgO and ZnO: A Density-Functional Study of Impurity Pairs. *Physical Review Letters*, 105(26):267203, December 2010.

[129] S.-W. Chung, T. Kishi, J. W. Park, M. Yoshikawa, K. S. Park, T. Nagase, K. Sunouchi, H. Kanaya, G. C. Kim, K. Noma, M. S. Lee, A. Yamamoto, K. M. Rho, K. Tsuchida, S. J. Chung, J. Y. Yi, H. S. Kim, Y.S. Chun, H. Oyamatsu, and

S. J. Hong. 4Gbit density STT-MRAM using perpendicular MTJ realized with compact cell structure. In *2016 IEEE International Electron Devices Meeting (IEDM)*, pages 27.1.1–27.1.4, San Francisco, CA, USA, December 2016. IEEE.

[130] N V Volkov, C G Lee, P D Kim, E V Eremin, and G S Patrin. Optically driven conductivity and magnetoresistance in a manganite-based tunnel structure. *Journal of Physics D: Applied Physics*, 42(20):205009, October 2009.

[131] Tomoyasu Taniyama, Eiji Wada, Mitsuru Itoh, and Masahito Yamaguchi. Electrical and optical spin injection in ferromagnet/semiconductor heterostructures. *NPG Asia Materials*, 3(7):65–73, July 2011.

[132] C. K. Chiang, C. R. Fincher, Y. W. Park, A. J. Heeger, H. Shirakawa, E. J. Louis, S. C. Gau, and Alan G. MacDiarmid. Electrical Conductivity in Doped Polyacetylene. *Physical Review Letters*, 39(17):1098–1101, October 1977.

[133] Sebastian Reineke, Frank Lindner, Gregor Schwartz, Nico Seidler, Karsten Walzer, Björn Lüssem, and Karl Leo. White organic light-emitting diodes with fluorescent tube efficiency. *Nature*, 459(7244):234–238, May 2009.

[134] W. U. Huynh. Hybrid Nanorod-Polymer Solar Cells. *Science*, 295(5564):2425–2427, March 2002.

[135] Jingbo Zhao, Yunke Li, Guofang Yang, Kui Jiang, Haoran Lin, Harald Ade, Wei Ma, and He Yan. Efficient organic solar cells processed from hydrocarbon solvents. *Nature Energy*, 1(2):15027, February 2016.

[136] Tatsuo Hasegawa and Jun Takeya. Organic field-effect transistors using single crystals. *Science and Technology of Advanced Materials*, 10(2):024314, April 2009.

[137] Z. G. Yu. Impurity-band transport in organic spin valves. *Nature Communications*, 5(1):4842, December 2014.

[138] L. Zuppiroli, M. N. Bussac, S. Paschen, O. Chauvet, and L. Forro. Hopping in disordered conducting polymers. *Physical Review B*, 50(8):5196–5203, August 1994.

[139] V. Dediu, M. Murgia, F.C. Matacotta, C. Taliani, and S. Barbanera. Room temperature spin polarized injection in organic semiconductor. *Solid State Communications*, 122(3-4):181–184, April 2002.

[140] Z H Xiong, Di Wu, Z Valy Vardeny, and Jing Shi. Giant magnetoresistance in organic spin-valves. *Nature*, 427:4, 2004.

[141] F.J. Wang, Z.H. Xiong, D. Wu, J. Shi, and Z.V. Vardeny. Organic spintronics: The case of Fe/Alq3/Co spin-valve devices. *Synthetic Metals*, 155(1):172–175, October 2005.

[142] W J M Naber, S Faez, and W G van der Wiel. Organic spintronics. *Journal of Physics D: Applied Physics*, 40(12):R205–R228, June 2007.

[143] Jagadeesh S. Moodera, Bert Koopmans, and Peter M. Oppeneer. On the path toward organic spintronics. *MRS Bulletin*, 39(07):578–581, July 2014.

[144] Karthik V. Raman, Alexander M. Kamerbeek, Arup Mukherjee, Nicolae Atodiresei, Tamal K. Sen, Predrag Lazić, Vasile Caciuc, Reent Michel, Dietmar Stalke, Swadhin K. Mandal, Stefan Blügel, Markus Münzenberg, and Jagadeesh S. Moodera. Interface-engineered templates for molecular spin memory devices. *Nature*, 493(7433):509–513, January 2013.

[145] Vonika Ka-Man Au, Di Wu, and Vivian Wing-Wah Yam. Organic Memory Devices Based on a Bis-Cyclometalated Alkynylgold(III) Complex. *Journal of the American Chemical Society*, 137(14):4654–4657, April 2015.

[146] Jianhui Hou, Olle Inganäs, Richard H. Friend, and Feng Gao. Organic solar cells based on non-fullerene acceptors. *Nature Materials*, 17(2):119–128, February 2018.

[147] Yasunori Takeda, Kazuma Hayasaka, Rei Shiwaku, Koji Yokosawa, Takeo Shiba, Masashi Mamada, Daisuke Kumaki, Kenjiro Fukuda, and Shizuo Tokito. Fabrication of Ultra-Thin Printed Organic TFT CMOS Logic Circuits Optimized for Low-Voltage Wearable Sensor Applications. *Scientific Reports*, 6(1):25714, September 2016.

[148] Jonathan Rivnay, Sahika Inal, Alberto Salleo, Róisín M. Owens, Magnus Berggren, and George G. Malliaras. Organic electrochemical transistors. *Nature Reviews Materials*, 3(2):17086, February 2018.

[149] B. Averill and P. Eldredge. *General Chemistry: Principles, Patterns, and Applications*. Saylor Foundation, 2011.

[150] J. E. House. *Inorganic Chemistry*. Academic Press/Elservier, Amsterdam ; Boston, 2008. OCLC: ocn213765950.

[151] Jens Brede, Nicolae Atodiresei, Stefan Kuck, Predrag Lazić, Vasile Caciuc, Yoshitada Morikawa, Germar Hoffmann, Stefan Blügel, and Roland Wiesendanger. Spin- and Energy-Dependent Tunneling through a Single Molecule with Intramolecular Spatial Resolution. *Physical Review Letters*, 105(4), July 2010.

[152] Sriharsha V. Aradhya and Latha Venkataraman. Single-molecule junctions beyond electronic transport. *Nature Nanotechnology*, 8(6):399–410, June 2013.

[153] Lapo Bogani and Wolfgang Wernsdorfer. Molecular spintronics using single-molecule magnets. *NANOSCIENCE AND TECHNOLOGY*, 7:8, 2009.

[154] Paolo Ballirano, Ruggero Caminiti, Claudio Ercolani, Adriana Maras, and Maria Antonietta Orrù. X-ray Powder Diffraction Structure Reinvestigation of the α and β Forms of Cobalt Phthalocyanine and Kinetics of the α → β Phase Transition. *Journal of the American Chemical Society*, 120(49):12798–12807, December 1998.

[155] M. Ashida, N. Uyeda, and E. Suito. Thermal transformation of vacuum-condensed thin films of copper-phthalocyanine. *Journal of Crystal Growth*, 8(1):45–56, January 1971.

[156] Manuel Gruber, Fatima Ibrahim, Samy Boukari, Hironari Isshiki, Loïc Joly, Moritz Peter, Micha\l Studniarek, Victor Da Costa, Hashim Jabbar, Vincent Davesne, Ufuk Halisdemir, Jinjie Chen, Jacek Arabski, Edwige Otero, Fadi Choueikani, Kai Chen, Philippe Ohresser, Wulf Wulfhekel, Fabrice Scheurer, Wolfgang Weber, Mebarek Alouani, Eric Beaurepaire, and Martin Bowen. Exchange bias and room-temperature magnetic order in molecular layers. *Nature materials*, 14(10):981–4, 2015.

[157] M. Evangelisti, J. Bartolomé, L. J. de Jongh, and G. Filoti. Magnetic properties of α -iron(II) phthalocyanine. *Physical Review B*, 66(14):144410, October 2002.

[158] Wei Wu, A. Kerridge, A. H. Harker, and A. J. Fisher. Structure-dependent exchange in the organic magnets Cu(II)Pc and Mn(II)Pc. *Physical Review B*, 77(18):184403, May 2008.

[159] S Nešpůrek, H Podlesak, and C Hamann. Structure and photoelectrical behaviour of vacuum-evaporated metal-free phthalocyanine films. *Thin Solid Films*, 249(2):230–235, September 1994.

[160] S. Heutz, S. M. Bayliss, R. L. Middleton, G. Rumbles, and T. S. Jones. Polymorphism in Phthalocyanine Thin Films: Mechanism of the α → β Transition. *The Journal of Physical Chemistry B*, 104(30):7124–7129, August 2000.

[161] S. Yim, S. Heutz, and T. S. Jones. Model for the A → β1 phase transition in phthalocyanine thin films. *Journal of Applied Physics*, 91(6):3632–3636, March 2002.

[162] Michele Serri, Wei Wu, Luke R. Fleet, Nicholas M. Harrison, Cyrus F. Hirjibehedin, Christopher W.M. Kay, Andrew J. Fisher, Gabriel Aeppli, and Sandrine Heutz. High-temperature antiferromagnetism in molecular semiconductor thin films and nanostructures. *Nature Communications*, 5(1), December 2014.

[163] Xi Chen, Ying-Shuang Fu, Shuai-Hua Ji, Tong Zhang, Peng Cheng, Xu-Cun Ma, Xiao-Long Zou, Wen-Hui Duan, Jin-Feng Jia, and Qi-Kun Xue. Probing Superexchange Interaction in Molecular Magnets by Spin-Flip Spectroscopy and Microscopy. *Physical Review Letters*, 101(19), November 2008.

[164] H. Wende, M. Bernien, J. Luo, C. Sorg, N. Ponpandian, J. Kurde, J. Miguel, M. Piantek, X. Xu, Ph. Eckhold, W. Kuch, K. Baberschke, P. M. Panchmatia, B. Sanyal, P. M. Oppeneer, and O. Eriksson. Substrate-induced magnetic ordering and switching of iron porphyrin molecules. *Nature Materials*, 6(7):516–520, July 2007.

[165] A. Scheybal, T. Ramsvik, R. Bertschinger, M. Putero, F. Nolting, and T.A. Jung. Induced magnetic ordering in a molecular monolayer. *Chemical Physics Letters*, 411(1-3):214–220, August 2005.

[166] Sebastian Loth, Christopher P Lutz, and Andreas J Heinrich. Spin-polarized spin excitation spectroscopy. *New Journal of Physics*, 12(12):125021, December 2010.

[167] Ying-Shuang Fu, Tong Zhang, Shuai-Hua Ji, Xi Chen, Xu-Cun Ma, Jin-Feng Jia, and Qi-Kun Xue. Identifying Charge States of Molecules with Spin-Flip Spectroscopy. *Physical Review Letters*, 103(25):257202, December 2009.

[168] R L Stamps. Mechanisms for exchange bias. *Journal of Physics D: Applied Physics*, 34(3):444–444, 2001.

[169] W. H. Meiklejohn and C. P. Bean. New Magnetic Anisotropy. *Physical Review*, 102(5):1413–1414, June 1956.

[170] Florin Radu. *Fundamental aspects of exchange bias effect in AF/F bilayers and multilayers*. PhD thesis, Ruhr-Univarsitat Buchum, 2005.

[171] F. Radu, M. Etzkorn, R. Siebrecht, T. Schmitte, K. Westerholt, and H. Zabel. Interfacial domain formation during magnetization reversal in exchange-biased CoO/Co bilayers. *Physical Review B*, 67(13):134409, April 2003.

[172] S. S. P. Parkin, K. P. Roche, M. G. Samant, P. M. Rice, R. B. Beyers, R. E. Scheuerlein, E. J. O'Sullivan, S. L. Brown, J. Bucchigano, D. W. Abraham, Yu Lu, M. Rooks, P. L. Trouilloud, R. A. Wanner, and W. J. Gallagher. Exchange-biased magnetic tunnel junctions and application to nonvolatile magnetic random access memory (invited). *Journal of Applied Physics*, 85(8):5828–5833, April 1999.

[173] B. Dai, Y. Lei, X.P. Shao, and J. Ni. Improved exchange bias of PtCr antiferromagnets with FeMn or Mn addition. *Journal of Alloys and Compounds*, 490(1-2):427–430, February 2010.

[174] Junhyeon Jo, Jinho Byun, Inseon Oh, Jungmin Park, Mi-Jin Jin, Byoung-Chul Min, Jaekwang Lee, and Jung-Woo Yoo. Molecular Tunability of Magnetic Exchange Bias and Asymmetrical Magnetotransport in Metalloporphyrin/Co Hybrid Bilayers. *ACS Nano*, 13(1):894–903, January 2019.

[175] K. O'Grady, L.E. Fernandez-Outon, and G. Vallejo-Fernandez. A new paradigm for exchange bias in polycrystalline thin films. *Journal of Magnetism and Magnetic Materials*, 322(8):883–899, April 2010.

[176] Stefano Sanvito. The rise of spinterface science: Molecular spintronics. *Nature Physics*, 6(8):562–564, August 2010.

[177] Marta Galbiati, Sergio Tatay, Clément Barraud, Alek V. Dediu, Frédéric Petroff, Richard Mattana, and Pierre Seneor. Spinterface: Crafting spintronics at the molecular scale. *MRS Bulletin*, 39(07):602–607, July 2014.

[178] Alexandre R. Rocha, Víctor M. García-suárez, Steve W. Bailey, Colin J. Lambert, Jaime Ferrer, and Stefano Sanvito. Towards molecular spintronics. *Nature Materials*, 4(4):335–339, April 2005.

[179] K. Bouzehouane, S. Fusil, M. Bibes, J. Carrey, T. Blon, M. Le Dû, P. Seneor, V. Cros, and L. Vila. Nanolithography Based on Real-Time Electrically Controlled Indentation with an Atomic Force Microscope for Nanocontact Elaboration. *Nano Letters*, 3(11):1599–1602, November 2003.

[180] M. Bowen, M. Bibes, A. Barthélémy, J.-P. Contour, A. Anane, Y. Lemaıtre, and A. Fert. Nearly total spin polarization in La2/3Sr1/3MnO3 from tunneling experiments. *Applied Physics Letters*, 82(2):233–235, January 2003.

[181] S. Javaid, M. Bowen, S. Boukari, L. Joly, J.-B. Beaufrand, Xi Chen, Y. J. Dappe, F. Scheurer, J.-P. Kappler, J. Arabski, W. Wulfhekel, M. Alouani, and E. Beaurepaire. Impact on Interface Spin Polarization of Molecular Bonding to Metallic Surfaces. *Physical Review Letters*, 105(7):077201, August 2010.

[182] Stefan Lach, Anna Altenhof, Kartick Tarafder, Felix Schmitt, Md. Ehesan Ali, Michael Vogel, Jens Sauther, Peter M. Oppeneer, and Christiane Ziegler. Metal-Organic Hybrid Interface States of A Ferromagnet/Organic Semiconductor Hybrid Junction as Basis For Engineering Spin Injection in Organic Spintronics. *Advanced Functional Materials*, 22(5):989–997, March 2012.

[183] C. Iacovita, M. V. Rastei, B. W. Heinrich, T. Brumme, J. Kortus, L. Limot, and J. P. Bucher. Visualizing the Spin of Individual Cobalt-Phthalocyanine Molecules. *Physical Review Letters*, 101(11), September 2008.

[184] Humberto Soscún, Ysaías Alvarado, Javier Hernández, Paola Hernández, Reinaldo Atencio, and Alan Hinchliffe. Experimental and theoretical determination of the dipole polarizability of dibenzothiophene: DIPOLE POLARIZABILITY DETERMINATION OF DIBENZOTHIOPHENE. *Journal of Physical Organic Chemistry*, 14(10):709–715, October 2001.

[185] Clément Barraud, Karim Bouzehouane, Cyrile Deranlot, Stéphane Fusil, Hashim Jabbar, Jacek Arabski, Rajib Rakshit, Dong-Jik Kim, Christophe Kieber, Samy Boukari, Martin Bowen, Eric Beaurepaire, Pierre Seneor, Richard Mattana, and Frédéric Petroff. Unidirectional Spin-Dependent Molecule-Ferromagnet Hybridized States Anisotropy in Cobalt Phthalocyanine Based Magnetic Tunnel Junctions. *Physical Review Letters*, 114(20), May 2015.

[186] C. Barraud, K. Bouzehouane, C. Deranlot, D. J. Kim, R. Rakshit, S. Shi, J. Arabski, M. Bowen, E. Beaurepaire, S. Boukari, F. Petroff, P. Seneor, and R. Mattana. Phthalocyanine based molecular spintronic devices. *Dalton Transactions*, 45(42):16694–16699, 2016.

[187] C. F. Hirjibehedin. Spin Coupling in Engineered Atomic Structures. *Science*, 312(5776):1021–1024, May 2006.

[188] Andrea Droghetti, Philip Thielen, Ivan Rungger, Norman Haag, Nicolas Großmann, Johannes Stöckl, Benjamin Stadtmüller, Martin Aeschlimann, Stefano Sanvito, and Mirko Cinchetti. Dynamic spin filtering at the Co/Alq3 interface mediated by weakly coupled second layer molecules. *Nature Communications*, 7(1):12668, November 2016.

[189] P F Siles, T Hahn, G Salvan, M Knupfer, F Zhu, D R T Zahn, and O G Schmidt. Tunable charge transfer properties in metal-phthalocyanine heterojunctions. *Nanoscae*, 8(8607):12, 2016.

[190] Takeshi Kawabe, Koki Shimose, Minori Goto, Yoshishige Suzuki, and Shinji Miwa. Magnetic tunnel junction with Fe(001)/Co phthalocyanine/MgO(001) single-crystal multilayer. *Applied Physics Express*, 11(1):013201, January 2018.

[191] Junwei Tong, Liuxia Ruan, Xiannian Yao, Gaowu Qin, and Xianmin Zhang. Defect states dependence of spin transport in iron phthalocyanine spin valves. *Physical Review B*, 99(5):054406, February 2019.

[192] Kai Yang, Hui Chen, Thomas Pope, Yibin Hu, Liwei Liu, Dongfei Wang, Lei Tao, Wende Xiao, Xiangmin Fei, Yu-Yang Zhang, Hong-Gang Luo, Shixuan Du, Tao Xiang, Werner A. Hofer, and Hong-Jun Gao. Tunable giant magnetoresistance in a single-molecule junction. *Nature Communications*, 10(1):3599, December 2019.

[193] E Urbain. *Utilisation de semi-conducteurs organiques comme barrière tunnel pour l'électronique de spin*. PhD thesis, Universite de Strasbourg, 2017.

[194] Dali Sun, Lifeng Yin, Chengjun Sun, Hangwen Guo, Zheng Gai, X.-G. Zhang, T. Z. Ward, Zhaohua Cheng, and Jian Shen. Giant Magnetoresistance in Organic Spin Valves. *Physical Review Letters*, 104(23), June 2010.

[195] W. G. Wang, A. Pearse, M. Li, S. Hageman, A. X. Chen, F. Q. Zhu, and C. L. Chien. Parallel fabrication of magnetic tunnel junction nanopillars by nanosphere lithography. *Scientific Reports*, 3(1), December 2013.

[196] Samy Boukari, Hashim Jabbar, Filip Schleicher, Manuel Gruber, Garen Avedissian, Jacek Arabski, Victor Da Costa, Guy Schmerber, Prashanth Rengasamy, Bertrand Vileno, Wolfgang Weber, Martin Bowen, and Eric Beaurepaire. Disentangling Magnetic Hardening and Molecular Spin Chain Contributions to Exchange Bias in Ferromagnet/Molecule Bilayers. *Nano Letters*, 18(8):4659–4663, August 2018.

[197] Karthik V. Raman. Interface-assisted molecular spintronics. *Applied Physics Reviews*, 1(3):031101, September 2014.

[198] R. Lin, F. Wang, J. Rybicki, M. Wohlgenannt, and K. A. Hutchinson. Distinguishing between tunneling and injection regimes of ferromagnet/organic semiconductor/ferromagnet junctions. *Physical Review B*, 81(19):195214, May 2010.

[199] Sayani Majumdar and Himadri S. Majumdar. On the origin of decay of spin current with temperature in organic spintronic devices. *Organic Electronics*, 13(11):2653–2658, November 2012.

[200] T. Lan Anh Tran, T. Quyen Le, Johnny G. M. Sanderink, Wilfred G. van der Wiel, and Michel P. de Jong. The Multistep Tunneling Analogue of Conductivity Mismatch in Organic Spin Valves. *Advanced Functional Materials*, 22(6):1180–1189, March 2012.

Kostantine KATCKO

Probing inorganic and organic paths through spin-driven transport

Résumé

La spintronique s'est avérée très performante dans le domaine des nanotechnologies grâce à sa contribution importante aux technologies de stockage d'informations. Ce doctorat de thèse a eu pour objectif de clarifier les réalisations spintroniques modernes et d'étendre au-delà de l'état actuel de la technique en dévoilant de nouvelles applications en spintronique telles que la production d'énergie ou la spintronique moléculaire. Premièrement, à travers des études expérimentales on ait révélé la présence de lacunes en oxygène dans les jonctions tunnel magnétiques ordinaires à base de MgO, nous avons ensuite caractérisé leur empreinte énergétique dans la bande interdite du MgO par le biais du transport de spin. De plus, nous avons démontré la modification des propriétés de spintronique dans ces jonctions tunnel magnétiques grâce à l'adressage optique de chemins nano-spintroniques formés par des lacunes d'oxygène. Deuxièmement, nous avons confirmé les rapports pionniers précédents sur la spintronique organique à base des phtalocyanines et développé les concepts de leur opération très prometteuse. Troisièmement, nous avons présenté le modèle analytique d'un moteur à spin capable de récolter les fluctuations thermiques sur des états d'énergie dégénérés en spin et de le convertir en énergie électrique utile. De plus, ce moteur de spin conceptuel a été reproduit expérimentalement dans une simple jonction tunnel magnétique à base de MgO-C à température ambiante.

Mots-clés: Spintronique Organique et Inorganique, Défauts Ponctuels, Récolte d'Énergie, Magnetotransport, Adressage Optique, Nanotechnologies

Abstract

Spintronics proved to be a high performer in the field of nanotechnologies through its significant input into information-storage technologies. This Ph.D. thesis aims to clarify the modern spintronic achievements and to expand beyond the current state of the art by unveiling novel applications in spintronics such as power generation or molecular spintronics. First, though multifunctional experimental studies we revealed the presence of oxygen vacancies in commonplace MgO-based magnetic tunnel junctions, further we characterized their energetic footprint in the band-gap of MgO through spin-driven transport. Additionally, we demonstrated the modification of spintronic properties in magnetic tunnel junctions through the optical addressing of nano-spintronic paths formed by oxygen vacancies. Secondly, we've confirmed the previous pioneering reports on phthalocyanine-based organic spintronics and further developed the concepts of their very promising operation. Thirdly, we introduced the analytical model of a spin-engine capable of harvesting thermal fluctuations on degenerate spin-split energy states and converting it into useful electrical power. further, this conceptual spin-engine was experimentally reproduced within a simple MgO-C based magnetic tunnel junctions at room-temperature.

Keywords: Organic-Inorganic Spintronics, Point-Defects, Energy-Harvesting, Magnetotransport, Optical addressing, Nanotechnologie